IMPERIAL COLLEGE LONDON

Pseudospectral Collocation Method for Viscoelastic Guided Wave Problems in Generally Anisotropic Media

by

Francisco Hernando Quintanilla

A thesis submitted to Imperial College London for the degree of
Doctor of Philosophy

Department of Mechanical Engineering
Imperial College London
London SW7 2BZ
United Kingdom

February 2016

Acknowledgements

In these two pages, I would like to express my gratitude to Professor Mike Lowe, my patient supervisor, Professor Peter Cawley and Doctor Frederic Cegla from the NDT group at Imperial College London for giving me the opportunity of pursuing my doctoral studies within their group, for their academic advice and for their financial support. I would also like to thank Miss Nina Hancock for her assistance and patience in dealing with all the travel arrangements and bureaucracy throughout these years.

My special thanks to Professor Richard Craster from the Mathematics Department at Imperial for his unconditional and continued support in every respect and also to Doctor Guillermo Rein from the Mechanical Engineering Department for his assistance in the examination process and advice.

I would also like to express in advance my gratitude, and perhaps even condolences, to my external examiners Professor John Chapman at Keele University and Professor Michel Castaings at the University of Bordeaux for their patience in going through the 200+ pages of this thesis.

Thanks to all my colleagues at Imperial College for making my stay a pleasure by sharing more drinks than tears (hopefully there will not be many of the latter after the VIVA) and especially to former group member Doctor Zheng Fan who kindly gave his permission to include and reproduce section 3.4 of this thesis and for his patience when carrying out the validations and SAFE simulations.

Thanks to the late Professor Pedro Mejias Arias, to his widow Professor Rosario Martinez Herrero and to Professor Marina Ramon Medrano from the Physics Faculty at the Universidad Complutense de Madrid for their excellent and enlightening lectures and for their advice and support before, during and after coming to Imperial College. Also, thanks to Doctor Alberto Gonzalez Martinez from the Mining Engineering Faculty at Universidad de Leon for his constant support and encouragement. My thanks, and apologies, go also to all my other teachers from University down to Primary School who, due to the finiteness of this page and limitations of my own memory, I can neither name nor remember in full.

Many, many thanks to my Mum, to my Grandmum, who died shortly after I started my PhD, and to the rest of my family for their care and patience in my education and for their loving support throughout these years.

To all my friends, new and old alike, thanks for their friendship, encouragement, short- and long-distance support and constructive criticism: *I do not need friends who nod when I nod. My shadow does it much better.* Plutarco.

And last but not least, thanks to my loving girlfriend Egle whom I had the luck and pleasure of meeting more than two years ago and who stood by side in the ups and downs of this adventure.

Copyright Declaration

The copyright of this thesis rests with the author and is made available under a Creative Commons Attribution Non-Commercial No Derivatives licence. Researchers are free to copy, distribute or transmit the thesis on the condition that they attribute it, that they do not use it for commercial purposes and that they do not alter, transform or build upon it. For any reuse or redistribution, researchers must make clear to others the licence terms of this work.

Declaration of Originality

I declare that the content of this thesis is the product of my own work and all else has been appropriately referenced and acknowledged.

Abstract

In Non-Destructive Evaluation (NDE) applications guided waves are attractive to perform rapid inspections of long lengths and large areas. However, they are complicated, therefore it is important to have as much information and understanding about their physical properties as possible in order to design the most efficient and robust inspection process as well as to draw the correct conclusions from the measurement results. The main piece of information to gain insight into the guided wave's properties is dispersion curves which, for isotropic structures such as plates and cylinders, have been available for many years. There are many robust algorithms which are currently used to compute them: finite element simulations, partial wave based root finding routines (PWRF) and semi-analytical finite element simulations (SAFE). These methodologies have been generalized and also used to study and compute dispersion curves of more complicated anisotropic materials though the range of tractable cases was limited.

Although robust, all these approaches present several challenges, mostly computational, such as missing modes (PWRF), the so called "large-fd" problem (PWRF), artificially increased stiffness (FE, SAFE) or improvement of dispersion curve tracing routines (FE, PWRF, SAFE). In addition, when studying complicated anisotropic materials with a low degree of symmetry or unusual axes configurations where propagation does not take place along any of the principal axes, PWRF routines are frequently unreliable and one must resort to specific SAFE simulations which also present their own challenges and, depending on the SAFE scheme used, can yield spurious modes which need to be carefully filtered. Recently, Pseudospectral Methods (Galerkin and Collocation schemes), were introduced in the field of elastic guided waves, providing a powerful, yet strikingly and conceptually simple alternative to the above algorithms by successfully finding the dispersion curves in isotropic structures and in some simple anisotropic problems.

However, a systematic and general approach for accurately and robustly computing dispersion curves of guided waves in anisotropic media, up to the most general case of *triclinic* symmetry, has not yet been developed. The goal of the work presented in this thesis is to develop such a tool by means of the Pseudospectral Collocation Method (SCM) and to take advantage of its particular features to make it as robust as possible.

Firstly, a PSCM scheme is developed for computing dispersion curves of guided waves in anisotropic *elastic* media by finding all the frequencies for a given value of the real wavenumber. The results are validated with the existing literature as well as with the results provided by the software DISPERSE developed in the NDT group at Imperial College London. Many of

4

the most remarkable features of the PSCM (spectral accuracy, speed, and its failure to miss modes for instance) are already observed in this simple, yet important, class of problems in elastic media.

Secondly, guided waves in *viscoelastic* anisotropic media are studied. In this case, modes present attenuation due to material damping which is reflected in the wavenumber being complex. In order to handle complex wavenumbers the PSCM schemes developed for elastic materials are appropriately extended by means of the *Companion Matrix Method*. It will be seen that, apart from lowly attenuated propagating modes, all the other highly attenuated modes are found, yielding the full three-dimensional spectrum of the problem under consideration. Moreover, when the PSCM schemes for viscoelastic media are used to compute the dispersion curves of guided waves in an elastic medium, all the remaining, imaginary as well as complex, roots of the elastic problem which were not computed by the simpler PSCM elastic schemes are found, providing the full three-dimensional picture of the dispersion curves.

These PSCM schemes, as any other of the aforementioned approaches, only find pairs (ω, k). If dispersion curves are to be plotted, those pairs must be linked correctly in order to plot the desired dispersion curves, which is non-trivial when crossings amongst modes occur. Motivated by this, an investigation of the parity and coupling properties of guided wave solutions is carried out in detail for all crystal classes. This investigation provides a robust alternative to conventional tracing routines and avoids the problem of mode crossings by exploiting the parity and coupling properties of the solutions.

Finally, the most complicated problems involving embedded structures are investigated by including a *Perfectly Matched Layer* (PML) in the previously developed PSCM schemes for viscoelastic media. The dispersion curves for leaky and trapped modes in an isotropic elastic plate and in a similar cylinder immersed in an infinite ideal fluid are found, showing very good agreement with the results given by PWRF routines in a large range of frequencies. Last, but not least, an illustration of a two-dimensional PSCM scheme is presented to study a vibrating membrane. The results are compared with the available analytical solution showing again excellent agreement.

List of Publications

1. F. Hernando Quintanilla, M. J. S. Lowe and R. V. Craster; *Dispersion Curves for Guided Elastic Waves in Multi-layered Anisotropic Media Generated with the Spectral Method*; Conference Proceedings of the 41st Annual Review of Progress in Quantitative Nondestructive Evaluation, Vol.**33**, 2014.

2. F. Hernando Quintanilla, M. J. S. Lowe and R. V. Craster; *Full 3D Dispersion Curve Solutions for Guided Waves in Generally Anisotropic Media*; Journal of Sound and Vibration, **363**, pp. 545-559, 2015.

3. F. Hernando Quintanilla, Z. Fan, M. J. S. Lowe and R. V. Craster; *Guided Waves' Dispersion Curves in Anisotropic Viscoelastic Single- and Multi-layered Media*; Proceedings of the Royal Society A, **471**, pp. 1-23, 2015.

4. F. Hernando Quintanilla, M. J. S. Lowe and R. V. Craster; *Modelling Guided Elastic Waves in Generally Anisotropic Media using a Spectral Collocation Method*; Journal of the Acoustical Society of America, **137 (3)**, pp. 1180-1194, 2015.

5. F. Hernando Quintanilla, Z. Fan, M. J. S. Lowe and R. V. Craster; *Dispersion Loci of Guided Waves in Viscoelastic Composites of General Anisotropy*; Conference Proceedings of the 42n Annual Review of Progress in Quantitative Nondestructive Evaluation, Vol.**34**, 2015.

6. F. Hernando Quintanilla, M. J. S. Lowe and R. V. Craster; *Symmetry and Coupling Properties of Guided Waves in Generally Anisotropic Flat and Cylindrical Multiple-layer Systems*; **Submitted to Journal of the Acoustical Society of America**, 2016.

7. F. Hernando Quintanilla, M. J. S. Lowe and R. V. Craster; *Dispersion Curves for Waves in Fluid-loaded Orthorhombic Waveguides with Pseudospectral Collocation Method and Perfectly Matched Layer*; **In preparation**, 2016.

Contents

Chapter 1

Introduction

1.1 Motivation

Guided waves play an important role in many branches of physics and engineering. In particular, they are an essential tool for engineers working in non-destructive evaluation (NDE) or structure health monitoring (SHM) where they are widely deployed to inspect large regions of structure. Selecting the most appropriate mode to propagate in a structure in order to detect a particular type of defect relies on the knowledge of the guided waves' dispersion curves for that particular structure. The pioneering works of Lord Rayleigh and Horace Lamb laid the foundation of the investigations and developments which were to be made in years to come.

Some of the first studies of guided waves and their dispersion curves in flat and cylindrical structures were carried out by Mindlin ([1]), Pao ([2],[3]) and Gazis ([4]) to cite a few. Later, Auld ([5]), Graff ([6]) or Achenbach ([7]) for instance continued these investigations. Solie and Auld also studied anisotropic materials with cubic symmetry ([8]). These investigations of anisotropic media were continued by other researchers such as Nayfeh, Chimenti ([9], [10], [11]), Rokhlin and Wang ([12]) or Li and Thompson ([13]).

Several methods were proposed to study and compute these dispersion curves. Most notably, the Transfer Matrix and Global Matrix algorithms, based in the Partial Wave decomposition approach (see [5] for instance), have been extensively used for decades with excellent results for a broad range of cases and materials, a thorough review can be found in [14]. In order to meet the demands of the research and engineering communities a software package (DISPERSE) for the computation of dispersion curves based on the aforementioned methods was developed, primarily, by Lowe, Pavlakovic *et .al* [15] at Imperial College. It has been widely and robustly tested during its development and in the subsequent years and it can solve a wide range of prob-

lems: free or embedded structures and isotropic as well as some anisotropic materials. The algorithm used to compute the dispersion curves is based on the PW approach and the aforementioned matricial methods to derive a dispersion relation for the problem whose roots are found by means of a root-finding algorithm. An interpolation routine is then used to link these roots and yields the mode curves. It also provides with mode shapes for the displacement field, stress components or energy of a given mode amongst other features. See [16] for more details. It has become an established and well-known tool used worldwide by engineers and researchers working with guided waves.

An alternative to partial wave based root-finding (PWRF) routines have been Finite Element (FE) simulations, in particular the Semi-Analytical Finite Element (SAFE) method. They provide with more flexibility designing the waveguide and have been extensively and successfully used to model those cases which posed a challenge for PWRF routines, see [17], [18] and [19] for example. In addition, pseudospectral (Galerkin and Collocation) methods have been recently used to tackle guided wave problems in acoustics or geophysics for instance, see [20], [21] and [22].

In past years the development of new materials such as composites for aerospace and aircraft applications has led to the need of state-of-the-art tools to inspect and study these structures. Some of the above approaches have successfully addressed these demands but many problems remain unsolved and there is no systematic yet simple numerical approach to guided wave problems in anisotropic materials which allows researchers and engineers to obtain dispersion curves for the variety of structures and problems they are faced with. Some of these challenges comprise plates or cylinder where the fibres of the composite are arbitrarily oriented with respect to the axes of the structure. Multilayer systems composed of several layers of anisotropic materials also pose a great challenge for conventional routines. Finally, roots with a large imaginary part are problematic and difficult to find, especially in cases of strong anisotropy, and they are essential in order to have a complete picture of the spectrum of the problem at hand.

The investigations presented in this thesis aim to fill those gaps and provide with as general a method as possible to study and solve acoustic guided wave problems in generally anisotropic media. The approach used belongs to the family of numerical methods known as pseudospectral methods ([23] and [24]). In particular, a Pseudospectral Collocation Method (PSCM) has been chosen for its conceptual simplicity, ease of code, flexibility and accuracy. More details will be given later in the thesis but, briefly, the PSCM discretizes the physical domain with a grid of points and uses a family of suitably chosen *global interpolant polynomials* (as opposed to the local inter-

polant polynomials used by FE approaches) to expand the functions in the problem. Another key ingredient of the PSCM are the differentiation matrices associated to the family of global interpolants chosen. These substitute the differential operators in a partial differential equation (PDE) turning it into a matricial equation thus allowing for the problem to be recast into a general eigenvalue problem form. This is readily solved with any of the packages available for solving eigenvalue problems.

The advantages of the PSCM with respect to other approaches are various. It is conceptually very simple and intuitive thus allowing for a quick familiarization with it, the book by Trefethen [25] provides with a rich selection of easy examples which illustrate the simplicity of the method. This results in an easier coding task and reduces the likelihood of bugs in the code. Spectral accuracy and the use of global interpolant polynomials makes the method more accurate than approaches using local interpolants. It has also been shown to be faster [21] than some conventional root-finding routines. Its great flexibility allows for the solution of the most complicated and general problems, such as those involving triclinic materials, with almost no extra effort on the side of the practitioner. Another very interesting and advantageous feature is that it solves the problem algebraically and hence it computes equally well real and complex eigenvalues. This will be seen to be particularly convenient when viscoelastic materials are studied.

The issue of modes crossing will also be addressed. This issue has been widely studied in the literature, see [26], [27], [28], [29] and [30] for instance. However no systematic approach to this problem had been proposed and only particular cases were studied. The investigation contained in this thesis also aims to provide with a general approach to this issue and the conclusions are tested with numerical examples. This problem is closely related to mode tracing which is normally done by either using interpolating routines [14] or by exploiting orthogonality (biorthogonality) of modes and energy arguments [5]. It is hoped that the results presented here will facilitate this task.

1.2   Outline of the Thesis

This thesis has been divided into different chapters according to the particular problem studied in them. In Chapter 2 the propagation of guided waves in perfectly elastic materials is studied. Single as well as multi-layered systems in flat and cylindrical geometry will be investigated. Examples will be presented for a number of different anisotropic materials including the triclinic crystal class which is the most general type of anisotropic material one can have. Flat structures will be studied first since they will serve later

for validation of the cylindrical cases by taking the *thin plate limit* to be explained in more detail later. Then, cylindrical structures will be addressed making use of several flat examples to validate the results and compare.

Chapter 3 extends the PSCM scheme to the more general and realistic group of viscoelastic materials. Guided waves traveling in these materials are attenuated due to material damping and viscosity. In this chapter it will be shown how the PSCM is modified to tackle these problems and how it is possible to obtain the full spectrum of guided wave problems with no extra coding effort regardless of how large or small the imaginary part of the wavenumber is. The codes for these cases are validated with the aid of a SAFE simulation since there are no references in the literature for the most general cases. In Chapter 4, several examples of dispersion curves in three-dimensions will be presented by using the codes developed and validated in the previous chapter. This way of visualization often helps to clarify many aspects of the problem which are not clear in its more conventional and common two-dimensional counterparts.

The next two chapters address the problem of mode crossing and classification. In Chapter 5 the parity properties of the guided wave solutions for all anisotropic crystal classes are studied. It is also shown how this can be exploited to design more efficient codes in which the different families of modes are plotted separately thus avoiding the problem of mode crossings and also freeing some of the codes from the need of interpolating routines. In Chapter 6, the previous results are used to classify anisotropic crystals into fewer classes according to their properties regarding coupling and decoupling of modes as well as the parity of their solutions. Thereafter, the study of multi-layered systems is built upon this basis and several results about how the arrangement of layers affects the parity properties of the guided wave solutions are presented. The generalization to systems with an arbitrary number of layer is presented in the simplest case of SH modes and the more general cases of Lamb and coupled modes is only explained since it does not entail any new techniques and follows exactly along the same lines.

Chapters 7 and 8 present further generalizations and developments of the PSCM to tackle more complicated problems. The case of a flat plate immersed in fluid is presented in chapter 7 and compared to the results given by PWRF routines. The challenges that these problems pose to the PSCM are discussed. Chapter 8 provides an example of a two-dimensional implementation of the PSCM to solve the simple problem of a square vibrating membrane. The results are confronted to the exact known solution and excellent agreement is found. It is hoped that these examples serve as a motivation for further investigating the improvements and developments of

PSCM schemes to solve acoustic wave problems.

The thesis is closed with Chapter 9 where the discussion and conclusion of the main results are given.

Chapter 2

Waves in Elastic Waveguides.

In this first chapter guided waves in perfectly elastic waveguides will be studied. Given the well-established nature of the field, I begin with a short review of the area to set this chapter in context. Analytical methods of solution for the simplest problems, such as that of an elastic plate in vacuum, have been known since times dating back to Lord Rayleigh. Some of these, as well as a copious bibliography, are to be found in texts such as [6], [5], [31] or [7]. Some exact solutions for isotropic media and a few standard geometries are available in textbooks or papers such as Mindlin [1] or Pao [2] and references therein. Most of the general cases for anisotropic materials in flat geometry, although widely-studied, can be found in three papers: Solie and Auld [8] studied the Christoffel equation for modes propagating at various angles in a plate of copper with cubic symmetry. Nayfeh and Chimenti [9] studied a free plate with orthorhombic symmetry and, by means of a rotation, of monoclinic symmetry as well. A more general account of anisotropic plates by the previous authors can be found in [32]. Later, Li and Thompson [13] studied in more detail materials with orthorhombic symmetry and presented various dispersion curves for a variety of orthorhombic materials at different angles of propagation; these are used later to validate the results. In NDE it is essential to treat wave propagation in cylinders and rods since applications such as pipe inspection are commonplace. The isotropic case has been extensively studied by Onoe *et al.* [33], Mindlin and Pao [3], Zemanek [34], Pao [2], or more recently Towfighi *et al.* [20] amongst others.

Multi-layered systems have also been extensively studied by assembling the individual solutions, via interface conditions, into matrix relationships from which a dispersion relation for the whole system emerges. Two exemplars of matrix methods for guided waves in multi-layered waveguides, taken from a rich literature over many years, are the Transfer and Global Matrix methods, described in [14]; some extensions to flat multi-layered anisotropic systems

15

are in [10] and [11]. These approaches have all been based on the representation of the fields in layers by partial waves; they create system matrices with root-finding methods producing dispersion curves. The development of robust root-finding methods is itself a significant challenge [14]. More recently, other authors [20], [35], [36], [21] or [37] have used different methods, which will be briefly described in the paragraphs below, to handle multi-layered systems, mainly in cylindrical geometry. Partial-wave root-finding becomes cumbersome if robust solutions for general anisotropy are desired, so commonly the implementation has been restricted to isotropic, transversely isotropic, orthorhombic and monoclinic materials, [8], [9] and [13]. The upshot is that, to the best of my knowledge, there is no robust, versatile and general method available for the full anisotropic system. FE element methods, though flexible and general enough to treat fully anisotropic systems, can produce spurious modes which need to be filtered, this situation does not arise with PSCM. It is hoped that these investigations will remedy this situation.

Three important challenges with root-finding methods emerge [14]: firstly, it is possible that root-finding routines fail to find a mode and simply skip it, jumping onto the next one, thus missing one solution. In particular, this phenomenon was observed for the general purpose root-finding routine used by the author based on looking for minima of the dispersion relation determinant and then using a two dimensional bisecant method, a more detailed description can be found in [16]. This is normally solved by changing and adjusting the convergence parameters of the routine to make a finer search, but the author is not aware of any successful approach to completely avoid missing roots. Secondly, the so-called "large fd" problem exists; this arises from the existence in the dispersion relation of real positive and negative exponential factors which, when being too large and too small respectively, render the matrix numerically ill-conditioned. This was cured by the use of the Global Matrix Method as described in [14], and by other methods such as the Delta Operator method [38], the Stiffness method [12], and the Impedance method [39], although in all cases this has involved an increase in complexity of the formulation. Finally, a third issue emerges: the matrix becomes singular, yielding a spurious solution, when the wavenumber of the wave in the plate is equal to any of the bulk wavenumbers of the layers of the system. Routines can be programmed to discard such solutions straightaway, but it is troublesome to eliminate these spurious solutions when genuine modes are nearby.

An alternative, philosophically closer approach, is the Semi Analytical Finite Element (SAFE) method popularised by Gavric's [40] work to compute dispersion curves in a free rail. This approach allows for more geometrical flexibility than root-finding and has been successfully used in various

waveguide contexts: Leaky waves travelling along arbitrary cross sectional waveguides surrounded by an infinite medium [17], torsional waves propagating along arbitrary cross sectional waveguides immersed in perfect fluid [41], trapped waves propagating along a welded joint between plates [42], guided waves in viscoelastic media with rectangular, arbitrary cross-sections [18] and axisymmetric cross-section [43].

For the modelling of waveguides of constant cross-section with SAFE, and limiting to flat or cylindrical geometries, one takes a one-dimensional mesh across the thickness of the system, see [43] for instance; the spectral method also uses a grid of points across the thickness but as a global interpolant rather than a local one. The SAFE method requires the use of Hamilton's Principle and finite elements to generate an eigenvalue equation, one advantage of spectral collocation vis-a-vis SAFE is the relative ease of coding and construction of the eigenvalue problem with only matrix methods required.

Probably the most important difference between these methods is the convergence rate of the spatial representation or discretisation, which impacts on the results' accuracy and speed of computation. The convergence rate of the (Pseudo) Spectral Collocation Method (PSCM, Spectral Collocation Method is also found in the literature) [25] is $O(N^{-m})$ for *every m*, where N is the number of grid points (or nodes) and m is a constant, provided the solution is sufficiently differentiable, whereas that of SAFE and other finite element methods is only $O(N^{-m})$ for *some m* which depends on the order of approximation and smoothness of the function. This has serious consequences in terms of accuracy versus matrix size and this comes to the fore when multi-layered media are considered as eigenvalue problems remain manageable in scale. This is a consequence of the PSCM using a global interpolant whilst the finite element method uses local interpolants such as piecewise polynomials; accuracy up to eleven decimal digits is commonplace using the PSCM. These convergence properties can be shown to arise directly from those of Fourier series by the change of coordinates $x = \cos \theta$ which relates Fourier to Chebyshev series, see [44, 25]. The reader is referred to [45, 24] and references therein for details about the relative advantages of spectral versus finite element methods.

Finally, a Weighted Residuals Method has been used by Towfighi *et al.*, [20], later improved by Vasudeva *et al.* [35], to look at annular wave propagation in anisotropic homogeneous multi-layered cylinders. The method consists of expanding the unknowns in a series of some basis functions. The residual function is calculated, and by equating to zero the suitably defined "inner product" of the residual function with the "weight or test functions" a system of algebraic functions is obtained that yields the coefficients of the expansion. This is akin to the Galerkin method for solving differential

equations and can become cumbersome as one moves to more generality in anisotropy.

Given the importance of dispersion curves in this field it is unsurprising that there has been all this prior activity. However, as noted above, there is certainly scope to develop a robust, versatile and general purpose capability that allows for any kind of anisotropic homogeneous, or inhomogeneous, material in any desired orientation of the crystal axes in flat as well as cylindrical, geometry. This is particularly attractive in terms of overcoming the complexities and limitations of the partial-waves root-finding (PWRF) methods summarised above. In so doing, one would want to develop a methodology, that can be implemented to run automatically, for the complete solution without the need for *any* intermediate intervention from the modeller. The approach taken in this thesis is the Spectral Collocation Method (PSCM), a well-established approach used for the numerical solutions of differential equations. The PSCM has already shown great promise when used to calculate guided wave properties for some simple elastic waveguides [21], as will be discussed shortly. The main goal and contribution of this chapter is to go much further by developing and validating its use for general anisotropy in arbitrarily multi-layered perfectly elastic waveguides, in both flat and cylindrical geometries. It must be highlighted that in this chapter only modes with real wavenumber will be computed but the reader must be aware that even for elastic waves, purely imaginary and an infinite number of complex wavenumbers also exist [5], these will be studied in detail in the forthcoming chapters.

A brief outline of the main characteristics and advantages of PSCM as well as a review of the previous work done in this direction is given in the next section. Section 2.2 presents various cases used to validate the results and for which I explore numerical issues of accuracy and convergence. In Sections 2.3 new cases are presented and comments given upon the relevant physics and further extensions. Section 2.4 provides with a general discussion and summary of the findings of the chapter. Section 2.5 gives the numerical data used for the results and examples presented in the chapter. The contents of this chapter were the basis for a publication, see [46] or the List of Publications at the begining of the thesis.

2.1 Spectral Collocation Method (PSCM)

As this is the method to be employed in the thesis it is necessary to explain the spectral collocation method (PSCM) scheme and its advantages. Spectral schemes are often used for differential equations but, instead of solving a differential equation directly they use a spectral approximation for the so-

lution that satisfies the differential equation and boundary conditions. If the problem is recast in the form of an eigenvalue problem, differentiation matrices approximate the derivative operators with spectral accuracy so there is a concise matrix eigenvalue problem that is solved for both the eigenvalues and eigenvectors. There is an extensive literature on spectral methods mainly from the point of view of solving partial differential equations where it is often the method of choice [23], [25], [45] and [24].

Although this method is well-established and has been successfully used for solving a wide range of differential equations, there has been little activity aimed at using it for dispersion curves in the field of waveguides. [21] introduced it as a potential method, and explored some simple cases, and motivated by this initial success, several papers have appeared illustrating the use of the spectral method for specific classes of waveguide problems: Karpfinger *et al.*,[36], have successfully used this method to handle multi-layered cylindrical systems with isotropic materials and later [22] extended this to porous elastic media and to geophysical applications involving boreholes [47]. Yu *et al.*, [37], used the spectral method, combined with root finding routines, for multi-layered isotropic cylinders with axial propagation and weak and perfect interfaces. Finally, Zharnikov *et al.*, [48], plot the dispersion curves of a waveguide of inhomogeneous anisotropic material using this methodology.

As shall be demonstrated, spectral schemes are easy to formulate and code, much more so than root finding routines, and following an entirely algebraic approach they are both robust and reliable. Also, if one is just interested in the lowest M modes, say $M = O(10)$, they are much faster than root finding routines [21], especially for complicated problems, such as multi-layered or anisotropic materials. However, the most advantageous aspect of the PSCM is that it can be deployed to model general anisotropy, and simultaneously avoid, without any special or conditional treatments, all of the challenges cited above: the PSCM approach is guaranteed not to miss any of the modes, it is immune to instabilities from large values of fd, and it does not deliver spurious solutions at the bulk wavenumbers of the constituent materials. These capabilities will be illustrated later with suitable examples. Finally, see Boyd [24], spectral accuracy is anticipated for the first half of the eigenvalues found. A more detailed discussion on the advantages of PSCM over root finding routines, with a special emphasis on elastic waveguides, can be found in [21].

For definiteness, in this thesis a waveguide as shown in Figure 2.1 is considered; cylindrical cases are analogous with a change in coordinate system shown. Whenever this is not the case, it will be indicated explicitly. Assuming a harmonic wave propagating along the $\{z\}$ axis, the equations of
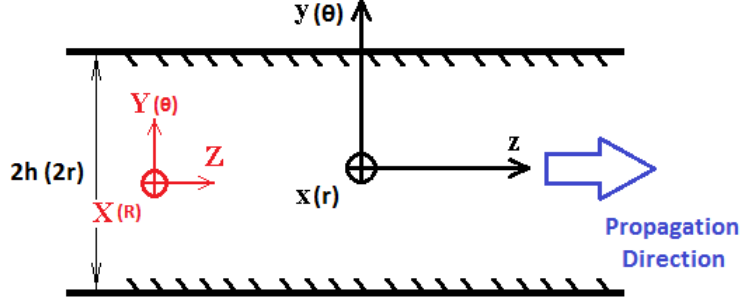
Figure 2.1: Geometry and axes for flat waveguide: {X,Y,Z} are the crystal axes which can rotate about the fixed spatial axes {x,y,z} according to the choice of orientation of the material within the waveguide. In the flat case the {z} axis is the phase direction of the propagating waves (normal to the plane of the wavefront), and in the cylindrical case it is the axis of the cylinder. For the cylindrical case, {x} and {y} should be replaced by {θ} and {r} respectively.

motion for a linear elastic anisotropic homogeneous medium are:

$$\nabla_{iK} c_{KL} \nabla_{Lj}^{sym} u_j = -\rho \, \omega^2 \, u_i \tag{2.1}$$

where the summation convention over the indices has been used and c_{KL} is the medium's stiffness matrix in reduced index notation, [5], u_j are the components of the displacement vector field

$$u_j = U_j(y) \, e^{i(kz - \omega t)} \, ; \qquad j = x, y, z \tag{2.2}$$

and the differential operators are of first order in the coordinate derivatives; their explicit expressions can be found in [5]. In the following sections structures in vacuum are considered so one must consider traction-free boundary conditions which require the vanishing of the following three components of the *stress tensor field* defined below, T_{ij}.

Taking the faces of the plate to be located at $y = \pm h$, see Figure 2.1, the boundary conditions (BCs) are summarized as:

$$T_{yy}|_{y=\pm h} = T_{yx}|_{y=\pm h} = T_{yz}|_{y=\pm h} = 0. \tag{2.3}$$

The expression of the *stress tensor field* in terms of the *strain tensor field* reads:

$$T_{ij} = c_{ijkl} \, S_{kl} \tag{2.4}$$

20

Where c_{ijkl} is the fourth-rank stiffness tensor, which relates to c_{KL} as described in [5]. And the *strain tensor field*, S_{ij}, in terms of the *displacement vector field*, u_j:

$$S_{ij} = \frac{1}{2}\left(\frac{\partial u_i}{\partial x_j} + \frac{\partial u_j}{\partial x_i}\right) \rightarrow S_K = \nabla^{sym}_{Kj}u_j : \qquad (2.5)$$

thus one has a set of three equations of motion and an additional six equations for the boundary conditions. To utilise PSCM the derivatives are discretised and substituted by Differentiation Matrices (DMs). Since the physical interval is bounded, the appropriate choice is to use Chebyshev DMs, based on a non-uniform Chebyshev grid of N points, these are $N \times N$ matrices; the generation of DMs is covered in [25], [45]. The m-th derivative with respect to y is approximated by the corresponding m-th order Chebyshev DM:

$$\frac{\partial^{(m)}}{\partial y^{(m)}} \Longrightarrow \mathbf{D}^{(m)} := [DM_{Cheb}]^{(m)}_{N \times N} \qquad (2.6)$$

The elastic stiffness tensor does not undergo any modification; its entries multiply the matrices in the differential operators following the usual multiplication rule for tensors. From (2.1) one has three coupled equations, one for each component of the displacement. These are discretised with each displacement component given at the grid points and represented by a vector $\mathbf{U}_j$. Each of (2.1) becomes represented in matrix form as, for instance, for the x component of displacement:

$$\mathfrak{A}_{N \times N}(c_{KL}; ik\mathbf{I}, \mathbf{D}^{(1)}, \mathbf{D}^{(2)})\, \mathbf{U}_x + \mathfrak{B}_{N \times N}\, \mathbf{U}_y + \mathfrak{C}_{N \times N}\, \mathbf{U}_z = -\rho\, \omega^2\, \mathbf{U}_x. \quad (2.7)$$

A similar matrix representation emerges for each of the other components of the displacement vector field. The prefactors $\mathfrak{A}_{N \times N}, \mathfrak{B}_{N \times N}, \mathfrak{C}_{N \times N}$ are $N \times N$ matrices that are formed of a linear combination of the DMs up to second degree and the identity matrix with the elastic stiffness constants, c_{KL}, as its coefficients.

This is a matrix system where the unknowns are the vectors $\mathbf{U}_j$ and the coefficients are the matrices $\mathfrak{A}_{N \times N}, \mathfrak{B}_{N \times N}$.... It becomes clearer when this system is rearranged as

$$\begin{pmatrix} \mathfrak{A} & \mathfrak{B} & \mathfrak{C} \\ \mathfrak{D} & \mathfrak{E} & \mathfrak{F} \\ \mathfrak{G} & \mathfrak{H} & \mathfrak{I} \end{pmatrix}_{3N \times 3N} \begin{pmatrix} \mathbf{U}_x \\ \mathbf{U}_y \\ \mathbf{U}_z \end{pmatrix}_{3N \times 1} = \omega^2 \begin{pmatrix} -\rho\,\mathbf{I} & 0 & 0 \\ 0 & -\rho\,\mathbf{I} & 0 \\ 0 & 0 & -\rho\,\mathbf{I} \end{pmatrix} \begin{pmatrix} \mathbf{U}_x \\ \mathbf{U}_y \\ \mathbf{U}_z \end{pmatrix}$$
$$(2.8)$$

Or more concisely:

$$\mathfrak{L}(k)\, \mathbf{U} = \omega^2\, \mathfrak{M}\, \mathbf{U} \qquad (2.9)$$

Where $\mathbf{U}$ is the *vector of vectors*: $\mathbf{U} = [\mathbf{U}_x, \mathbf{U}_y, \mathbf{U}_z]^T$. Before proceeding, the boundary conditions must be included; the six equations (2.3) are

discretised and rearranged, as in [21] or [25], so

$$\mathfrak{S}(k) := \begin{pmatrix} \mathfrak{T}_A & \mathfrak{T}_B & \mathfrak{T}_C \\ \mathfrak{T}_D & \mathfrak{T}_E & \mathfrak{T}_F \\ \mathfrak{T}_G & \mathfrak{T}_H & \mathfrak{T}_I \end{pmatrix} \begin{pmatrix} \mathbf{U}_x \\ \mathbf{U}_y \\ \mathbf{U}_z \end{pmatrix} = \begin{pmatrix} 0 \\ 0 \\ 0 \end{pmatrix} \qquad (2.10)$$

Then, one returns to (2.8) and replace the $1, N, (N+1), 2N, (2N+1)$ and $3N$ rows of the $\mathfrak{L}$ matrix with those of the $\mathfrak{S}$ matrix of (2.10). These rows correspond, for each component of the *displacement vector field*, to the grid points $y = \pm h$, that is, rows 1 and N go with $\mathbf{U}_x$ evaluated at $y = h$ and $y = -h$ respectively, rows $N+1$ and $2N$ go with $\mathbf{U}_y$ evaluated at $y = h$ and $y = -h$ and so on. Similarly, one replaces the same rows of the matrix $\mathfrak{M}$ on the right hand side with rows filled with zeroes. The resultant system then has both the governing equation and boundary conditions incorporated in a consistent manner and this is then a standard generalised eigenvalue problem ideally suited for coding; MATLAB (version R2012b) has been used and its eigenvalue routine `eig` which, given a value of k, provides the angular frequencies, ω, of the first $3N$ modes. As an added bonus the eigenvectors $\mathbf{U}$ contain the mode shapes. Note that not all the $3N$ eigenvalues are accurate, as it was explianed before only the first half should be regarded as reliable. It must also be remembered that it is the real wavenumber which is being fixed and the real frequencies for that wavenumber computed, therefore the spectrum one obtains is not the full spectrum since purely imaginary and complex wavenumbers are missing, they will be the object of study of chapter 4.

Multiple layers follow this methodology and one assembles as many systems, using (2.8), as the number of layers in the system, and then compose the boundary conditions. The boundary conditions are still given by equations (2.3), but for multiple layers one also imposes continuity at the interfaces for the displacement fields as well as for the three components of the stress tensor field.

As a specific example consider a system of n layers of triclinic material, the equation analogous to (2.9) is:

$$\begin{pmatrix} \mathfrak{L}_1 & \mathfrak{o} & \dots & \mathfrak{o} \\ \mathfrak{o} & \mathfrak{L}_2 & \dots & \mathfrak{o} \\ \vdots & \vdots & \ddots & \vdots \\ \mathfrak{o} & \mathfrak{o} & \dots & \mathfrak{L}_n \end{pmatrix}_{3nN \times 3nN} \begin{pmatrix} \mathbf{U}_1 \\ \mathbf{U}_2 \\ \vdots \\ \mathbf{U}_n \end{pmatrix}_{3nN \times 1} =$$

$$\omega^2 \begin{pmatrix} \mathfrak{M}_1 & \mathfrak{o} & \dots & \mathfrak{o} \\ \mathfrak{o} & \mathfrak{M}_2 & \dots & \mathfrak{o} \\ \vdots & \vdots & \ddots & \vdots \\ \mathfrak{o} & \mathfrak{o} & \dots & \mathfrak{M}_n \end{pmatrix}_{3nN \times 3nN} \begin{pmatrix} \mathbf{U}_1 \\ \mathbf{U}_2 \\ \vdots \\ \mathbf{U}_n \end{pmatrix}_{3nN \times 1} \qquad (2.11)$$

Each of the labelled matrices: $\mathfrak{L}_i$, $\mathfrak{M}_i$ and $\mathbf{U}_i$ (where $i = 1..N$ indicates the block matrices, vectors for the displacements etc in each layer i) has the single layer form shown in equation (2.9).

Having arranged the boundary conditions for a single layer in matrix form in equations (2.10), for the external boundary conditions one proceeds in a similar fashion to that outlined for a single layer. For the upper layer one has its corresponding boundary condition matrix $\mathfrak{S}_1$ whose $1, (N + 1)$ and $(2N + 1)$ rows give the three components of the stress tensor field at the upper external boundary (2.3). These three rows replace the *first three* rows $1, N$ and $(N + 1)$ of the multilayer system matrix (2.11). One follows an analogous procedure for the bottom external boundary: take the $N, 2N$ and $3N$ rows of the bottom layer boundary condition matrix $\mathfrak{S}_n$ and replace the $((3n-1)N), ((3n-1)N+1)$ and $3nN$ of the multilayer system matrix (2.11) with them.

Continuity conditions across the internal interfaces are also imposed. For an interface, say first interface between layers 1 and 2, the continuity conditions for the stress tensor field are:

$$(T_{yy})_{(1)} - (T_{yy})_{(2)}|_{y=1^{st}} = 0$$
$$(T_{yx})_{(1)} - (T_{yx})_{(2)}|_{y=1^{st}} = 0$$
$$(T_{yz})_{(1)} - (T_{yz})_{(2)}|_{y=1^{st}} = 0 \qquad (2.12)$$

Where $y = 1^{st}$ means evaluation at the first interface. The continuity conditions in a perfect interface for the displacement fields are:

$$(u_x)_{(1)} - (u_x)_{(2)}|_{y=1^{st}} = 0$$
$$(u_y)_{(1)} - (u_y)_{(2)}|_{y=1^{st}} = 0$$
$$(u_z)_{(1)} - (u_z)_{(2)}|_{y=1^{st}} = 0 \qquad (2.13)$$

This gives a total of six equations for each interface. Therefore for a system of n layers, one $n-1$ interfaces and $6n-6$ interface equations, plus 6 boundary condition equations make a total of $6n$ equations that must replace the appropriate rows in the system matrix (2.11).

Specialising now to a concrete example including interface conditions: Lamb modes in a flat plate with the axes configuration of Figure 2.1. Lamb modes decouple from SH modes so, for this example, there are only two displacement fields, u_y and u_z, and the associated stress tensor field components T_{yy} and T_{yz}. The matrix incorporating the interface and boundary lines is shown in Figure 2.2 which is easily extended to more general cases.

The construction of the matrix is absolutely key to the method and so it is

described in detail. In Figure 2.2, the superscripts a,b,c and d make reference to the different elements of the matrix expression for the given j-th layer $\mathfrak{L}_j$ which forms the blocks of the whole system matrix in (2.11). Each of these layer matrices is a $2N$ by $2N$ ($3N$ by $3N$ in the general case) non-diagonal matrix, and is, in turn, composed of four different sub-blocks. The a and b sub-blocks incorporate the equation of motion for the U_y component: the a sub-block acts upon the U_y, whereas the b sub-block acts upon the U_z. The c and d sub-blocks incorporate the equation of motion for the U_z component: the c sub-block acts upon the U_y, whereas the d sub-block acts upon the U_z. The placing of the boundary conditions in matrix expressions in general using the Spectral Method is also explained and discussed in detail in [25]. To make this layered structure of the Matrix more apparent, the blocks of the matrix corresponding to different layers have been enclosed in boxes of different colours (green for the first layer (top), brown for the second and purple for the n-th layer (bottom)).

In Figure 2.2, the first two rows of the system matrix are replaced by the 1-st rows of the tensor components T_{yy} and T_{yz} (the components are represented by $\mathfrak{T}$ as in equation (2.10)) evaluated at the top of the first layer (the top boundary of the system), labelled with a 1. An analogous substitution is made in the last two rows for the $n-th$ layer. But now one takes the bottom N-th row of the matrices since the stress tensor field components are being evaluated at the bottom of the layer (the bottom boundary of the system). The boundary conditions of equation (2.12) are thus accounted for, and in Figure 2.2 these are framed in red boxes.

The first set of interface conditions corresponding to the first interface of the system linking layers 1 and 2 is framed inside orange boxes in Figure 2.2. These make a total of four equations: two for the displacement vector field and two for the stress tensor field. Let us begin with the continuity of T_{yy} at the interface: one replaces the $(N+1)$-th row of the system with this continuity condition as shown in Figure 2.2. Note that this condition comprises two parts: the first refers to the bottom of layer 1, so one takes the bottom row, N-th, of the matrix expression for the stress tensor field T_{yy} in layer 1. The second refers to the top of layer 2 so the top row is taken, 1-st, of the matrix expression of T_{yy} in layer 2. One should not forget the relative sign between them. An analogous substitution is made for T_{yz} and the $(2N)$-th row of the system is replaced.

The second set of interface conditions are the continuity conditions for the displacement vector field, see equations (2.13). The system matrix is acting upon the components of the vector field within each layer (recall the column vector to the right of the matrix in (2.11)), so wherever one sees a $\mathfrak{U}_{j(y)}(N)$ it must be understood that it is the corresponding row of the identity matrix

one is dealing with, in this case it would be the bottom row. For U_y there are again two parts: the first refers to the bottom of layer 1, so the bottom N-th row of the identity matrix is taken which means one is taking U_y evaluated at the bottom of the layer 1. The second refers to the top of layer 2 so one must take the first row of the identity matrix which means U_y is being evaluated at the top of layer 2, with the substitutions on the $(2N+1)$-th row of the system have finished. A similar procedure will account for the U_z component. One then deals with the remaining interfaces in an analogous fashion. In Figure 2.2 are some indications for the second and $(n-1)$-th interfaces. A worked out example of a two-layer system can be found in [21]. In addition, it is anticipated that, if certain symmetry conditions in the layer arrangement of the system are met, it is possible to reduce the size of the system matrix and implement symmetric/antysimmetric boundary conditions at the middle plane of the system in order to obtain the solution. These conditions and situations will be studied in detail in Chapter 6.

A common example of interest is that of an inviscid fluid layer in between solid layers, for example the important situation of a fluid filled pipe falls into this category. Whether in flat or cylindrical geometry, this requires a modification of the scheme described so far as the fluid does not support shear: one retains the displacement fields for the adjacent solid layers, thus allowing one to handle any kinds of material and orientation of the crystal within the solid layers, but a longitudinal (compressional) potential is used for the fluid layer. Perfect fluids can be modelled as isotropic solids with the shear stiffness constant μ equal to zero, see [16] and references therein. It must be noted however, that the boundary conditions when perfect fluids are present, equations (2.12) and (2.13), must be modified accordingly since fluids do not support shear. This means that only normal components of stress and displacement are continuous across the boundary whereas the rest are free to slip with respect to each other. Failure to modify the PSCM scheme as described above, leads to an error in the fluid-solid boundary conditions giving spurious modes and the distortion of the correct modes in the vicinity of the bulk wavenumber of the fluid. Thus, the PSCM presented here can handle systems with a fluid layer placed between elastic layer without any problems as the following example will show.

Cylindrical cases are completely analogous with cylindrical coordinates replacing Cartesians. All the wave families present in cylindrical geometry are studied: Torsional, Longitudinal and Flexural modes. The ansatz used in the early literature [6] for Flexural modes in terms of sines and cosines is not appropriate for more general anisotropic materials such as Triclinic since these terms cannot be taken out as common factors. Therefore, to handle
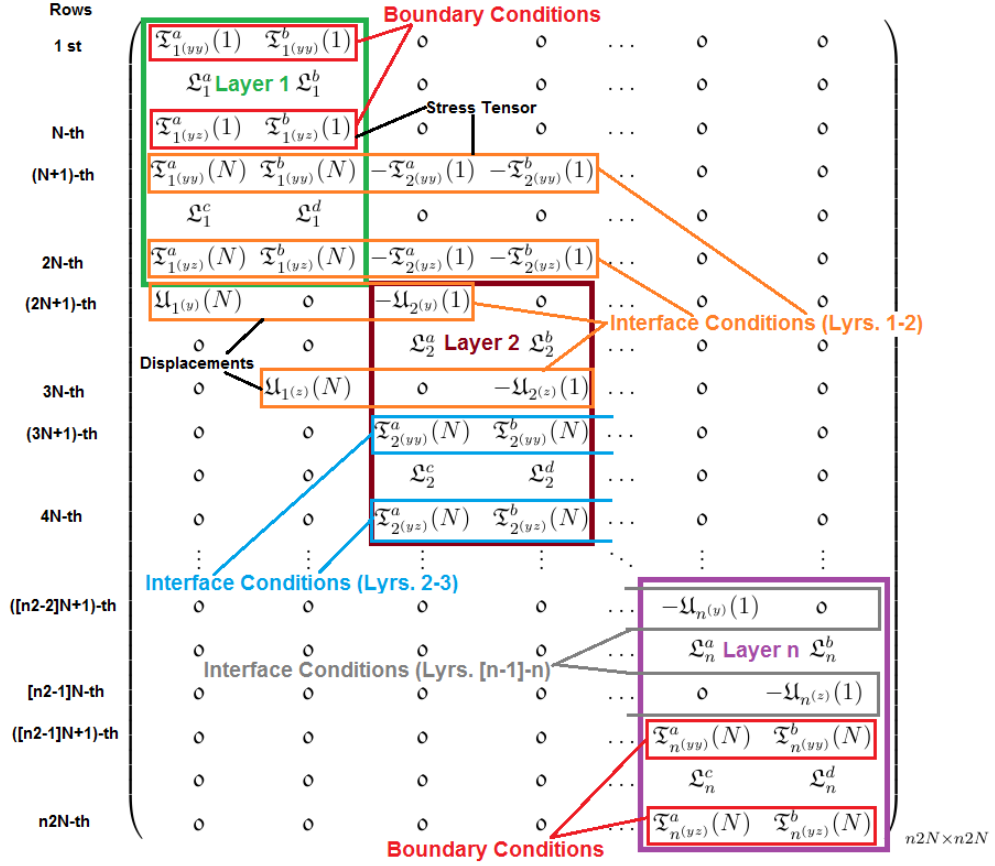
Figure 2.2: Collocation scheme for the n-layer system matrix. The scheme shown here corresponds to a case where only two displacement fields enter the equations, such as Lamb modes. Only the first, second, and last layers are shown in detail. Analogous blocks model the rest of the layers.

the full range of materials, the general form is used:

$$u_j = U_j(r)\, e^{i(kz+n\theta-\omega t)}\,; \qquad j = r, \theta, z \qquad (2.14)$$

Finally, often a spring interface condition is used when interfaces with finite stiffness need to be modelled, for example when a sufficiently thin adhesive bond can be approximated by a compliant boundary or simply when an imperfect contact condition must be accounted for (sliding boundaries or partially-contacting boundaries for example). These require a slight modification of the internal interface conditions based on the spring model developed by Rokhlin and Wang [49], the reader is referred to their paper for details of the derivation. In their model it is only the continuity conditions for the displacement fields that are modified, so, instead of having equations (2.13) one has (recalling that the upper layer is labelled with (1) and the lower with (2)):

$$\left[\frac{(T_{yy})_{(1)}}{K_n} - \left((u_y)_{(1)} - (u_y)_{(2)} \right) \right]|_{y=1^{st}} = 0$$

$$\left[\frac{(T_{yx})_{(1)}}{K_t} - \left((u_x)_{(1)} - (u_x)_{(2)} \right) \right]|_{y=1^{st}} = 0$$

$$\left[\frac{(T_{yz})_{(1)}}{K_t} - \left((u_z)_{(1)} - (u_z)_{(2)} \right) \right]|_{y=1^{st}} = 0 \qquad (2.15)$$

where K_n and K_t are the normal and transverse stiffness coefficients, which according to the definition in [49], have dimensions of N/m^3. It is straightforward to account for this modification; one only needs to modify the corresponding rows of the system matrix.

Spring models are useful in practise since, when this representation is valid, it replaces a very thin layer by spring interface conditions thereby reducing the size of the matrix system. For example, two steel plates bonded by a thin EPOXY adhesive layer can be represented as a two layer system with a spring model instead of having a three layer system with perfect internal interface conditions; such an approximation is only valid for very thin interface layers.

2.2 Comparing with existing results

The PSCM scheme is validated by choosing exemplar cases of dispersion curves from the literature that illustrate important points, a root-finding algorithm is used to provide examples to compare with the PSCM. Flat plates are addressed first, then torsional and longitudinal modes in cylinders, then the more complex case of flexural modes in cylinders.

The axis configuration for the cases with plane geometry is as follows: the axes x and z lie within the plane of the plate, see Figure 2.1, and the axis y along the thickness of the plate; wherever this is not the case it will be stated explicitly. The propagation direction will invariably be along the z axis unless otherwise stated. For different configurations we rotate the crystal axes whilst preserving the propagation direction.

2.2.1 Free Anisotropic and Homogeneous Plate

This section begins by finding the modes for the single-layer flat plate in vacuum: In principal orientation configuration, Lamb (in-plane) modes and SH (out-of-plane) modes are found. Also dispersion curves are presented for configurations with arbitrary orientation of the crystal axes where modes are coupled, that is, Lamb and SH are no longer independent of each other due to the boundary conditions and anisotropy and give rise to a more general family of modes involving all the three components of the displacement vector field. Following (2.2), the form of the displacement field is the following:

$$u_j = U_j(y) \, e^{i(kz-\omega t)} \, ; \qquad j = x, y, z \qquad (2.16)$$

For an isotropic plate, SH modes are not coupled to the Lamb modes. This splitting of modes also occurs in certain cases for anisotropic materials as shown in Table 2.1. This table is constructed using the software Maple (version 17), for the axes configuration shown in Figure 2.1 (use Maple for computing the boundary conditions and equations of motion symbolically, the structure of these equations yields the type of modes existing in each case). The transformations refer to the crystal axes rotating about the spatial $\{y\}$ axis.

Similar tables can be built for the other two possible configurations ($\{x\}$ or $\{z\}$ axis perpendicular to the plane of the plate) with similar results except for a few exceptions to be discussed in Chapter 5. For more general rotations, *e.g.* two consecutive rotations different from 90 degrees about different axes, SH and Lamb modes are then coupled and each of these cases must be studied separately.

Materials with Orthorhombic symmetry are studied first, they have nine different constants in the stiffness matrix: c_{11}, c_{12}, c_{13}, c_{22}, c_{23}, c_{33}, c_{44}, c_{55} and c_{66} (in reduced index notation, see [5] for details). These materials have been extensively studied by Li and Thompson [13] and Nayfeh and Chimenti [9] and provide a challenging test for our methodology. In addition, results have been compared to those given by PWRF methods always finding excellent agreement.

Figure 2.3 compares the results obtained by the PSCM with those obtained

Crystal	Transformation
Isotropic	*Lamb and SH modes decouple for any angle.*
Cubic	*Lamb and SH modes decouple for 0 and 90 degrees.*
Hexagonal	*Lamb and SH modes decouple for 0 and 90 degrees.*
Tetragonal 6	*Lamb and SH modes decouple for 0 and 90 degrees.*
Tetragonal 7	*Lamb and SH modes decouple only for 90 degrees.*
Trigonal 6	*Lamb and SH modes decouple only for 0 degrees.*
Trigonal 7	*No modes decouple unless one chooses the axes orientation in which Trigonal 7 takes the form of Trigonal 6. See paragraph below (3.73) in volume 1 of [50].*
Orthogonal 9	*Lamb and SH modes decouple for 0 and 90 degrees.*
Monoclinic 13	*No modes decouple.*
Triclinic 21	*No modes decouple.*

Table 2.1: Conditions for decoupling mode families in the different classes of anisotropic crystals.

by PWRF for the case of Lamb modes in a single plate in vacuum. The plate is Orthorhombic (more details can be found in section 2.5 for this and the forthcoming figures) and the crystal axes are rotated such that the crystal {Z} axis aligns with the {z} of the plate (the propagation direction), while the crystal {X} axis aligns with the {y} axis of the plate (normal to the plate).

As can be seen in Figure 2.3 all the modes were found, and the PSCM's solutions (red circles) lie very close to corresponding locations on the lines plotted by the general purpose PWRF routines used by the author. As a point of note, the PWRF routine did not find the fundamental extensional mode (the mode crossing the phase velocity axis of the plot at 1.5 m/ms). Although it is easily found by performing a finer search using PWRF the PSCM did not miss it. This illustrates the important capability of the PSCM to find all modes automatically without missing any.

The configuration of Figure 2.3, with the crystal axes aligned with the spatial axes, implies, according to Table 2.1, that the Lamb and SH modes decouple; for clarity and brevity only the Lamb modes are shown, these are the more complicated case. The SH modes are easy to compute, and compare, and equally satisfactory results are found.

Figure 2.4 shows the result obtained with the PSCM for a reproduction of the Figure 14 from Li and Thompson's paper [13] displaying modes in an Orthorhombic plate in vacuum. The crystal axes configuration is as follows: the Z axis is perpendicular to the plane of the plate and with the propa-
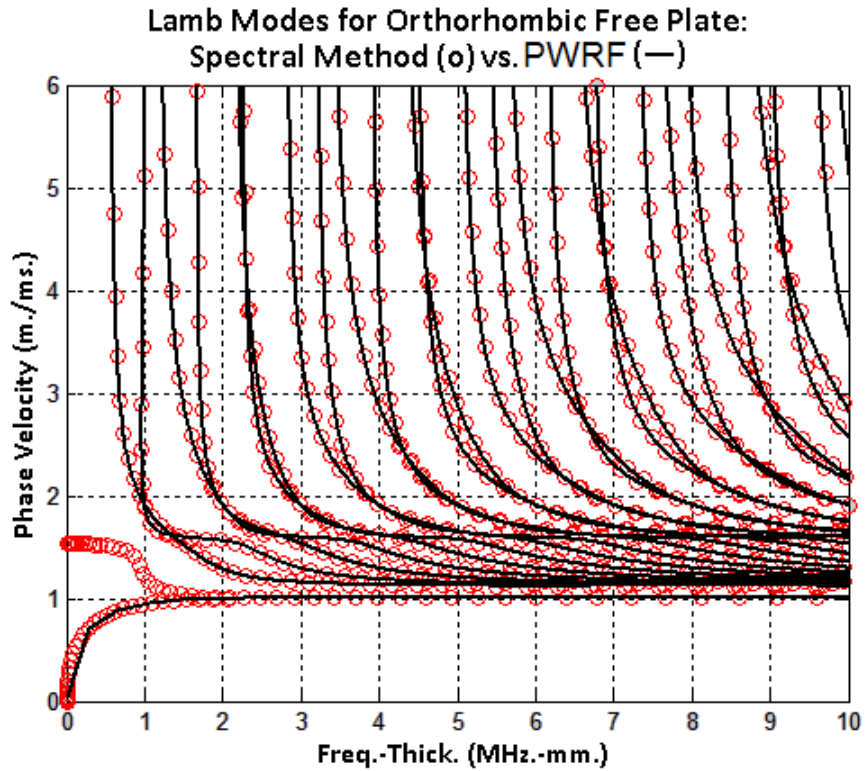
Figure 2.3: Free Plate Orthorhombic Lamb Modes: PSCM (circles) *vs.* PWRF (solid lines). Geometry and spatial axes configuration as in Figure 2.1. The crystal axes have been rotated to match the configuration followed by the PWRF model: propagation along the {z} axis and the {x} axis perpendicular to the plane of the plate. The SH family of modes in this case are uncoupled from the Lamb modes, and have not been included in the plot, although they may be obtained with similar accuracy.

gation direction at 30 degrees with respect to the X axis. Note that it is different from the axes configuration used in the previous cases. As a result of this rotation the stiffness matrix which enters the equations of motion has Monoclinic symmetry with the plane of mirror symmetry contained in the plane of the plate as explained in [13], so we can regard this case either as a rotated Orthorhombic example, or as an example of a Monoclinic material. This case is of particular importance because it constitutes a necessary step before studying the most general problem of Triclinic media which must contain Monoclinic materials as one of the limiting cases. The dispersion curves obtained by the PSCM are identical to those shown in the paper [13]. Since one can regard this configuration as that of a Monoclinic material, its properties apply and according to Table 2.1, Lamb and SH modes are coupled. Further rotating the crystal about an axis different from the {Z} axis will result in a stiffness matrix of a Triclinic Material. One can therefore generalize our methodology to Triclinic materials, which is a generality that has not been treatable with other methods.

Figure 2.5 shows the coupled modes computed by the PSCM in a flat free Triclinic plate and the axes orientation is as described in Figure 2.1: propagation along the {Z} axis and {Y} axis perpendicular to the plane of the plate, in this case the crystal axes and spatial axes are aligned. The physical parameters used are given in the last section of this chapter..

This is an important, and to the best of the author's knowledge, new result: It is the most general material symmetry with 21 different constants in the stiffness matrix and therefore, one can *also* make use of the Triclinic algorithm to solve problems of simpler symmetry (orthorhombic for instance) but with completely arbitrary orientations.

2.2.2 Free Anisotropic and Homogeneous Cylinder: Torsional and Longitudinal Modes

In cylindrical geometry the axes configuration is the conventional one: taking the axis of the cylinder along the {z} axis. The form of the solution is as follows:

$$u_j = U_j(r)\, e^{i(kz - \omega t)}\; ; \qquad j = r, \theta, z \tag{2.17}$$

First the Longitudinal modes will be studied, these are analogous to the Lamb modes in flat geometry. When possible, PWRF routines will be used to test the results given by the PSCM, however, their capabilities are more limited in cylindrical geometry than in flat geometry. When PWRF cannot provide a reliable solution and there is no available data in the literature, the dispersion curves of flat plates will be used to investigate the results' accuracy in cylindrical geometry. This is possible because one may take the *thin plate limit* by making $h/r \ll 1$, where h stands for thickness and r for

31

Modes for Free Orthorhombic Plate with the Spectral Method
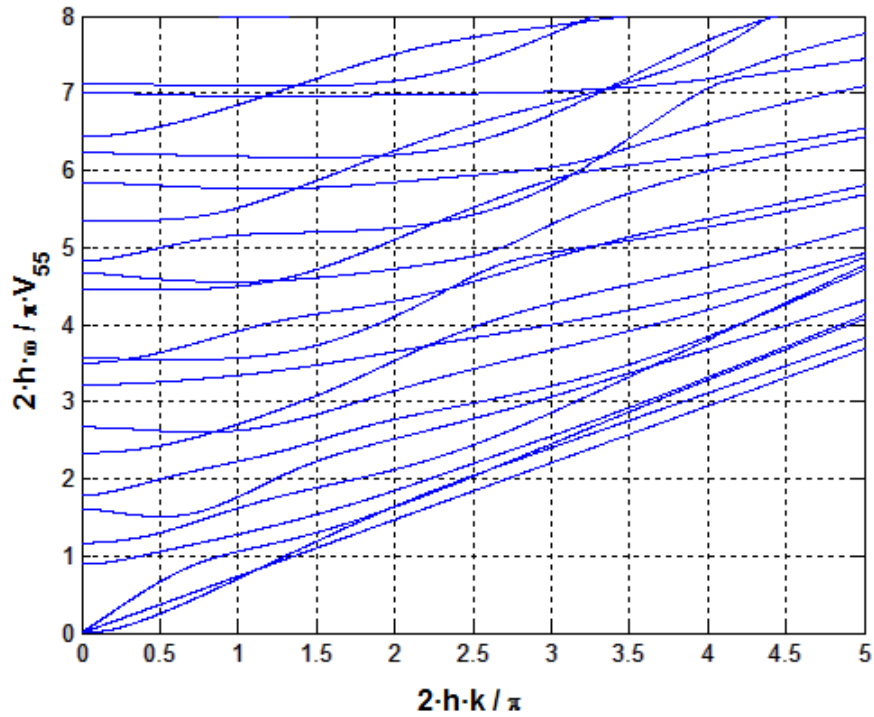
Figure 2.4: Reproduction with the PSCM of the results of Figure 14 in the paper by Li and Thompson [13]. This is for an orthorhombic free plate, the {Z} axis of the crystal is perpendicular to the plate and the propagation direction is at 30 degrees with respect to the {X} axis. Note that it is different from the axes configuration used in the previous cases. More details about the parameters may be found in the last section of this chapter. In the graph, the {y} axis is a normalized adimensional frequency and the {x} axis is a normalized adimensional wavenumber.
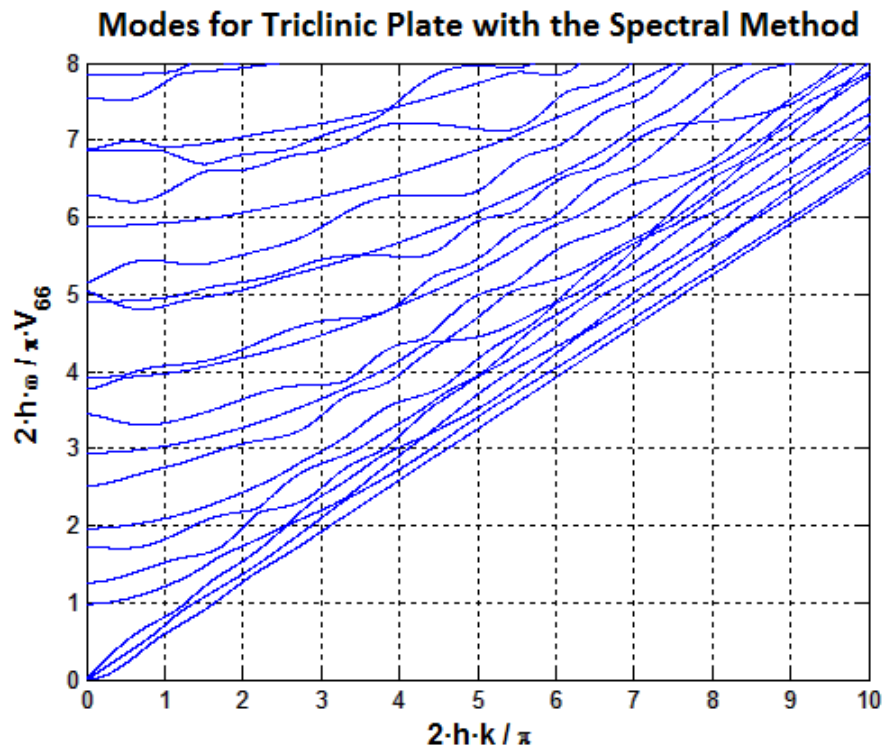
Figure 2.5: Coupled modes in Triclinic free Plate obtained by the PSCM with the spatial axes' orientation shown in Figure 2.1. The crystal axes coincide with the spatial axes. The graph displays again normalized adimensional frequency and wavenumber in the {y} and {x} axis respectively.

internal radius of the cylinder, and expect to obtain the same dispersion curves of a plate with similar physical properties. In this limit, the Torsional and Longitudinal modes look like the SH and Lamb modes of a flat plate respectively. Note that, this limit is valid as long as the wavelength of the guided wave remains small compared to the radius of the cylinder and therefore the effects of the curvature (inverse of the radius) can be neglected. An exhaustive study of this and other limiting cases and its ranges of validity lies out of the scope of this chapter but the interested reader can find a full account of them and the latest developments regarding thin shell approximations and related topics are addressed in detail in recent books by Kaplunov *et al.* [51] and more recently by Wang *et al.* [52]. However, for these validating purposes, the conventional *thin plate limit* is sufficient to test the good performance of the codes as will be seen in the next sections.

The solutions for the isotropic cylinder were easily solved by the PSCM and upon comparison with available data from the literature and PWRF perfect agreement was found between both sets of dispersion curves; for brevity these are not shown here and the results for more complicated problems that cannot be solved by PWRF are presented next. To demonstrate the generality of this approach Figure 2.6 displays dispersion curves of a Triclinic cylinder in the Thin Plate Limit (circles) and those of the corresponding flat Triclinic plate (solid lines). This example is, to the best of the author's knowledge, also new and provides a consistency check for the flat plate since both solutions show excellent agreement as expected. The axes configuration is as follows: propagation along the principal crystal axis {Z}; crystal axes are aligned with spatial axes {r}, {θ} and {z}.

2.2.3 Free Anisotropic and Homogeneous Cylinder: Flexural Modes

Continuing the study of cylindrical geometries Flexural modes are studied in this section. The solutions for isotropic materials were successfully reproduced by the PSCM so one focuses on materials with triclinic symmetry due to their importance. Our PSCM results displayed the typical behaviour of flexural modes: the higher the value of the *harmonic order n* is, the higher the cut-off frequency of the first mode. The curves were smooth and the pattern was similar to the flexural modes for isotropic materials encountered in the literature [3] and [34].

In order to verify the PSCM approach for the Flexural modes the previously studied cases both in flat and cylindrical geometry are used. This verification proceeds in two steps. Firstly, in the Thin Plate Limit one confirms that the Flexural modes, regardless of the harmonic order n chosen, agree with those of a plate of the same properties. This independence of the
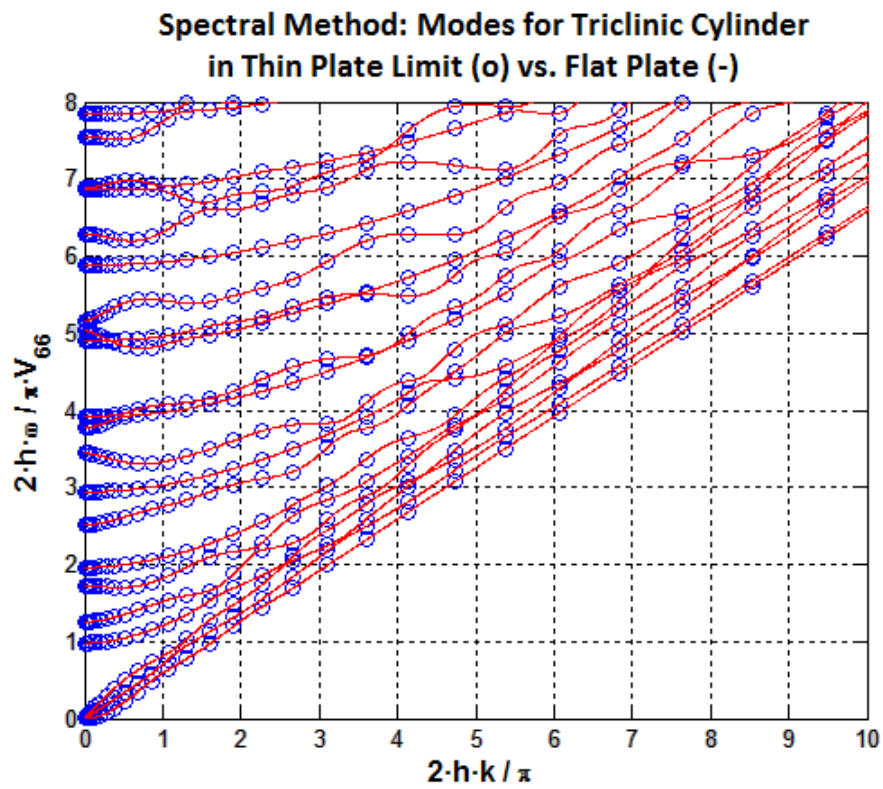
Figure 2.6: Coupled modes in Triclinic Cylinder in Thin Plate Limit (circles) *vs.* Triclinic Plate (solid lines). The spatial axes' orientation is shown in Figure 2.1. The crystal axes coincide with the spatial axes. The graph displays normalized adimensional frequency and wavenumber in the {y} and {x} axis respectively. Both solutions were computed by the PSCM.

dispersion curves with respect to the harmonic order n in the Thin Plate Limit reflects the fact that in a flat plate there is no angular dependence whatsoever and, although our equations for the flexural modes depend on the harmonic order parameter n, upon taking the Thin Plate Limit the results should show complete independence of it and this is what was encountered. Secondly, it is corroborated that the family of flexural modes $n = 0$ agrees with the Torsional and Longitudinal modes of an identical cylinder without restricting to the Thin Plate Limit. This is explained by noticing that the equations and boundary conditions for the flexural modes, with n as parameter, decouple and reduce to those of Torsional and Longitudinal modes when $n = 0$, see [6]. Thus, it is correct to regard axially symmetric Longitudinal and Torsional modes as particular cases of flexural modes.

Figure 2.7 shows the dispersion curves for the family $n = 3$ of Flexural modes of a free Triclinic cylinder in the Thin Plate Limit (circles) compared to the results in a free plate of similar properties and equal thickness, 5 mm (solid lines). All the details may be found in the last section of this chapter. The axes' configuration is with wave propagation along the principal axis {Z}. Crystal axes are aligned with spatial axes {r}, {θ} and {z}. Note that the axes in the plate must match those in the cylinder for the comparison to be meaningful. The plate configuration is the same as that used for Figure 2.5. The results for the $n = 3$ Flexural modes in the cylinder agree perfectly with the dispersion curves of a flat plate of similar characteristics.

As explianed above, the next step is to verify that the $n = 0$ family of Flexural modes agrees with the Longitudinal and Torsional modes of a similar cylinder. These modes, $n = 0$ Flexural, Longitudinal and Torsional, are now coupled because we are dealing with a Triclinic material. The results are plotted in Figure 2.8. Note that the cylinder is no longer in the Thin Plate Limit but has internal radius $r = 100\ mm$ and wall thickness $h = 100\ mm$. The axes configuration is again with wave propagation along the principal axis {Z} and crystal axes aligned with spatial axes {r}, {θ} and {z}. Agreement between both solutions is again excellent. Having thus verified the code one can be confident that the results for different configurations and materials will be correct.

Notably one can treat solid rods using this methodology by choosing a very small inner radius $\backsim 10^{-12}$ m, however, for the sake of brevity, the results of their verifications are not presented here.
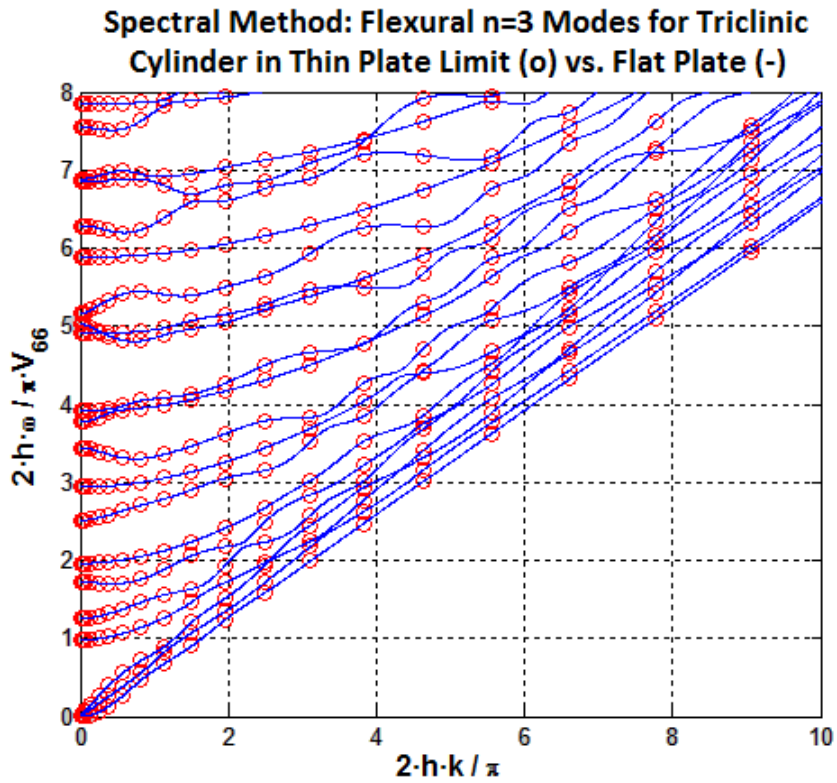
Figure 2.7: Free Triclinic Cylinder: Thin Plate Limit Flexural Modes $n = 3$ (circles) *vs.* Plate Coupled Lamb and SH Modes (solid lines). The spatial axes' orientation is shown in Figure 2.1. The crystal axes coincide with the spatial axes. The graph displays normalized adimensional frequency and wavenumber in the {y} and {x} axis respectively. Both solutions were computed by the PSCM.
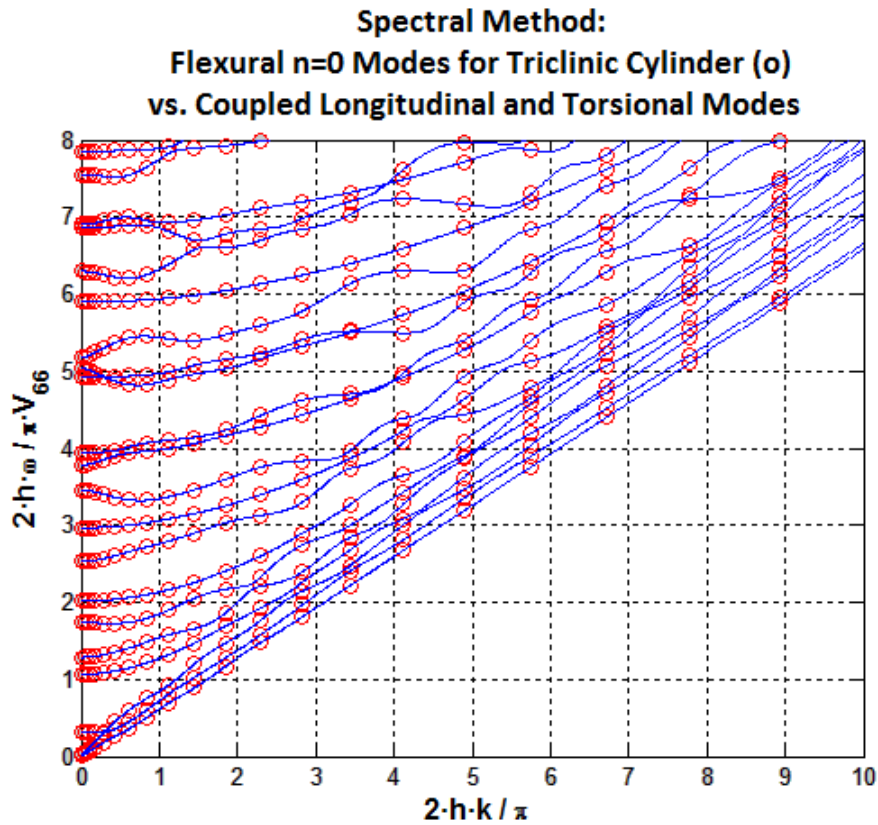
Figure 2.8: Free Triclinic Cylinder: Flexural Modes $n = 0$ (circles) *vs.* Coupled Longitudinal and Torsional Modes (solid lines). The spatial axes' orientation is shown in Figure 2.1. The crystal axes coincide with the spatial axes. The graph displays normalized adimensional frequency and wavenumber in the {y} and {x} axis respectively. Both solutions were computed by the PSCM.

2.2.4 Convergence of Results

An important feature of PSCM is that the first half of the N eigenvalues found are highly accurate, see for example [24] and [21]. In both references it is shown that roughly the first $N/2$ of the eigenmodes found should be regarded as reliable and accurate, the rest may be discarded.

In Table 2.2 the accuracy of the PSCM is assessed for the case previously shown in Figure 2.3 by comparing the numerical values from the first 5 eigenmodes with those obtained by PWRF. The PSCM was run with $N = 70$.

Mode	Freq.-Thick.	**PWRF**	**S. M.** $(N = 70)$	**Relative Error** **(R.E)**
	(MHz-mm)	V_{ph} (m/ms)	V_{ph} (m/ms)	10^{-3} %
1st	0.61227	0.87418	0.87419	1.14391
2nd	0.92790	1.32481	1.32483	1.50963
3rd	1.16137	1.65818	1.65818	0
4th	1.20336	1.71814	1.71813	0.58203
5th	1.67359	2.38950	2.38951	0.41849

Table 2.2: Relative error between the results given by the PSCM and PWRF for the case previously shown in Figure 2.3. The values correspond to the first 5 eigenvalues.

Due to the large amount of results presented it is not possible to give an account of their accuracy for each one, but whenever they were compared to PWRF very good agreement was found for the first $N/2$ eigenvalues and Table 2.2 is typical. Nevertheless, some features of accuracy and convergence are discussed in more detail. Two cases must be distinguished: first, problems, such as SH waves in a plate, with analytical solution and eigenvalues known exactly, and second, problems whose dispersion relation has (or not) been found analytically and whose numerical solution is an irrational number. Lamb waves belong to the second category, the analytical solution is known but the numerical values have a non-integral part which renders them a bad reference for numerical comparisons as it is unclear whether the root finder or the PSCM is more accurate, indeed arguably PSCM provides the reference value.

With problems of the first category, one can pursue accuracy and convergence studies by changing the number of grid points N and comparing the results with the exact solution. This was done for SH modes in an isotropic plate, where the solutions are integers in the appropriate scale, and excellent agreement was found within the first half of the eigenvalues. Generally, the accuracy decreases as one moves to higher eigenvalues, but there can

be exceptions, that is, the third eigenvalue might be less accurate than the fourth. This is in complete agreement with the results shown in the literature [24] and [25]. The convergence towards the exact solution is also very good, with accuracy of up to 11 digits. As one increases N the number of non-changing digits increases up to 11 which then, upon reaching a certain value of N, stay unchanged no matter how much one further increases N. For an iteration with $N = 70$, the difference between the computed and theoretical cut-off adimensional frequencies (the positive integers) is smaller than 10^{-12} for the first 26 eigenvalues. From then onwards, the difference increases exponentially, almost by an order of magnitude per eigenvalue. For the 35th eigenvalue, the difference is $\sim 10^{-5}$ which still a good result but far from the extraordinary accuracy of the lower eigenvalues.

In problems of the second category one does not have an exact reference to compare the numerical results with, an integer for example. Therefore, the most sensible way to proceed is to study the self-convergence by increasing N and monitoring how the solution changes. This has been done for Lamb modes in a plate and the agreement with the PWRF methods was very high (as can be seen in Table 2.2). It could also be confirmed that the number of unchanging digits increases up to 11 digits as N is increased up to a certain value. From this N value upwards these self-convergent digits stay the same. Again, and taking as reference the values given by PWRF routines, the rule by which the higher the eigenvalue is, the lower the accuracy, holds in general, although, not strictly.

In conclusion, one can state as a "rule of thumb" that the accuracy of the first half of eigenvalues can be safely relied upon and that the results given by the PSCM are self-convergent up to a very high number of digits. The accuracy of the results, when compared to the solution given by PWRF methods, is also very good. Note that the self-convergence of the results worsens as we handle more complicated problems, multi-layered cases for instance, where the number of self-convergent digits sometimes decreases to as low as 6; this notwithstanding, the accuracy is still far within the margins of acceptance.

2.3   Results for Single and Multilayer Systems

Now further results are presented which were obtained choosing examples that cover cases that were previously inaccessible.

2.3.1   Single-Layer Systems

To be as general as possible a problem of circumferential propagation in an anisotropic cylinder is studied first. In equation (2.18) the usual form of the

Spectral Method: Circumferential Propagation in Cylinder (Thin Plate Limit)(o) vs. Plate(—)
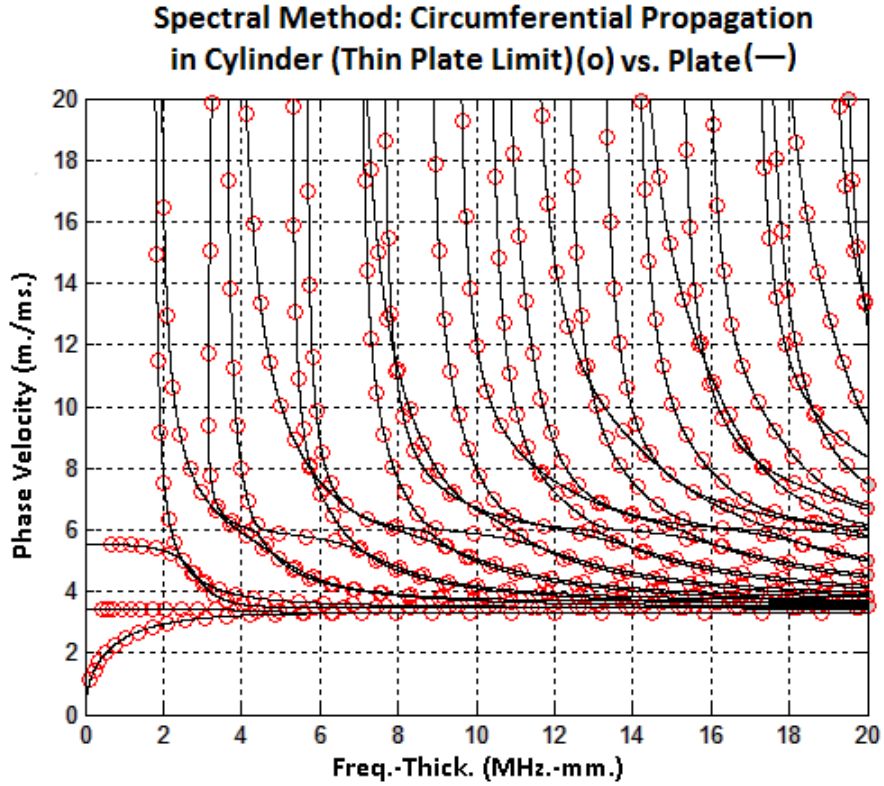
Figure 2.9: Free Orthorhombic Cylinder with {Z} crystal axis at 45 degrees with the {z} spatial axis: Longitudinal circumferential propagating modes (solid lines) *vs.* Plate Lamb modes (circles).

solution assumed for the case with circumferential propagation is shown.

$$\textit{Circumferential Propagating Modes:} \quad u_j = U_j(r)\, e^{i(k\theta - \omega t)}\,;\; j = r, \theta, z \tag{2.18}$$

Figure 2.9 displays the dispersion curves for circumferential propagation in a free cylinder for the thin plate limit cross-validated against its flat plate analogue. Both materials are Orthorhombic and, in the cylinder, the crystal axis {Z} is at 45 degrees with the spatial axis {z} which is aligned with the cylinder axis. Propagation is along the {θ} axis which is not parallel to the crystal {Θ} axis due to the rotation; from figure 2.9 both solutions are seen to coincide and agree very well. This general case is outside the scope of established PWRF routines, but poses no problem for the PSCM.

41

2.3.2 Multilayer Systems

For clarity results where the number of layers is relatively low are presented, but the author has extensively tested the scheme for many layered systems. The main change is that the time to plot the curves increases with the number of layers. Due to industrial interest in laminated composites and aggregates of plies made of different materials the first example is a system of three layers: isotropic-anisotropic-isotropic.

The results given by PWRF and the PSCM are compared in Figure 2.10 for the modes in this free plate three layer system. To be specific, the anisotropic medium is chosen to be a GRE layer, a fibre composite material, and it is sandwiched between two steel layers. The axes configuration is the same in every layer: propagation along the principal axis {Z} and {Y} axis perpendicular to the plane of the plate, so in this case the crystal axes and spatial axes are aligned.

This example is chosen to demonstrate how easily root searching methods such as the one used by the author can miss pieces of the dispersion curves; the PSCM finds the missing parts not entirely computed by PWRF. To be fair to PWRF, manual intervention can identify the missing parts by modifying the algorithm to perform a finer search, but the lines are left broken to illustrate the point that PSCM finds all solutions automatically without further intervention.

As noted earlier fluid layers are an important special case and so the section is closed with an example of a multilayer system with a fluid layer placed between two solid layers. As explained in section 2.1, lest one obtains spurious modes, the codes must be slightly modified when a perfect fluid layer is included between solid layers or at the core of the system (fluid-filled pipe for instance). The modification consists of using displacements for the spectral scheme of the solid layers and one single potential (longitudinal since one is dealing with inviscid fluids) for the spectral scheme of the fluid layer. Without loss of generality, this approach may be used satisfactorily for any isotropic or anisotropic solid layers. As an aside, the case of viscous fluids and exterior fluids surrounding the system require a different treatment studied in Chapter 7.

Figure 2.11 displays the dispersion curves for the water layer sandwiched between two steel layers (with $5 - 2 - 5$ mm thickness). The axes configuration is: propagation along the principal axis {Z} and {Y} axis perpendicular to the plane of the plate. The dispersion curves display only Lamb modes, the SH modes have not been plotted since water, a perfect fluid, has no effect on them. Importantly, this figure also shows an example of a spurious
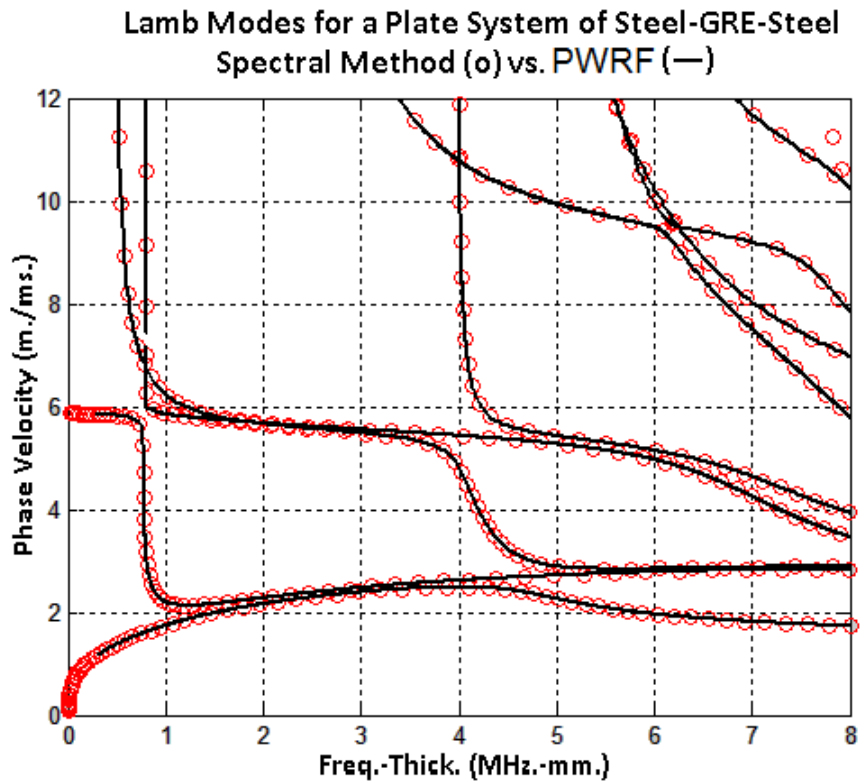
Figure 2.10: Steel-GRE-Steel $(2-2-2$ mm thick) Free Plate System: PSCM (circles) *vs.* PWRF (solid lines). GRE is a fibre composite whose physical parameters are given in the last section of this chapter. The product frequency-thickness of the graph's {x} axis refers to the total thickness of the system.
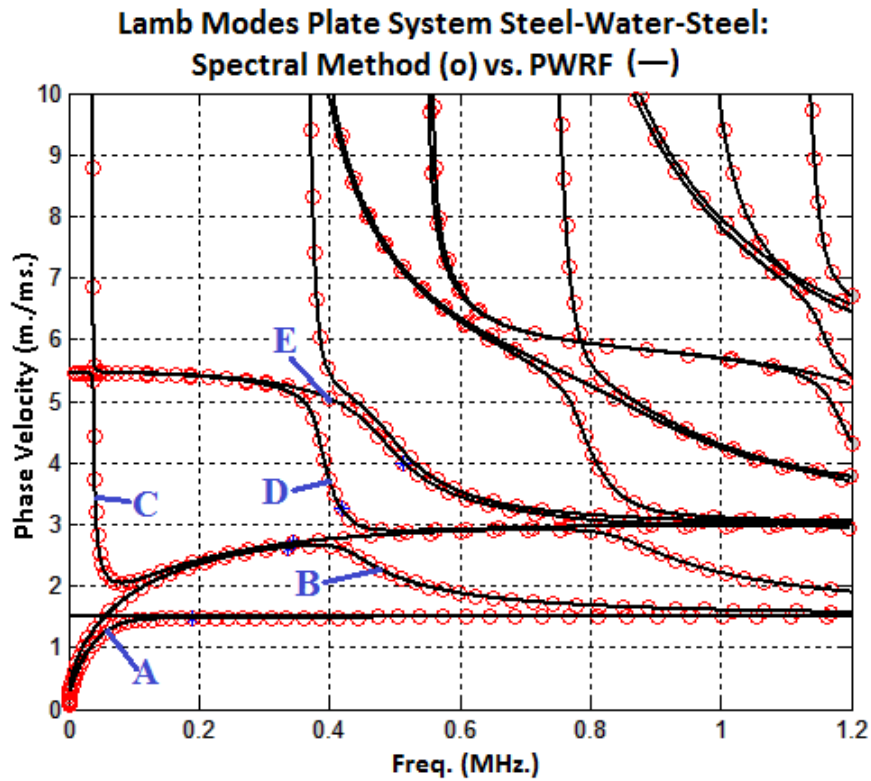
Figure 2.11: Steel-Water-Steel $(5 - 2 - 5$ mm thick) Plate System: PSCM (circles) *vs.* PWRF (solid lines). The axes' orientation is shown in Figure 2.1. The horizontal line at 1.5 m/ms is a spurious solution of the partial waves method. It is not found by the PSCM.

mode found by the PWRF model. The horizontal line at 1.5 m/ms is a spurious solution at the speed of bulk compression waves in the water. It is not found by the PSCM.

Figure 2.12 displays the mode shapes of the first five modes in this three-layered system Steel-Water-Steel: this illustrates another advantage of the PSCM, namely, one simultaneously obtains both the eigenvalues (modes) and eigenvectors (mode shapes). The mode shapes have the expected behaviour with the normal component of the displacement field continuous across the perfect fluid-solid interface whereas the tangential, or shear, component is discontinuous. It is notable that the mode shapes display no numerical noise or deviation despite the discontinuity.

Table 2.3 gives a typical numerical comparison between results obtained

44
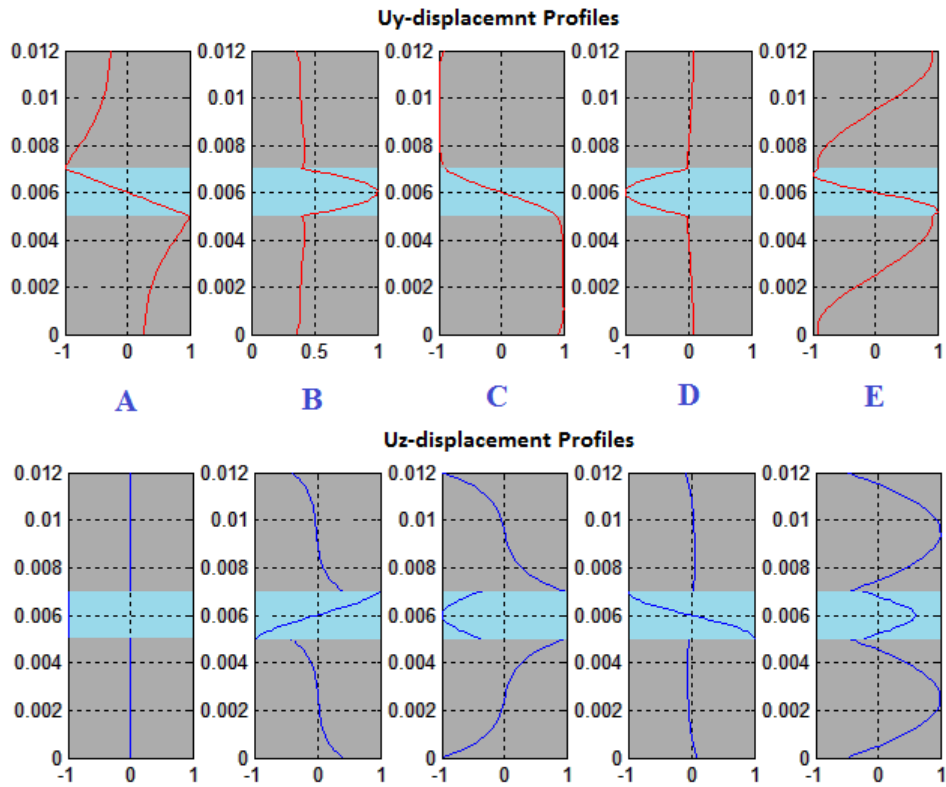
Figure 2.12: Steel-Water-Steel $(5-2-5$ mm thick) Plate System: Displacement Profiles of the system in Figure 2.11. Vertical axes plot the thickness of the system. Horizontal axes are adimensional and plot the relative amplitude of the field normalized to the maximum value. Profiles obtained with the PSCM.

by PSCM and PWRF, the example shown in Figure 2.11 is chosen. The values are at points for the first 5 eigenmodes and are all well within the desired accuracy margin. Running the code for $N = 110$ and computing the relative error between both sets of results shows the highest relative error between iterations lies below $10^{-3}\%$. Given the high accuracy of PSCM it is not clear which of the methods should be the reference "gold-standard" computation, this minor offset between the codes is due to the higher complexity of the problem vis-a-vis the single layer case. Nonetheless, the results sufficiently confirm the good convergence and reliability of the solution.

Mode	Freq.-Thick.	PWRF	S. M.	Relative Error
			($N = 110$)	
	(MHz-mm)	V_{ph} (m/ms)	V_{ph} (m/ms)	10^{-3} %
A	0.476536	2.27840	2.27900	26.3340
B	0.602921	2.88347	2.88350	1.0404
C	0.609561	2.91533	2.91522	3.7731
D	0.677135	3.23840	3.23840	0
E	0.686913	3.28530	3.28510	6.0877

Table 2.3: Relative error between the results given by the PSCM and PWRF for the case of Figure 2.11. The values correspond to the first 5 eigenvalues.

Similar comparisons were performed in cylindrical geometry again obtaining very good agreement between the PSCM and PWRF. Moreover, it was verified again that the PSCM did not compute any spurious modes when a fluid layer is present (a water-filled pipe for instance), a well-known problem of the PWRF approach [14].

2.3.3 Multilayered Systems *vs.* Spring Interface

To efficiently handle systems where an interface is modelled with finite stiffness, with very thin layers or has imperfect contact conditions, a spring interface is a sensible alternative. PSCM codes for perfectly matched (no imperfect boundary conditions) multi-layered systems require many more grid points when extreme cases exist, such as if the thicknesses of the constituent layers differ by several orders of magnitude (4 or more). This might be caused by the difference, and subsequent numerical ill conditioning of the matrix, in the system's matrix entries due to the extreme difference in the thicknesses of the layers. For these cases the Spring Model is preferable.

To cross-validate the Spring Model in the PSCM several examples were run in flat and cylindrical geometries and compared to the results given by existing and validated PWRF routines.

Figure 2.13 features both, the solution given by the PSCM and that given by a PWRF routine. For this example two steel 1mm thick layers were used. The spring constants are $K_t = 10^{12}$ N/m^3 and $K_n = 10^{16}$ N/m^3, these are arbitrary values that have been chosen to be within the range where variation of the values influences the dispersion curves; that is to say, they are not approaching either of the limiting cases of a decoupled interface or a perfectly coupled interface.

As anticipated, the PSCM solution agrees very well with that provided by the PWRF routine. Limiting cases with very high and very low spring constants have also been investigated and they reproduce the desired limiting cases of perfectly bonded layers and two unbonded layers respectively. Similarly, cross-verification for the cylindrical case in the thin plate limit shows perfect agreement with their corresponding flat analogues.

2.4 Discussion of Chapter 2

As has been demonstrated, the Spectral Method (PSCM) provides a powerful alternative to partial-wave root-finding routines and the other methods described in the brief review of the first. This has been comprehensively validated and cross-checked by means of various comparisons with available literature and papers; only the most general and illustrative cases are presented here. Additionally, several cases have also been validated with the established PWRF code.

The examples studied have highlighted the advantages of the PSCM approach as compared to widely used PWRF routines: PSCM overcomes the complexities and implementation difficulties of arbitrarily orientated axes and type of material encountered by PWRF formulations. It solves the most general cases of Triclinic materials and arbitrary orientations of the crystal axes, whether in cylindrical or in flat geometry. A key advantage is that PSCM does not miss any modes, so one can always be sure that the modes which are computed are all the modes that exist for that given case and frequency/wavenumber range. This removes the tedious task of searching for candidate missing modes, and removes the uncertainty of missing modes encountered by the author when using a general PWRF routine. It was also verified that the PSCM does not find any spurious modes in problems where PWRF routines do.

There is considerable industrial need for studying waves in all kinds of media and for multilayers, so the PSCM has been further extended to more general multilayer systems than those only involving isotropic media [36] and [37], to include both anisotropic layers and fluid layers. The accuracy
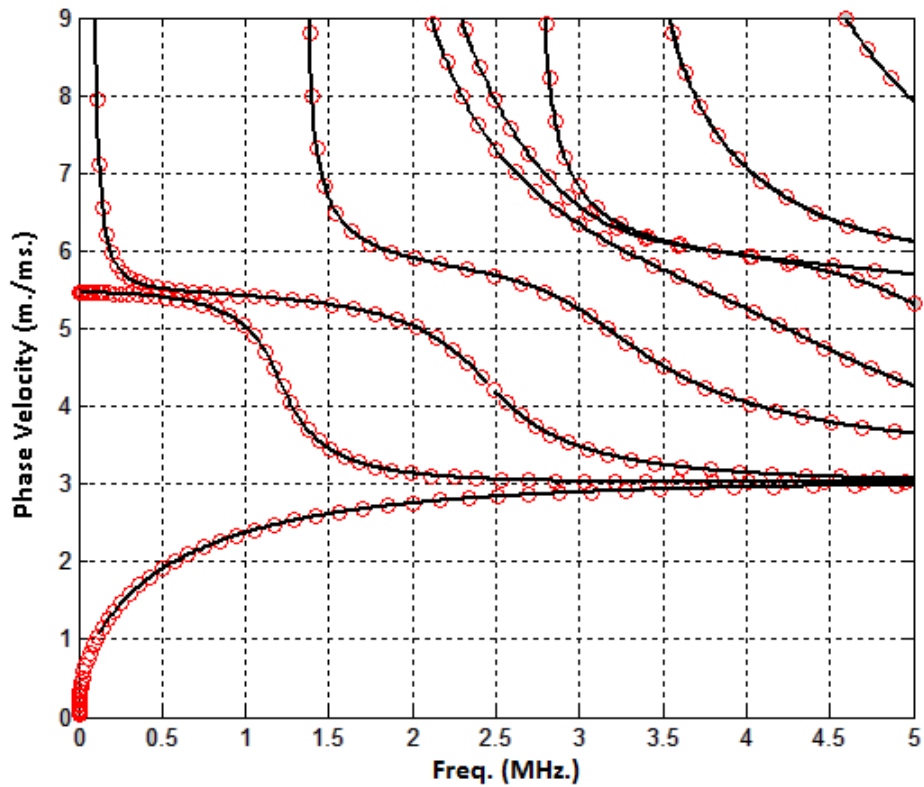
Figure 2.13: Two 1mm thick Steel layers imperfectly bonded: PSCM (circles) *vs.* PWRF (solid lines). The physical details of the spring interface can be found in the last section of the chapter. The spatial axes' configuration is shown in Figure 2.1. The plot features only the Lamb modes in the plate system.

of the results is very high and they present excellent self-convergence even for more complicated cases with various layers. Very complicated cases do require some care and convergence should be checked for increasing values of N. This notwithstanding, the accuracy and self-convergence remain within, more than acceptable, margins even for the most complicated cases of multi-layered systems of anisotropic materials.

Without any special treatment PSCM do not suffer from the "large-fd" problem inherent to many PW based methods, such as the Transfer Matrix method. This has been confirmed by running a code twice for different N to test the convergence and accuracy of the first modes. It was found that the modes are equally accurate for high values of the product "fd". Accuracy and convergence of the results was verified for as high a value as 25 MHz.-mm. in a 5 mm. steel plate and no errors or inaccuracies were found (cf. with the example for a titanium plate cited in [14] where the practical limit for the first two modes was set at 15 MHz.-mm.). Finally, on top of all the aforementioned advantages, the ease of coding makes PSCM very convenient when compared to other available options for solving waveguide problems.

2.5 Numerical data for examples of Chapter 2

The physical and geometrical information used for the figures presented in the chapter are given here; in certain cases the same material has been used in multiple figures. The number of grid points N varies from one example to another, but it is always at least double the number of modes plotted in the figure. On a practical level, one chooses N to achieve the shortest computation time, that is, if one is interested in the first 10 modes, running a code with $N = 100$ is unnecessary; a value of N between 25 and 30 has consistently been shown to be sufficient.
The parameters for the plate of Figure 2.3 are as follows (with the usual axes orientation):

$$\rho = 5300 \text{ kg/m}^3 \,; \qquad h = 5 \text{ mm} \tag{2.19}$$

h stands for the thickness of the plate. The elastic stiffness matrix is given in GPa:

$$\begin{pmatrix} 23.9 & 10.4 & 5 & & & \\ & 24.7 & 5.2 & & & \\ & & 13.5 & & & \\ & & & 6.5 & & \\ & & & & 6.6 & \\ & & & & & 7.6 \end{pmatrix} \tag{2.20}$$

The parameters for the plate of Figure 2.4 are (note that the axis configuration is that used in [13], and detailed in the caption of the figure):

$$\rho = 8938.4 \text{ kg/m}^3 \, ; \qquad h = 5 \text{ mm} \, ; \qquad V_{55} = \sqrt{c_{55}/\rho} \text{ m/ms} \qquad (2.21)$$

The elastic stiffness matrix is given in GPa:

$$\begin{pmatrix} 182.1 & 119.1 & 111.8 & & & \\ & 167.7 & 126.2 & & & \\ & & 174.9 & & & \\ & & & 92.1 & & \\ & & & & 53.5 & \\ & & & & & 67.6 \end{pmatrix} \qquad (2.22)$$

The parameters for the plate of Figure 2.5 are (with the usual axes orientation):

$$\rho = 8938.4 \text{ kg/m}^3 \, ; \qquad h = 5 \text{ mm} \, ; \qquad V_{66} = \sqrt{c_{66}/\rho} \text{ m/ms} \qquad (2.23)$$

The elastic stiffness matrix is given in GPa:

$$\begin{pmatrix} 207.87 & 109.06 & 93.41 & 16.57 & -16.15 & -23.18 \\ & 167.70 & 136.24 & -24.72 & 11.28 & 8.68 \\ & & 185.91 & 8.14 & 8.21 & 14.50 \\ & & & 100.23 & 14.50 & 5.84 \\ & & & & 35.11 & 16.57 \\ & & & & & 59.47 \end{pmatrix} \qquad (2.24)$$

Parameters for the cylinder of figures 2.6 and 2.7 are (with the usual axes orientation):

$$\rho = 8938.4 \text{ kg/m}^3 \, ; \qquad h = 5 \text{ mm}; \qquad r_i = 5 \cdot 10^3 \text{ mm} \qquad (2.25)$$

r stands for the inner radius. The elastic stiffness matrix is the same as in (2.24).

Parameters for Figure 2.8 are as follows (with the usual axes orientation):

$$\rho = 8938.4 \text{ kg/m}^3 \, ; \qquad h = 100 \text{ mm}; \qquad r_i = 100 \text{ mm} \qquad (2.26)$$

The elastic stiffness matrix is the one given in (2.24).

Parameters for the cylinder of Figure 2.9 are as follows (with the $\{Z\}$ axis at 45 degrees with the spatial $\{z\}$ axis):

$$\rho = 5300 \text{ kg/m}^3 \, ; \qquad h = 1 \text{ mm}; \qquad r_i = 1 \cdot 10^3 \text{ mm} \qquad (2.27)$$

The elastic stiffness matrix is given in (2.20).

Parameters for the three-plate system of Figure 2.10 are as follows (with the usual axes orientation): For the steel plates we have:

$$\rho = 7932 \text{ kg/m}^3 ; \qquad h = 2 \text{ mm}; \qquad \mu = 84.29 \text{ GPa}; \qquad \lambda = 113.16 \text{ GPa} \tag{2.28}$$

For the GRE plate we have

$$\rho = 1605 \text{ kg/m}^3 ; \qquad h = 2 \text{ mm} \tag{2.29}$$

The elastic stiffness matrix of the GRE layer is given in GPa:

$$\begin{pmatrix} 11.69 & 5.85 & 5.61 & & & \\ & 11.69 & 5.61 & & & \\ & & 130.19 & & & \\ & & & 3.7 & & \\ & & & & 3.7 & \\ & & & & & 2.92 \end{pmatrix} \tag{2.30}$$

Parameters for the system of Figure 2.11 are as follows (with the usual axes orientation). For the steel plate the thickness is $h = 5$ mm and the other physical parameters are those given in (2.28). For the water layer we have:

$$\rho = 1000 \text{ kg/m}^3 ; \qquad h = 2 \text{ mm}; \qquad \lambda = 2.25 \text{ GPa} \tag{2.31}$$

The stiffness matrix in rectangular coordinates must be rearranged in a similar fashion to [20] when dealing with problems in cylindrical coordinates.

The system of Figure 2.13 is composed of two imperfectly coupled steel layers. The two steel layers are each 1 mm thick, with properties given in (2.28). The spring constants for the interface are $K_t = 10^{12}$ N/m^3 and $K_n = 10^{16}$ N/m^3.

Chapter 3

Waves in Viscoelastic Waveguides.

Robust and reliable computation of dispersion curves is key for the successful development of Non Destructive Evaluation (NDE) techniques using guided waves as has been pointed out in introduction. Dispersion curves provide the information required to correctly select propagating modes for the study of the NDE of a particular type of defect, or some property of the materials, in a structure. The usage of dispersion curves for NDE is well established as the copious literature and studies on the subject show: analytical solutions using potentials or the partial wave decomposition for the isotropic plate and cylinder were found by Mindlin [1], Pao [3],[2], Gazis [4] and Zemanek [34]. Studies and solutions for anisotropic media in flat, and in cylindrical, geometry are in Solie and Auld [8], Nayfeh and Chimenti [9] and, more recently, Li and Thompson [13] or Towfighi *et al.* [20]. Also, attention has been given to multi-layer systems where fluid layers could also be present, such as fluid-filled pipes or plates surrounded by infinite fluid (or solid). Solutions based on the Transfer or Global Matrix method are in [14], [10] or [11] and references therein. Finally, some classical texts on the subject of guided waves are [6], [5], [31], [7] or [53]. These texts treat a variety of the problems above and their different applications in engineering and NDE.

In the previous chapter and in most of the calculations cited above materials are assumed to be perfectly elastic. However, a more general and realistic approach to guided wave problems is to allow the materials to possess some kind of material damping, such as viscoelasticity. By doing so, one allows for dissipation and loss of energy by various microscopic mechanisms within the material. As a consequence of this, waves propagating within the structure generally present attenuation and decay of their amplitude as they propagate. The development of efficient and reliable NDE techniques to inspect these kinds of media, commonly encountered in industry, is based on

a thorough understanding of their physical behaviour, as well as on robust and accurate tools to model and plot the dispersion curves of the modes they support. In the previous chapter, which led to a recent paper [46], a Spectral Collocation Method (PSCM), [21], was generalized as an alternative to the classical Partial Wave Root Finding (PWRF) routines for solving elastic (lossless) guided wave problems. This method presented a number of advantages over the PWRF which made it more robust and reliable. Moreover, due to its generality, the PSCM solved cases that were very difficult or not possible to solve with the PWRF. A range of illustrative examples, ranging from single layer to multilayer systems in flat and cylindrical geometry was presented and the different ways of validating the PSCM were discussed.

The focus of this chapter is on lossy media in the NDE context, but the methodology developed is relevant in broader settings and it is worth highlighting that attenuated guided waves appear not only in the context of elasticity and NDE but also in other branches of physics and engineering. For this reason, the PSCM deployed in this thesis is perfectly transferable across a wide range of disciplines. As pointed out in [21], spectral methods were introduced in the 1970s in the field of fluid dynamics by Kreiss and Oliger [54], Orszag [55] and Fornberg [56] and have remained a standard computational tool in the field ever since. Recently, the PSCM has been successfully used in the fields of seismology and geophysics to study wave propagation, see for instance [36, 22, 57]. Guided wave problems in other contexts such as electromagnetic waveguides can also be tackled by means of the PSCM, see for instance [58] where metal-insulator-metal electromagnetic lossless and lossy waveguides are studied. A last example of the wide applicability of the methodology presented in this chapter is provided by [59] where the eigenstates of the Schrödinger wavefunction in quantum rings are studied with the aid of a PSCM. In general, the PSCM can be applied to solve problems which are posed in the form of an eigenvalue problem.

In addition, laminates consisting of multiple layers of viscoelastic anisotropic materials, such as carbon fibre composites, as studied in this chapter, are being widely introduced in many engineering structures particularly in aerospace applications. These materials exhibit damping that varies hugely across the different modes, frequencies and directions of propagation. Also, the popular subject of Structural Health Monitoring (SHM) has strong interest in using guided waves to monitor large areas of composite plate structure by means of permanently attached transducers. The ability to calculate the dispersion curves with damping is essential for that purpose. Therefore, it is intended that the results and methodology presented in this chapter will be helpful to applications across a breadth of disciplines.

Attenuation of elastic guided waves can be caused by material damping,

fluid viscosity or by energy leakage into an infinite medium surrounding the waveguide. In this chapter structures are surrounded by a vacuum so the only mechanisms causing attenuation are material damping and fluid viscosity when fluids are present. Being intrinsic properties of the medium, damping and viscosity will cause attenuation of any perturbation within the medium. For propagating modes, attenuation will describe the decay of the amplitude of the fields as the wave travels through the structure. For non-propagating (local) elastic waves, attenuation describes the spatial decay of the fields in the waveguide; the former is the object of study of this chapter. However, solutions for attenuated local non-propagating elastic waves can also be found by the same procedure described in the following sections.

One of the methods usually used to approach guided wave problems in viscoelastic materials is the PWRF approach mentioned above, which, *for a given value of the frequency*, searches for the values of the wavenumber k satisfying the dispersion relation. In contrast to perfectly elastic cases, in which the search for roots is performed in $\mathbb{R}$, a one dimensional space; when damping is present, k is generally complex, and the search must be carried out in $\mathbb{C}$ which is two dimensional. This is the new challenge that damping brings to modelling in viscoelastic media, apart from those already cited and discussed in the previous chapter and in [46] and references therein.

The PWRF has been successfully used by various authors to model guided waves in viscoelastic materials. Nagy and Nayfeh [60] studied the effect of viscosity of the loading fluid on the longitudinal waves propagating in a multilayer system of cylinders. The model used for the fluid was a hypothetical isotropic solid and the attenuation was described using the Kelvin-Voigt model described in the next section. More recently, members of the NDE group at Imperial College have successfully investigated the propagation of guided waves in viscoelastic composites [61] using DISPERSE ([16], [15]), a Partial Wave based software package developed by them. In [61] the authors preferred to use the Hysteretic model although PWRF, and DISPERSE in particular, can accommodate both Hysteretic and Kelvin-Voigt approaches. The solution of the equations for a given value of the frequency, as the PWRF and PSCM approaches do, is not limited to those two models but allows for a very wide variety of damping models. More information about them is in [16], [15]. Finally, Bernard, Lowe and Deschamps [62] studied how energy velocity was affected by absorbing layers using PWRF.

Another alternative recently and successfully used to solve viscoelastic guided wave problems, [18] and [43], is the Semi Analytical Finite Element (SAFE) method. In this approach it is also possible to implement the Kelvin-Voigt and Hysteretic models as described in [18]. The SAFE methodology is a valuable tool for the study of guided waves, particularly because of its pow-

erful treatment of waveguides of arbitrary cross-section, however it does present some difficulties such as the overestimation of frequencies due to the higher stiffness of discretized structures [43]. This higher stiffness is caused by the discretization process and results in guided waves propagating with a slightly higher phase velocity. This results in either an overestimation of frequency or underestimation of wavenumber depending on which parameter is held fixed, this problem can be cured by using a finer mesh. In addition, when using SAFE, spurious modes produced in the simulation must be filtered and although some automation has been used, more usually, this has to be done manually. Besides, the implementation of a SAFE model requires sound knowledge of the finite element (FE) procedure and use of specialist FE codes.

In this chapter, propagating modes in viscoelastic media are studied. The main contribution is the successful extension of the PSCM approach ([21], [46]) presented in Chapter 2 for finding guided waves in generally anisotropic viscoelastic media in flat and cylindrical geometry by means of a companion matrix technique as described in the following paragraphs and in section 3.1.

As mentioned above, the greatest difficulty that arises in the modelling of viscoelastic materials is the search for complex roots. Generally, if the PWRF algorithm is capable of performing searches in both variables, it looks for pairs (ω, k) that satisfy the dispersion relation, that is, it searches in $\mathbb{R} \times \mathbb{C}$, a three dimensional space. If the frequency is fixed, the search is reduced to $\mathbb{C}$. In either case, the solution space is one dimension higher than the solution space in the perfectly elastic case, two dimensions and one dimension respectively since (ω, k) are both real for non-attenuating propagating modes. This extra dimension of the solution space makes the search for roots in the viscoelastic case even harder than in the perfectly elastic case and the probability of missing a root is therefore increased. The roots of attenuated modes are also very important for NDE practitioners, engineers or researchers in the field, but they are relatively difficult to find, especially for demanding cases such as those involving multiple layers, anisotropy or cylindrical geometry. Therefore, robust and reliable new methods to compute all roots of the dispersion relation are extremely valuable. In this chapter the methodology will be somewhat different from that of Chapter 2: a real frequency ω is fixed and the algorithm finds the eigenvalues that are precisely the complex k. This approach differs fundamentally from the one used in the previous chapter and in the paper [46] studying elastic materials in which k is fixed and solutions for real ω are sought.

The PSCM overcomes these difficulties since it solves the equations algebraically by finding the eigenvalues of an analogous matrix problem ([21], [46] and previous chapter). The PSCM is equally applicable to problems

with complex or real eigenvalues at no extra cost or effort on the part of the modeller and it has the noteworthy advantage of not missing any modes. Since the PSCM computes all the eigenvalues rather than looking for zeroes of a function, as the PWRF does, one can be sure to obtain a complete solution. A more detailed description of the PSCM's features shall not be pursued here again, the interested reader will find an exhaustive discussion of the PSCM and its applications to elastic guided wave problems in [21], [46] or in the previous chapter; additionally the books by Boyd [24], Trefethen [25] and Fornberg [23] are established references in the field of Spectral Methods and contain rigorous derivations of several features of the PSCM.

The dispersion curves of a viscoelastic material are often very different from those of its perfectly elastic counterparts depending on the value of the damping. In viscoelastic media, it no longer makes sense to speak about cut-off frequencies since the solutions are complex. When one sets a limit to the attenuation of the mode for it to be considered a propagating one, the dispersion curves might look incomplete or two different modes appear to merge or cross at a point where no crossing was seen in the perfectly elastic counterpart. These difficulties, added to the ones explained above, sometimes render the PWRF approach misleading or not very robust when modelling viscoelastic media. This highlights the need for a robust and reliable algorithm to find dispersion curves in viscoelastic materials. In addition, a robust and reliable algorithm based on the PSCM serves as a solid foundation for the development of more complicated models for the leaky and trapped modes that occur in embedded structures to be discussed in Chapter 7.

The chapter is structured as follows. In section 3.1, the viscoelastic models presented here, as well as the necessary modifications for the PSCM scheme to handle them, are described, and references are given for descriptions of more basic PSCM schemes. Section 3.2 summarizes the SAFE models used to validate the results which are due to my collaborator Dr. Zheng Fan. Section 3.3 is devoted to systems in flat geometry, single and multilayer examples of the most relevant or general cases are shown and compared to the results given by the SAFE simulation. Section 3.4 deals with single and multilayer systems in cylindrical geometry, the results and how they were validated are presented. In many cases the validation of the cylindrical cases has followed the same steps as their perfectly elastic counterparts, therefore, when appropriate, references are given to the relevant literature. Due to its paramount importance in NDE, section 3.5 focuses on viscoelastic or perfectly elastic pipes filled with perfect or viscous fluids. The challenges posed to the PSCM by this family of problems are described as well as the theoretical framework chosen to model the fluid layers. In section 3.6 a summary

and a discussion of the results is presented. As is customary, the numerical data used in the examples of the chapter are collected in the last section. The material of this chapter led to the second publication [63] of the List of Publications at the begining.

3.1 Spectral Collocation Scheme and the Companion Matrix

This chapter begins with a description of the viscoelastic models to be used. The equations of time-harmonic motion for a linear elastic anisotropic homogeneous medium are:

$$\nabla_{jK} c_{KL} \nabla_{Lq}^{sym} u_q = -\rho\, \omega^2\, u_j \tag{3.1}$$

where the summation convention over the indices has been used and c_{KL} is the medium's stiffness matrix in reduced index notation, [5] , u_j are the components of the displacement vector field:

$$u_j = U_j(y)\, e^{i(kz-\omega t)}\,; \qquad j = 1,2,3 \tag{3.2}$$

and the differential operators are of first order in the coordinate derivatives; their explicit expressions are in [5]. The axis configuration used in the examples of this chapter for flat and cylindrical geometry is shown in figure 2.1. It is the same as in the previous chapter and it will be stated explicitly when it is otherwise.

For structures in a vacuum, traction-free boundary conditions must be taken into account that require the vanishing of the following three components of the *stress tensor field* defined below, T_{ij}. Taking the faces of the plate to be located at $y = \pm h/2$ the boundary conditions (BCs) are given by:

$$T_{yy}|_{y=\pm h/2} = T_{yx}|_{y=\pm h/2} = T_{yz}|_{y=\pm h/2} = 0. \tag{3.3}$$

The expression of the *stress tensor field* in terms of the *strain tensor field* for a *perfectly elastic* material reads:

$$T_{ij} = c_{ijkl}\, S_{kl} \tag{3.4}$$

where c_{ijkl} is the fourth-rank stiffness tensor, related to c_{KL} as described in [5]. When material damping is taken into account, the entries of the stiffness tensor of the material are no longer real but have a complex part as well. The *strain tensor field*, S_{ij}, in terms of the *displacement vector field*, u_j is:

$$S_{ij} = \frac{1}{2}\left(\frac{\partial u_i}{\partial x_j} + \frac{\partial u_j}{\partial x_i}\right) \rightarrow S_K = \nabla_{Kj}^{sym} u_j : \tag{3.5}$$

so one has a set of three equations of motion and six additional equations for the boundary conditions.

The Kelvin-Voigt (KV) model is well established for describing viscoelastic media and it is briefly described below. In this model, the imaginary part of the stiffness matrix depends on the frequency. Thus, following Auld [5], one has the extended version of (3.4):

$$T_{pj} = \left(c_{pjkl} + \kappa_{pjkl} \frac{\partial}{\partial t} \right) S_{kl} \tag{3.6}$$

For time harmonic behaviour such that $S_{kl} \propto e^{-i\omega t}$ etc assumed henceforth then one is left with:

$$T_{pj} = \left(c_{pjkl} - i\omega \kappa_{pjkl} \right) S_{kl} \tag{3.7}$$

the viscoelastic stiffness matrix is defined as:

$$\tilde{c}_{pjkl}^{KV} \equiv c_{pjkl} - i\omega \kappa_{pjkl} \tag{3.8}$$

Note that κ_{pjkl} has units of sPa, not Pa as c_{pjkl}; to have the same units in both entries and avoid possible confusion the following tensor is defined:

$$\kappa_{pjkl} \equiv \frac{\eta_{pjkl}}{\hat{\omega}} \tag{3.9}$$

Where $\hat{\omega}$ is the normalization frequency at which the damping constants of the material were measured. This yields the familiar expression for the stiffness matrix with homogeneous units:

$$\tilde{c}_{pjkl}^{KV} = c_{pjkl} - i \frac{\omega}{\hat{\omega}} \eta_{pjkl} \tag{3.10}$$

Where c_{pjkl} and η_{pjkl} have the same units and the prefactor $\omega/\hat{\omega}$ is non-dimensional.
The second model considered is the Hysteretic (H) model that is a simplification of the previous one. In this model one takes the viscoelastic stiffness matrix to be frequency independent:

$$\tilde{c}_{pjkl}^{H} = c_{pjkl} - i \eta_{pjkl} \tag{3.11}$$

Further discussion of these models is in [5], [31], [18] and references therein.

The PSCM scheme for viscoelastic materials is similar to that used for their perfectly elastic counterparts in the previous chapter, see also for instance [21], [46]. The novelty in the present case, with respect to the study for elastic materials presented before and in [46], is that the PSCM will be deployed to search for complex values of the wavenumber k rather than real ones as

in the perfectly elastic case and this has consequences in how the PSCM is implemented as described in the next paragraphs. In fact, in the perfectly elastic case, the real value of k is fixed and one solves the eigenvalue problem for the real values of frequency. This was more convenient in perfectly elastic cases since the frequency only enters the equations in one term of the PDE so they can be directly recast into a general eigenvalue problem.

In the case of viscoelastic materials it is better to fix a real frequency (one dimensional space) and solve for the complex values of k (two dimensional space) that satisfy the dispersion equation. The issue now is that k does not enter linearly into the equations of motion. This appears to make it impossible to recast them into a general eigenvalue problem but an algebraic manipulation known as the *Linear Companion Matrix Method* allows for this to be rearranged into the more convenient form of a general eigenvalue problem. This is achieved at the cost of doubling the dimension of the matrices involved, see Bridges and Morris [64] and references therein for further mathematical details about this method and their impact on the eigenvalues computation. More recently other authors have successfully used this approach in guided wave problems, see Pagneux and Maurel [65] or Postnova [66] for instance. This success has motivated the choice of this linearization scheme and since the results have been satisfactory an extension to other schemes has not been pursued. A brief outline of the manipulations is given in the following paragraph. It must be noted that this manipulation has only been performed in the PSCM scheme.

For the viscoelastic case the equations of motion (3.1), and boundary conditions (3.3), are recast into a general eigenvalue problem by the standard PSCM procedure: one discretises and substitutes the derivatives by Differentiation Matrices (DMs). For a single layer in a vacuum, since one has a bounded interval, the appropriate choice is to use Chebyshev DMs, based on a non-uniform Chebyshev grid of N points, these are $N \times N$ matrices; the generation of DMs is covered in [25], [45]. The m-th derivative with respect to y is approximated by the corresponding m-th order Chebyshev $N \times N$ DMs:

$$\frac{\partial^{(m)}}{\partial y^{(m)}} \Longrightarrow \mathbf{D}^{(m)} := [DM_{Cheb}]_{N \times N}^{(m)} \tag{3.12}$$

The above substitution is made in the equations of motion (2.1), and boundary conditions (2.3), yielding their matrix analogue that is succinctly written as:

$$\mathfrak{L}(k) \, \mathbf{U} = \omega^2 \, \mathfrak{M} \, \mathbf{U} \tag{3.13}$$

and

$$\mathfrak{S}(k) := \begin{pmatrix} \mathfrak{T}_A & \mathfrak{T}_B & \mathfrak{T}_C \\ \mathfrak{T}_D & \mathfrak{T}_E & \mathfrak{T}_F \\ \mathfrak{T}_G & \mathfrak{T}_H & \mathfrak{T}_I \end{pmatrix} \begin{pmatrix} \mathbf{U}_1 \\ \mathbf{U}_2 \\ \mathbf{U}_3 \end{pmatrix} = \begin{pmatrix} 0 \\ 0 \\ 0 \end{pmatrix} \tag{3.14}$$

respectively, where $\mathbf{U}$ is the *vector of vectors*: $\mathbf{U} = [\mathbf{U}_1, \mathbf{U}_2, \mathbf{U}_3]^T$, these vectors $\mathbf{U}_i$ are the components of the displacement vector field. The matrix $\mathfrak{L}(k)$ contains the differential operators of the PDEs and the matrix $\mathfrak{M}$ is the identity multiplied by $-\rho$. The Boundary Conditions (BCs) in equation (3.3) are taken into account by appropriately substituting the corresponding rows of (3.13) by those of (3.14) in the following fashion: the $1, N, (N+1), 2N, (2N+1)$ and $3N$ rows of the $\mathfrak{L}$ matrix have been replaced with those of the matrix equation $\mathfrak{S}$ for the boundary conditions of (3.14). Similarly, we replace the same rows of the matrix $\mathfrak{M}$ on the right hand side with rows filled with zeroes. The resultant system has both the governing equation and boundary conditions incorporated in a consistent manner and furthermore has the structure of a standard generalised eigenvalue problem ideally suited for coding. This scheme can be extended to multilayer systems but a description of the procedure will not be pursued in this chapter because it follows exactly the procedure set out in the previous chapter and in [46] with no need for modifications specific to the damped cases.

The $\mathfrak{L}(k)$ matrix contains terms proportional to k^0, k^1 and k^2. Let us rearrange the terms in the matrix equation (3.13) and decompose the $\mathfrak{L}(k)$ matrix in such a way that the k dependence of the different terms becomes more apparent. One can write:

$$\left(\mathbf{Q}_2 \, k^2 + \mathbf{Q}_1 \, k + \mathbf{Q}_0(\omega^2)\right) \mathbf{U} = 0 \tag{3.15}$$

It should be clear now that, once the value of ω is fixed, this does not have the structure of a general eigenvalue problem in k. To achieve this, the following definitions are required. Let $\hat{\mathbf{U}}$ be the *companion displacement vector field*:

$$\hat{\mathbf{U}} \equiv k \, \mathbf{U} \tag{3.16}$$

The companion matrices to (3.15) are:

$$\mathbf{M}_1 \equiv \begin{pmatrix} -\mathbf{Q}_1 & -\mathbf{Q}_0 \\ \mathbf{I} & \mathbf{Z} \end{pmatrix} \qquad \mathbf{M}_2 \equiv \begin{pmatrix} \mathbf{Q}_2 & \mathbf{Z} \\ \mathbf{Z} & \mathbf{I} \end{pmatrix} \tag{3.17}$$

where $\mathbf{I}$ is the identity matrix and $\mathbf{Z}$ is a matrix of zeroes. With the above definitions, equation (3.15) is more conveniently expressed as:

$$\mathbf{M}_1 \begin{pmatrix} \hat{\mathbf{U}} \\ \mathbf{U} \end{pmatrix} = k \, \mathbf{M}_2 \begin{pmatrix} \hat{\mathbf{U}} \\ \mathbf{U} \end{pmatrix} \tag{3.18}$$

Equation (3.18) is easily solved using an eigensolver routine that yields the complex eigenvalues k; we use the routine `eig` of MATLAB (version R2012b) on an HP desktop computer.

To better process the results obtained and retain only the propagating modes

which are the object of study in the present chapter, a ratio between the real and imaginary parts of $k = \alpha + i\,\beta$ is defined. Note that all possible four combinations of wavenumber are obtained but for symmetry and physical reasons only one of the two with exponential decay is kept.

$$R \equiv \frac{\beta}{\alpha} \tag{3.19}$$

After the eigenvalues k have been found, R is used to select only those with a low value of attenuation within the range of wavenumbers under study, these are the propagating modes. Here, the propagation direction of the harmonic perturbation is taken in the positive direction of the $\{z\}$ axis, the displacement vector field was taken to be proportional to $\mathbf{U} \sim e^{ikz}$ in equation (3.2), therefore $\beta \geq 0$ to ensure the decay of $\mathbf{U}$ with distance. A good initial guess for this ratio is to take it closer to the quotient of the imaginary and real parts of one of the principal stiffness constants, c_{11} for instance.

3.2 The Semi analytical finite element models for validation of results (*Section written by Dr. Zheng Fan and reproduced here for completeness with his kind permission.*)

The Semi-Analytical Finite Element (SAFE) method is popular for studying properties of guided waves along waveguides with arbitrary cross section, such as railway lines [40], beams [67], [68], welded [42] or stiffened plates [19], etc. It uses Finite Elements (FE) to represent the cross section of the waveguide, plus a harmonic description along the propagation direction, thus limiting the FE model to two dimensions. SAFE analysis can be deployed using specific programming [18], or advanced use of a flexible commercial code such as COMSOL (2014). In this chapter a method described by [69] is implemented to validate results from the PSCM method. These simulations are all due to Dr. Zheng Fan.

The SAFE method assumes that there is no geometric variation of the cross-section along the axis of the waveguide, so the behaviour in the wave propagation direction can be written in analytical form. Thus the displacement vector in the waveguide is written as:

$$u_j(x, y, z, t) = U_j(x, y)e^{i(kz - \omega t)} \tag{3.20}$$

in which k is the wavenumber, $\omega = 2\pi f$ is the angular frequency, f is the frequency, t is the time variable and the subscript $j = 1, 2, 3$ The function U_j represents the behaviour in the cross-section of the waveguide, for which

the geometry is irregular, such that it is incorporated in the model by a two-dimensional FE discretization. For general anisotropic media, the equation of dynamic equilibrium is written in the following form of an eigenvalue problem:

$$c_{iqjl}\frac{\partial^2 U_j}{\partial x_q \partial x_l} + I(c_{i3jq} + c_{iqj3})\frac{\partial(kU_j)}{\partial x_q} - kc_{i3j3}(kU_j) + \rho\omega^2\delta_{ij}U_j = 0, \ (3.21)$$

with summation over the indices $j = 1, 2, 3$ and $q, l = 1, 2$. The coefficients c_{ijkl} are the stiffness moduli and δ_{ij} is the Kronecker symbol. The equation is reconstructed and solved in the format of a standard eigenvalue problem in the commercial FE code COMSOL (2014), and the full details are provided in [69].

The geometry is meshed by square elements of second order, with side length of 0.05mm. Periodic boundary conditions [69] were imposed at the lateral boundaries of the domain in the plate models. The number of degree of freedom in our models is less than 11000, and the typical calculation time for each SAFE model on a standard PC (Intel Core i7, 8GB memory) was less than 15 seconds. For chosen values of angular frequency ω, eigenvalues of complex wavenumber k are found, in which the real part describes the harmonic wave propagation while its imaginary part presents the attenuation. Each solution at a chosen frequency reveals the wavenumbers of all possible modes at that frequency; then the full dispersion curve spectrum is constructed by repeating the eigenvalue solutions over the desired range of frequencies. In the following sections, SAFE models will be applied to both flat and cylindrical structures, and the results are used for validation of those obtained by the PSCM.

3.3 Flat Geometry

In this section some illustrative examples in flat geometry are presented. Orthorhombic materials are treated firstly as a preparatory example and because they have already been studied in the literature, see references below. Then, a few novel cases of the most general choice of anisotropic material, triclinic, are presented and the section finishes with a multi-layer example.

Orthorhombic materials are commonly encountered in industry and have already been studied in two references given in the introduction, namely [18] and [61]. In the PSCM context, a code for an orthorhombic medium can also be used for all those materials whose stiffness matrix has a similar block structure, such as hexagonal or isotropic; the section begins by presenting an example of a viscoelastic orthorhombic plate in vacuum. The thickness of the plate is 1mm, the propagation takes place along the $\{Z\}$

crystal axis and the $\{Y\}$ crystal axis is perpendicular to the plane of the plate. More details about the physical properties of this plate are given in the appendix at the end. This example has been done using the Kelvin-Voigt model described in the previous section and the parameter $R = 0.5$ for both Lamb and SH modes.

The aforementioned first case is presented in Figures 3.1.a and 3.1.b that show the phase velocity curves and the attenuation of the Lamb and SH modes respectively. The comparison between the results given by the PSCM (blue circles) and those given by the corresponding SAFE simulation (red asterisks) is excellent. In Figure 3.2 a detail of Figure 3.1.a is shown, and some spurious solutions found by the SAFE simulation are clearly seen, which are pleasingly not given by the PSCM approach.

The next case presented is a 1mm thick viscoelastic triclinic plate using the Kelvin-Voigt model. The propagation takes place along the $\{Z\}$ crystal axis and the $\{Y\}$ crystal axis is perpendicular to the plane of the plate. Figure 3.3.a features the dispersion curves and Figure 3.3.b the attenuation for this case. The solution given by the PSCM (blue circles) is compared to that given by SAFE (red circles) and the agreement between both solutions is very good. This case is of particular importance since triclinic materials are the most general type of anisotropic material; with 21 independent constants and only one centre of symmetry which imposes no restriction over the stiffness constants this case poses a great challenge for PWRF routines due to its complicated dispersion relation. In [32] the reader can find a brief discussion about these materials. Further physical properties for this case, as well as the parameter R used in the PSCM code, are given in the appendix.

The last case of single plate systems uses the Hysteretic model to compute the attenuation and dispersion curves showing that the PSCM works equally well with this simpler damping model. A 50mm thick viscoelastic triclinic plate is studied, the physical elastic properties of this plate are the same as the one of the previous examples and are given in the appendix. The propagation takes place along the $\{Z\}$ crystal axis and the $\{Y\}$ crystal axis is perpendicular to the plane of the plate. This last example is plotted in Figures 3.4.a and 3.4.b, displaying the dispersion curves and attenuation respectively. The PSCM solution (blue circles) is compared with excellent agreement to the solution given by the SAFE simulation (red asterisks).

Three illustrative single plate examples have been presented to illustrate how the PSCM can handle equally well two of the most used models to account for attenuation, the Kelvin-Voigt model and the Hysteretic model; the agreement with the SAFE simulation was excellent for all the examples.
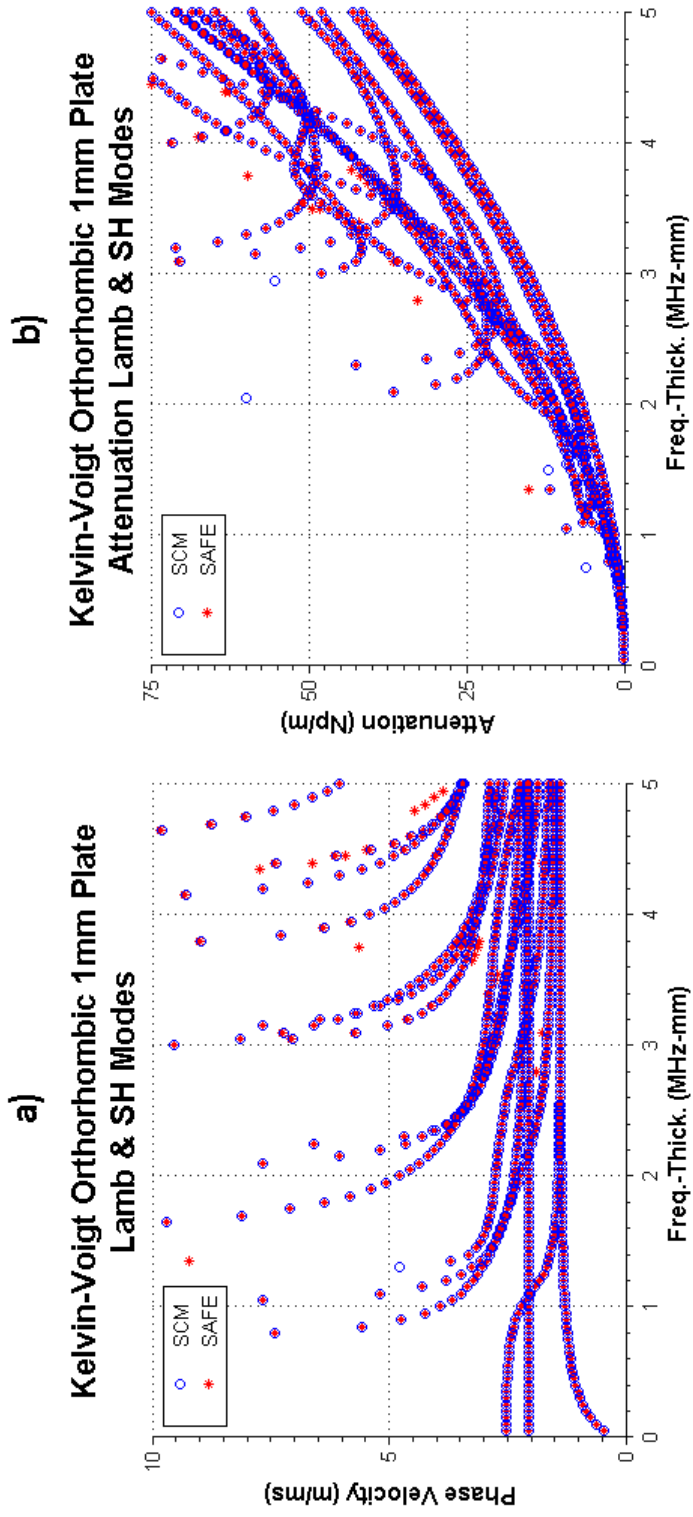
Figure 3.1: Lamb and SH modes phase velocity (a) and attenuation (b) for a 1 mm thick free viscoelastic orthorhombic plate with Kelvin-Voigt-type damping: PSCM (blue circles) *vs.* SAFE (red asterisks). Geometry and spatial axes configuration as in Figure 2.1: propagation is along the $\{Z\}$ axis, and the $\{Y\}$ axis is perpendicular to the plane of the plate.
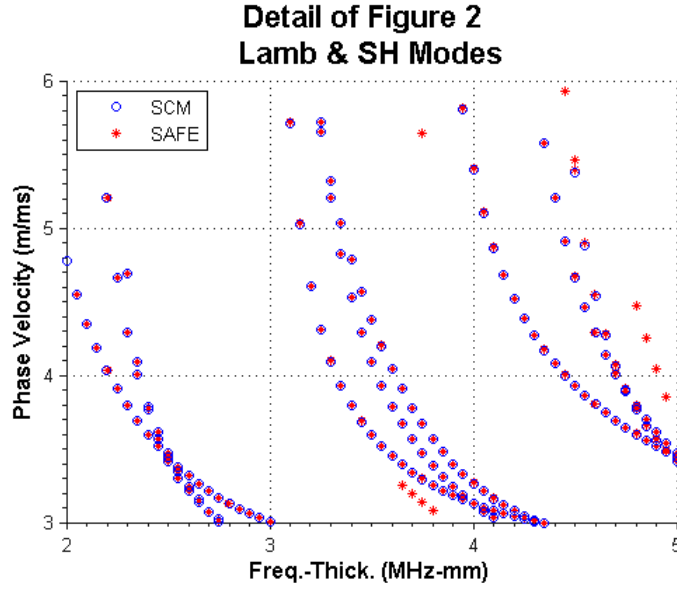
Figure 3.2: Detail of Figure 3.1.a: Dispersion curves for Lamb and SH modes for a 1 mm thick free viscoelastic orthorhombic plate with Kelvin-Voigt-type damping: PSCM (blue circles) *vs.* SAFE (red asterisks).

This section is closed with a multilayer example shown in Figures 3.5.a and 3.5.b. The system is composed of three plate: the top plate is 8mm thick and it is made of a viscoelastic triclinic material, the middle plate is 5mm thick and it is made of a viscoelastic orthorhombic material, and the bottom plate is a 3 mm thick perfectly elastic triclinic layer. Note that the total thickness has been used for the x axis in both figures. The materials of all three layers are different and the physical parameters of the system are retrieved from section 3.7. In all the layers the propagation takes place along the $\{Z\}$ crystal axis and the $\{Y\}$ crystal axis is perpendicular to the plane of the plate, crystal and spatial axes are aligned and the Hysteretic model was chosen to account for the damping in the materials. Figure 3.5.a displays the dispersion curves and Figure 3.5.b the attenuation. The solutions given by the PSCM (blue circles) are once more validated with those given by the SAFE simulation (red asterisks) showing good agreement.

It should be noted that the first case of the section studying orthorhombic materials involved propagation along a principal axis and nothing explicit has been said about propagation at an arbitrary angle with respect to the principal axis which can also be seen as a case of monoclinic material with propagation within its plane of symmetry, see for instance [9]. This case as well as the even more general one of a monoclinic material with propagation

65
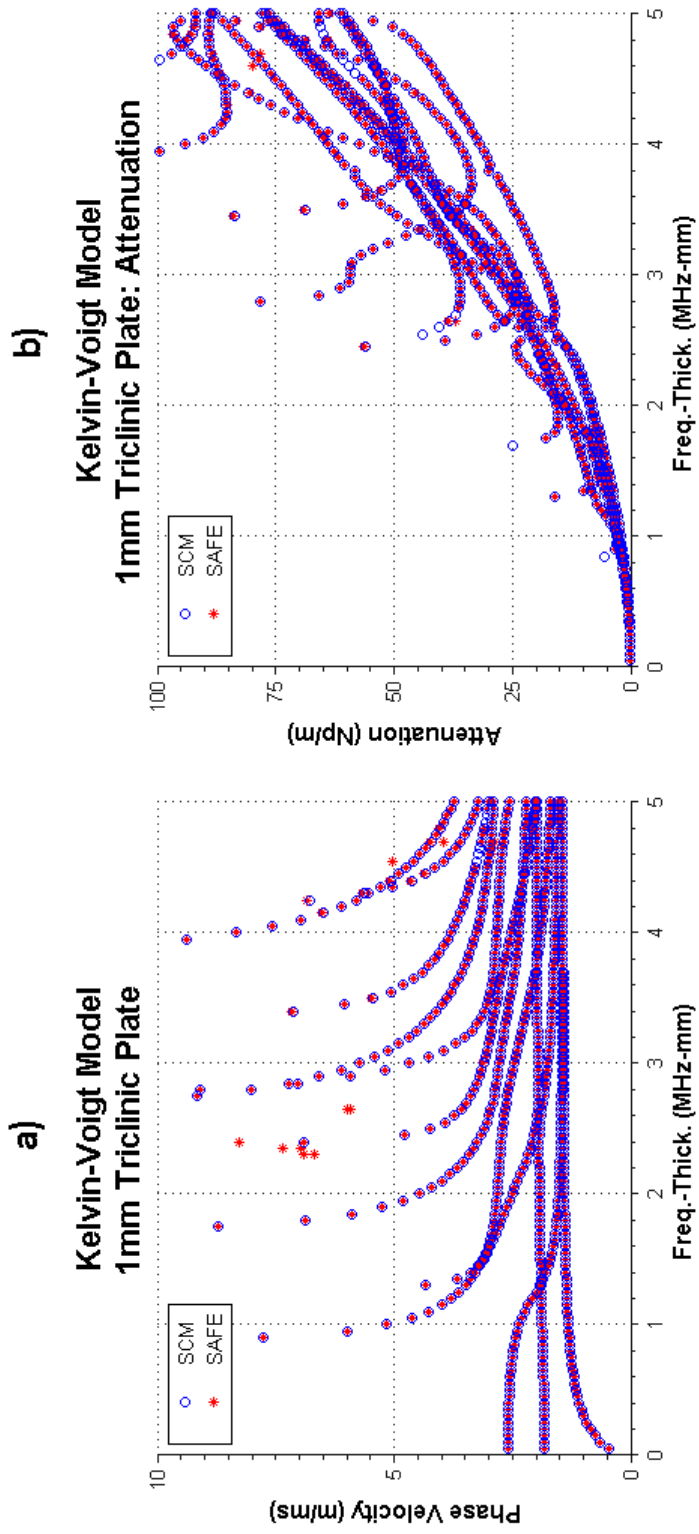
Figure 3.3: Phase velocity (a) and attenuation (b) for a 1 mm thick free viscoelastic triclinic plate with Kelvin-Voigt-type damping: PSCM (blue circles) *vs.* SAFE (red asterisks). Geometry and spatial axes configuration as in Figure 2.1: propagation is along the {Z} axis, and the {Y} axis is perpendicular to the plane of the plate.
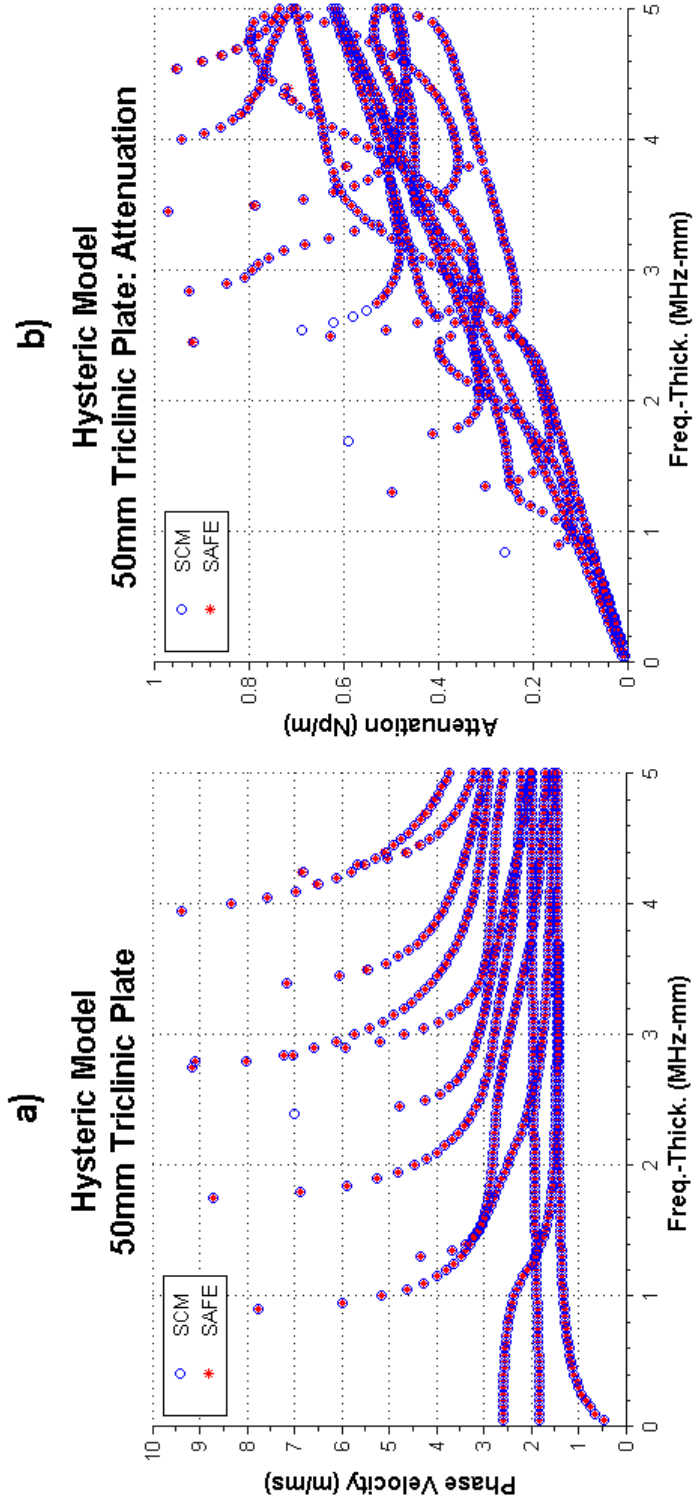
Figure 3.4: Phase velocity (a) and attenuation (b) for a 50 mm thick free viscoelastic triclinic plate with hysteretic-type damping: PSCM (blue circles) *vs.* SAFE (red asterisks). Geometry and spatial axes configuration as in Figure 2.1: propagation is along the $\{Z\}$ axis, and the $\{Y\}$ axis is perpendicular to the plane of the plate.
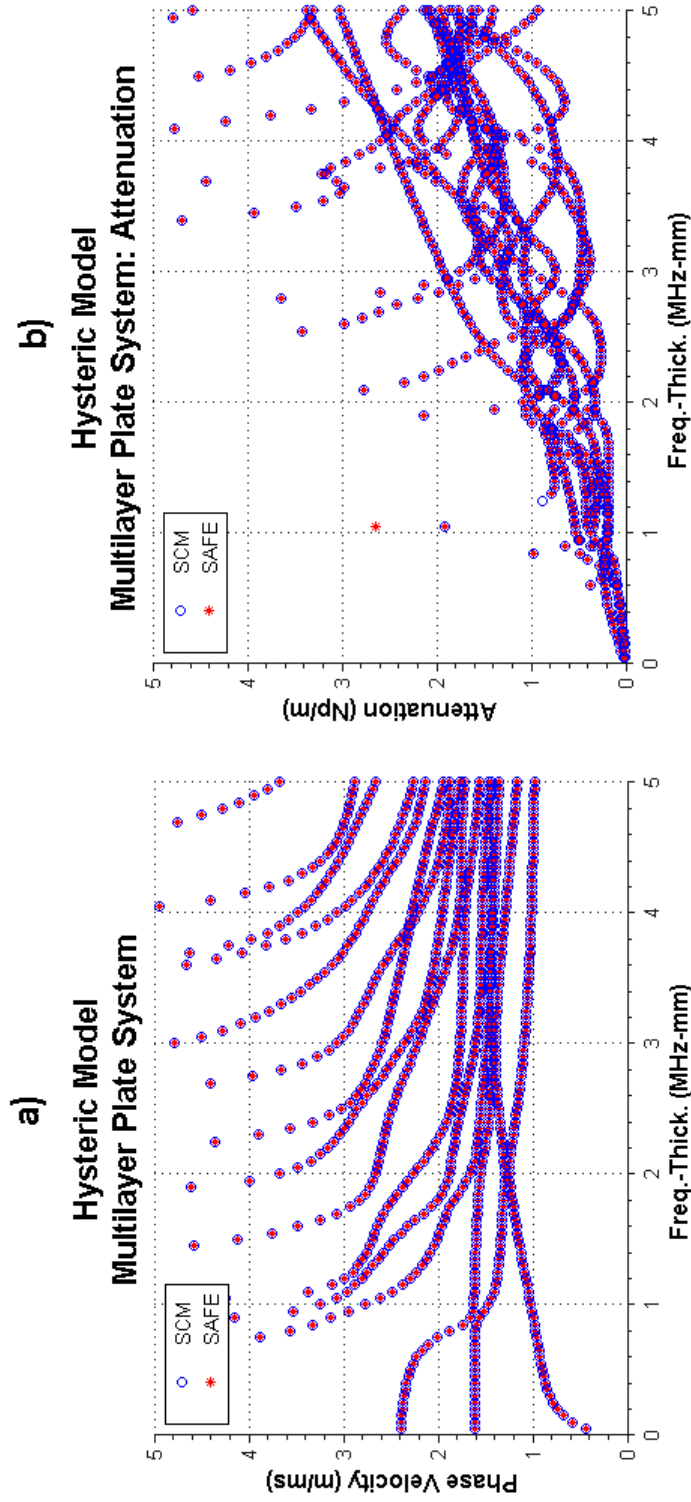
Figure 3.5: Phase velocity (a) and attenuation (b) for a 3-layered system with hysteretic-type damping: viscoelastic 8 mm thick triclinic layer (top), viscoelastic 5 mm thick orthorhombic layer (middle) and elastic 3 mm thick triclinic layer (bottom). Note that the total thickness has been used for the x axis in the figure. The solutions are plotted as follows: PSCM (blue circles) *vs.* SAFE (red asterisks). Geometry and spatial axes configuration as in Figure 2.1: propagation is along the {Z} axis, and the {Y} axis is perpendicular to the plane of the plate.

direction at an arbitrary angle with respect to the plane of symmetry, which after rotation yields a triclinic stiffness matrix, can be solved by employing the codes for triclinic materials which have been studied and validated here. Therefore, for the sake of brevity, these "particular" cases have not been studied explicitly and attention has been given only to the general triclinic case containing them as limit cases.

3.4 Cylindrical Geometry

For the cylindrical geometry, with guided waves propagating along the $\{Z\}$ crystal axis, the solutions are classified according to their *circumferential harmonic order*: n. In general the solutions have the following form:

$$u_j = U_j(r)\, e^{i(kz+n\theta-\omega t)}\,; \qquad j = r, \theta, z \qquad (3.22)$$

In materials such as isotropic or orthorhombic, the solutions with $n = 0$ yield two decoupled independent modes, the reader is referred to the previous chapter and to [46] for the procedure to find out whether there is decoupling of modes or not in the different materials. These modes are known in the literature as Torsional and Longitudinal modes, see [6] or [5] for instance. The former are the cylindrical analogues of the plate SH modes, the latter are the analogues of the plate Lamb waves. In the literature (see previous references), the solutions with $n \neq 0$ are called Flexural modes. The different families are labelled by the *circumferential harmonic order*, n. Note that in materials such as monoclinic or triclinic the splitting of the $n = 0$ family into Torsional and Longitudinal modes does not take place due to their lower degree of symmetry so one simply calls them Flexural modes of order $n = 0$. Unless otherwise stated, in the following examples the propagation is along the $\{Z\}$ crystal axis. The crystal axes are also aligned with those of the cylinder as described in section 3.1 and shown in Figure 2.1.

The PSCM codes for viscoelastic materials in cylindrical geometries are validated in exactly the same way as their perfectly elastic analogues: by taking the *thin plate limit* making the internal radius of the cylinder very large compared to its thickness, and comparing the results with those of a plate of equal properties. This procedure was explained in detail and illustrated with examples for all types of cylindrical solutions, including circumferential propagation, in Chapter 2 and [46]. For the cases presented in this chapter, the same testing procedure was followed and the reference cases were those presented in the previous section which comprise all types of anisotropic materials and have been successfully validated with the SAFE method.

It is also interesting to see the agreement between the results given by the

PSCM and SAFE when the *thin plate limit* is not taken. In Figures 3.6.a and 3.6.b a comparison between the results given by the PSCM and SAFE is presented. It is a viscoelastic hexagonal cylinder with inner radius $r_i = 50$ mm, thickness $h = 15$ mm and axial propagation. The Kelvin-Voigt model has been chosen for modelling the material damping of this case. The figure only displays a short range of frequencies since the number of modes present for higher frequencies increases enormously and this renders the comparison of both solutions unclear. The modes computed by the PSCM have been plotted with squares of different colours according to the family to which they belong: $n = 0$ in black squares, $n = 1$ in blue squares, $n = 2$ in red squares and $n = 3$ in green squares. The solution computed by SAFE is plotted in asterisks with the same colour scheme as above. Note that the PSCM gives the results for each family *separately*, once the value of n has been fixed the code computes only the modes belonging to that family.

Because of the central role played by fibre reinforced composites in industry, this section is closed with an example of a hexagonal (transversely isotropic) viscoelastic material, such as is found in fibre-reinforced composites. An interesting and challenging problem for more conventional approaches such as PWRF routines, though not for the PSCM, is the case of a composite where the fibres along the $\{Z\}$ axis of the crystal were chosen to form an angle of 35 degrees with the axis of the cylinder, this angle does not correspond to any symmetry of the hexagonal system. Thus, the fibres follow a helical path around the axis of the cylinder. The cylinder has inner radius $r_i = 20$ mm, thickness $h = 7$ mm and the propagation is along the axis of the cylinder. The dispersion curves and attenuation for the family $n = 0$ using the PSCM are shown in Figures 3.7.a and 3.7.b respectively. This example was done with the Kelvin-Voigt model for damping and the physical parameters for this example are given in the last section at the end of the chapter.

3.5 Pipes containing fluids

Due to the importance of pipes filled with fluids in various sectors of industry, NDE engineers need to have robust tools to perform studies on them and obtain the necessary information about modes that propagate and of their peculiarities. The examples shown in this section deal with viscous fluids as well as with ideal fluids in viscoelastic or elastic pipes, the different models suitable to describe the fluid are also discussed. They are validated by comparison to relevant examples from the literature and to results obtained by using the PWRF approach. Because of the way the implementation of the PSCM is done to handle cases with material damping, the pipes can be chosen to be elastic or viscoelastic, therefore, throughout this section, the reader should bear in mind that whenever we encounter an example of
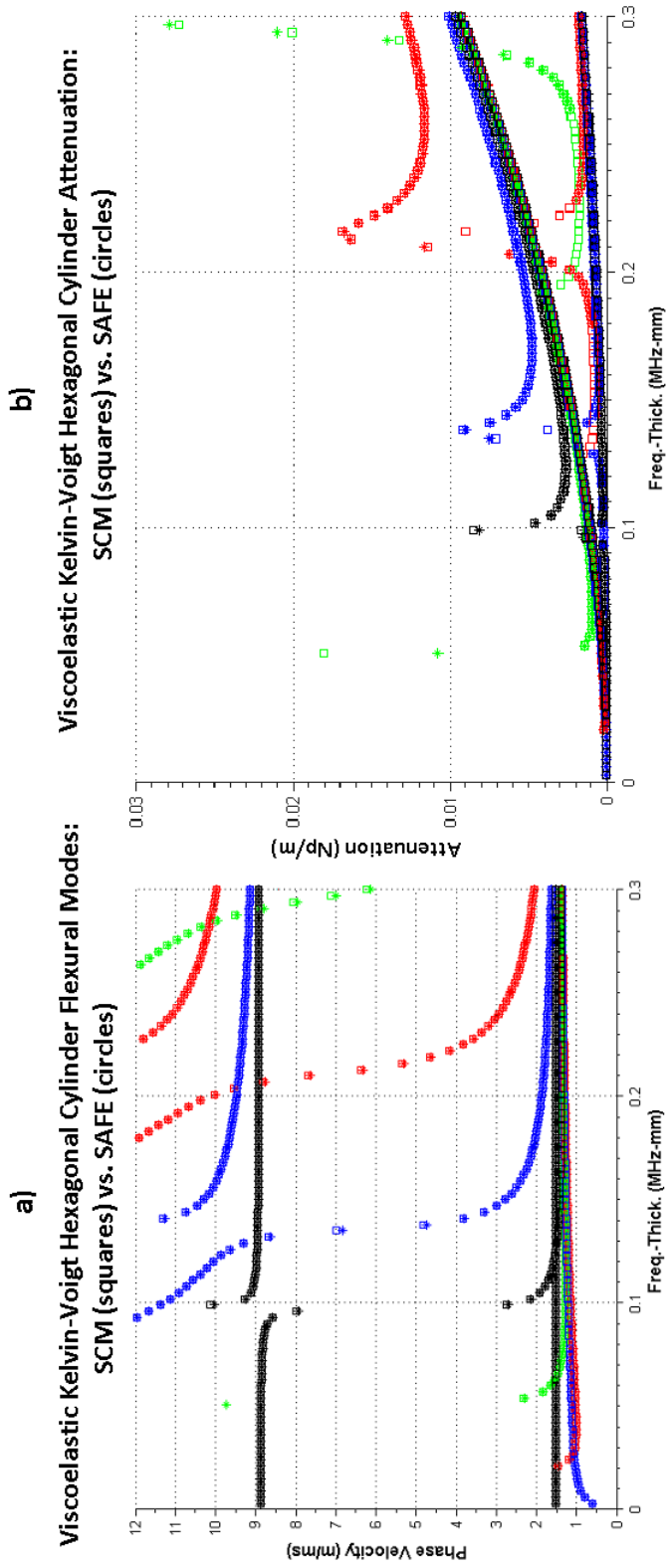
Figure 3.6: Phase velocity of flexural modes (a) and attenuation (b). Comparison between PSCM and SAFE for a free Kelvin-Voigt-type viscoelastic hexagonal 15 mm thick cylinder of inner radius 50mm. PSCM: $n = 0$ (black squares), $n = 1$ (blue squares), $n = 2$ (red squares) and $n = 3$ (green squares). SAFE: asterisks with the same colour scheme as for the PSCM. Fibres and propagation along the $\{z\}$ axis of the cylinder.

71
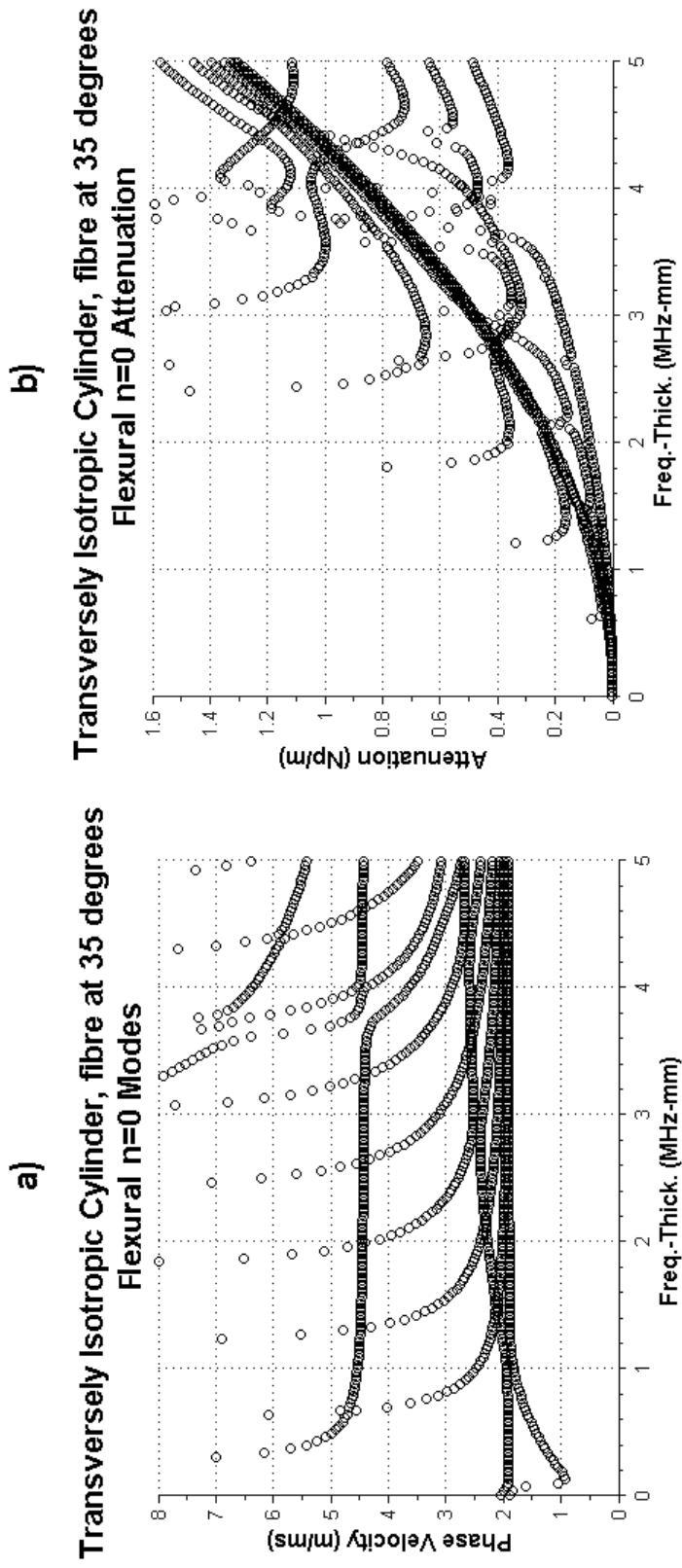
Figure 3.7: PSCM solution for the phase velocity of flexural ($n = 0$) modes phase velocity (a) and attenuation (b) in hexagonal (transversely isotropic) viscoelastic 7 mm thick cylinder of 20 mm inner radius. Kelvin-Voigt-type material damping and fibres at 35 degress with respect to the propagation direction along the $\{z\}$ axis of the cylinder.

elastic pipe, it is equally possible to study its viscoelastic counterpart using exactly the same code and *vice versa*. To better study the effects of fluid viscosity and material damping, these two mechanisms are isolated from each other in the study cases. The section closes with a more general and illustrative example of an orthorhombic pipe with viscous fluid inside.

Before presenting the results, a brief discussion about the different approaches to fluid viscosity and their effects on the results is given. In the context of guided wave NDE, the most established model for viscous fluids regards them as hypothetical solids. For constructing this hypothetical solid two main alternatives have been proposed. The first alternative consists of simply regarding the fluid as a *true solid* with the appropriate stiffness constants: the real part of shear elastic modulus μ must be taken to be zero, since in absence of viscosity one must recover the case of ideal fluids that do not support shear waves; also the imaginary part of the longitudinal elastic modulus λ is set to zero since viscosity is assumed to arise solely from shear motion. The stiffness matrix entries are exactly the same as those of an isotropic solid. In the second alternative λ and μ are taken as in the previous one, but the contribution of the viscosity (non-zero imaginary part of μ) is split amongst the stiffness matrix entries differently than usually done in solid mechanics. Viscosity also enters in those entries with only longitudinal contribution, this model is often referred to as the Stokes Model. A more detailed discussion is in [70] and the equations for these models can be retrieved in [16]. A final comment about the two models described above: as explained in [70] the numerical results given by each of the models will differ in general. Since there is no solid conceptual reason for choosing *a priori* one or the other model, which of them is more suitable in a particular case is determined by the results from experiments or other measurements obtained in similar cases.

The first cases studied in this section are pipes with viscous fluid inside. Without loss of generality, the pipes will be elastic so that the attenuation is solely caused by the viscosity of the fluid. The dynamical viscosity η for most fluids of interest ranges from orders of 10^{-1} (very low viscosity fluids) to 10^{+1} (high viscous fluids), and in all cases the coefficients representing this viscosity are several orders of magnitude smaller than those of the elastic solids. When the problem, pipe and fluid, is described by displacement fields, spurious modes are present due to the numerical ill conditioning caused by the big differences amongst terms in the equations produced in turn by the difference in orders of magnitude of the constants entering the problem. One avoids this by turning to a mixed description of the problem using potentials in the fluid layer and displacements in the solid layer. This enables a homogenization of the terms in the equations of motion of the fluid without any loss of generality regarding the solid layer:

recall that a potential description of anisotropic solids is not possible so the displacement description is necessary lest generality is lost. A similar issue was also found in elastic pipes with ideal fluids, see Chapter 2 and [46].

Since the potential description can also be used for isotropic solid materials, the first example computes the longitudinal modes of a hypothetical viscoelastic brass solid rod of radius $r_i = 23$ mm coated with a layer of elastic steel of thickness $h = 5$ mm; the hysteretic model has been chosen to account for material damping within the solid rod and the propagation takes place along the axis of the pipe. This case serves as a test bench for the PSCM code that is validated by comparison with results given by the PWRF approach. This case is chosen for its numerical simplicity, since all the elastic constants involved are of similar orders of magnitude and it is not quite as challenging as that of viscous fluids.

The dispersion curves and the attenuation of the modes is shown in Figures 3.8.a and 3.8.b respectively. The results given by the PSCM are shown in red circles and the solution given by the PWRF approach is shown in black solid lines: The agreement between both approaches is excellent.

The next two examples show the agreement of the results given by the PSCM code just validated when used for modelling viscous fluids with those given in the paper by Ma *et al.* [71]. In the following two cases the Stokes model is assumed throughout to model the viscous fluid. The first example in Figure 3.9 shows a more detailed comparison of the attenuation curves of longitudinal modes propagating along the axis of the pipe obtained with the PSCM solution to the PWRF solution given in Figure 11 of the paper [71]. The pipe is made of steel with inner radius $r_i = 4.5$ mm and thickness $h = 0.5$ mm. The fluid is glycerol, the solutions given by the PSCM for the viscosities $\eta = 0.8$ Pas, $\eta = 0.94$ Pas and $\eta = 1.1$ Pas are shown in black hollow squares, red diamonds and blue circles respectively. The corresponding PWRF solutions in solid black lines are indicated by the arrows in the background figure taken from the reference [71], the black solid squares are the experimental results obtained in the experiment described therein. The PSCM solution shows excellent agreement not only with the PWRF solution but also with the experimental data shown in solid black squares.

The second example in Figure 3.10 computed by the PSCM displays the attenuation curve for one longitudinal mode propagating along the axis of a steel pipe with the same properties as before filled with a Cannon VP8400 fluid of viscosity $\eta = 18.8$ Pas. The solid black squares in the background corresponding to Figure 14 of [71] display experimental results and the solid black line (lying between the two dashed lines) corresponds to the solution for the same value of viscosity $\eta = 18.8$ Pas obtained with DISPERSE. The
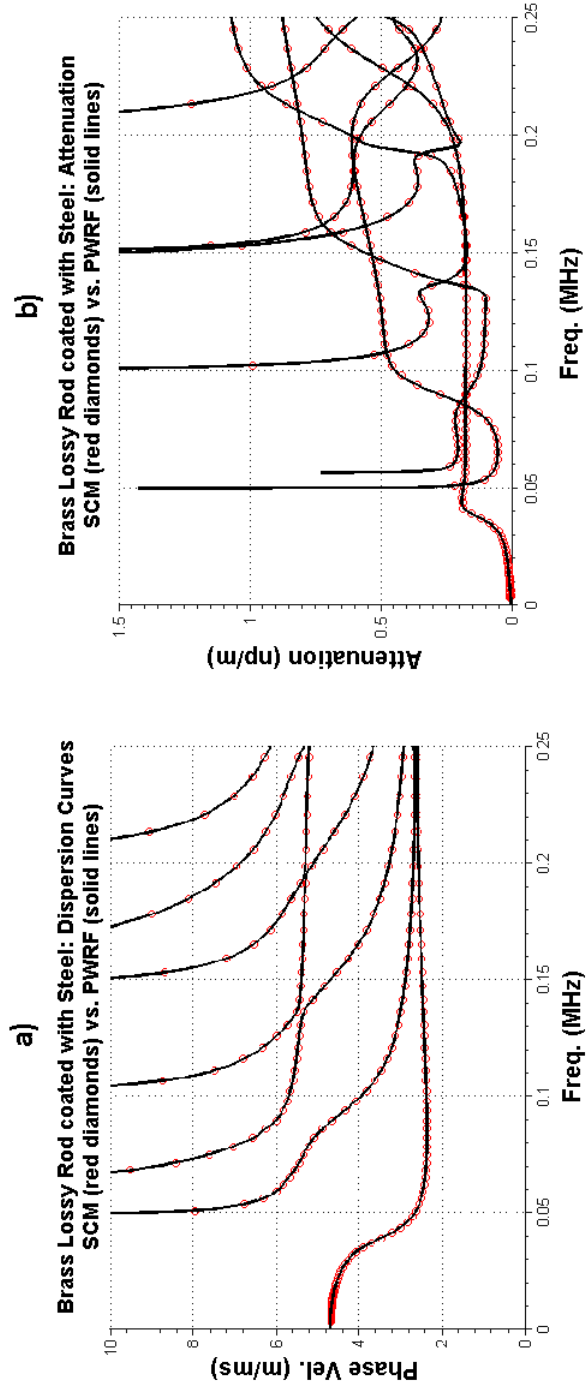
Figure 3.8: Phase velocity (a) and attenuation (b) of longitudinal modes of a viscoelastic brass rod ($r_i = 23$ mm) coated with an elastic 5 mm thick layer of steel: PSCM (red circles) vs. PWRF (solid lines). Propagation along the $\{z\}$ axis of the cylinder.
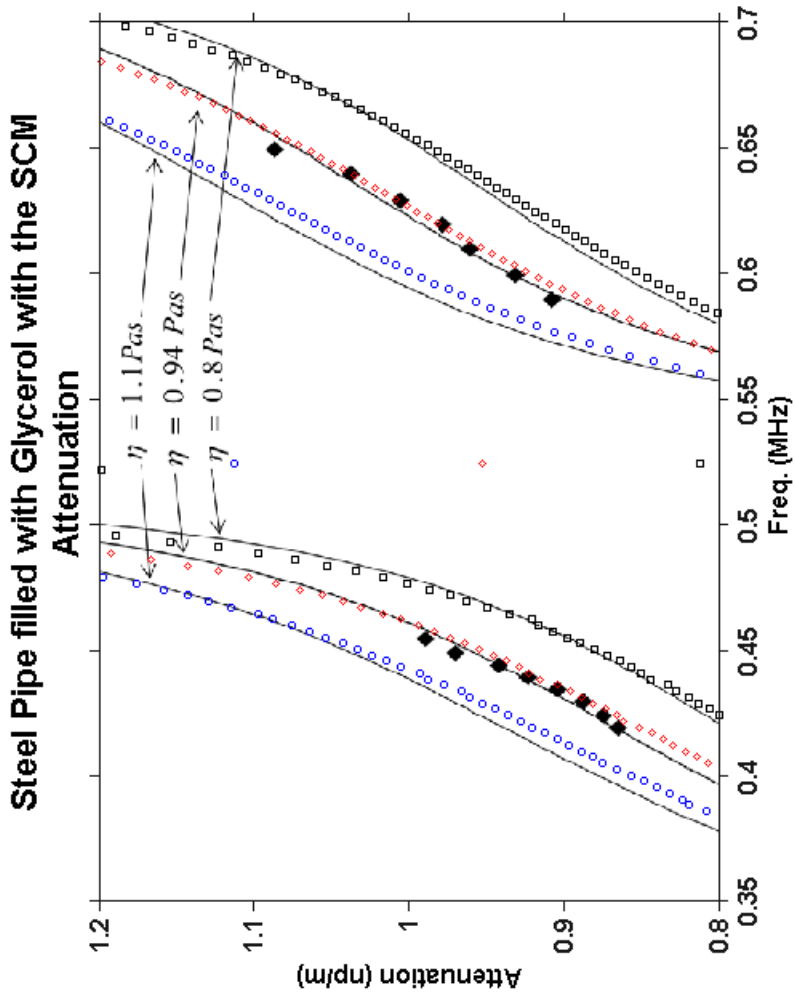
Figure 3.9: Attenuation of longitudinal modes in a 0.5 mm thick elastic steel pipe with 4.5 mm inner radius for three different values of the viscosity of glycerol filling the pipe. For the PSCM solution: $\eta = 0.8$ Pas (black squares), $\eta = 0.94$ Pas (red diamonds) and $\eta = 1.1$ Pas (blue circles). In the background Figure 11 of [71] is displayed. The predictions given by DISPERSE are given in solid lines and the black solid squares are the results from the experiment carried out and described in the paper.

dashed lines correspond to close but different values of viscosity, more details of this figure are in the original reference [71]. Once again, the solution given by the PSCM shows excellent agreement with both experiment and PWRF prediction.

The above examples were also run using the *true solid* model described at the beginning, for brevity not shown here. As a consequence of the different splitting of the viscosity amongst the entries of the stiffness matrix it was seen that the peaks appearing in the attenuation curves were lower than those yielded by the Stokes model. In the regions of the spectrum where experimental results were available, the solution given by the *true solid* model agrees very well with them, though it was not as good a match as with the Stokes model.

All the cases studied in this section involved a perfectly elastic pipe with either a viscoelastic solid or a viscous fluid filling the inside. Figures 3.11.a and 3.11.b show respectively the dispersion curves and attenuation of longitudinal modes propagating along the axis of a viscoelastic steel pipe of inner radius $r_i = 30$ mm and thickness $h = 8$ mm filled with water (modelled as an ideal fluid without viscosity). The solution given by the PSCM is given in red circles and that computed by the PWRF method in solid black lines. Both solutions show very good agreement and can be compared to the perfectly elastic analogue in [46] thus showing that low material damping has little effect on the dispersion curves. The hysteretic model is used in this case and the values of the viscoelastic constants of the pipe are in the last section of the chapter. Note that the solution given by the PWRF is not complete, some of the curves had to be traced manually and even after some work it was very difficult to find the incomplete intervals. This highlights one of the advantages of the PSCM, namely completeness of solutions, over conventional PWRF routines.

This section concludes with a brief comment on the ill-conditioning of the PSCM when studying problems involving fluids of very low viscosity. It has been found in the course of this investigation that for viscosity values of the order of ~ 0.1 Pas or less, some pieces of the dispersion curves and the corresponding mode shapes obtained in the region close to zero frequency are not as smooth as one normally observes in more simple problems. This phenomenon has been observed in a variety of different combinations of materials and geometric parameters which suggests it is an inherent feature of the PSCM when used to model fluids which lie at the frontier between ideal and viscous fluids. However, a useful trend has been observed: the higher the viscosity is, the closer one can go towards zero frequency keeping smooth profiles in dispersion curves and mode shapes.
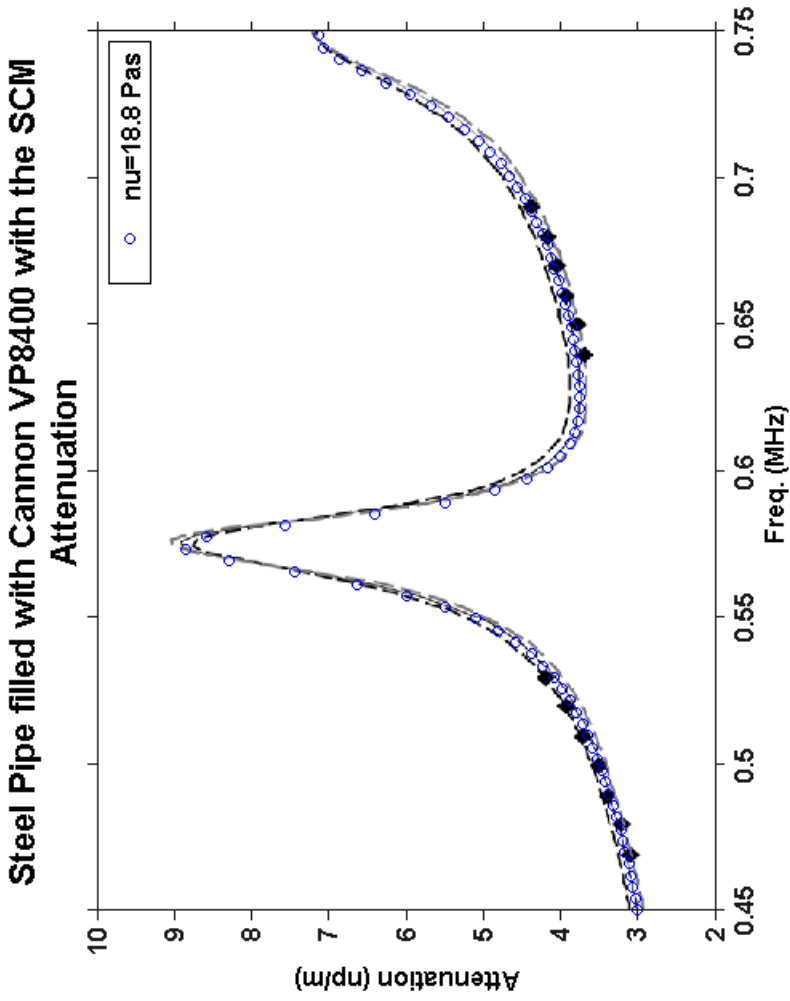
Figure 3.10: Attenuation of a longitudinal mode in a 0.5 mm thick elastic steel pipe with a fluid: Cannon VP8400. For the PSCM solution: $\eta = 18.8$ Pas (blue circles). In the background Figure 14 of [71] is displayed. The predictions given by DISPERSE are given in solid lines (between the dashed lines) for the same viscosity value of $\eta = 18.8$ Pas. The dashed lines correspond to close but different values of viscosity, see [71] for more details. The black solid squares are the results from the experiment carried out and described in the paper.
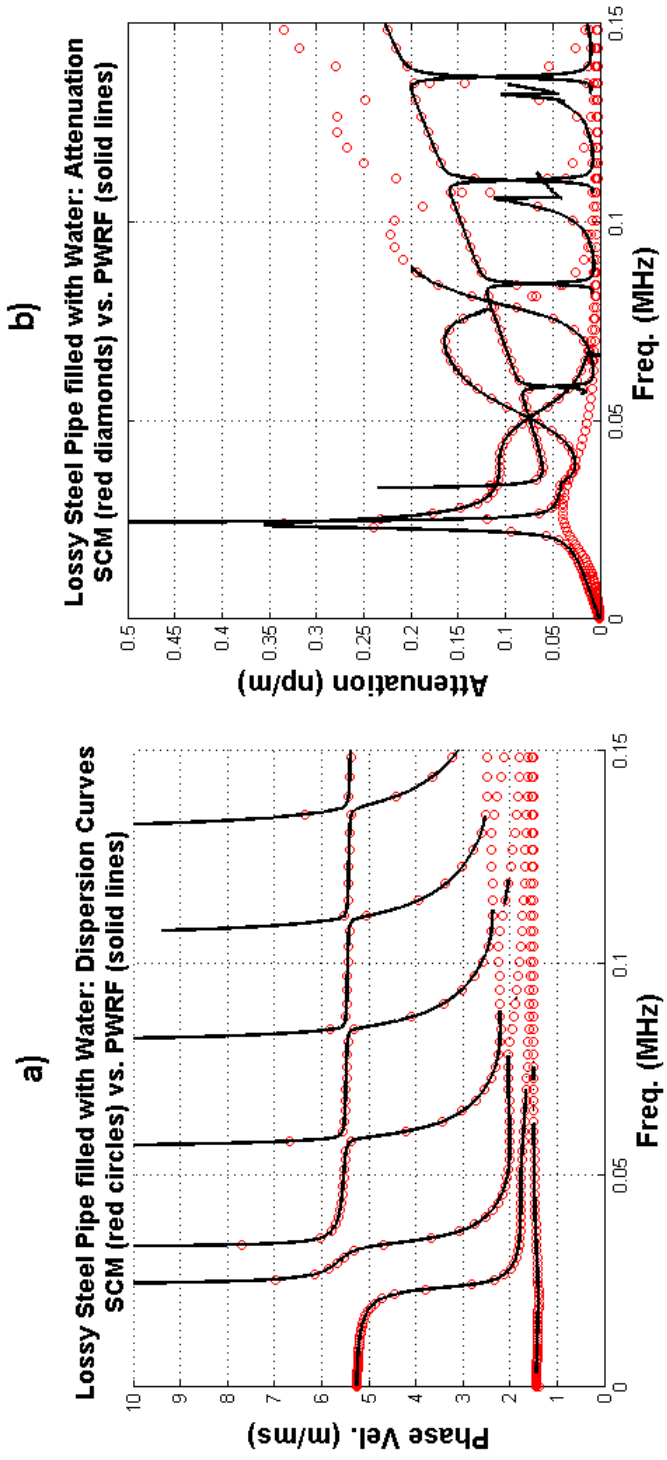
Figure 3.11: Phase velocity (a) and attenuation (b) of longitudinal modes of an 8 mm thick viscoelastic steel pipe ($r_i = 30$ mm) filled with water (ideal fluid): PSCM (red circles) vs. PWRF (solid lines). Hysteretic model for material damping. Propagation along the $\{z\}$ axis of the pipe.

3.6 Discussion of Chapter 3

In this chapter, an extension of the PSCM to guided wave problems in viscoelastic media with the possibility of containing viscous fluids has been presented. Cases in flat, as well as in cylindrical, geometry have been studied and validated with numerous examples from the literature, solutions obtained with the conventional PWRF approach and when this approach was not possible, in the case of triclinic media for instance, a SAFE simulation was used to confirm the results. Since the wavenumber k entered the equations nonlinearly the *Linear Companion Matrix Method* was introduced to rearrange the problem into a generalized eigenvalue problem.

The PSCM shows excellent performance solving guided wave problems in viscoelastic media and some of its advantages with respect to the SAFE method or PWRF routines have become apparent in the course of this chapter and are summarized below. Even though the aforementioned *Linear Companion Matrix Method* is required to recast the problem into the desired form, the PSCM remains conceptually simpler than the SAFE method and the amount of previous knowledge required for its implementation is significantly less. As the examples and comments in the sections III and IV have highlighted, the SAFE method is known to give spurious solutions very close to the physical solutions that need to be carefully filtered, mostly by manual intervention. This phenomenon has not been observed to occur with the PSCM even though some very simple post processing is useful to retain the desired propagating mode solutions. This has been done by introducing at the end of section II the ratio R between the real and imaginary parts of the wavenumber.

When complex roots must be found the PSCM is easier to code than the conventional PWRF routines since it transforms the set of partial differential equations for the acoustic waves into a purely algebraic problem, see [46] and [21] for more details on this important point. In addition, the PSCM is generally faster than the PWRF method since it does not require any intervention on the part of the practitioner who sometimes has to manually complete or find solutions when using the PWRF approach. This is because the PSCM does not miss any eigenvalues and therefore one can be certain that the solution is complete and no modes have been missed. Mode missing is a recurrent problem encountered in PWRF routines specially when solving complicated cases involving complex roots or anisotropic materials. Finally, the PSCM is capable of solving cases that are not currently solved by PWRF routines such as propagation in anisotropic media in an arbitrary

direction as was pointed out at the end of section IV or as the last case in section VI shows.

In conclusion, the PSCM presents itself as a powerful and robust complement to the already established SAFE and PWRF approaches. The PSCM scheme, and the study of guided waves in viscoelastic generally anisotropic media, as presented in this chapter are expected to be of interest in very different branches of physics dealing with guided wave phenomena and engineering applications working with composite materials and guided waves. Finally, as mentioned in the introduction, the implementation of the PSCM described in this chapter can also be used to calculate the non-propagating solutions, without any further development of the computational method. For brevity, such examples have not been included here, but these will be an important subject of attention in the next chapter.

3.7 Numerical data for examples of Chapter 3

The physical and geometrical information used for the figures presented in this chapter are given here. The number of grid points N varies from one example to another, but it is always at least double the number of modes plotted in the figure. On a practical level N is chosen to achieve the shortest computation time, that is, if one is interested in the first 10 modes, running a code with $N = 100$ is unnecessary; a value of N between 25 and 30 has consistently been shown to be sufficient.

The parameters for the plate of figures 3.1.a and 3.1.b are as follows (with the usual axes orientation shown in figure 2.1):

$$\rho = 1500 \text{ kg/m}^3 \, ; \qquad h = 1 \text{ mm} \tag{3.23}$$

h stands for the thickness of the plate. The elastic stiffness matrix is given in GPa:

$$c = \begin{pmatrix} 132 & 6.9 & 5.9 & & & \\ & 12.3 & 5.5 & & & \\ & & 12.1 & & & \\ & & & 3.32 & & \\ & & & & 6.21 & \\ & & & & & 6.15 \end{pmatrix} \tag{3.24}$$

The viscosity matrix in GPa is:

$$\eta = \begin{pmatrix} 0.4 & 0.001 & 0.016 & & & \\ & 0.037 & 0.021 & & & \\ & & 0.043 & & & \\ & & & 0.009 & & \\ & & & & 0.015 & \\ & & & & & 0.02 \end{pmatrix} \tag{3.25}$$

The parameters for the plate of figures 3.3.a and 3.3.b are as follows (with the usual axes orientation shown in figure 2.1):

$$\rho = 1500 \text{ kg/m}^3 \; ; \qquad h = 1 \text{ mm} \; ; \qquad \hat{f} = 2 \text{ MHz} \tag{3.26}$$

h stands for the thickness of the plate and $\hat{f}$ is the normalization frequency in equation (3.10). The elastic stiffness matrix is given in GPa:

$$c = \begin{pmatrix} 74.29 & 28.94 & 5.86 & 0.20 & -0.11 & 37.19 \\ & 25.69 & 5.65 & 0.0928 & -0.0801 & 17.52 \\ & & 12.11 & 0.0133 & -0.0086 & 0.22 \\ & & & 4.18 & 1.31 & 0.0949 \\ & & & & 5.35 & -0.0705 \\ & & & & & 28.29 \end{pmatrix} \tag{3.27}$$

The viscosity matrix in MPa is:

$$\eta = \begin{pmatrix} 218 & 76.5 & 16.4 & -3.60 & 0.688 & 116 \\ & 71.1 & 19.2 & -0.771 & 2.15 & 50 \\ & & 42.2 & -0.9644 & 0.627 & -3.07 \\ & & & 11.1 & 2.89 & -1.15 \\ & & & & 13.6 & 1.48 \\ & & & & & 93.5 \end{pmatrix} \tag{3.28}$$

The parameters for the plate of figures 3.4.a and 3.4.b are the same as above, equations (3.26), (3.27) and (3.28) except for the thickness which now is $h = 50$ mm.

The multilayer system of figures 3.5.a and 3.5.b is composed of three layers. The top layer has a thickness of $h = 8$ mm and the rest of the properties are given in (3.26), (3.27) and (3.28). The middle layer has a thickness of

$h = 5$ mm and the other properties are given in (3.23), (3.24) and (3.25). The bottom layer parameters are as follows:

$$\rho = 8938.4 \text{ kg/m}^3\,; \qquad h = 3 \text{ mm} \tag{3.29}$$

h stands for the thickness of the plate. The elastic stiffness matrix is given in GPa:

$$c = \begin{pmatrix} 2.0787 & 1.0906 & 0.9341 & 0.16574 & -0.1615 & -0.23188 \\ & 1.677 & 1.3624 & -0.24719 & 0.1128 & 0.086831 \\ & & 1.8591 & 0.081453 & 0.082076 & 0.14505 \\ & & & 1.0023 & 0.14505 & 0.058388 \\ & & & & 0.35110 & 0.16574 \\ & & & & & 0.59472 \end{pmatrix} \tag{3.30}$$

The parameters for the cylinder of figures 3.6.a and 3.6.b are as follows (with the usual axes orientation shown in 2.1):

$$\rho = 1605 \text{ kg/m}^3\,; \qquad h = 15 \text{ mm}; \qquad r_i = 50 \text{ mm}; \qquad \hat{f} = 2.242 \text{ MHz} \tag{3.31}$$

h stands for the thickness of the plate and $\hat{f}$ is the normalization frequency in equation (3.10). The elastic stiffness matrix is given in GPa:

$$c = \begin{pmatrix} 11.6911464939 & 5.85222031944 & 5.61629715501 & & & \\ & 11.6911464939 & 5.61629715501 & & & \\ & & 130.195979503 & & & \\ & & & 3.7 & & \\ & & & & 3.7 & \\ & & & & & \frac{c_{11}-c_{12}}{2} \end{pmatrix} \tag{3.32}$$

The viscosity matrix in GPa is given by:

$$\eta_{ij} = 0.025\ c_{ij} \tag{3.33}$$

The parameters for the cylinder of figures 3.7.a and 3.7.b are as follows (with the usual axes orientation shown in 2.1):

$$\rho = 2350 \text{ kg/m}^3\,; \qquad h = 7 \text{ mm}; \qquad r_i = 20 \text{ mm}; \qquad \hat{f} = 2.242 \text{ MHz} \tag{3.34}$$

h stands for the thickness of the plate and $\hat{f}$ is the normalization frequency in equation (3.10). The elastic stiffness matrix is given in GPa:

$$
c = \begin{pmatrix}
132 & 6.9 & 5.9 & & & \\
 & 132 & 5.9 & & & \\
 & & 12.1 & & & \\
 & & & 3.32 & & \\
 & & & & 3.32 & \\
 & & & & & \frac{c_{11}-c_{12}}{2}
\end{pmatrix}
\tag{3.35}
$$

The viscosity matrix in GPa is:

$$
\eta = \begin{pmatrix}
0.4 & 0.001 & 0.016 & & & \\
 & 0.4 & 0.016 & & & \\
 & & 0.043 & & & \\
 & & & 0.009 & & \\
 & & & & 0.009 & \\
 & & & & & \frac{\eta_{11}-\eta_{12}}{2}
\end{pmatrix}
\tag{3.36}
$$

A rotation of 35 degrees about the $\{r\}$ axis must performed on these matrices so that the fibres follow an helicoidal path around the cylinder.

The parameters for the cylindrical system of figures 3.8.a and 3.8.b are as follows. For the outer elastic steel cylinder:

$$\rho = 7932 \text{ kg/m}^3; \qquad h = 5 \text{ mm}; \qquad r_i = 23 \text{ mm}; \qquad c_L = 5960 \text{ m/s}; \qquad c_S = 3260 \text{ m/s} \tag{3.37}$$

The viscoelastic isotropic material in the inner core filling the outer layer of the cylinder has the following physical properties similar to those of brass:

$$\rho = 4000 \text{ kg/m}^3 \tag{3.38}$$

The elastic stiffness matrix is given in GPa:

$$
c = \begin{pmatrix}
100 & 50 & 50 & & & \\
 & 100 & 50 & & & \\
 & & 100 & & & \\
 & & & 25 & & \\
 & & & & 25 & \\
 & & & & & 25
\end{pmatrix}
\tag{3.39}
$$

The viscosity matrix in GPa is given by:

$$\eta_{ij} = 0.0025 \, c_{ij} \tag{3.40}$$

For the system in figure 3.9 the parameters for the steel pipe are:

$$\rho = 7932 \text{ kg/m}^3; \quad h = 0.5 \text{ mm}; \quad r_i = 4.5 \text{ mm}; \quad c_L = 5959 \text{ m/s}; \quad c_S = 3260 \text{ m/s} \tag{3.41}$$

The fluid inside is glycerol and has the following properties:

$$\rho = 1258 \text{ kg/m}^3; \quad c_L = 1918 \text{ m/s}; \quad c_S = 0 \text{ m/s} \tag{3.42}$$

The values for the dynamic viscosity of glycerol for the different curves (see figure 3.9)are:

$$\eta_1 = 0.8 \text{ Pas}; \quad \eta_2 = 0.94 \text{ Pas}; \quad \eta_3 = 1.1 \text{ Pas} \tag{3.43}$$

For the system in figure 3.10 the parameters for the steel pipe are the same as for figure 3.9. The fluid inside is Cannon VP8400 and has the following properties:

$$\rho = 885 \text{ kg/m}^3; \quad c_L = 1525 \text{ m/s}; \quad c_S = 0 \text{ m/s}; \quad \eta = 18.8 \text{ Pas} \tag{3.44}$$

For the system in figures 3.11.a and 3.11.b the parameters for the steel pipe are:

$$\rho = 7932 \text{ kg/m}^3; \quad h = 8 \text{ mm}; \quad r_i = 30 \text{ mm}; \quad c_L = 5960 \text{ m/s}; \quad c_S = 3260 \text{ m/s} \tag{3.45}$$

and the viscosity matrix is obtained from the stiffness matrix:

$$\eta_{ij} = 0.0025 \, c_{ij} \tag{3.46}$$

The fluid inside is water (treated as an ideal fluid) and has the following properties:

$$\rho = 1500 \text{ kg/m}^3; \quad c_L = 1000 \text{ m/s}; \quad c_S = 0 \text{ m/s} \tag{3.47}$$

Chapter 4

Full 3D Spectrum of Guidedwaves.

Dispersion curves for propagating and non-propagating modes are often computed for zero, or low, attenuation values and presented as two or three dimensional plots. See for instance [1], [33], [72] or more recently [65], [30] and [29]. However, cases where high values of attenuation are present and arbitrary anisotropy in single or multi-layered structures is considered have been hardly studied due to the great difficulties encountered when computing their dispersion curves. For instance, dispersion curves for viscoelastic monoclinic plates have been found and, for low values of the attenuation, presented in two dimensional plots [18], but in general, a better understanding of the nature of the modes, and a clearer visualization of the solutions, is achieved when dispersion loci are reliably found for low *as well as* high values of attenuation and therefore dispersion curves are required in three dimensions.

In the literature, modes have been categorised in a number of ways and here the classification of Auld [5] is used: propagating modes have real wavenumber, for this reason they are often the most useful for engineering application in NDT since they propagate and transport energy within the structure without attenuation. The second type of solution is non-propagating modes with complex or purely imaginary wavenumber. Note that these modes with complex or purely imaginary wavenumbers are also present in perfectly elastic materials without any energy leakage, those solutions represent local modes that would exist at discontinuities. In addition, non-propagating modes are of interest in certain applications such as the solution of scattering problems using modal summations where a knowledge of the full set of possible modes is essential, [73]. A detailed discussion about the physical properties and energy transportation of non-propagating modes in elastic (lossless) media is in the second volume of Auld [5]. For viscoelas-

tic materials, only propagating modes with complex wavenumber exist lest unphysical results are obtained as pointed out in [29]. Propagating modes in viscoelastic media can in turn be split into: lowly attenuated modes, with almost real wavenumbers and therefore very useful for inspection purposes in NDT; and highly attenuated modes, with dominant imaginary part for the wavenumbers. The reader must be aware that there does not seem to be a consensus about this nomenclature, see for example [5], [6] and [31]. In this thesis, the convention by Auld [5] is adopted and I will try to make it clear what kind of modes are being studied in each case by specifying the nature of the wavenumber. Collectively, these types of modes constitute the complete spectrum for a given problem and their study and visualization is the object of our current investigation.

Several methods have been developed, and successfully deployed, to compute two-dimensional, and less often three-dimensional, dispersion curves for guided waves in flat and cylindrical geometry: finite element (FE), semi-analytical finite element (SAFE) simulations, root-finding routines based on the partial wave approach (Partial Wave Root Finding, PWRF) and lately, spectral methods have become more popular as a powerful alternative, see [65], [21] or [20]. More recently, one of these variants known as Spectral Collocation Method (PSCM) has been successfully used to model guided waves in elastic and viscoelastic generally anisotropic media, [46] and [63] respectively.

The main contribution of this chapter is the deployment of a PSCM to compute the full three-dimensional spectrum, including highly attenuated and non-propagating purely imaginary modes, for guided wave problems in three cases (Figures 4.4.a, 4.5.a, 4.7 and 4.9.) which, to the best of the author's knowledge, have not been studied before and comprise up to the *most general type of anisotropy*, namely triclinic crystals. Several other well-known cases have also been presented for validation purposes. Regardless of the case under study, this investigation also emphasizes that with the PSCM no additional coding effort is needed to obtain the complete three-dimensional spectrum which contrasts with conventional approaches for which the algorithms become significantly more inefficient when searching in a three-dimensional space and which may require substantial modification to obtain robust solutions. The PSCM used here was first presented in the previous chapter and in the work by Hernando *et. al* [63], though there, attention was restricted solely to lowly attenuated modes. The present work goes one step further and, by carefully sorting the eigenvalues provided by the PSCM, completes the picture giving the remaining branches of the dispersion loci for the most general anisotropic triclinic class. It is notable that with technological advances there is a need for this full anisotropic generality and for the robust generation of the corresponding three-dimensional dispersion

curves presented in this thesis.

Additional contributions of this chapter, arising from the undertaken investigations, are the clarifications concerning the apparent crossing of modes within the same symmetry family for viscoelastic media (section 4.2) and the discussion of the implications of the centre of symmetry of *all* crystal classes for the solution (section 4.4). The results of this chapter were published in [74].

The chapter is organized as follows. In section 4.1 a very brief remark regarding the PSCM scheme for obtaining full solutions is given. Details about the PSCM implementation and an extensive discussion of its principal features when used to solve acoustic guided wave problems can be found in the previous two chapters and [21], [46] and [63]. In section 4.2, classical examples in flat geometry both for elastic and viscoelastic media are presented as a further validation of the PSCM approach. The crossing of modes, which is an important detail in practice, is discussed and elucidated with the aid of a new three-dimensional plot for the dispersion curves of a monoclinic material. The full solution for a new multilayer flat case is presented at the end of section 4.2. Section 4.3 treats cylindrical geometry, firstly a classical example is briefly presented for validation and the section closes with a new illustrative multilayer cylindrical system. Section 4.4 is devoted to the discussion of the results and the last section, 4.5, provides as usual the numerical data of the examples presented in the chapter.

4.1 Remarks about the PSCM for the full solutions

The PSCM is known to produce some spurious eigenvalues as pointed out in [24] and [21] for instance. The methodologies to deal with them have been extensively discussed there and a similar discussion will not be pursued here. These general procedures apply equally in the present case, in elastic and viscoelastic materials the *full solution* comprises all possible modes described in the introduction: purely real, purely imaginary (only present in the perfectly elastic case) and complex. Therefore no physical eigenvalues will be discarded as would be done if one was only interested in propagating modes with low attenuation. The same filter (3.19) used in the previous chapter and in [63] to retain only propagating modes is deployed to classify the different solutions. The filter uses the ratio between the real and imaginary parts of $k = \alpha + i\beta$ defined as:

$$R \equiv \frac{\beta}{\alpha} \tag{4.1}$$

Once this filter is introduced the classification of the modes is rather straight-forward for a given range of frequencies and wavenumbers. For the elastic case, they are split into the aforementioned categories according to the nature of the wavenumber: propagating modes with real wavenumber and non-propagating modes with complex wavenumber and non-propagating modes with imaginary wavenumber. For the viscoelastic case, only propagating modes exist and these are split into two categories as indicated earlier, lowly and highly attenuated modes (see discussion in the previous section). Since now all the modes have complex wavenumber, once a value of R is fixed, the modes are split into those with a higher value of the wavenumber's imaginary part, propagating strongly attenuated modes, and those with a lower value that are propagating but less attenuated modes. In some regions of the spectrum of viscoelastic materials the wavenumber is *almost* purely imaginary and in figures this will be indicated, when necessary, with a different colour for clarity. Even though dispersion branches can start far from the origin in the complex plane, when they become propagating (lowly attenuated or real) the point at which this occurs lies much closer to the origin. Thus for a given frequency it is always possible to find all propagating modes (lowly attenuated or real) and only finite number of purely complex or highly attenuated modes lie amongst these. The rest of the infinite set of complex or highly attenuated modes will extend further into the complex plane.

4.2   Solutions for Systems in Flat Geometry

The first case to consider is for the symmetric Lamb modes of a flat isotropic perfectly elastic free plate, [1], later reproduced in numerous textbooks on the subject such as [5] and [6]. Fig.4.1 shows the dispersion curves obtained by the PSCM. Its excellent agreement with those shown in the original paper by Mindlin was checked by the author but no difference was found between the two sets. Therefore, Mindlin's results were not reproduced here but can be found in his paper [1] or in any of the aforementioned more recent references. This serves as a further validation of the PSCM approach. A complete description of the validation of the PSCM for the study of guided waves in anisotropic media, elastic and viscoelastic, is in [46] and, of particular importance to the present case, in [63].

Throughout this chapter the conventional non-dimensional axis convention is adopted for the three-dimensional plots. The non-dimensional frequency is defined as follows:
$$\Omega = \frac{h\omega}{\pi V_{66}} \tag{4.2}$$
where ω is the angular frequency, h is the half thickness of the single plate or the thickness of the multilayer system and $V_{66} = \sqrt{C_{66}/\rho}$. C_{66} is the cor-
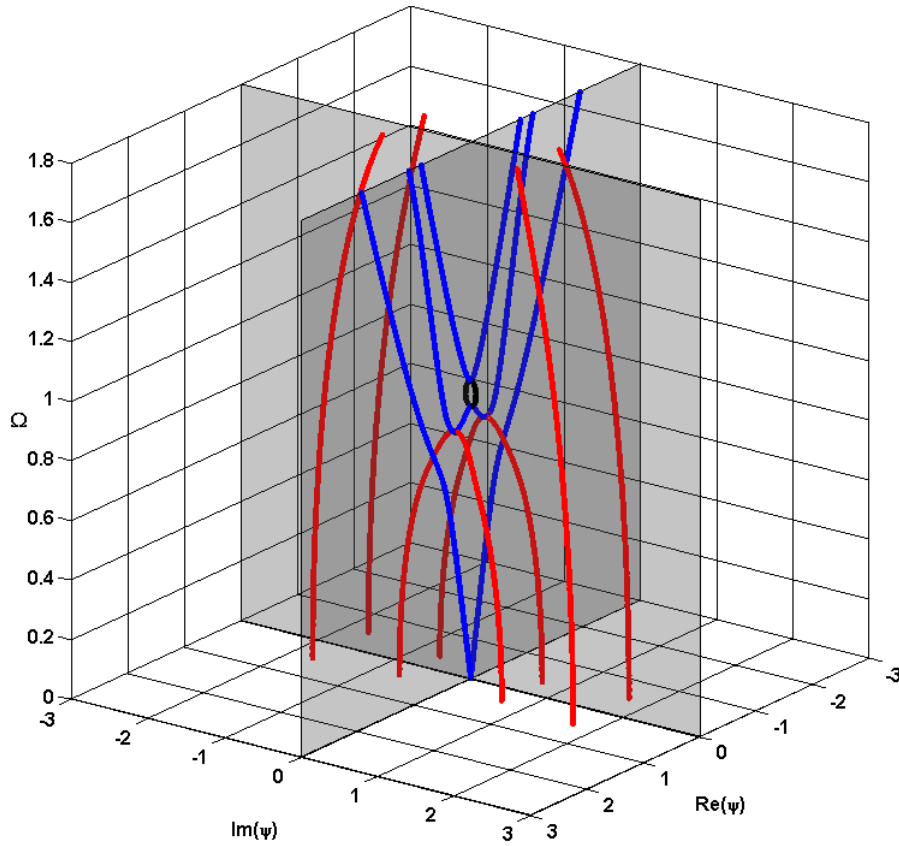
Figure 4.1: First three symmetric Lamb modes in a free elastic steel plate computed with the PSCM. Propagating modes in blue. Non-propagating modes in red and black. The non-dimensional axes are $\Omega = h\omega \ / \ \pi V_{66}$ and $\Psi = hk \ / \ \pi$. Note that in this and the rest of the figures, all the four cuadrants have been plotted in order to provide with the complete loops and dispersion branches which prolong into the complex plane.

responding entry in the stiffness matrix and ρ is the density of the medium. V_{66} reduces to the customary c_2 for isotropic media. The non-dimensional wavenumber is similarly defined as:

$$\Psi = \frac{hk}{\pi} \tag{4.3}$$

where k is the wavenumber of the wave.

Next we turn our attention to a viscoelastic isotropic free steel plate, the symmetric and antisymmetric Lamb modes are shown separately in different projections. The wave propagates within the plane of the plate. In Fig.4.2.a and Fig.4.2.b the full solutions for symmetric and antisymmetric modes are shown respectively with the same colour scheme as in Fig.4.1 but no regions of the spectrum have been coloured in black (strictly speaking, only the points at which the loci intersect the plane $\text{Re}(\Psi) = 0$ would be in black) to highlight that now all modes are propagating with higher (red)or lower (blue) values of attenuation, and none with zero attenuation; in absorbing media all modes are of the propagating kind lest we obtain unphysical results, this has been discussed in detail in section 3 of [29]. The set of dispersion curves shown in Fig.4.3. computed with the PSCM have been found to present very good agreement with those in [29] which are not reproduced here for being identical to those in Fig.4.3, the original figures can be found in the aforementioned reference. Note that all axes in the present figures are rescaled by a factor $1/2$ due to the definition of the non-dimensional constants Eq.(4.2) and Eq.(4.3) where the half thickness h has been used instead of the total thickness of the plate $2h$ as it was done in [29]. The choice of colouring makes it clear when a branch of a mode runs in front of the branch of a different mode in three-dimensional space. The physical properties of this, and the previous example, are in section 4.5.

It is important to note already that the *apparent* crossing of modes within the same family, something *forbidden* in the elastic case, does not actually take place in the viscoelastic case either. This is explained by noticing that for the viscoelastic case one *still has two independent* dispersion relations for Lamb modes whose entries are now complex, thus yielding generally complex roots. See also Rose [31] or Graff [6] for a more detailed discussion about this. The splitting of modes into families of symmetric and antisymmetric is related to the geometrical symmetries of the crystal and axes configuration for the crystal chosen in each case, not to the dynamical properties of the material itself such as damping. Therefore, regardless of the material being elastic or viscoelastic, if the crystal configuration is such that modes can be classified according to their symmetry with respect to the middle plane of the plate, those two families will remain independent from each other for any kind of media and no crossings between them will occur. This is seen by

91
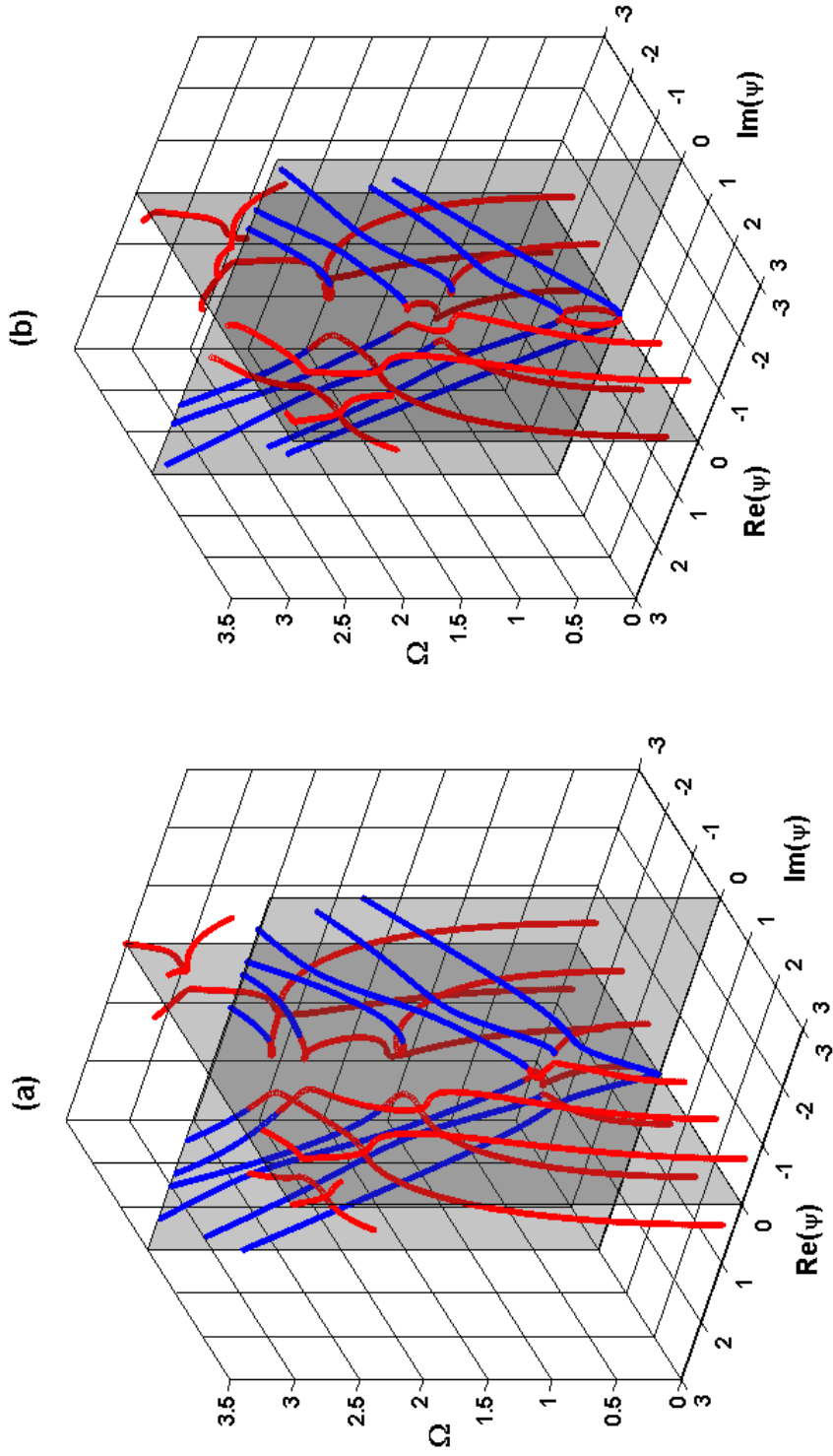
Figure 4.2: Symmetric (a) and Antisymmetric (b) Lamb modes in a free hysteretic-type viscoelastic steel plate computed with the PSCM. Propagating modes in blue (lowly attenuated) and red (highly attenuated). Non-dimensional axes: $\Omega = h\omega$ / πV_{66} and $\Psi = hk$ / π.
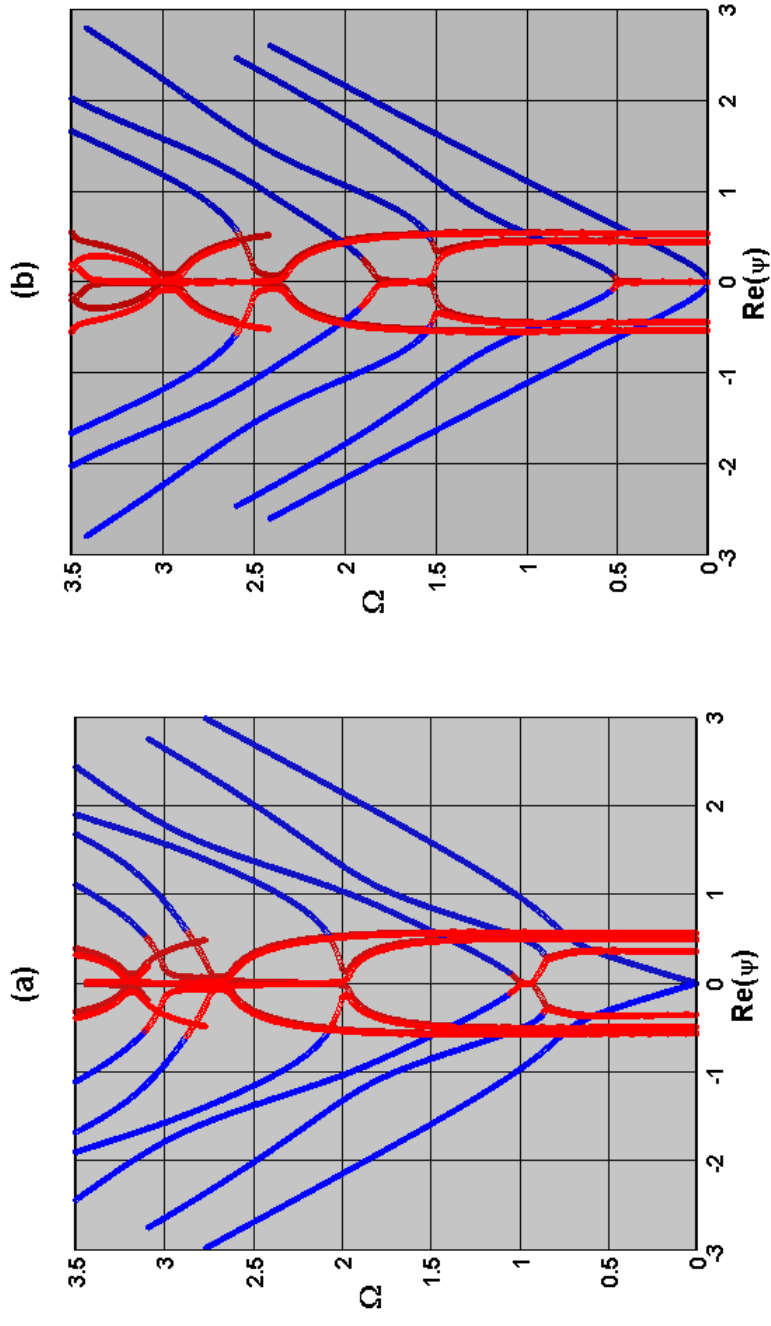
Figure 4.3: 2D projection of the symmetric (a) and antisymmetric (b) Lamb modes in a free hysteretic-type viscoelastic steel plate computed with the PSCM shown in figure 4.2. Propagating modes in blue and red.

looking at the full $3D$ picture of the dispersion curves and noting that what seems to be a crossing in the $2D$ projection is nothing more than one line passing in front of the other in the complete and clearer $3D$ picture. This is a recurrent point of discussion in the literature, to cite only a few, see for instance [26], [27] and [28], it has also been addressed in [29] and in [30] for elastic plates with fluid loading, further references to other related papers can be found therein. The next example will further verify this assertion in the case of a more complex material.

Now a free viscoelastic plate of monoclinic material is investigated. The crystal configuration is as follows: the $\{Y\}$ axis of the crystal is normal to the plane of the plate and propagation takes place along the $\{Z\}$ axis, further details about the physical properties of the material are in the appendix. Fig. 4.4.a and Fig. 4.5.a present the full three-dimensional solution for symmetric and antisymmetric coupled modes respectively in a monoclinic plate which, to the best of the author's knowledge, has not been presented before. Its corresponding two-dimensional plots for propagating modes and attenuation are shown in Fig.4.4.b and Fig.4.4.c for symmetric modes and in Fig.4.5.b and Fig.4.5.c for antisymmetric modes respectively. It is shown in Fig. 4.4.b that two of the symmetric modes, labelled as B and C, *cross* at roughly 0.50 MHz, a similar result was obtained and discussed in figure 5 of [18] for a different monoclinic plate. Note that the modes labelled A and B do not cross. Once more, it is worth emphasizing that no real crossing occurs in this case for the same reasons mentioned in the previous paragraph. For instance, Li and Thompson [13] derived the two generalized Lamb dispersion relations for symmetric and antisymmetric modes in a monoclinic plate with propagation within the plane of symmetry of the crystal, these were also derived in [32].

These two independent dispersion relations derived in [13] hold also for the case of viscoelastic materials and therefore, having only one dispersion relation which cannot be further factorized into a simpler product of factors for each independent family, no crossings can occur amongst modes given by the corresponding non-reducible dispersion relation for the independent family under study. The fact that these dispersion relations cannot be further factorized has a physical interpretation as explained by Solie and Auld [8]: each dispersion relation is the determinant of the coefficient matrix of a set of equations whose unknowns are the amplitudes of the partial waves which give rise to the family of modes considered and the order of this non-reducible determinant is equal to the minimum number of partial waves needed for satisfying the boundary conditions. The six partial waves will be coupled by the boundary conditions and anisotropy of the crystal in various ways which depend on the problem under study. Note that the partial waves are mentioned here because they are a known valid means of representing
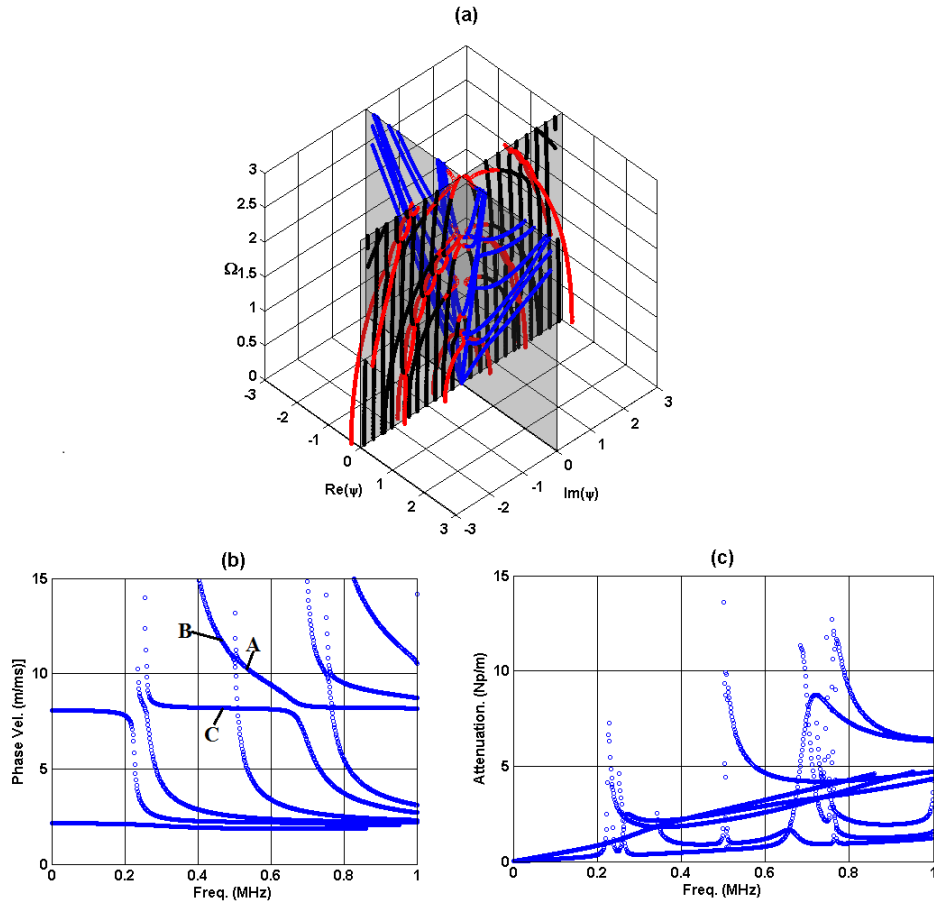
Figure 4.4: Top: Symmetric generalized Lamb modes in a free hysteretic-type viscoelastic monoclinic plate computed with the PSCM (a). Propagation is along the {Z} axis, and the {Y} axis is perpendicular to the plane of the plate. Propagating Modes: low attenuated modes in blue, complex wavenumber modes in red and *almost* imaginary wavenumber modes in black. Plot non-dimensional axes: $\Omega = h\omega \ / \ \pi V_{66}$ and $\Psi = hk \ / \ \pi$. Bottom: 2D dispersion curves (b) and attenuation (c) of the symmetric generalized Lamb modes in the viscoelastic monoclinic plate. Note the apparent crossing of modes B and C in (b) at roughly 0.5 MHz.
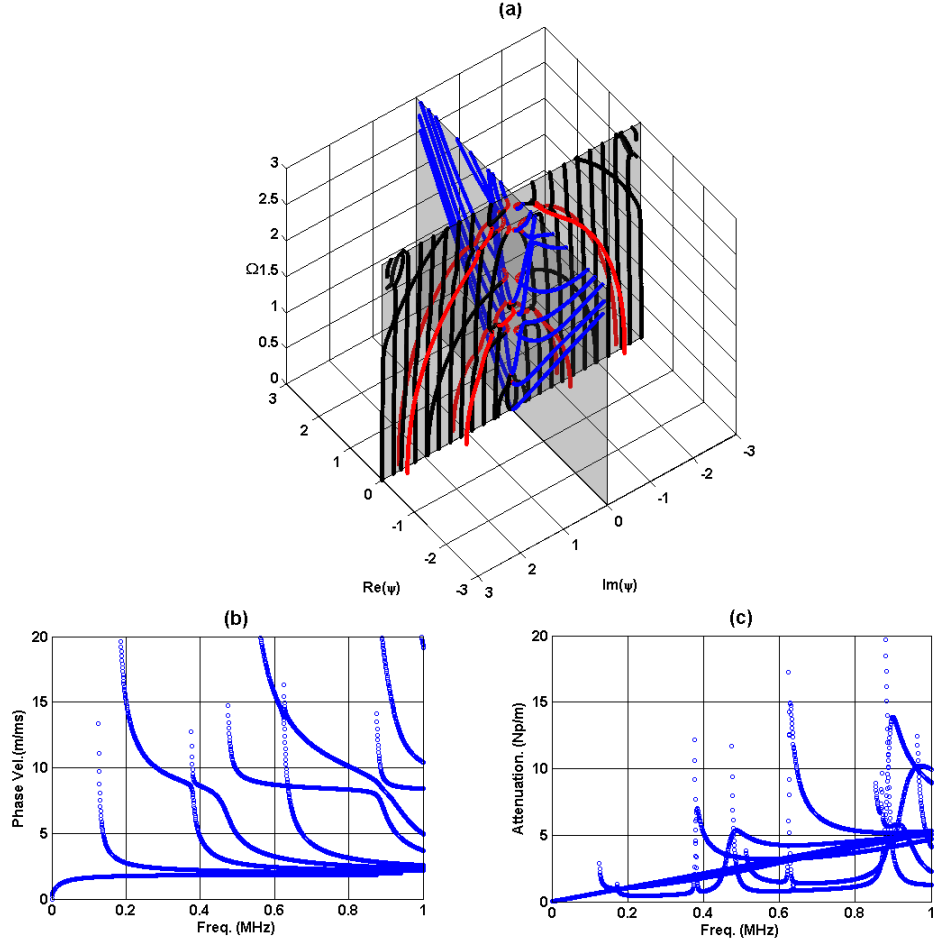
Figure 4.5: Top: Antiymmetric generalized Lamb modes in a free hysteretic-type viscoelastic monoclinic plate computed with the PSCM (a). Propagation is along the {Z} axis, and the {Y} axis is perpendicular to the plane of the plate. Propagating Modes: low attenuated modes in blue, complex wavenumber modes in red and *almost* imaginary wavenumber modes in black. Plot non-dimensional axes: $\Omega = h\omega \; / \; \pi V_{66}$ and $\Psi = hk \; / \; \pi$. Bottom: 2D dispersion curves (b) and attenuation (c) of the antisymmetric generalized Lamb modes in the viscoelastic monoclinic plate.
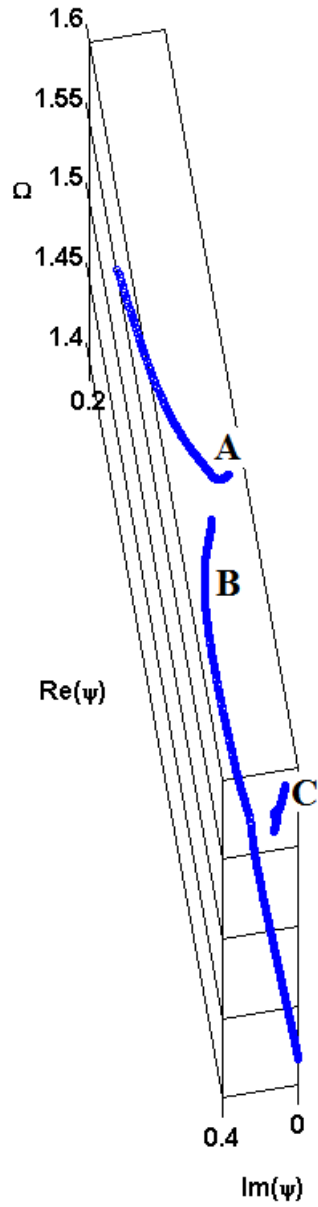
Figure 4.6: 3D detail of the region where the apparent crossing of symmetric generalized Lamb modes B and C in figure 4.4 (b) appears. When shown in three-dimensional space under the appropriate angle it is seen that actually no crossing between modes B and C occurs.

the guided wave fields, and are thus a useful tool to aid the explanation, but it must be emphasised that partial waves are not part of the alternative PSCM approach presented in this work. In the present case, three partial waves are coupled (coupling symmetric SH and Lamb modes) to give rise to the coupled symmetric modes, analogously for antisymmetric modes. Similar considerations and explicit formulae for the monoclinic case can be found also in [75].

The assertion that no crossings occur and the solution given by each of these non-reducible dispersion relations is unique can be explained as follows: Firstly, the non-reducibility of an $N \times N$ dispersion determinant implies that one needs at least as many partial waves as the order of the determinant to satisfy the boundary conditions, that is, N. Secondly, in order to have non-trivial solutions one requires the $N \times N$ determinant to vanish, this means the rank of the determinant is no bigger than $(N-1)$.

It can be seen that the rank is in fact $(N-1)$ thus yielding a unique non-trivial solution by the following consideration: if this was not so, and let us assume for definiteness that it was $(N-2)$, one could find non-trivial solutions expressing $(N-2)$ partial wave amplitudes in terms of the two remaining ones. In particular, one could set one of these latter amplitudes to zero while still having a non-trivial solution constructed from $(N-1)$ partial waves. This is in stark contradiction with the need for at least N partial waves implied by the non-reducibility of the $N \times N$ dispersion determinant.

Interestingly, this can be confirmed by the PSCM which uses an algebraic approach. It has been observed that for each independent family of modes the multiplicity of the eigenvalues, roots of the dispersion relation, is one. This means that the eigenspace spanned by the corresponding eigenvector (mode) is one-dimensional, which is tantamount to saying that only one dispersion curve runs through that point. Moreover, when a code for the most general case of triclinic is used to study the dispersion curves in an isotropic plate, the four independent families of modes (Symmetric/Antisymmetric Lamb and SH) are obtained and, up to the accuracy allowed by computer precision, it can be seen that eigenvalues with multiplicity two are obtained for the crossing points. Their two eigenvectors are orthogonal which means there are two different modes for that given eigenvalue: for instance an SH and a Lamb mode. In Fig.4.6, a detail of the problematic region in Fig.4.4.b around 0.50 MHz is presented in three-dimensional space and it is seen very clearly that these two modes do not cross.

Finally for flat geometry we consider a bilayered system composed of a viscoelastic triclinic plate and an elastic orthorhombic plate. Figure 4.7 shows its three-dimensional complete spectrum which, to the best of the author's

knowledge, has not yet been published for this or similar systems involving crystals of triclinic symmetry. The axis configuration is the same as in the previous example: the $\{Y\}$ axis of the crystal is normal to the plane of the plates and the propagation takes place along the $\{Z\}$ axis. More details about the physical properties of the plates are given in section 4.5. This highlights the usefulness of the PSCM approach for calculating the full spectrum of complicated cases of single or even multi-layered systems with different viscoelastic materials or combinations of elastic/viscoelastic materials. Similar solutions for much simpler systems are sometimes incomplete when they are computed by conventional root-finding routines for instance, which highlights the importance of the methodology and results shown in the present work. As a consequence of this, some of the modes might also appear to merge with each other. These difficulties are easily overcome by using a PSCM that provides, without any extra coding effort, the full three-dimensional solution; a detailed discussion of further advantages of the PSCM for guided wave problems is given in the two previous chapters and in [21], [46] or [63]. The choice of materials, in particular the triclinic layer, has been done in order to provide the solution for as general a case as possible, thus a triclinic layer has been included. Note that in the previous chapter, only the conventional two dimensional dispersion curves for lowly attenuated modes was presented though *not* a complete solution as the one given here.

4.3 Solutions for Systems in Cylindrical Geometry

Only two examples are shown in this section since the procedure to obtain the full solution in cylindrical geometry follows exactly the same lines as that for flat plates. In addition, a detailed study of these systems for non-attenuating and low-attenuating modes has been already carried out in the previous chapters and in [63]. Therefore, a classical example from the literature and a sufficiently general new case suffices to illustrate the capabilities of the PSCM when obtaining full solutions in cylindrical geometry.

Throughout this section for cylindrical geometry, the conventional non-dimensional axes convention is adopted for the three-dimensional plots. The non-dimensional frequency is defined as follows:

$$\Omega = \frac{a\omega}{V_{66}} \tag{4.4}$$

where ω is the angular frequency, a is the thickness of the cylindrical shell system or the radius of the rod and $V_{66} = \sqrt{C_{66}/\rho}$. C_{66} is the corresponding entry in the stiffness matrix and ρ is the density of the medium. V_{66} reduces to the customary c_2 for isotropic media. The non-dimensional wavenumber
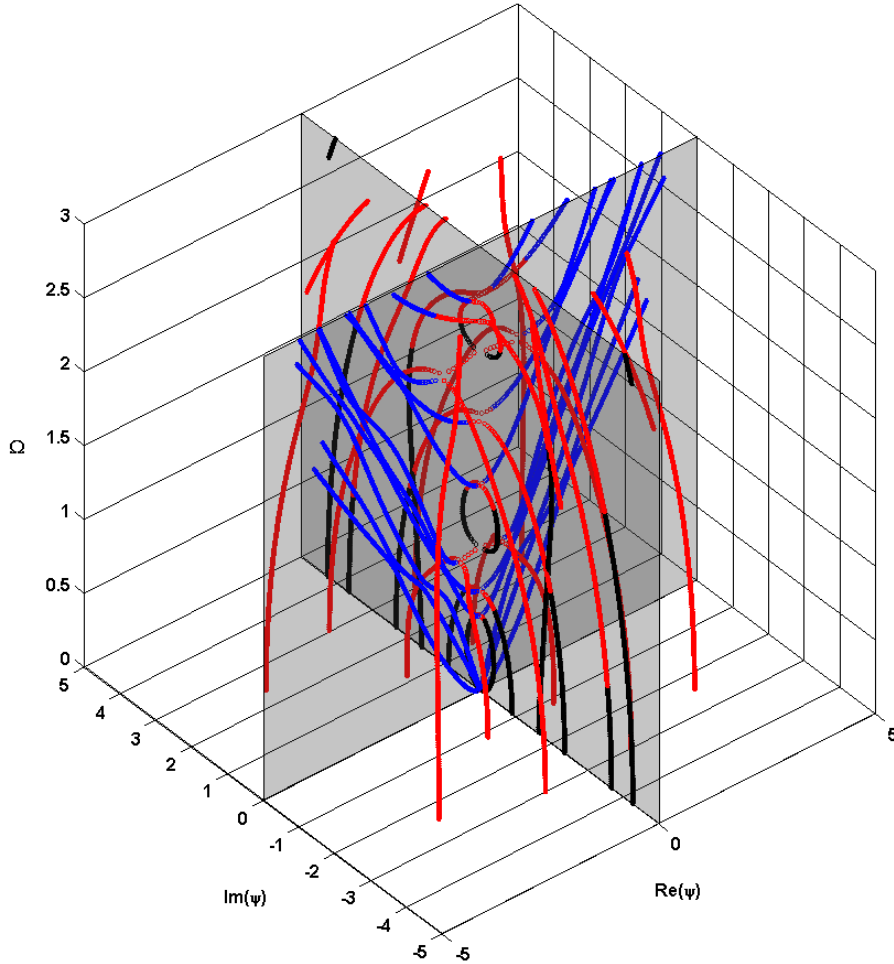
Figure 4.7: Modes in a free bilayer plate system: 5 mm thick elastic orthorhombic plate and 3 mm hysteretic-type viscoelastic triclinic plate computed with the PSCM. Propagation along the {Z} axis and the {Y} axis perpendicular to the plane of the plate. Propagating Modes: low attenuated modes in blue, complex wavenumber modes in red and *almost* imaginary wavenumber modes in black. Plot non-dimensional axes: $\Omega = h\omega \ / \ \pi V_{66}$ and $\Psi = hk \ / \ \pi$.

is similarly defined as:

$$\Psi = ak \qquad (4.5)$$

where k is the wavenumber of the wave.

The first example shows the dispersion curves for flexural modes with harmonic order $n = 1$ in an elastic cylindrical steel rod where the propagation takes place along the axis of the cylinder. Fig.4.8 shows the spectrum computed by the PSCM which were compared by the author to the two-dimensional plot in Pao [2] showing excellent agreement. The original figure by Pao has not been included in this chapter in order to avoid repetition of identical figures but the reader can easily find it in the reference provided. As pointed out in the literature [6], it can be seen in Fig.4.8 that the *incomplete* imaginary black branches (non-propagating purely imaginary modes) are linked in three-dimensional space by complex red branches (non-propagating modes with complex wavenumber). Further details about the physical and geometrical properties are in section 4.5.

To close this section a final new case is presented. Flexural $n = 0$ modes (Longitudinal coupled with Torsional) in a hollow cylinder composed of two different layers are studied with propagation along the axis of the cylinder. The innermost layer is a triclinic viscoelastic plate of thickness $h_o = 3$ mm and the outer layer is an elastic orthorhombic plate of thickness $h_i = 5$ mm whose *fibres* along the $\{z\}$ axis have been rotated 45 degrees to form an helicoidal path around the cylinder's axis, the internal radius of the cylinder is $r_i = 17$ mm. The three-dimensional spectrum computed by the PSCM is shown in Fig.4.9 for the first five modes; two-dimensional dispersion curves for the propagating modes have already been shown in the literature for similar systems, see [63], but the full spectrum for anisotropic materials presented here has not been published elsewhere to the best of the author's knowledge. Due to the presence of an absorbing layer, all modes are propagating: with very low attenuation showing in blue, with highly attenuated modes showing in red and modes with *almost* imaginary wavenumber showing in black. Note that, strictly speaking, these latter modes should have been coloured in red too. However, since the system contains a perfectly elastic layer some branches show behaviour closer to that featured in the perfectly elastic case and thus have a very small real part, though not strictly zero. In order to make this more apparent and clear, the author has chosen to colour them in black for this figure. Again, the triclinic layer has been chosen because of its generality, thus showing that the PSCM can provide the complete three-dimensional spectrum for the most general cases in cylindrical geometry. It is notable that with advances in technology it is these complicated multilayer and generally anisotropic cases that now require modelling.
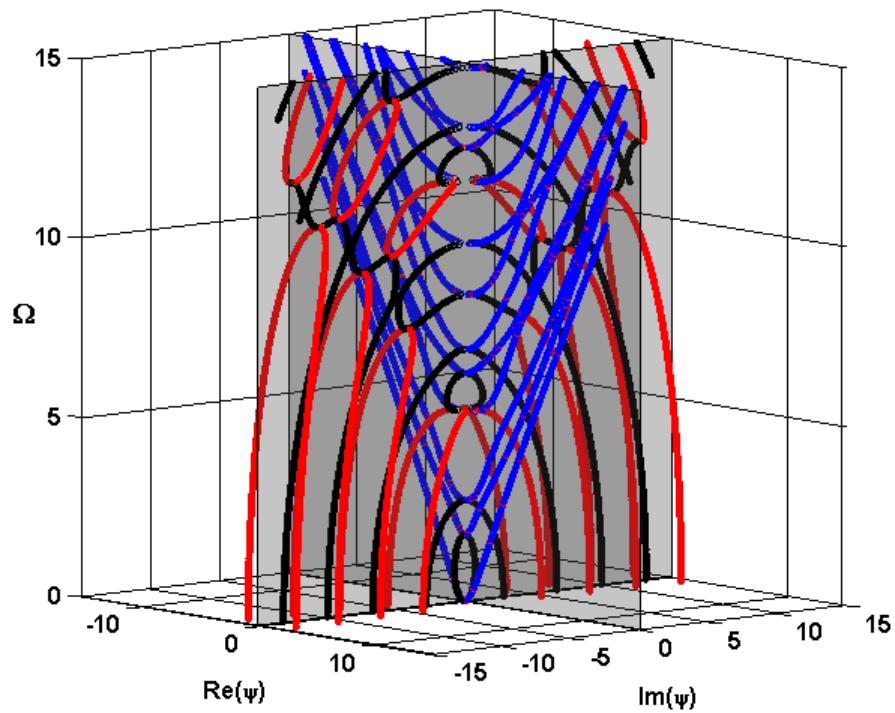
Figure 4.8: Flexural $n = 1$ modes in free elastic steel rod with radius $r = 20$ mm. This agrees well with the corresponding 2D plot first published by Pao [2]. Wave propagation along the {z} axis of the cylinder. Propagating modes in blue. Non-propagating modes in red and black. Plot non-dimensional axes: $\Omega = a\omega \ / \ V_{66}$ and $\Psi = ak$.
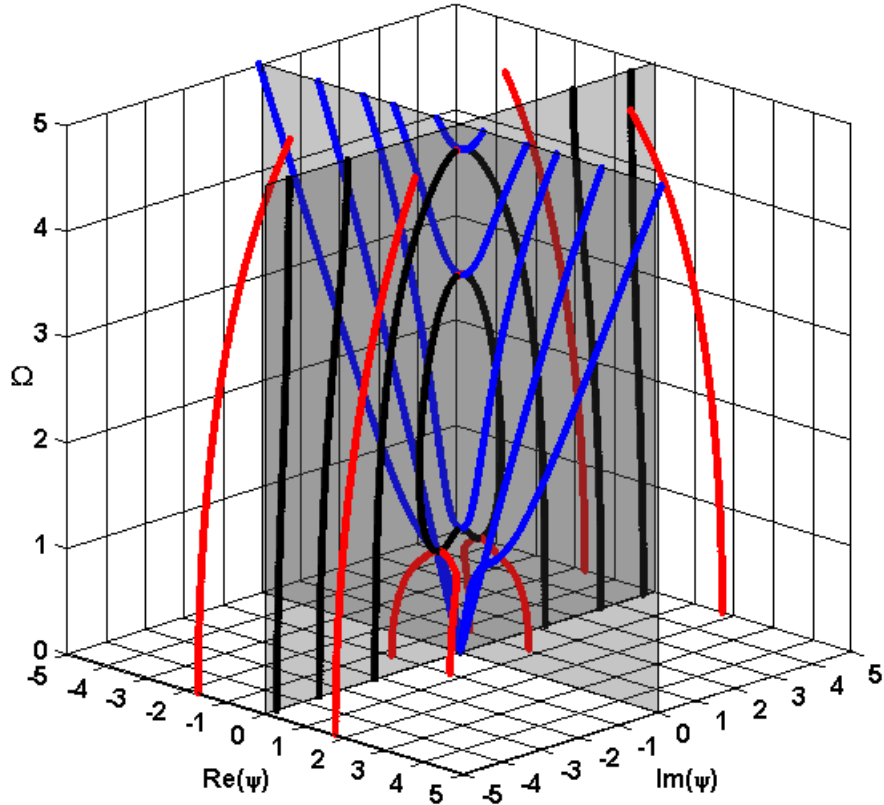
Figure 4.9: Flexural $n = 0$ modes in free two-layered cylinder. The inner layer is a kelvin-voigt-type viscoelastic triclinic crystal of thickness $h_i = 5$ mm and the outer layer is an elastic orthorhombic crystal of thickness $h_o = 3$ mm whose *fibres* along the {z} axis have been rotated 45 degrees to form an helicoidal path around the cylinder's axis. The cylinder's inner radius is $r_i = 17$ mm. Propagation along the {z} axis of the cylinder. Propagating Modes: low attenuated modes in blue, complex wavenumber modes in red and *almost* imaginary wavenumber modes in black. Plot non-dimensional axes: $\Omega = a\omega \ / \ V_{66}$ and $\Psi = ak$.

4.4 Discussion of Chapter 4

The capability of the PSCM approach to find full three-dimensional solutions for dispersion curves has been demonstrated here. The PSCM has computed the complete spectrum of various known cases, as well as some new settings, efficiently and accurately, without modifying the algorithm, to find all the eigenvalues. This advantage of not missing any modes has been repeatedly emphasized in the literature in other contexts ([25] or [24]) and in previous papers on guided waves ([21], [46] or [63]), the interested reader can find a detailed discussion about this and other advatages of the PSCM in those references.

The PSCM throws new light onto problems involving elastic or viscoelastic media which are often very demanding for conventional approaches (root-finding routines or FE simulations), for instance, for a two-layer system of isotropic and orthorhombic viscoelastic materials. For those cases where the root-finding routines work, one often finds that the solutions are incomplete and the path of the dispersion curves is unclear thus giving the impression of mode merging and similar unusual phenomena. This troublesome situation can sometimes be elucidated by tedious work refining the search algorithm to complete the missing parts in a three-dimensional space and get the full picture of the spectrum. FE simulations are a good and useful alternative to root-finding routines and can also model any material and configuration. However, FE simulations require a far greater coding effort, understanding of the methodology and a careful examination of the solutions to discard the spurious unphysical modes; a more detailed discussion about this is in Chapters 2, 3 and [63]. It is seen that the PSCM yields the complete solution straightforwardly, only an adequate post processing of the results is needed to clearly plot the different parts of the spectrum according to the nature of the wavenumber.

In addition to the classical examples from the literature, the PSCM has successfully computed the complete three-dimensional spectrum of the most general and complicated cases which, to the best of the author's knowledge, had not been presented before. Even though similar general cases have been solved in Chapter 2 for perfectly elastic media and in Chapter 3 for viscoelastic materials, they focus solely on lowly attenuated modes and their corresponding two-dimensional dispersion curves. Therefore, it is hoped that the investigations presented here contribute to complete the picture in the most general and until now unknown cases.

The general examples involving triclinic materials presented earlier have highlighted the need of a clarification regarding the symmetries of crystals and the consequences on the waves propagating within them. In the liter-

ature, the symmetry properties of the Lamb dispersion equations are often used for simplification or to draw certain conclusions about the nature of the solution. For instance in [65] they take advantage of the symmetry $k \leftrightarrow -k$ to reduce the dimension of the matrix. Another example of this assertion can be found in Graff [6] (chapter 8, page 455). From this and similar examples, one might draw the erroneous conclusion that when the dispersion relation lacks that symmetry, so will its solutions. Triclinic materials' dispersion relation, for instance, lack this symmetry as shown in [32]. In the course of the present investigation one can see that in spite of the absence of this symmetry in triclinic materials, its solution shows this $k \leftrightarrow -k$ symmetry. This apparent paradox is solved by noticing that the mentioned symmetry has a deeper source than the formal structure of the dispersion relation: *all crystal classes* possess one centre of symmetry, see for example [50], which means that they are invariant under the change $\vec{r} \leftrightarrow -\vec{r}$, which in general is not the same as a mirror symmetry through the plane normal to the direction of the wave vector. Therefore, regardless of the formal structure of the dispersion relation, every crystal will display that intrinsic symmetry as the examples in the present work reveal.

Apart from the observation made in the previous paragraph, it has also been pointed out and explained at the end of section 4.2 why the modes of the same symmetry family in a free viscoelastic plate do not cross. This apparent crossing is merely a visual effect of the projection of the dispersion loci onto a two-dimensional plane which is readily clarified when one looks at the full three-dimensional solution and realizes that for each independent family there is only one dispersion relation, the very same as in the elastic case, which cannot be further factorized. It is also important to notice the following: one might argue that the very example presented in Fig.4.1 is actually a perfect counterexample for the statement given in section 4.2, namely, that having only one dispersion relation which cannot be further factorized for each family, no crossings can occur amongst modes within the same family. Careful consideration shows that this is not the case. As explained by Auld [5] (Chapter 10, Volume II), at these "crossing points" (also termed *cutoff points* in the literature), rightgoing and leftgoing modes meet. These modes correspond to different branches of the square root of the imaginary wavenumber entering the dispersion relations and are *physically* distinguishable by energy arguments ([5, 29]). Therefore they must be considered as different families: symmetric rightgoing Lamb modes and symmetric leftgoing Lamb modes for instance. Unfortunately, bringing this to the fore by deriving explicit expressions for both branches of the complex wavenumber in terms of the angular frequency within a given family of modes is, to the best of the author's knowledge, only possible for SH modes but not for the rest due to the complexity of the dispersion relations. This distinction has been achieved numerically, though no details are given, in

[65] for symmetric Lamb modes and their results confirm that for a given branch, within a given family of independent modes, *strictly* no crossings are seen in the dispersion loci. For the viscoelastic case, as pointed out by Auld [5] not cutoff points exist and the problematic of the crossings disappears.

The progress made here is vital as it tackles a fundamental issue, the accurate 3D representation of complex modes that also arises in other areas, most notable for the equally important leaky mode cases where energy leakage into the surrounding medium contributes to the attenuation of the waves. In those cases this also modifies the dispersion loci demanding that the complete solution must be visualised in three-dimensional space for better understanding, [30]. This, unfortunately, is not a simple task as it requires substantial modifications to account for the infinite nature of the surrounding embedding layers, but the work here does tackle a key point required for this allied leaky mode problem.

4.5   Numerical data for examples of Chapter 4

The physical properties of the materials used for the figures in this chapter are given here. The number of grid points N varies from one example to another, but it is always at least double the number of modes plotted in the figure.

The physical properties for the steel plate whose dispersion curves are shown in Fig.4.1 are:

$$\rho = 7932 \text{ kg/m}^3; \qquad c_L = 5960 \text{ m/s}; \qquad c_S = 3260 \text{ m/s} \qquad (4.6)$$

For Fig.4.2.a and Fig.4.3 the viscoelastic steel plate has the following properties:

$$\rho = 7932 \text{ kg/m}^3; \qquad c_L = 5960 \text{ m/s}; \qquad c_S = 3260 \text{ m/s} \qquad (4.7)$$

with the viscoelastic matrix given in terms of the isotropic stiffness matrix by:

$$\eta_{ij} = 0.015 \ c_{ij} \qquad (4.8)$$

The monoclinic plate of Fig.4.4, Fig.4.5 and Fig.4.6 has the following properties:

$$\rho = 1500 \text{ kg/m}^3 ; \qquad h = 3 \text{ mm} \qquad (4.9)$$

The elastic stiffness matrix is given in GPa:

$$
c =
\begin{pmatrix}
21.93 & 5.85 & 26.05 & & 14.33 & \\
 & 12.30 & 6.55 & & 0.61 & \\
 & & 81.88 & & 37.59 & \\
 & & & 5.44 & & 1.22 \\
 & & & & 26.36 & \\
 & & & & & 4.03
\end{pmatrix}
\tag{4.10}
$$

The viscosity matrix in MPa is:

$$
\eta =
\begin{pmatrix}
66.44 & 16 & 81.81 & & 39.30 & \\
 & 37 & 6 & & -8.66 & \\
 & & 244.94 & & 115.29 & \\
 & & & 17.25 & & 4.76 \\
 & & & & 80.81 & \\
 & & & & & 11.75
\end{pmatrix}
\tag{4.11}
$$

The multilayer system of Fig.4.7 is composed of two layers. The top layer has the following properties:

$$
\rho = 1500 \text{ kg/m}^3 \; ; \qquad h = 5 \text{ mm}
\tag{4.12}
$$

The elastic stiffness matrix is given in GPa:

$$
c =
\begin{pmatrix}
132 & 6.90 & 5.90 & & & \\
 & 12.30 & 5.50 & & & \\
 & & 12.10 & & & \\
 & & & 3.32 & & \\
 & & & & 6.21 & \\
 & & & & & 6.15
\end{pmatrix}
\tag{4.13}
$$

The bottom layer has the following properties:

$$
\rho = 8938.4 \text{ kg/m}^3 \; ; \qquad h = 3 \text{ mm}
\tag{4.14}
$$

The elastic stiffness matrix is given in GPa:

$$
c =
\begin{pmatrix}
2.08 & 1.09 & 0.93 & 0.16 & -0.16 & -0.23 \\
 & 1.68 & 1.36 & -0.25 & 0.11 & 0.09 \\
 & & 1.86 & 0.08 & 0.08 & 0.14 \\
 & & & 1.00 & 0.14 & 0.06 \\
 & & & & 0.35 & 0.16 \\
 & & & & & 0.59
\end{pmatrix}
\tag{4.15}
$$

The viscosity matrix in GPa is given by:

$$\eta_{ij} = 0.025 \, c_{ij} \tag{4.16}$$

The parameters for the steel cylindrical rod of Fig.4.8 are as follows:

$$\rho = 7932 \text{ kg/m}^3; \qquad r = 20 \text{ mm}; \qquad c_L = 5960 \text{ m/s}; \qquad c_S = 3260 \text{ m/s} \tag{4.17}$$

r stands for the radius of the rod.

In Fig. 4.9 dispersion curves for a cylinder composed of two different layers is presented. The outer layer is an hexagonal (transversely isotropic) elastic material which has been rotated so that the fibres follow an helical path around the cylinder, it has the following properties:

$$\rho = 1605 \text{ kg/m}^3 \, ; \qquad h = 3 \text{ mm} \, ; \qquad \phi_r = \frac{\pi}{4} \tag{4.18}$$

where ϕ_r is the angle of rotation with respect to the {r} axis. The elastic stiffness matrix is given in GPa:

$$c = \begin{pmatrix} 11.69 & 5.85 & 5.62 & & & \\ & 11.69 & 5.67 & & & \\ & & 130.19 & & & \\ & & & 3.70 & & \\ & & & & 3.70 & \\ & & & & & \frac{c_{11}-c_{12}}{2} \end{pmatrix} \tag{4.19}$$

The inner layer is a viscoelastic triclinic material whose properties are:

$$\rho = 1500 \text{ kg/m}^3 \, ; \qquad h = 5 \text{ mm} \, ; \qquad r_i = 17 \text{ mm} \tag{4.20}$$

h stands for the thickness of the plate and r_i is the inner radius of the cylinder. The elastic stiffness matrix is given in GPa:

$$c = \begin{pmatrix} 74.29 & 28.94 & 5.86 & 0.20 & -0.11 & 37.19 \\ & 25.69 & 5.65 & 0.09 & -0.08 & 17.52 \\ & & 12.11 & 0.01 & -0.01 & 0.22 \\ & & & 4.18 & 1.31 & 0.09 \\ & & & & 5.35 & -0.07 \\ & & & & & 28.29 \end{pmatrix} \tag{4.21}$$

The viscosity matrix in MPa is:

$$\eta = \begin{pmatrix} 218 & 76.50 & 16.40 & -3.60 & 0.69 & 116 \\ & 71.10 & 19.20 & -0.77 & 2.15 & 50 \\ & & 42.20 & -0.96 & 0.63 & -3.07 \\ & & & 11.10 & 2.89 & -1.15 \\ & & & & 13.60 & 1.48 \\ & & & & & 93.50 \end{pmatrix} \tag{4.22}$$

The above material's stiffness matrix has been generated by two successive rotations of an orthorhombic material about different axes. An analogous procedure was used by Nayfeh and Chimenti [9] and Li and Thompson [13]. Due to its higher degree of anisotropy and complexity, triclinic materials often feature negative entries, see [76] for another example of triclinic elastic constants for albite.

Chapter 5

Symmetry and Coupling of Guided Wave Solutions in Generally Anisotropic Flat and Cylindrical Layers

Guided waves and their physical properties have been the subject of study for several decades and constitute an essential tool in Non-Destructive Evaluation (NDE) engineering applications. The first analytical solutions were obtained for the case of a free isotropic plate (Rayleigh-Lamb and SH waves). Its properties have been exhaustively studied and can be found in the literature on the subject or in any standard book about elastic waves, see for instance [5] and [6].

After finding the solutions for the isotropic case in flat and cylindrical geometry, attention gradually moved towards less understood anisotropic media. Materials such as fibre composites display a wide range of physical properties and phenomena which are not present in the simpler isotropic case making them a very useful alternative in numerous applications such as in aerospace engineering. Analytical solutions were obtained for free plates in some of the cases with higher symmetry such as cubic [8] and later the more complicated cases of orthorhombic and monoclinic were solved, see [32]. More recently and by means of the Stroh formalism, dispersion relations were obtained for generally anisotropic plates and some general properties of the modes derived analytically as well as the asymptotic behaviour of the first fundamental modes at high and low frequencies, see [77, 78]. The case of SH waves propagating in multilayer systems composed of anisotropic layers has also been addressed and solved by Nayfeh [10]. In the cylindrical case, to the best of my knowledge, solutions have also been obtained but only in high symmetry materials such as hexagonal and cubic [79].

The range of cases solved by numerical methods or finite element (FE) simulations is of course larger reaching up to triclinic materials in flat or cylindrical geometry but a review of them is out of the scope of the present chapter. For some recent developments and an account of the various numerical methods employed in the computation of dispersion curves see Chapters 2 and 3 of this thesis or [46, 63].

Numerical approaches for guided wave problems yield pairs (ω, k) which are later linked by means of tracing and interpolation algorithms to draw the corresponding dispersion curves. Unless the nature of the analytical solution is known *a priori* it is sometimes difficult to tell from the collection of points obtained for a given problem whether crossings amongst modes take place or not and to know which point must be linked with which other point to produce the correct dispersion curve. This sometimes renders the tracing algorithms unstable and unreliable which might result in jumps from one mode to a different one; an example of a tracing algorithm is described in [14].

As briefly explained in the previous paragraph, one of the needs and motivations for the study of the nature of the modes in single layer systems presented in this chapter stems from the fact that computing algorithms only find points in the frequency-wavenumber space. Additional subroutines must be included to link these points and draw the dispersion curves such as the one described in [14]. For the most complicated cases of general anisotropy the nature of the curves cannot be anticipated reliably, and these subroutines might not work reliably, therefore the dispersion curves are not always correctly traced. If one manages to separate the solutions of a given problem into different and independent families of modes, then one can be sure that crossings do not take place amongst dispersion curves within each of these families and the problem of crossings is avoided, see Chapter 4 of this thesis and [74].

In order to surmount the problems inherent to mode tracing in any guided wave problem, the question to be answered is the following: *Given a system of one (or more) anisotropic plates (flat or cylindrical) with certain axes configuration and a guided wave that propagates parallel to its boundaries how many families of independent modes exist?*

The answer to this question will also determine whether crossings occur or not, and if they do occur amongst which families. This knowledge can be exploited in order to write more efficient codes which trace the independent families separately thus avoiding the problem of crossing points.

Literature and investigations available to date can provide an answer to the above question in a limited range of cases, mostly those of greatest practical interest or, if more general, results are unfortunately limited to the low and high asymptotic limits of the solutions due to their analytical complexity. Those investigations leave a range of anisotropic crystal classes and axes configurations unexplored whose properties are not trivial to foresee due to the presence of anisotropy. This chapter aims to fill that gap and its main contribution is to present a thorough and complete investigation of the dispersion curves and mode properties of guided waves in single-layered anisotropic plates and cylinders in axes configurations not studied to date. The results of this investigation will help to answer the question posed above and provide an efficient and robust methodology for tracing dispersion curves in the most complicated and less known problems as well as in the already known ones. No attempt is made to find explicit expressions for the dispersion relations or their solutions in any case but very valuable information about their mathematical and physical properties can be drawn from the structure of the dispersion determinant without the need of either solving it or knowing the analytical solution for the displacement field, to this end the intuitive and well-known partial wave approach has been employed throughout.

The investigation is presented and illustrated with dispersion curves not restricted to the low and high frequency ranges. Thus, complete dispersion loci up to a sufficiently high frequency and not limited to the first fundamental modes are provided for the new cases considered. Mode shapes are also discussed and plotted for a better understanding of their properties and symmetries. All the numerical examples have been computed using a PSCM [45]. The PSCM has proved to be a powerful approach to solve the most general cases of anisotropy, see previous chapters and [21] or [46], and therefore it is the approach employed in the present investigation.

The main idea which led to this investigation was to find an invariant property of the modes existing in any anisotropic waveguide which could be known *a priori*, before any computation was carried out, and exploited in order to compute and trace the dispersion curves in such a way that the problem of crossing modes was avoided. For instance, Auld [5] and other authors resort to the energy propagation direction of the modes in order to label them and classify the different dispersion branches; though very good, this approach fails to tell us anything before computing the dispersion curves and even then, one needs to proceed on a case-by-case basis. The most promising option left was to investigate the symmetry properties of the solutions (these are well known in solutions for isotropic materials for instance) which can be derived from the mathematical structure of the Christoffel equation arising from the crystal symmetries of the problem un-

der consideration. The boundary conditions and axes configuration will impose further constraints on the nature of the modes existing in a given waveguide. It is hoped that this chapter shows the potential of this approach for efficient and reliable dispersion curve tracing and lays the foundation for generalizations to multiple layer systems. It must be emphasized that the results of this investigation are not restricted to the PSCM, they will be useful for other numerical approaches such as root finding routines or finite element simulations.

Cases which have already been studied in some detail will be dealt with in less depth and only the important conclusions regarding the properties of the solutions will be highlighted and summarized for completion, relevant references will be given where appropriate.

Finally, the problems investigated here might seem *exotic* or *rare*, evidence of this is the little attention they have been given. However, a general description of guided waves in anisotropic media in all its generality remains incomplete until all of these cases have been covered. In addition, they are very likely to arise in contexts and applications where materials of certain anisotropy are given an arbitrary orientation and these cases are becoming of more interest with modern materials evidence. This arbitrary orientation is illustrated in an example of the first volume of Auld's book [5] where a cubic crystal is rotated in such a way that the stiffness matrix referred to the old axes has the same structure as that of a tetragonal crystal. If a wave propagated in a cubic crystal which has undergone such rotation, the stiffness matrix which would enter the acoustic differential equations would be like that of a tetragonal medium instead of cubic. Thus, for practical purposes and from the guided wave point of view, these two configurations are indistinguishable. Note however, that a cubic crystal can always be *returned* to its original form by means of the inverse rotation whereas a truly tetragonal crystal will never display higher symmetry no matter the rotations made upon the crystal. This was also exploited in studies of orthorhombic plates in [32] and later in [13]. Analogous arguments can be given for any other anisotropic crystal class. This is another motivation for the study of these seemingly rarer anisotropic media and configurations.

The chapter is organized as follows. In section 5.1 free flat plates of anisotropic materials are studied. The exposition begins with the most general case of triclinic crystals and gradually proceeds towards higher symmetry classes. In section 5.2 free cylindrical plates and rods of anisotropic materials are studied. Figures of relevant examples displaying dispersion curves as well as mode shapes are included throughout the chapter. Section 5.3 closes the chapter presenting conclusions and a discussion of results and possibilities for generalization to multilayer systems. The numerical data used in the

examples is given in section 5.4. The contents of the present and the next chapter conform the basis for a paper in preparation.

5.1 Anisotropic Crystals in Flat Geometry

In this section free anisotropic plates are examined. Two sets of axes will be used throughout this section: spatial axes fixed to the plate, denoted with small letters {x,y,z} and crystal axes denoted by capital letters {X,Y,Z}. For definiteness, the *default configuration* will be with both sets of axes aligned. Different configurations will be obtained by rotation of the crystal axes {X,Y,Z} with respect to the fixed spatial axes {x,y,z}.

The fixed spatial axes {x,y,z} are disposed as follows: the plane {x,z} is contained in the plane of the plate and the {y} is normal to the plate. Propagation takes place *invariably* along the {z} axis (that is, along the {Z} axis of the crystal when the *default configuration* is considered). Unlike other approaches [13], and without loss of generality, propagation along the {z} axis will be kept fixed since the crystal axes can always be rotated to obtain propagation at an angle with the {Z} axis of the crystal if one so desires.

The equations of motion for the elastic wave field without any external force sources are the coupled set of partial differential equations (PDE):

$$\nabla_{iK} c_{KL} \nabla_{Lj}^{sym} u_j = \rho \frac{\partial^2}{\partial t^2} u_i \tag{5.1}$$

with the subscripts running as follows: $i, j = x, y, z$ and $K, L = 1, 2, 3, 4, 5, 6$. The latter corresponds to the reduced index convention, see for instance [5]. c_{KL} is the stiffness matrix of the crystal c_{ijkl} but in reduced index notation. Note that no assumptions except for homogeneity are made regarding its entries which, therefore, can be real or complex, thus the discussion remains valid for viscoelastic media as well. The differential operators on the left hand side can be found explicitly in cartesian and cylindrical coordinates in the book by Auld [5]; u_i are the displacement vector field components.

For flat geometry the partial wave approach will be used to develop and illustrate the logic of the arguments. One begins with a harmonic type solution of the form:

$$u_j = U_j \, e^{i(\xi y + kz - \omega t)} \tag{5.2}$$

The equations of motion (5.1) for this type of solution reduce to:

$$\nabla_{iK} c_{KL} \nabla_{Lj}^{sym} u_j = -\rho \, \omega^2 \, u_i \tag{5.3}$$

The boundary conditions must be accounted for. The strain tensor field is defined by:

$$S_{ij} = \frac{1}{2}\left(\frac{\partial u_i}{\partial x_j} + \frac{\partial u_j}{\partial x_i}\right) \rightarrow S_K = \nabla^{sym}_{Kj} u_j \qquad (5.4)$$

and the stress tensor field T_{ij} is in turn defined in terms of the strain tensor field as:

$$T_{ij} = c_{ijkl}\ S_{kl} \qquad (5.5)$$

where all the quantities used have been defined above. The stress free conditions at the upper and lower boundaries in the spatial axes configuration chosen are expressed by the following set of six equations:

$$T_{yy}|_{y=\pm h} = T_{yx}|_{y=\pm h} = T_{yz}|_{y=\pm h} = 0 \qquad (5.6)$$

This completes the description of the problem. In problems where symmetric and antisymmetric modes exist, the above boundary conditions must be substituted by their symmetric and antisymmetric counterparts. The reader is referred to any standard book about elastic waves such as [5] and [6] for further details.

5.1.1 Triclinic Crystals

This most general crystal class is presented here with additional comments to those already given in [32, 75] and an illustrative example is also provided. Crystals belonging to the triclinic class have a stiffness matrix with 21 independent constants and only a centre of symmetry which means the transformation $\mathbf{r} \leftrightarrow -\mathbf{r}$ leaves the stiffness matrix unchanged. Note that this symmetry is present in *all* crystal classes as can be checked in any book dealing with crystal symmetries [50] .

$$\begin{pmatrix} c_{11} & c_{12} & c_{13} & c_{14} & c_{15} & c_{16} \\ & c_{22} & c_{23} & c_{24} & c_{25} & c_{26} \\ & & c_{33} & c_{34} & c_{35} & c_{36} \\ & & & c_{44} & c_{45} & c_{46} \\ & & & & c_{55} & c_{56} \\ & & & & & c_{66} \end{pmatrix} \qquad (5.7)$$

After performing the matrix multiplications in equation (5.3) and equating to zero the determinant for non-trivial solutions of the fields' amplitudes U_i, one obtains the *Christoffel* equation.

$$\mathbf{\Gamma}(\omega, k, \xi) = 0 \qquad (5.8)$$

where the matrix $\boldsymbol{\Gamma}$ is symmetric, $\Gamma_{ij} = \Gamma_{ji}$. For the triclinic case, its relevant entries are given by:

$$
\begin{aligned}
\Gamma_{11} &= \rho\omega^2 - (c_{55}k^2 + 2c_{56}k\xi + c_{66}\xi^2) \\
\Gamma_{12} &= -(c_{45}k^2 + (c_{25} + c_{46})k\xi + c_{26}\xi^2) \\
\Gamma_{13} &= -(c_{35}k^2 + (c_{36} + c_{45})k\xi + c_{46}\xi^2) \\
\Gamma_{22} &= \rho\omega^2 - (c_{44}k^2 + 2c_{24}k\xi + c_{22}\xi^2) \\
\Gamma_{23} &= -(c_{34}k^2 + (c_{23} + c_{44})k\xi + c_{24}\xi^2) \\
\Gamma_{33} &= \rho\omega^2 - (c_{33}k^2 + 2c_{34}k\xi + c_{44}\xi^2)
\end{aligned}
\tag{5.9}
$$

Equation (5.8) with the entries given above yields a polynomial equation of sixth degree in ξ (see also [32]). The six roots of this equation will be labelled as ξ_n with $n = 1, 2...6$ and therefore the solution (5.2) can be now expressed as the superposition of six independent partial waves. This was to be expected since there are three coupled PDE's of second order for the displacement fields u_j. The partial wave expansion reads:

$$
u_j = \left(\sum_{n=1}^{6} U_j^{(n)} e^{i\xi_n y} \right) e^{i(kz - \omega t)}
\tag{5.10}
$$

Following [32, 75], the fields' amplitude ratios can be defined with the help of the Christoffel equation (5.8):

$$
V^{(n)} \equiv \frac{U_y^{(n)}}{U_x^{(n)}} = \frac{\Gamma_{11}\Gamma_{23} - \Gamma_{13}\Gamma_{12}}{\Gamma_{13}\Gamma_{22} - \Gamma_{12}\Gamma_{23}}
\tag{5.11}
$$

$$
W^{(n)} \equiv \frac{U_z^{(n)}}{U_x^{(n)}} = \frac{\Gamma_{11}\Gamma_{23} - \Gamma_{13}\Gamma_{12}}{\Gamma_{12}\Gamma_{33} - \Gamma_{13}\Gamma_{23}}
\tag{5.12}
$$

These are substituted into (5.10) and one is left with only six field amplitudes to determine, namely $U_x^{(n)}$.

The boundary conditions must now be taken into account to obtain the dispersion relation of the problem. After another matrix multiplication, equations (5.6) yield the following expressions for the tensor fields at the boundaries:

$$
\begin{aligned}
T_{yx}|_{y=\pm h} &= \sum_{n=1}^{6} U_x^{(n)} D_{xn} e^{\pm i\xi_n h} \\
T_{yy}|_{y=\pm h} &= \sum_{n=1}^{6} U_x^{(n)} D_{yn} e^{\pm i\xi_n h} \\
T_{yz}|_{y=\pm h} &= \sum_{n=1}^{6} U_x^{(n)} D_{zn} e^{\pm i\xi_n h}
\end{aligned}
\tag{5.13}
$$

where the following quantities have been defined:

$$
\begin{aligned}
D_{xn} &\equiv i\Big\{ (c_{56}k + c_{66}\xi_n) + (c_{46}k + c_{26}\xi_n)V^{(n)} + (c_{36}k + c_{46}\xi_n)W^{(n)} \Big\} \\
D_{yn} &\equiv i\Big\{ (c_{25}k + c_{26}\xi_n) + (c_{24}k + c_{22}\xi_n)V^{(n)} + (c_{23}k + c_{24}\xi_n)W^{(n)} \Big\} \\
D_{zn} &\equiv i\Big\{ (c_{45}k + c_{46}\xi_n) + (c_{44}k + c_{24}\xi_n)V^{(n)} + (c_{34}k + c_{44}\xi_n)W^{(n)} \Big\}
\end{aligned}
\tag{5.14}
$$

Equations (5.13) constitute a system of six linear algebraic equations in the six unknowns $U_x^{(n)}$. In order to have non-trivial solutions for the amplitudes $U_x^{(n)}$, the 6×6 determinant $\mathfrak{D}$ of its coefficients must vanish:

$$\mathfrak{D}(\omega, k, \xi_n(\omega, k)) = 0 \qquad (5.15)$$

The entries of this determinant are products of the form $D_{jn}e^{\pm i\xi_n h}$. Nayfeh and Chimenti [32] finish their discussion of triclinic crystals at this point due to the complexity of the equations which renders them numerically intractable. However, some valuable conclusions can be drawn from the previous analysis which will elucidate the nature of the modes propagating in these crystals. Noting that the Christoffel equation (5.8) and (5.9) lacks the symmetry $\xi \leftrightarrow -\xi$, and hence so do the roots ξ_n, a factorization of the 6×6 determinant $\mathfrak{D}$ into a product of two 3×3 subdeterminants is not possible. In other words, no linear combination of definite parity (symmetric and antisymmetric) can be constructed from the six independent partial waves in (5.10). Therefore, since there is only one non-reducible dispersion determinant (5.15), there is only *one family* of independent modes with no definite parity with respect to the middle plane of the plate. As a consequence of the non-reducibility of the dispersion determinant, only one field configuration with 6 partial waves will correspond to a given pair (ω, k), see also [74] for a more detailed explanation of this and [75] for a similar derivation in the case of bulk elastic waves. Therefore, no crossings occur amongst the modes in a triclinic crystal. Note that this conclusion holds in both elastic and viscoelastic materials since no assumptions have been made about the stiffness matrix (5.7) being real or complex, only that the medium be homogeneous, that is the entries are independent of the spatial coordinates.

The above analysis is illustrated with an example, the dispersion curves computed with an PSCM scheme (this approach has been validated in [21], [46] and [63]) for a strongly anisotropic triclinic plate in *default configuration* are presented in figure 5.1.a. It can be seen clearly that the modes do not cross. The displacement vector fields, or mode shapes, for the first five modes at $fd = 5$ MHz-mm are also shown in a two-dimensional plot in figure 5.1.b and in a three-dimensional plot in figure 5.1.c. In order to discuss the mode shapes and their new features it will help to write explicitly which part of the solution has a physical meaning. The solution in equation (5.2) was:

$$u_j(y, z; t) = U_j(y) \, e^{i(kz - \omega t)} = \|U_j(y)\| \, e^{\phi_j(y)} \, e^{i(kz - \omega t)} \qquad (5.16)$$

From which only the real part is physically meaningful:

$$\mathrm{Re} \, u_j(y, z; t) = \|U_j(y)\| \, e^{-\beta z} \cos(\alpha z - \omega t + \phi_j(y)) \qquad (5.17)$$

where $k = \alpha + i\beta$. The phase of the complex displacement vector field can in general depend on the coordinate {y} as a result of anisotropy. In figure 5.1.b the norm, normalized to one, of the displacement vector components is plotted in black circles whereas the phase is plotted in a solid red line. In this and the subsequent two-dimensional plots, the horizontal axis gives the radians of the phase in terms of π, no axis or scale has been chosen for the norm which has been normalized so that the point with maximum amplitude has value one, only the origin of the horizontal axes is the same for both norm and phase. The vertical axis is the thickness or half-thickness of the plate as appropriate, this will be indicated in each case explicitly.

It is remarkable to note that the norm is symmetric and the phase anti-symmetric with respect to the middle plane of the plate but the solution given by equation (5.17) has no parity as seen from the preceding analysis. It will be seen that, the feature of having a phase which depends on {y} is inherent to all configurations where the solution has no definite parity. Otherwise, if the phase was coordinate independent as in the case of an isotropic or cubic plate for instance, the solution would display parity in contradiction with the analysis above. This can be easily seen from the form of the equation (5.17) where a constant term inside the cosine does not change the parity properties of the solution whereas if this factor has *any* {y} dependence the solution will no longer possess any definite parity.

In figure 5.1.c the norm of the vector and the phase are plotted in a three-dimensional space where the vertical axis corresponds to the spatial {y} axis running across the thickness of the plate and the horizontal plane is just the complex plane in polar coordinates, so each point in the graph has coordinates $\{\|U_j(y)\|\cos(\phi_j(y)), \|U_j(y)\|\sin(\phi_j(y)), y\}$. Since the phase depends on {y} the curve does not lie within a two-dimensional plane but twists around in space. Note however, that this plot does not correspond to the actual physical process and movement of the structure but it is just a way of presenting the results so that the properties of the solution become more apparent. The physical and elastic properties of the material used are given in section 5.4 at the end.

The same procedure and analysis carried out above will be applied to the remaining crystal classes, simplifications are done where possible and the corresponding conclusions drawn in each case. For the sake of brevity and to avoid unnecessary repetition not all the equations will be written explicitly and sometimes only the results will be given bearing in mind that the procedure is simpler than the one just carried out in this section.
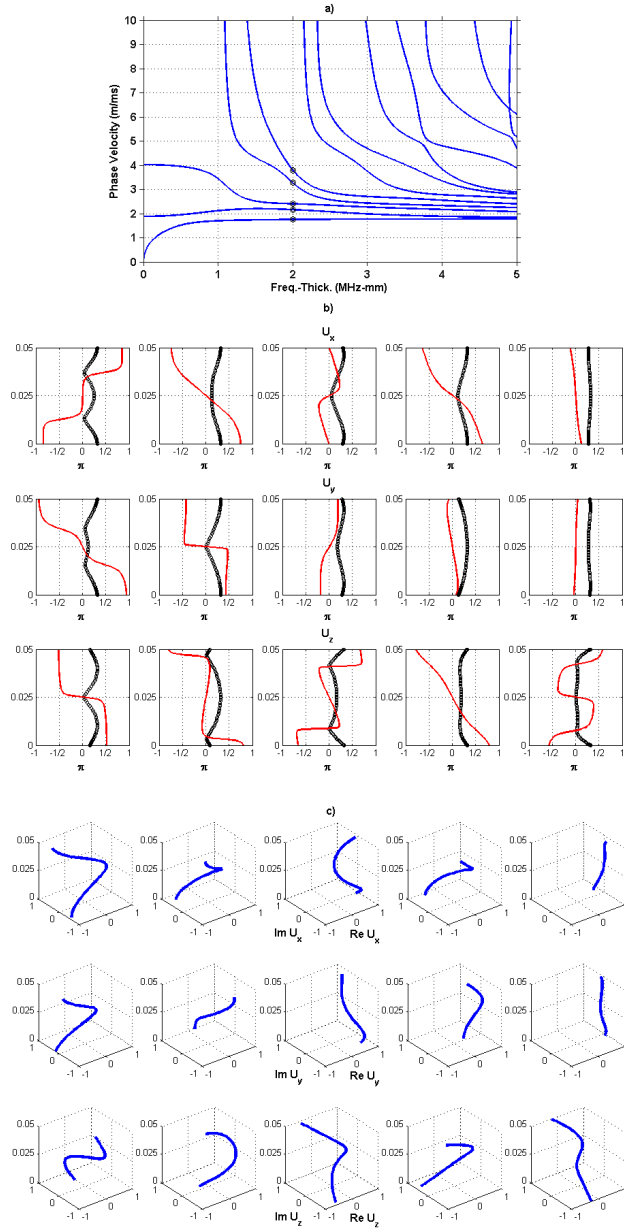
Figure 5.1: In a): Modes in a triclinic 5mm. thick free plate with propagation along the {Z} axis of the crystal. In b) and c): two- and three-dimensional mode shapes of the first five modes signalled in circles in a). In b) the norm of the complex vector field normalized to one is shown in black circles whereas the phase is shown in solid red lines. In c) the coordinate of the displacement complex vector in complex polar coordinates is shown at each point of the thickness of the plate. Note how the phase is not constant through the thickness thus yielding solutions with no definite parity.

5.1.2 Monoclinic Crystals

The next material in number of independent constants is monoclinic. These crystals have 13 independent elastic constants. The dyad axis is conventionally taken along the {Z} axis, as a consequence of this, the plane normal to this axis is a plane of mirror symmetry. With this convention, the stiffness matrix takes the form, [50]:

$$\begin{pmatrix} c_{11} & c_{12} & c_{13} & 0 & 0 & c_{16} \\ & c_{22} & c_{23} & 0 & 0 & c_{26} \\ & & c_{33} & 0 & 0 & c_{36} \\ & & & c_{44} & c_{45} & 0 \\ & & & & c_{55} & 0 \\ & & & & & c_{66} \end{pmatrix} \tag{5.18}$$

As before, the default Y configuration is studied first. According to the convention above and taking into account the arrangement of the axes in this configuration, the mirror symmetry plane is orthogonal to the plane of the plate and propagation takes place in a direction normal to this plane of mirror symmetry. Performing the matrix multiplications as before and equating to zero the determinant for non-trivial solutions of the fields' amplitudes U_i one obtains the *Christoffel* equation (5.8) whose elements in the present case are given by:

$$\begin{aligned} \Gamma_{11} &= \rho\omega^2 - (c_{55}k^2 + c_{66}\xi^2) \\ \Gamma_{12} &= -(c_{45}k^2 + c_{26}\xi^2) \\ \Gamma_{13} &= -(c_{36} + c_{45})k\xi \\ \Gamma_{22} &= \rho\omega^2 - (c_{44}k^2 + c_{22}\xi^2) \\ \Gamma_{23} &= -(c_{23} + c_{44})k\xi \\ \Gamma_{33} &= \rho\omega^2 - (c_{33}k^2 + c_{44}\xi^2) \end{aligned} \tag{5.19}$$

The Christoffel equation with the entries given above yields a polynomial equation of the sixth degree in ξ. The six roots of this equation will be labelled as ξ_n with $n = 1, 2...6$ and therefore the solution (5.2) can be now expressed as the superposition of six independent partial waves (5.10). Once more, one defines the amplitude ratios given in (5.11) and (5.12) with the elements Γ_{ij} shown in (5.19).

It is evident that the problem does not decouple but looking at the elements of the Christoffel equation one can notice that the elements of the determinant only contain *even* powers of ξ. From (5.19) it is easily seen that the terms in the determinant contain the following powers:

$$\begin{aligned} \Gamma_{11}\Gamma_{22}\Gamma_{33} &\sim \xi^6, \xi^4, \xi^2, \xi^0 \\ \Gamma_{12}\Gamma_{23}\Gamma_{13} &\sim \xi^4, \xi^2 \\ \Gamma_{23}^2\Gamma_{11} &\sim \xi^4, \xi^2 \\ \Gamma_{13}^2\Gamma_{22} &\sim \xi^4, \xi^2 \\ \Gamma_{12}^2\Gamma_{33} &\sim\sim \xi^6, \xi^4, \xi^2, \xi^0 \end{aligned} \tag{5.20}$$

Clearly the Christoffel equation possesses the symmetry: $\xi \leftrightarrow -\xi$. Hence, its six roots will reflect this symmetry:

$$\xi_{n+1} = -\xi_n \qquad n = 1, 3, 5 \tag{5.21}$$

As a consequence, the ratios defined in (5.11) and (5.12) will now present the following symmetries:

$$\begin{aligned} V_{n+1} &= V_n & n &= 1, 3, 5 \\ W_{n+1} &= -W_n & n &= 1, 3, 5 \end{aligned} \tag{5.22}$$

The boundary conditions must now be taken into account to obtain the dispersion relation of the problem. Equations (5.6) yield the analogous expressions to (5.13) for the tensor fields at the boundaries. But now the elements D_{jn} are given by:

$$\begin{aligned} D_{xn} &\equiv i \left\{ c_{66}\xi_n + c_{26}\xi_n V^{(n)} + c_{36}kW^{(n)} \right\} \\ D_{yn} &\equiv i \left\{ c_{26}\xi_n + c_{22}\xi_n V^{(n)} + c_{23}kW^{(n)} \right\} \\ D_{zn} &\equiv i \left\{ c_{45}k + c_{44}kV^{(n)} + c_{44}\xi_n W^{(n)} \right\} \end{aligned} \tag{5.23}$$

From (5.21) and (5.22) further symmetries for the above coefficients follow for $n = 1, 3, 5$:

$$\begin{aligned} D_{xn+1} &= -D_{xn} \\ D_{yn+1} &= -D_{yn} \\ D_{zn+1} &= D_{zn} \end{aligned} \tag{5.24}$$

Proceeding in the same way as in the triclinic case the determinant obtained from the boundary conditions (5.13) for the monoclinic case is:

$$\mathfrak{D}(\omega, k, \xi_n(\omega, k)) =$$
$$\begin{bmatrix} D_{x1}e^{i\xi_1 h} & D_{x2}e^{i\xi_2 h} & D_{x3}e^{i\xi_3 h} & D_{x4}e^{i\xi_4 h} & D_{x5}e^{i\xi_5 h} & D_{x6}e^{i\xi_6 h} \\ D_{x1}e^{-i\xi_1 h} & D_{x2}e^{-i\xi_2 h} & D_{x3}e^{-i\xi_3 h} & D_{x4}e^{-i\xi_4 h} & D_{x5}e^{-i\xi_5 h} & D_{x6}e^{-i\xi_6 h} \\ D_{y1}e^{i\xi_1 h} & D_{y2}e^{i\xi_2 h} & D_{y3}e^{i\xi_3 h} & D_{y4}e^{i\xi_4 h} & D_{y5}e^{i\xi_5 h} & D_{y6}e^{i\xi_6 h} \\ D_{y1}e^{-i\xi_1 h} & D_{y2}e^{-i\xi_2 h} & D_{y3}e^{-i\xi_3 h} & D_{y4}e^{-i\xi_4 h} & D_{y5}e^{-i\xi_5 h} & D_{y6}e^{-i\xi_6 h} \\ D_{z1}e^{i\xi_1 h} & D_{z2}e^{i\xi_2 h} & D_{z3}e^{i\xi_3 h} & D_{z4}e^{i\xi_4 h} & D_{z5}e^{i\xi_5 h} & D_{z6}e^{i\xi_6 h} \\ D_{z1}e^{-i\xi_1 h} & D_{z2}e^{-i\xi_2 h} & D_{z3}e^{-i\xi_3 h} & D_{z4}e^{-i\xi_4 h} & D_{z5}e^{-i\xi_5 h} & D_{z6}e^{-i\xi_6 h} \end{bmatrix}$$
$$\tag{5.25}$$

Monoclinic is the most general case in which a factorization of the determinant is possible. Therefore, this case is presented in detail to illustrate the procedure which is analogous but simpler in the cases studied later. One begins by using the symmetry properties in equations (5.21) and (5.26) to

simplify the entries of the determinant in (5.25):

$$
\begin{bmatrix}
D_{x1}e^{i\xi_1 h} & -D_{x1}e^{-i\xi_1 h} & D_{x3}e^{i\xi_3 h} & -D_{x3}e^{-i\xi_3 h} & D_{x5}e^{i\xi_5 h} & -D_{x5}e^{-i\xi_5 h} \\
D_{x1}e^{-i\xi_1 h} & -D_{x1}e^{i\xi_1 h} & D_{x3}e^{-i\xi_3 h} & -D_{x3}e^{i\xi_3 h} & D_{x5}e^{-i\xi_5 h} & -D_{x5}e^{i\xi_5 h} \\
D_{y1}e^{i\xi_1 h} & -D_{y1}e^{-i\xi_1 h} & D_{y3}e^{i\xi_3 h} & -D_{y3}e^{-i\xi_3 h} & D_{y5}e^{i\xi_5 h} & -D_{y5}e^{-i\xi_5 h} \\
D_{y1}e^{-i\xi_1 h} & -D_{y1}e^{i\xi_1 h} & D_{y3}e^{-i\xi_3 h} & -D_{y3}e^{i\xi_3 h} & D_{y5}e^{-i\xi_5 h} & -D_{y5}e^{i\xi_5 h} \\
D_{z1}e^{i\xi_1 h} & D_{z1}e^{-i\xi_1 h} & D_{z3}e^{i\xi_3 h} & D_{z3}e^{-i\xi_3 h} & D_{z5}e^{i\xi_5 h} & D_{z5}e^{-i\xi_5 h} \\
D_{z1}e^{-i\xi_1 h} & D_{z1}e^{i\xi_1 h} & D_{z3}e^{-i\xi_3 h} & D_{z3}e^{i\xi_3 h} & D_{z5}e^{-i\xi_5 h} & D_{z5}e^{i\xi_5 h}
\end{bmatrix}
$$

$$(5.26)$$

The following row operations are now performed:

$$
\begin{aligned}
(\tilde{n}) &= \tfrac{1}{2}((n) + (n+1)) \\
(\tilde{n}+1) &= \tfrac{1}{2i}((n) - (n+1))
\end{aligned}
\tag{5.27}
$$

where $(\tilde{n}), (n) = 1, 3, 5$ denote the old and new rows of $\mathfrak{D}$ respectively. This yields cosines and sines, for which the following shorthand is used:

$$
\begin{aligned}
\mathfrak{s}_n &\equiv \sin(\xi_n h) \\
\mathfrak{c}_n &\equiv \cos(\xi_n h)
\end{aligned}
\tag{5.28}
$$

The determinant reads:

$$
\begin{bmatrix}
D_{x1}\mathfrak{c}_1 & -D_{x1}\mathfrak{c}_1 & D_{x3}\mathfrak{c}_3 & -D_{x3}\mathfrak{c}_3 & D_{x5}\mathfrak{c}_5 & -D_{x5}\mathfrak{c}_5 \\
D_{x1}\mathfrak{s}_1 & D_{x1}\mathfrak{s}_1 & D_{x3}\mathfrak{s}_3 & D_{x3}\mathfrak{s}_3 & D_{x5}\mathfrak{s}_5 & D_{x5}\mathfrak{s}_5 \\
D_{y1}\mathfrak{c}_1 & -D_{y1}\mathfrak{c}_1 & D_{y3}\mathfrak{c}_3 & -D_{y3}\mathfrak{c}_3 & D_{y5}\mathfrak{c}_5 & -D_{y5}\mathfrak{c}_5 \\
D_{y1}\mathfrak{s}_1 & D_{y1}\mathfrak{s}_1 & D_{y3}\mathfrak{s}_3 & D_{y3}\mathfrak{s}_3 & D_{y5}\mathfrak{s}_5 & D_{y5}\mathfrak{s}_5 \\
D_{z1}\mathfrak{c}_1 & D_{z1}\mathfrak{c}_1 & D_{z3}\mathfrak{c}_3 & D_{z3}\mathfrak{c}_3 & D_{z5}\mathfrak{c}_5 & D_{z5}\mathfrak{c}_5 \\
D_{z1}\mathfrak{s}_1 & -D_{z1}\mathfrak{s}_1 & D_{z3}\mathfrak{s}_3 & -D_{z3}\mathfrak{s}_3 & D_{z5}\mathfrak{s}_5 & -D_{z5}\mathfrak{s}_5
\end{bmatrix}
\tag{5.29}
$$

The following column operations must be performed in order to obtain zeroes:

$$
\begin{aligned}
(\tilde{N}) &= \tfrac{1}{2}((N) + (N+1)) \\
(\tilde{N}+1) &= \tfrac{1}{2}((N) - (N+1))
\end{aligned}
\tag{5.30}
$$

where $(\tilde{N}), (N) = 1, 3, 5$ denote the old and new columns of $\mathfrak{D}$ respectively. The determinant now is greatly simplified:

$$
\begin{bmatrix}
0 & D_{x1}\mathfrak{c}_1 & 0 & D_{x3}\mathfrak{c}_3 & 0 & D_{x5}\mathfrak{c}_5 \\
D_{x1}\mathfrak{s}_1 & 0 & D_{x3}\mathfrak{s}_3 & 0 & D_{x5}\mathfrak{s}_5 & 0 \\
0 & D_{y1}\mathfrak{c}_1 & 0 & D_{y3}\mathfrak{c}_3 & 0 & D_{y5}\mathfrak{c}_5 \\
D_{y1}\mathfrak{s}_1 & 0 & D_{y3}\mathfrak{s}_3 & 0 & D_{y5}\mathfrak{s}_5 & 0 \\
D_{z1}\mathfrak{c}_1 & 0 & D_{z3}\mathfrak{c}_3 & 0 & D_{z5}\mathfrak{c}_5 & 0 \\
0 & D_{z1}\mathfrak{s}_1 & 0 & D_{z3}\mathfrak{s}_3 & 0 & D_{z5}\mathfrak{s}_5
\end{bmatrix}
\tag{5.31}
$$

after rearranging one is left with a factorized determinant:

$$
\begin{bmatrix}
D_{x1}\mathfrak{s}_1 & D_{x3}\mathfrak{s}_3 & D_{x5}\mathfrak{s}_5 & 0 & 0 & 0 \\
D_{y1}\mathfrak{s}_1 & D_{y3}\mathfrak{s}_3 & D_{y5}\mathfrak{s}_5 & 0 & 0 & 0 \\
D_{z1}\mathfrak{c}_1 & D_{z3}\mathfrak{c}_3 & D_{z5}\mathfrak{c}_5 & 0 & 0 & 0 \\
0 & 0 & 0 & D_{x1}\mathfrak{c}_1 & D_{x3}\mathfrak{c}_3 & D_{x5}\mathfrak{c}_5 \\
0 & 0 & 0 & D_{y1}\mathfrak{c}_1 & D_{y3}\mathfrak{c}_3 & D_{y5}\mathfrak{c}_5 \\
0 & 0 & 0 & D_{z1}\mathfrak{s}_1 & D_{z3}\mathfrak{s}_3 & D_{z5}\mathfrak{s}_5
\end{bmatrix}
\tag{5.32}
$$

This determinant yields the *generalized Lamb dispersion relations* (cf. [32, 75] and [13]) for symmetric and antisymmetric modes. Note that even though the plane of mirror symmetry of the crystal is not contained in the plane of the plate, this particular configuration allows for the existence of two families of modes with a definite parity with respect to the middle plane of the plate. The two dispersion relations derived from each non-reducible subdeterminant are independent and therefore crossings amongst modes from the two different families can occur. Again, no assumption has been made about the stiffness matrix so this conclusion holds for both elastic and for viscoelastic media. In the latter case however, apparent crossings might appear when the dispersion curves are projected in a two-dimensional plane, see [18] and [74].

This case is illustrated with an example computed with the PSCM as before. The results for the dispersion curves are presented in figure 5.2. Symmetric modes are plotted in blue solid lines and antisymmetric modes are plotted in dot-dashed red lines. Note how the two families do cross each other, yet there are no crossings within either family. Different codes exploiting the knowledge of the symmetry have been used for each family thus avoiding the problem of using tracing algorithms and having a much more efficient and reliable way to plot these dispersion curves. The physical and elastic properties of the material used are given in section 5.4 at the end.

The displacement fields are presented separately. Only the first five modes of each family for different frequencies have been plotted and signalled with circles in figure 5.2. For the symmetric modes, the two-dimensional plot of the mode shape norm (black circles) and phase (solid red lines) is presented in figure 5.3.a where, as anticipated, the phase, up to sign, does not depend on the {y} coordinate, thus yielding the desired symmetry of the solution with respect to the middle plane (that is, the only change, if any, that the phase suffers through the thickness is in sign). The three-dimensional plot for the complex displacement vector field is presented in figure 5.3.b. Similarly for antisymmetric modes whose two- and three-dimensional plots are presented in figures 5.4.a and 5.4.b respectively.

The *default configuration* just studied, with the {Y} axis normal to the
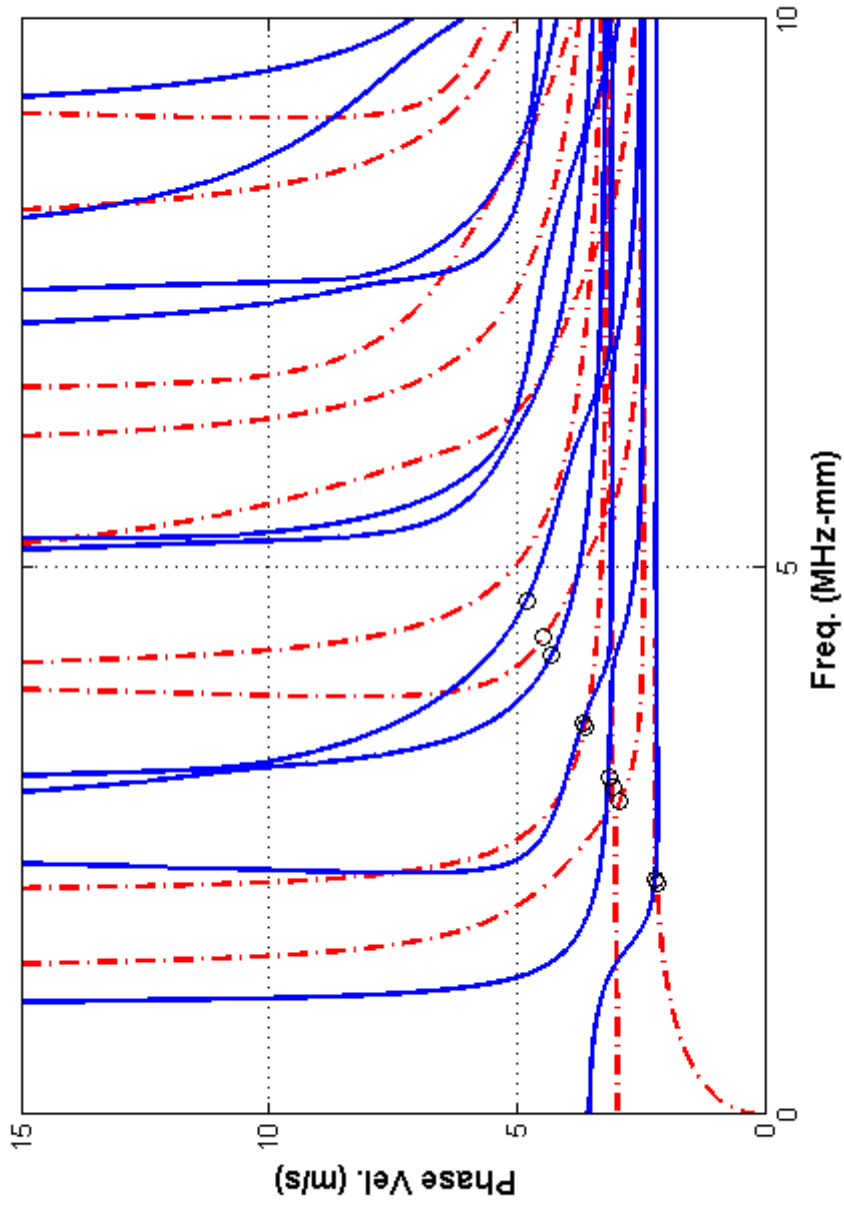
Figure 5.2: Symmetric (solid blue line) and antisymmetric (red dash-dotted line) modes in a monoclinic 5mm. thick free plate in Y configuration with propagation along the $\{Z\}$ crystal axis. Two different PSCM codes were used for each family in order to avoid the problem of the crossings amongst modes of different symmetry families.
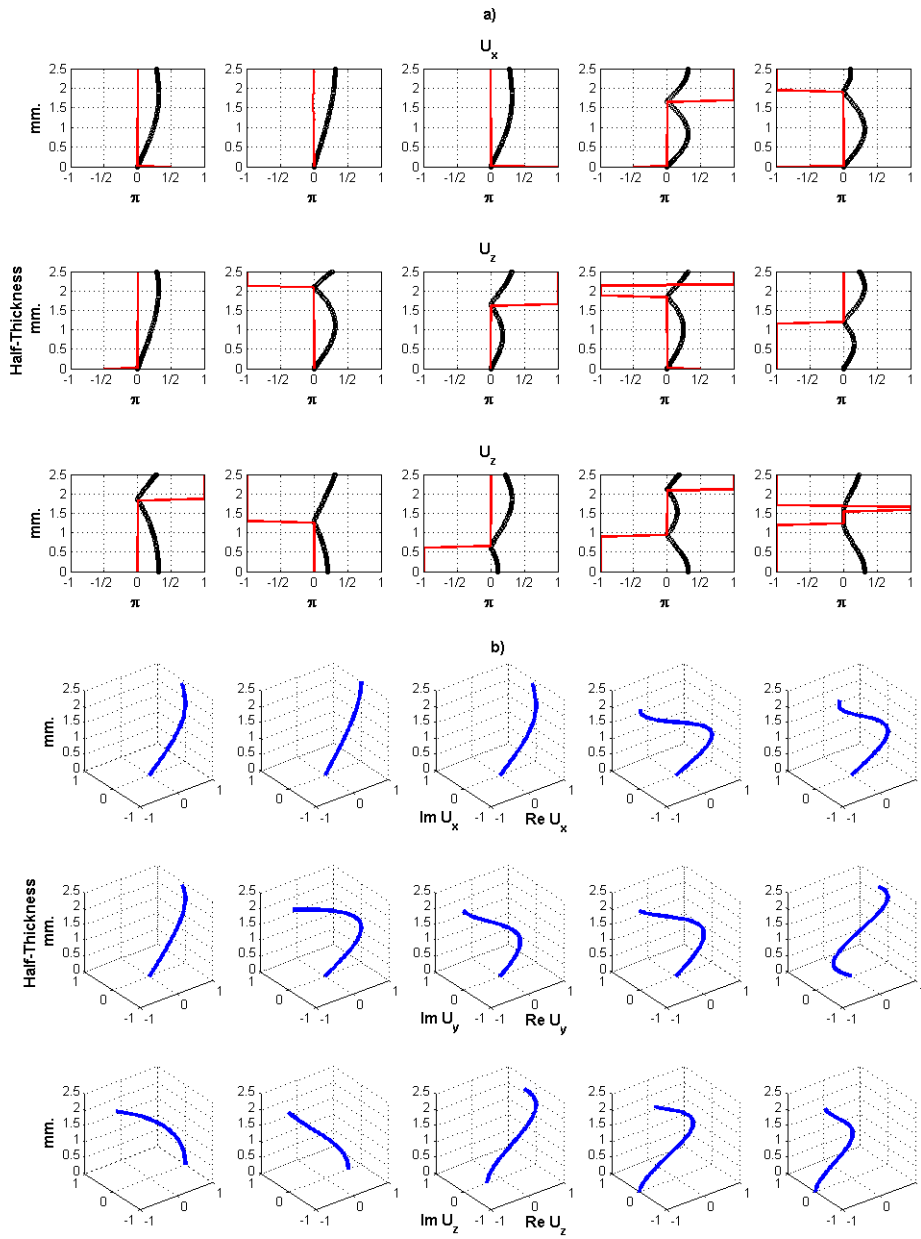
Figure 5.3: Two- and three-dimensional, a) and b) respectively, mode shapes of the first five modes of the symmetric family of modes for the monoclinic free plate of figure 5.2. The zero in the vertical axes coincides with the middle plane of the plate. In a) the norm of the complex vector field normalized to one is shown in black circles whereas the phase is shown in solid red lines. In b) the coordinate of the displacement complex vector in complex polar coordinates is shown at each point of the thickness of the plate. Note how the phase is now constant, up to a sign, through the thickness and thus the modes have parity.
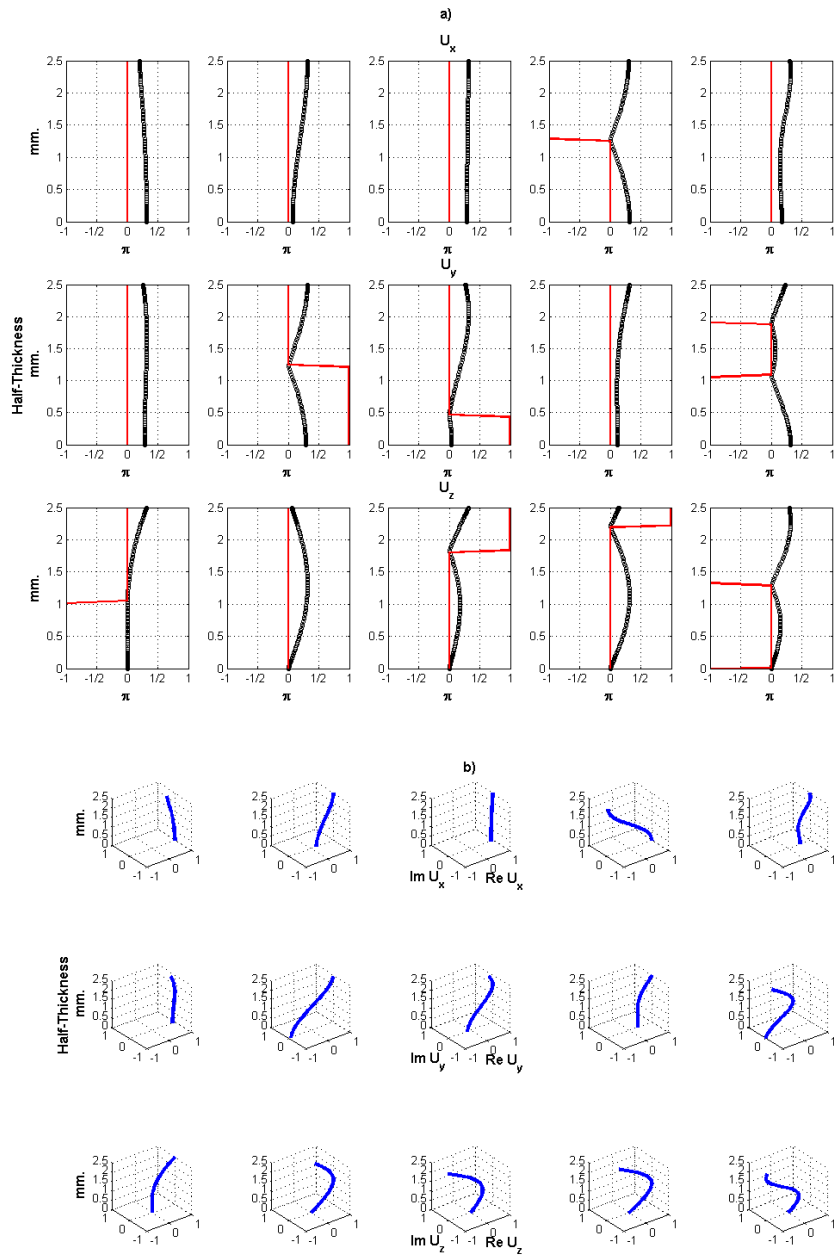
Figure 5.4: Two- and three-dimensional, a) and b) respectively, mode shapes of the first five modes of the antisymmetric family of modes for the mono-clinic free plate of figure 5.2. The zero in the vertical axes coincides with the middle plane of the plate. In a) the norm of the complex vector field normal-ized to one is shown in black circles whereas the phase is shown in solid red lines. In b) the coordinate of the displacement complex vector in complex polar coordinates is shown at each point of the thickness of the plate. Note how the phase is now constant, up to a sign, through the thickness and thus the modes have parity.

126

plane of the plate and propagation along the {Z} axis (recall that in this case space and crystal axes are aligned) will be henceforth referred to as configuration Y.

In configuration Z the {Z} axis is normal to the plane of the plate and propagation is along the {X} axis. The last configuration will be called configuration X with the {X} axis normal to the plane of the plate and propagation along the {Y} axis. The transformation matrices between these three configurations are formed by ones and zeroes appropriately placed and can be used to obtain the expression for the stiffness matrix via a *bond transformation* [5] referred to the fixed spatial axis {x,y,z}. These transformations will simply rearrange the entries of the stiffness matrix (5.18) in different positions but the values will be unchanged. The configurations to be considered are summarized in table 5.1.

Crystal Configuration Label	Axis Normal to the Plate	Propagation Axis
Default Y configuration	{Y}	{Z}
Z configuration	{Z}	{X}
X configuration	{X}	{Y}

Table 5.1: Table with the three different crystal axes configuration examined for each crystal class in this chapter. In the default Y configuration crystal and fixed spatial (plate) axes {x,y,z} are aligned.

In general, it must be noted that rotations about any axes proportional to $\pi/2$ will transform the matrix from one of the above described configurations to a different one or to an equivalently rotated configuration but the crystal type will be unchanged. For instance, a default Y configuration with a π rotation about the {Z} axis is completely equivalent to the original for monoclinic materials, for different materials sign changes might occur but the crystal class will not change. It is easy to realize that any rotation of a triclinic crystal will yield again a triclinic crystal. In summary, for any crystal class:

$$\phi_{X,Y,Z} = m\frac{\pi}{2} \quad m \in \mathbb{Z} \Rightarrow \text{Same Crystal in } X, Y, Z \text{ config. or equivalent.}$$
(5.33)

These rotations basically amount to a relabelling of the axes and a subsequent rearrangement of the stiffness matrix entries.

Following table 5.1, the next configuration to study would be the Z configuration, however, since it has been already studied in depth in [32, 75] or [13], its investigation will not be pursued here, the reader is referred to the

aforementioned references. At any rate, the situation is similar to the one just described for the default Y configuration giving rise to two families of modes: symmetric and antisymmetric with respect to the mirror symmetry plane which now coincides with the middle plane of the plate. Examples of this configuration can be found along with a detailed derivation in [32]. Later [13] and [18] have also provided several examples of dispersion curves in plates with monoclinic symmetry. And more recently [46], [63] and [74] used a PSCM to find dispersion curves in this configuration.

The last case is the X configuration. After performing the appropriate rotation of the axes to take the crystal from default Y configuration to X configuration via a bond rotation, the new stiffness matrix referred to the fixed spatial axes, which will be used in the equations of motion (5.3), takes the form:

$$
\begin{pmatrix}
c_{33} & c_{13} & c_{23} & c_{36} & 0 & 0 \\
 & c_{11} & c_{12} & c_{16} & 0 & 0 \\
 & & c_{22} & c_{26} & 0 & 0 \\
 & & & c_{66} & 0 & 0 \\
 & & & & c_{44} & c_{45} \\
 & & & & & c_{55}
\end{pmatrix}
\tag{5.34}
$$

The Christoffel equation in this case has the following entries:

$$
\begin{aligned}
\Gamma_{11} &= \rho\omega^2 - (c_{44}k^2 + 2c_{45}k\xi + c_{55}\xi^2) \\
\Gamma_{12} &= 0 \\
\Gamma_{13} &= 0 \\
\Gamma_{22} &= \rho\omega^2 - (c_{66}k^2 + 2c_{16}k\xi + c_{11}\xi^2) \\
\Gamma_{23} &= -(c_{26}k^2 + (c_{12} + c_{66})k\xi + c_{16}\xi^2) \\
\Gamma_{33} &= \rho\omega^2 - (c_{22}k^2 + 2c_{26}k\xi + c_{66}\xi^2)
\end{aligned}
\tag{5.35}
$$

The form of the Christoffel equation together with the expression of the tensor field components for the boundary conditions shows that the problem decouples into two independent problems: the analogues of the well-known SH and Lamb modes. However, it is important to note that these two families have no symmetry with respect to the middle plane of the plate as can be seen at once from the ξ dependence of $\mathbf{\Gamma}(\omega, k, \xi)$. Also, due to the zero entries and decoupling, the ratios in equations (5.11) and (5.12) are ill-defined. For cases where the problem decouples, one only needs to define one such ratio for the Lamb mode analogues:

$$
Q^{(n)} \equiv \frac{U_z^{(n)}}{U_y^{(n)}} = \frac{-\Gamma_{22}}{\Gamma_{23}}
\tag{5.36}
$$

First the case of plane strain involving only the x component of the displacement field is addressed. For this case, two different roots of ξ are obtained

from Γ_{11} and only one component of the stress tensor field involves the component u_x. Thus the boundary condition reads:

$$T_{yx}|_{y=\pm h} = \sum_{n=1}^{2} U_x^{(n)} D_{xn} e^{\pm i \xi_n h} \tag{5.37}$$

with

$$D_{xn} \equiv i\{c_{55}\xi_n + c_{45}k\} \tag{5.38}$$

This boundary condition yields a 2×2 determinant:

$$\mathfrak{D}_{SH}(\omega, k, \xi_n(\omega, k)) = 0 \tag{5.39}$$

Since both roots are different, this determinant cannot be further factorized in a simpler product of two factors. Therefore, the SH modes in this monoclinic configuration will have no symmetry with respect to the middle plane of the plate.

The modes involving the y and z components, the analogues to the Lamb modes, are found in a similar way. The 2×2 matrix in the Christoffel equation (5.35) yields the remaining four different roots of ξ. One can easily see that in this case the symmetry $\xi \leftrightarrow -\xi$ is not present either and therefore the modes will not have any symmetry with respect to the middle plane, unlike the conventional Lamb modes. The two remaining components of the tensor field involve only the u_y and u_z so the boundary conditions are:

$$\begin{aligned} T_{yy}|_{y=\pm h} = \sum_{n=1}^{4} U_y^{(n)} D_{yn} e^{\pm i \xi_n h} \\ T_{yz}|_{y=\pm h} = \sum_{n=1}^{4} U_y^{(n)} D_{zn} e^{\pm i \xi_n h} \end{aligned} \tag{5.40}$$

with:

$$\begin{aligned} D_{yn} \equiv i\left\{ ((c_{16}k + c_{11}\xi_n) + (c_{12}k + c_{16}\xi_n)Q^{(n)} \right\} \\ D_{zn} \equiv i\left\{ ((c_{66}k + c_{16}\xi_n) + (c_{26}k + c_{66}\xi_n)Q^{(n)} \right\} \end{aligned} \tag{5.41}$$

These two boundary conditions yield in turn a 4×4 determinant:

$$\mathfrak{D}_{Longitudinal}(\omega, k, \xi_n(\omega, k)) = 0 \tag{5.42}$$

This determinant cannot be further factorized on account of the four different roots of ξ so these modes will have no symmetry with respect to the middle plane of the plate.

In summary, for monoclinic crystals in the X configuration, only two independent families of modes with no definite symmetry with respect to the middle plane of the plate exist. One of them involves only the u_x (analogue to the SH modes) and the other the remaining u_y and u_z components (analogue to the Lamb modes). Since there are two dispersion relations, equations (5.39) and (5.42), crossings can occur amongst these two families

but not within modes of the same family as has been discussed previously.

This configuration's dispersion curves computed with the PSCM are presented in figure 5.5. "Lamb" modes are plotted in blue solid lines and "SH" modes are plotted in dot-dashed red lines. Again the two families do cross each other but none of them presents any symmetry. Different codes exploiting this symmetry have been used for each family thus avoiding the problem of using tracing algorithms and having a much more efficient and reliable way to plot these curves.

The displacement fields are presented separately. The first five modes of each family for different frequencies have been plotted and signalled with circles ("Lamb") and squares ("SH") in figure 5.5. For the "Lamb" modes, the two-dimensional plot of the mode shape norm (black circles) and phase (solid red lines) is presented in figure 5.6.a; note that the features of the phase are similar to those found in the triclinic case due to the lack of parity of the solution. The three-dimensional plot for the complex displacement vector field is presented in figure 5.6.b. Similarly for "SH" modes whose two- and three-dimensional plots are presented in figures 5.7.a and 5.7.b respectively. The physical and elastic properties of the material used are given in section 5.4 at the end.

To finish with the monoclinic crystal, a summary of how rotations of its axes different from those in equation (5.33) affect the stiffness matrix is presented. For definiteness the initial configuration will be the default Y configuration. Then, a certain rotation is performed on the crystal axes and one is interested in knowing what the stiffness matrix of the rotated crystal referred to the fixed spatial axes {x,y,z} will look like. Alternatively, one can also reason in terms of crystal axes only and think of the new rotated stiffness matrix as that of a newly defined crystal whose axes $\{\tilde{X}, \tilde{Y}, \tilde{Z}\}$ are again in default $\tilde{Y}$ configuration. In general, the new stiffness matrix will differ from the original (5.18); these results are summarized below, where, for instance, ϕ_X denotes the angle of rotation about the {X} axis of the crystal.

For rotations different from those in equation (5.33) and specifically for monoclinic crystals one has, see also [50]:

$$\begin{aligned} \phi_{X,Y} &\neq m\frac{\pi}{2} \quad m \in \mathbb{Z} \quad \implies \text{Triclinic} \\ \phi_Z &\neq m\frac{\pi}{2} \begin{cases} = m\pi & m \in \mathbb{Z} \implies \text{Invariant} \\ \neq m\pi & m \in \mathbb{Z} \implies \text{Monoclinic*} \end{cases} \end{aligned} \quad (5.43)$$

For appropriate rotations about the dyad axis, which corresponds to the crystal symmetries [50] the stiffness matrix is invariant. By *Monoclinic** it
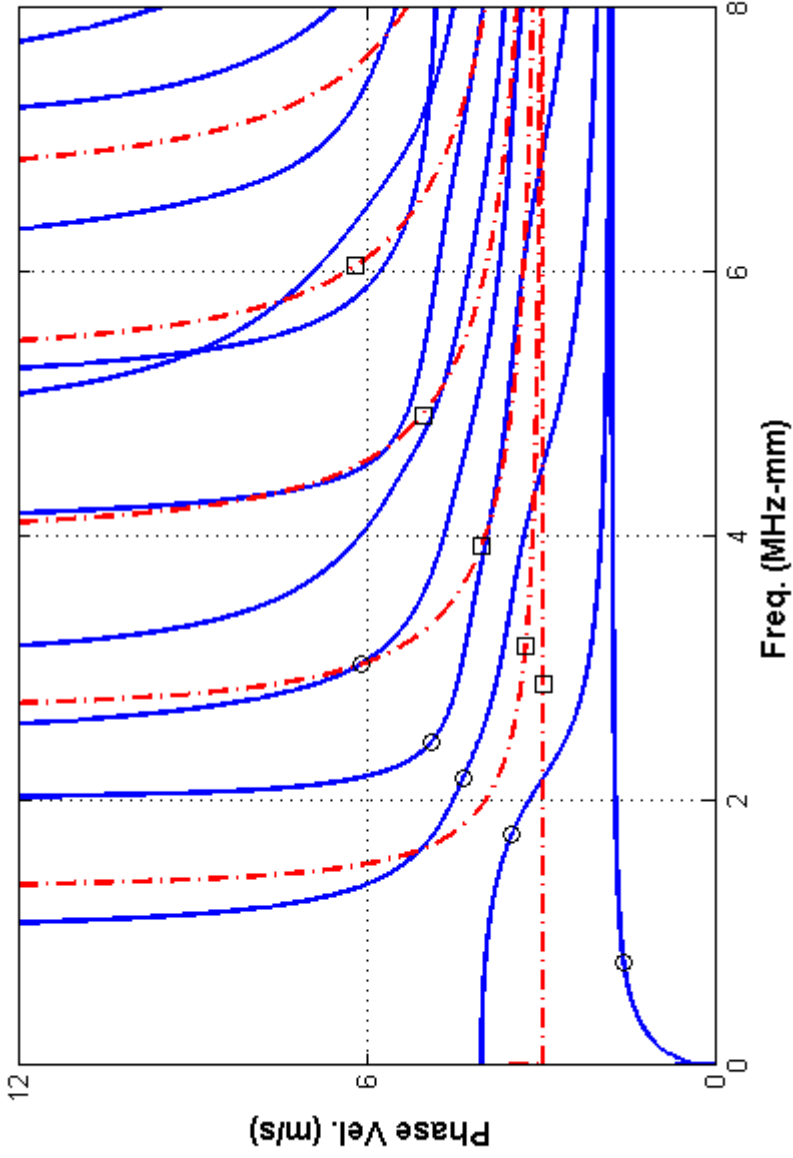
Figure 5.5: Lamb (solid blue line) and SH (red dash-dotted line) modes in a monoclinic 5mm. thick free plate in X configuration with propagation along the {Y} crystal axis. Again, two different PSCM codes were used for each family in order to avoid the problem of the crossings amongst modes and to plot Lamb and SH modes separately. Upon zooming in it is seen that the 8th and 9th Lamb modes do not cross even though it cannot be clearly appreciated in the figure. Marked with black circles and squares are the first five Lamb and SH modes respectively whose mode shapes are shown in the next two figures 5.6 and ??.
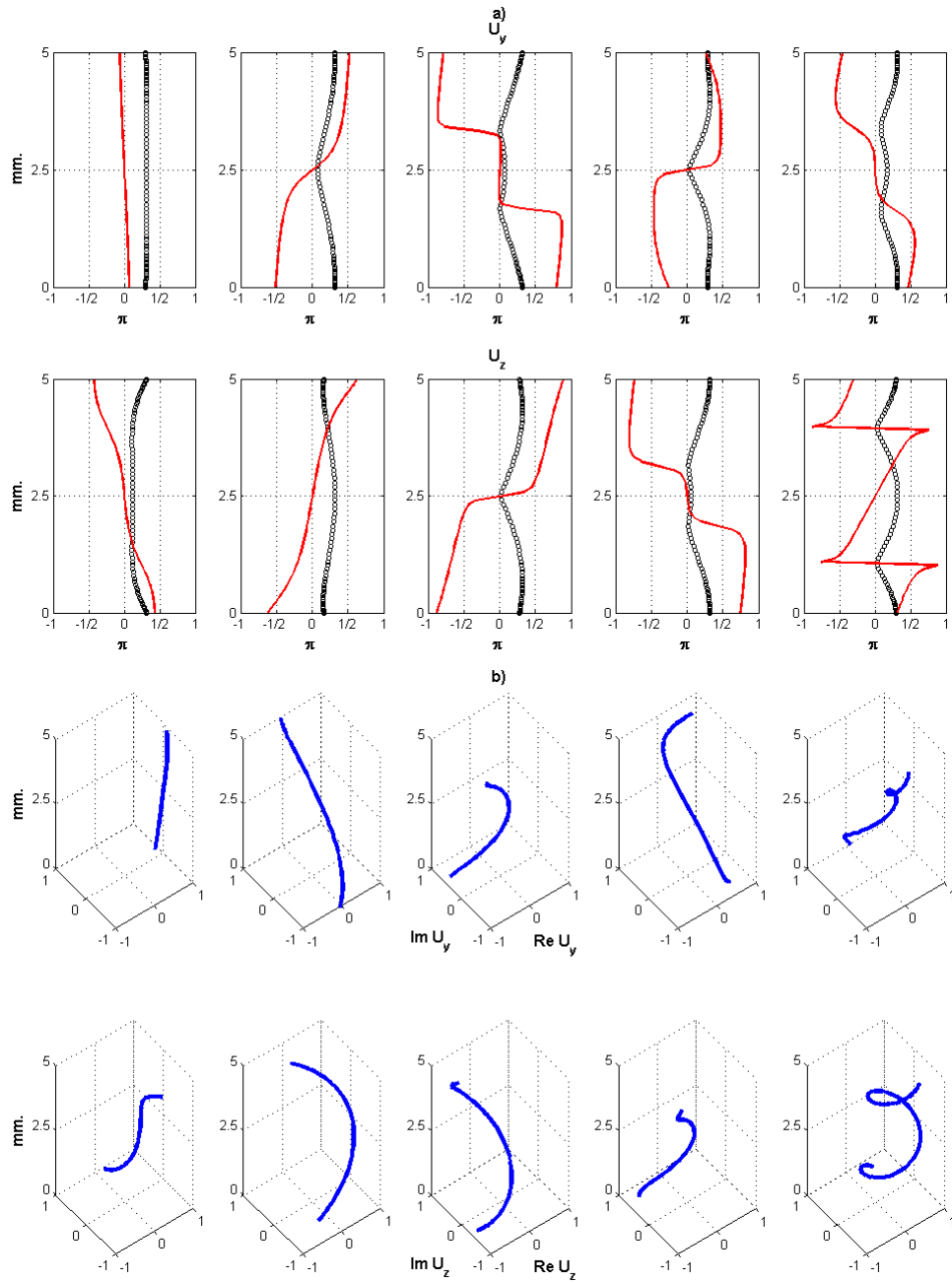
Figure 5.6: Two- and three-dimensional, a) and b) respectively, mode shapes of the first five Lamb modes for the monoclinic 5mm. thick free plate marked with black circles in figure 5.5. In a) the norm of the complex vector field normalized to one is shown in black circles and the phase is shown in solid red lines. In b) the coordinate of the displacement complex vector in complex polar coordinates is shown at each point of the thickness of the plate.
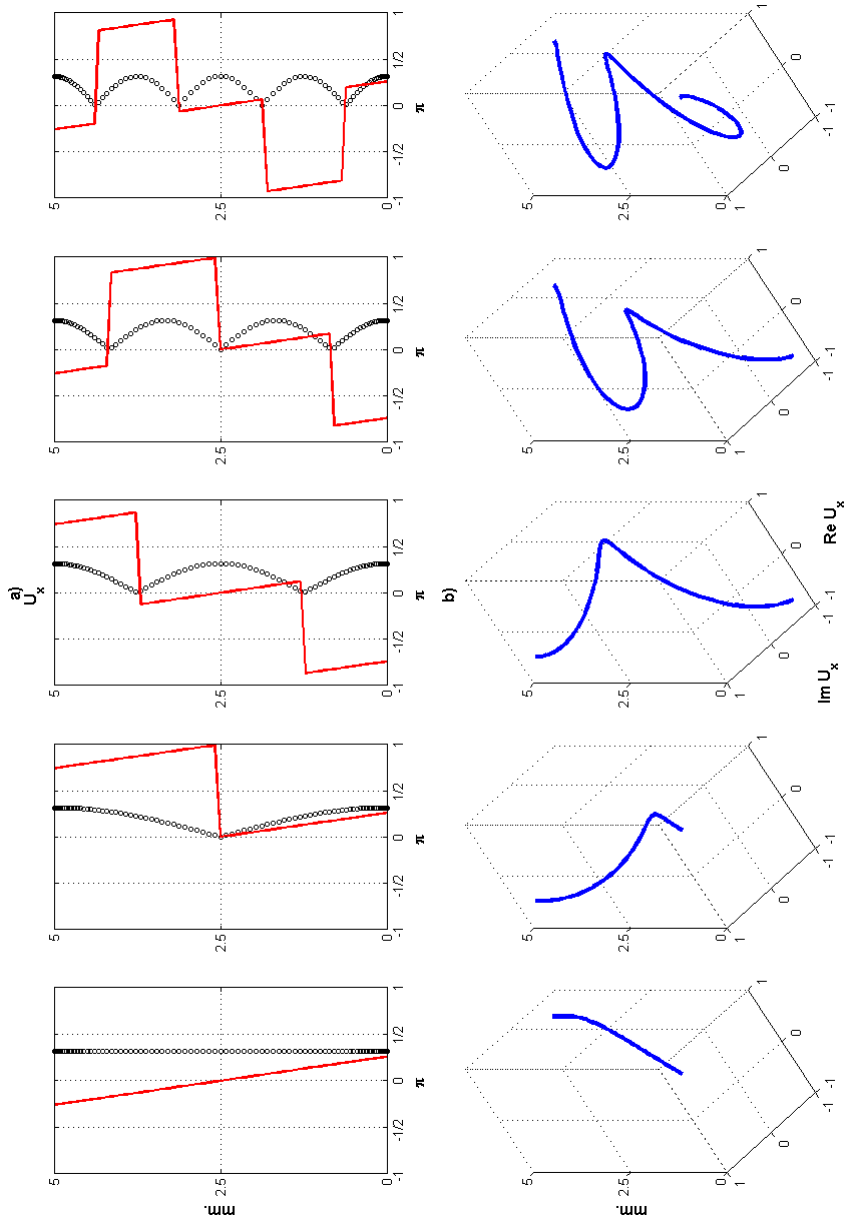
Figure 5.7: Two- and three-dimensional, a) and b) respectively, mode shapes of the first five SH modes for the monoclinic 5mm. thick free plate marked with black squares in figure 5.5. In a) the norm of the complex vector field normalized to one is shown in black circles and the phase is shown in solid red lines. In b) the coordinate of the displacement complex vector in complex polar coordinates is shown at each point of the thickness of the plate.

is meant a medium possessing monoclinic symmetry and whose stiffness matrix is like (5.18) but whose numerical values are different from the original ones. The new entries are given in terms of the old with coefficients from the rotation matrix depending on the angle of rotation about the {Z} axis according to the fourth rank tensor transformation law.

5.1.3 Orthorhombic Crystals

The next crystal class by number of independent elastic constants is the orthorhombic system. Crystals of this class have 9 independent constants and three mutually orthogonal dyad axes [50]. The stiffness matrix for these crystals has block form:

$$
\begin{pmatrix}
c_{11} & c_{12} & c_{13} & 0 & 0 & 0 \\
& c_{22} & c_{23} & 0 & 0 & 0 \\
& & c_{33} & 0 & 0 & 0 \\
& & & c_{44} & 0 & 0 \\
& & & & c_{55} & 0 \\
& & & & & c_{66}
\end{pmatrix}
\tag{5.44}
$$

This class has been widely studied elsewhere, see for instance [32] or [13], and its study will not be pursued here. However, a brief summary of the results is given.

Due to the three orthogonal dyad axes the three configurations in table 5.1 are equivalent up to reordering of the entries. In all these cases the problem decouples in SH and Lamb modes which in addition have definite parity: symmetric and antisymmetric with respect to the middle plane of the plate.

For rotations given in (5.43) different from $\pi/2$ the resulting stiffness matrix corresponds to monoclinic symmetry as shown in [32] and [13]. Therefore, all the previous discussion for monoclinic crystals carries over to rotated orthorhombic crystals. The monoclinic configuration X, Y or Z corresponding to the rotated crystal will obviously depend on the initial configuration of the orthorhombic medium and of the rotation performed.

5.1.4 Trigonal Crystals

Crystals belonging to the trigonal class have a stiffness matrix with at most 7 independent constants. They possess a third order principal axis which

conventionally is taken to be the {Z} axis, [50]. The stiffness matrix thus has the following form:

$$
\begin{pmatrix}
c_{11} & c_{12} & c_{13} & c_{14} & -c_{25} & 0 \\
 & c_{11} & c_{13} & -c_{14} & c_{25} & 0 \\
 & & c_{33} & 0 & 0 & 0 \\
 & & & c_{44} & 0 & c_{25} \\
 & & & & c_{44} & c_{14} \\
 & & & & & \frac{c_{11}-c_{12}}{2}
\end{pmatrix}
\tag{5.45}
$$

Following the same steps as in the previous cases one arrives again at the *Christoffel* equation (5.8) whose matrix $\boldsymbol{\Gamma}$ has the entries:

$$
\begin{aligned}
\Gamma_{11} &= \rho\omega^2 - (c_{44}k^2 + 2c_{14}k\xi + (\tfrac{c_{11}-c_{12}}{2})\xi^2) \\
\Gamma_{12} &= -2c_{25}k\xi \\
\Gamma_{13} &= -c_{25}\xi^2 \\
\Gamma_{22} &= \rho\omega^2 - (c_{44}k^2 - 2c_{14}k\xi + c_{11}\xi^2) \\
\Gamma_{23} &= -(c_{13}+c_{44})k\xi + c_{14}\xi^2 \\
\Gamma_{33} &= \rho\omega^2 - (c_{33}k^2 + c_{44}\xi^2)
\end{aligned}
\tag{5.46}
$$

Equation (5.45) with the entries given above yields a polynomial equation of sixth degree in ξ. The six roots of this equation will be labelled as ξ_n with $n = 1, 2...6$ and therefore the solution (5.2) can again be expressed as the superposition of six independent partial waves as in equation (5.10). Note that, for instance, one of the terms in the determinant contains odd powers of ξ, namely $\Gamma_{12}\Gamma_{23}\Gamma_{13} \sim \xi^5$. This means that the roots do not have the symmetry $\xi \leftrightarrow -\xi$ and therefore decomposition of the modes in symmetric and antisymmetric is not possible for this configuration either. Moreover, from the Christoffel equation one can see that all the components of the displacement field u_i are coupled again as in the triclinic case. One can anticipate now that the situation is analogous to that of triclinic crystals with only one dispersion relation for the only family of modes. No crossings will take place in this case either.

The expressions for the tensor fields at the boundaries are readily obtained from (5.13) and (5.14) with the help of the trigonal stiffness matrix (5.45) by simply setting to zero and relabeling the appropriate entries:

$$
\begin{aligned}
D_{xn} &\equiv i\Big\{(c_{14}k + (\tfrac{c_{11}-c_{12}}{2}))\xi_n + c_{25}kV^{(n)} + c_{25}\xi_n W^{(n)}\Big\} \\
D_{yn} &\equiv i\Big\{c_{25}k + (-c_{14}k + c_{11}\xi_n)V^{(n)} + (c_{13}k - c_{14}\xi_n)W^{(n)}\Big\} \\
D_{zn} &\equiv i\Big\{c_{25}\xi_n + (c_{44}k - c_{14}\xi_n)V^{(n)} + c_{44}\xi_n W^{(n)}\Big\}
\end{aligned}
\tag{5.47}
$$

This gives the boundary conditions and from them one obtains again a 6×6 determinant $\mathfrak{D}$ which constitutes the dispersion relation for this case. For

the reasons aforementioned it cannot be factorized in subdeterminants. Dispersion curves for this media and configuration can be obtained by using the same code used for triclinic materials.

For the Z and X configurations a computation analogous to the one leading to the Christoffel equation (5.46) shows again that in these configurations the problem does not decouple either and some terms in the determinant are proportional to odd powers of ξ. Hence, upon solving the Christoffel equation for the six different roots ξ_n and imposing the boundary conditions (5.13) with the appropriate expressions of (5.47) for each case one will arrive at one dispersion relation for the displacement field amplitudes $U_x^{(n)}$. As in the previous case no crossings will take place amongst the modes which will show no particular symmetry. Except for the rearranging of entries and the consequent difference in the Christoffel equation and boundary conditions, these two configurations lead to modes whose nature (no symmetries, no crossings) is completely analogous to those for the default Y configuration studied first.

A summary of the changes in the stiffness matrix under rotations is presented below:

$$
\begin{aligned}
\phi_{X,Y} \neq m\frac{\pi}{2} \qquad & m \in \mathbb{Z} \quad \implies \text{Triclinic-like} \\
\phi_Z \neq m\frac{\pi}{2} \begin{cases} = m\frac{2\pi}{3} & m \in \mathbb{Z} \quad \implies \text{Invariant} \\ \neq m\frac{2\pi}{3} & m \in \mathbb{Z} \quad \implies \text{Trigonal*} \end{cases}
\end{aligned} \tag{5.48}
$$

With the term *Triclinic-like* it is meant a stiffness matrix which is fully populated like (5.7) but whose entries are not necessarily different, thus it does not have 21 different constants. The conclusions obtained before for modes in triclinic materials remain valid in this case as can be easily checked with the aid of any software which allows for symbolic manipulations. Hence the term *Triclinic-like*.

For the rotations corresponding to the crystal symmetries [50] the stiffness matrix is invariant. Finally, by *Trigonal** it is meant either a trigonal medium whose stiffness matrix is like (5.45) but whose entries $\tilde{c}_{14}$ and $\tilde{c}_{25}$ are linear combinations of the old c_{14} and c_{25} with coefficients depending on the angle of rotation about the {Z} axis or simply with the same stiffness matrix (5.45) but with elements rearranged.

The trigonal crystal classes 32, $3m$ and $\bar{3}m$ constitute a particular and simpler case of the above. Due to higher symmetries imposed by dyad axes orthogonal to the principal axis one has $c_{15} = 0$ when one of these axes is taken along the crystal {X} axis. The stiffness matrix (5.45) is thus simplified. It will be shown that this has some interesting consequences.

For the default Y configuration the Christoffel equation is:

$$\begin{aligned}
\Gamma_{11} &= \rho\omega^2 - (c_{44}k^2 + 2c_{14}k\xi + (\tfrac{c_{11}-c_{12}}{2})\xi^2) \\
\Gamma_{12} &= 0 \\
\Gamma_{13} &= 0 \\
\Gamma_{22} &= \rho\omega^2 - (c_{44}k^2 - 2c_{14}k\xi + c_{11}\xi^2) \\
\Gamma_{23} &= -(c_{13}+c_{44})k\xi + c_{14}\xi^2 \\
\Gamma_{33} &= \rho\omega^2 - (c_{33}k^2 + c_{44}\xi^2)
\end{aligned} \tag{5.49}$$

From the ξ dependence of the Christoffel equation it is apparent that the modes in this configuration will not have any definite symmetry. The stress tensor field components lead to the decoupling of the problem so one may proceed in an analogous way as for the corresponding monoclinic case. The stress tensor field expressions in this case are:

$$\begin{aligned}
T_{yx}|_{y=\pm h} &= \sum_{n=1}^{2} U_x^{(n)} D_{xn} e^{\pm i\xi_n h} \\
T_{yy}|_{y=\pm h} &= \sum_{n=1}^{4} U_y^{(n)} D_{yn} e^{\pm i\xi_n h} \\
T_{yz}|_{y=\pm h} &= \sum_{n=1}^{4} U_y^{(n)} D_{zn} e^{\pm i\xi_n h}
\end{aligned} \tag{5.50}$$

with

$$\begin{aligned}
D_{xn} &\equiv i\left\{ (\tfrac{c_{11}-c_{12}}{2})\xi_n + c_{14}k \right\} \\
D_{yn} &\equiv i\left\{ ((-c_{14}k + c_{11}\xi_n) + (c_{13}k - c_{14}\xi_n)Q^{(n)} \right\} \\
D_{zn} &\equiv i\left\{ (c_{44}k - c_{14}\xi_n) + c_{44}\xi_n Q^{(n)} \right\}
\end{aligned} \tag{5.51}$$

with the ratio $Q^{(n)}$ defined as in equation (5.36). These boundary conditions will yield two independent and non-reducible dispersion relations, crossings can therefore occur amongst the ("Lamb") modes polarized in the sagittal plane and the x-polarized ("SH") modes normal to it. However, due to the form of the Christoffel equation neither of the families will present any symmetry with respect to the middle plane of the plate.

The dispersion curves for this trigonal configuration computed with the PSCM are presented in figure 5.8. As before, "Lamb" modes are plotted in blue solid lines and "SH" modes are plotted in dotted-dashed red lines. Again the two families do cross each other but none of them presents any symmetry. The first five mode shapes of each family for different frequencies have been plotted and signalled with circles in figure 5.8. For the "Lamb" modes, the two-dimensional plot of the mode shape norm (black circles) and phase (solid red lines) is presented in figure 5.9.a, note that the features of the phase are similar to those found in the triclinic case due to the lack of parity of the solution. The three-dimensional plot for the complex displacement vector field is presented in figure 5.9.b. Similarly for "SH" modes whose two- and three-dimensional plots are presented in figures 5.10.a and
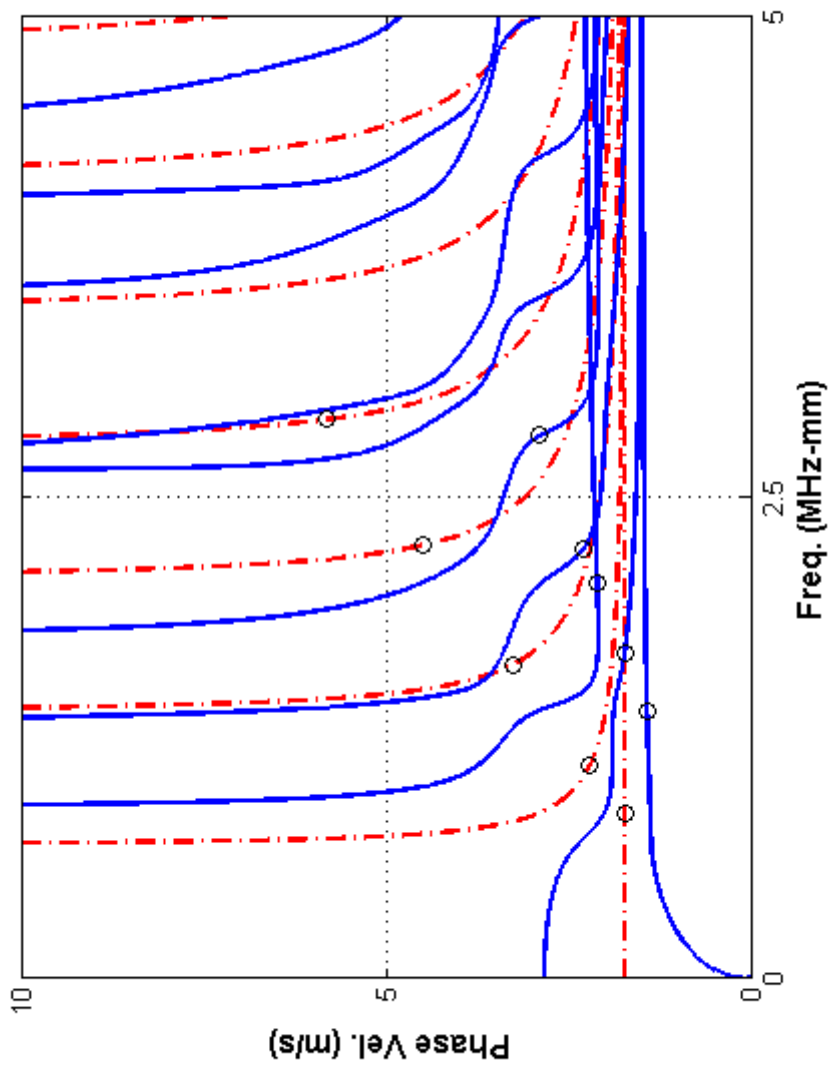
Figure 5.8: Lamb (solid blue line) and SH (red dash-dotted line) modes in a trigonal 5mm. thick free plate in *Y* configuration with propagation along the {Z} crystal axis. Again, different PSCM codes were used for each family in order to plot Lamb and SH modes separately. Marked with black circles the first five Lamb and SH modes respectively whose mode shapes are shown in the next two figures 5.6 and 5.7.
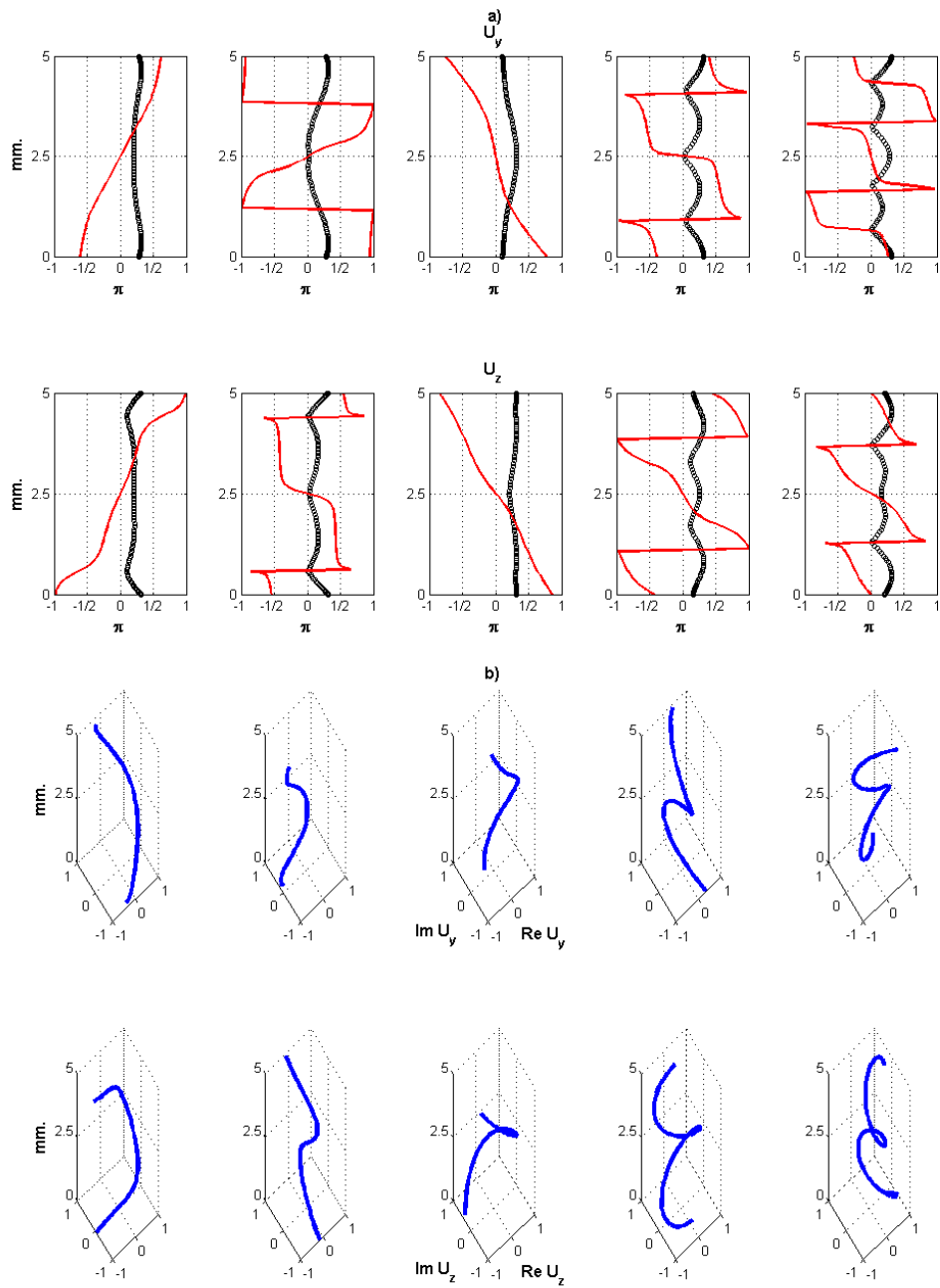
Figure 5.9: Two- and three-dimensional, a) and b) respectively, mode shapes of the first five Lamb modes for the trigonal 5mm. thick free plate marked with black circles in figure 5.8. In a) the norm of the complex vector field normalized to one is shown in black circles and the phase is shown in solid red lines. In b) the coordinate of the displacement complex vector in complex polar coordinates is shown at each point of the thickness of the plate.
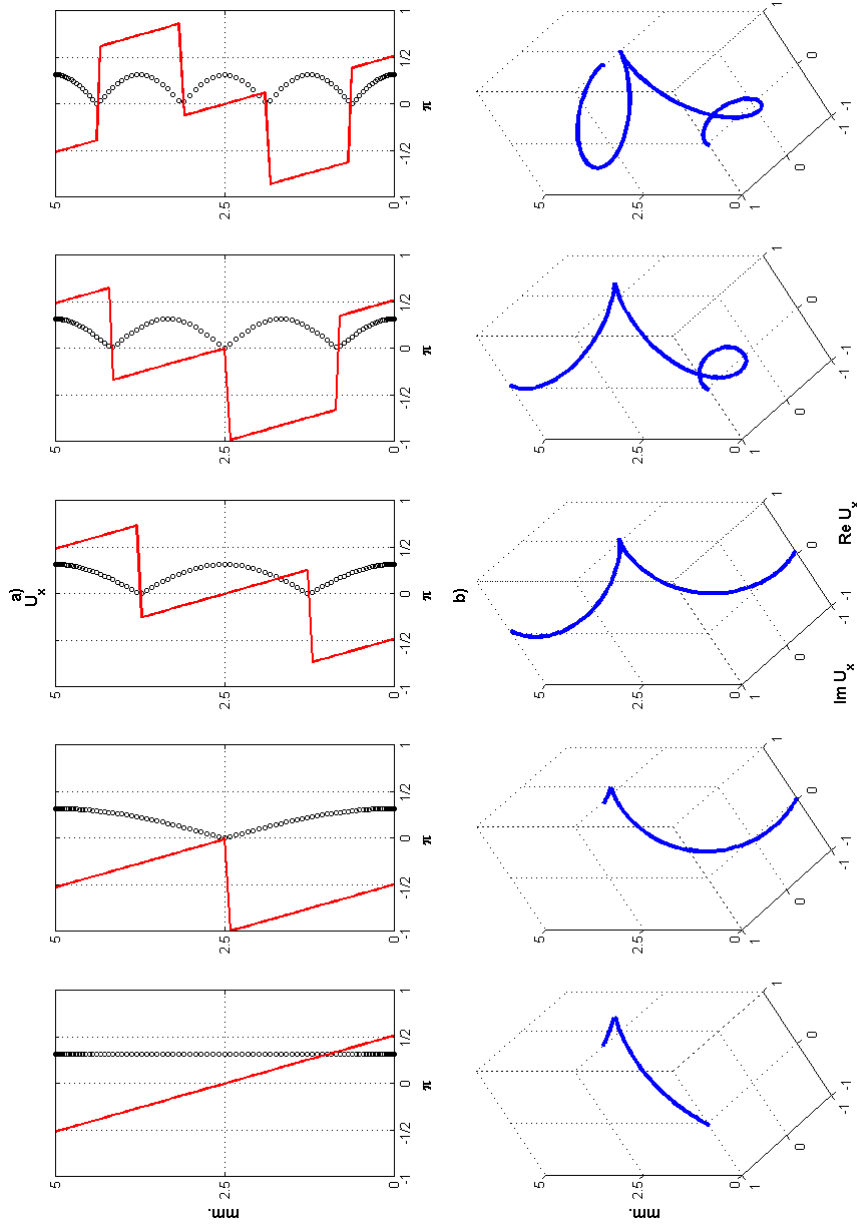
Figure 5.10: Two- and three-dimensional, a) and b) respectively, mode shapes of the first five SH modes for the trigonal 5mm. thick free plate marked with black circles in figure 5.8. In a) the norm of the complex vector field normalized to one is shown in black circles and the phase is shown in solid red lines. In b) the coordinate of the displacement complex vector in complex polar coordinates is shown at each point of the thickness of the plate.

5.10.b respectively. The physical and elastic properties of the material used are given in section 5.4 at the end.

For the Z configuration the Christoffel equation is:

$$
\begin{aligned}
\Gamma_{11} &= \rho\omega^2 - ((\tfrac{c_{11}-c_{12}}{2})k^2 + c_{44}\xi^2) \\
\Gamma_{12} &= -c_{14}k^2 \\
\Gamma_{13} &= -2c_{14}k\xi \\
\Gamma_{22} &= \rho\omega^2 - (c_{44}k^2 + c_{33}\xi^2) \\
\Gamma_{23} &= -(c_{13} + c_{44})k\xi \\
\Gamma_{33} &= \rho\omega^2 - (c_{11}k^2 + c_{44}\xi^2)
\end{aligned}
\tag{5.52}
$$

The elements of the determinant show the following ξ dependence:

$$
\begin{aligned}
\Gamma_{11}\Gamma_{22}\Gamma_{33} &\sim \xi^6, \xi^4, \xi^2, \xi^0 \\
\Gamma_{12}\Gamma_{23}\Gamma_{13} &\sim \xi^2 \\
\Gamma_{23}^2\Gamma_{11} &\sim \xi^4, \xi^2 \\
\Gamma_{13}^2\Gamma_{22} &\sim \xi^4, \xi^2 \\
\Gamma_{12}^2\Gamma_{33} &\sim \xi^2, \xi^0
\end{aligned}
\tag{5.53}
$$

Clearly the Christoffel equation possesses the symmetry: $\xi \leftrightarrow -\xi$. Hence, its six roots will reflect this symmetry and an analogous expression to equation (5.21) holds in this case. The ratios defined in equations (5.11) and (5.12) present the following symmetries:

$$
\begin{aligned}
V_{n+1} &= V_n & n &= 1, 3, 5 \\
W_{n+1} &= -W_n & n &= 1, 3, 5
\end{aligned}
\tag{5.54}
$$

The coefficients in the boundary condition equations (5.13) read now:

$$
\begin{aligned}
D_{xn} &\equiv i\left\{c_{44}\xi_n + c_{14}kW^{(n)}\right\} \\
D_{yn} &\equiv i\left\{c_{33}\xi_n V^{(n)} + c_{13}kW^{(n)}\right\} \\
D_{zn} &\equiv i\left\{c_{14}k + c_{44}kV^{(n)} + c_{44}\xi_n W^{(n)}\right\}
\end{aligned}
\tag{5.55}
$$

which, taking into account the symmetries $\xi \leftrightarrow -\xi$ and equation (5.54), are related as:

$$
\begin{aligned}
D_{xn+1} &= -D_{xn} \\
D_{yn+1} &= -D_{yn} \\
D_{zn+1} &= D_{zn}
\end{aligned}
\tag{5.56}
$$

The determinant from the boundary conditions can be factorized in a completely analogous way to the monoclinic case and yields two 3×3 determinants which constitute the dispersion relations for symmetric and antisymmetric modes.

Finally, the X configuration yields results very similar to the previous configuration, the Christoffel equation is:

$$
\begin{aligned}
\Gamma_{11} &= \rho\omega^2 - (c_{44}k^2 + c_{44}\xi^2) \\
\Gamma_{12} &= -2c_{14}k\xi \\
\Gamma_{13} &= c_{14}k^2 - c_{14}\xi^2 \\
\Gamma_{22} &= \rho\omega^2 - ((\tfrac{c_{11}-c_{12}}{2})k^2 + c_{11}\xi^2) \\
\Gamma_{23} &= -(\tfrac{c_{11}+c_{12}}{2})k\xi \\
\Gamma_{33} &= \rho\omega^2 - (c_{11}k^2 + (\tfrac{c_{11}-c_{12}}{2})\xi^2)
\end{aligned}
\tag{5.57}
$$

As in the previous case the determinant of the Christoffel equation possesses the symmetry: $\xi \leftrightarrow -\xi$. Hence, its six roots will reflect this symmetry and an analogous expression to equation (5.21) will hold in this case too. The ratios defined in equations (5.11) and (5.12) present the following symmetries:

$$
\begin{aligned}
V_{n+1} &= -V_n & n &= 1, 3, 5 \\
W_{n+1} &= W_n & n &= 1, 3, 5
\end{aligned}
\tag{5.58}
$$

The coefficients in the boundary condition equations (5.16) read now:

$$
\begin{aligned}
D_{xn} &\equiv i\left\{ c_{44}\xi_n + c_{14}kV^{(n)} + c_{14}\xi_n W^{(n)} \right\} \\
D_{yn} &\equiv i\left\{ c_{14}k + c_{11}\xi_n V^{(n)} + c_{12}kW^{(n)} \right\} \\
D_{zn} &\equiv i\left\{ c_{14}\xi_n + (\tfrac{c_{11}-c_{12}}{2})kV^{(n)} + (\tfrac{c_{11}-c_{12}}{2})\xi_n W^{(n)} \right\}
\end{aligned}
\tag{5.59}
$$

which, taking into account the symmetries $\xi \leftrightarrow -\xi$ and equation (5.58), are related as:

$$
\begin{aligned}
D_{xn+1} &= -D_{xn} \\
D_{yn+1} &= D_{yn} \\
D_{zn+1} &= -D_{zn}
\end{aligned}
\tag{5.60}
$$

The 6×6 determinant obtained from the boundary conditions can again be factorized into two independent dispersion relations for the symmetric and antisymmetric modes as in the previous configuration.

The study of this crystal class is concluded with the appropriate summary of rotations. As in the previous cases, it is assumed that the original configuration is the default Y configuration. Then one performs any of the rotations of the crystal axes shown below:

$$
\begin{aligned}
\phi_X &\neq m\tfrac{\pi}{2} & m &\in \mathbb{Z} & &\Longrightarrow \text{Monoclinic} \\
\phi_Y &\neq m\tfrac{\pi}{2} & m &\in \mathbb{Z} & &\Longrightarrow \text{Triclinic-like} \\
\phi_Z &= \begin{cases} \neq m\tfrac{\pi}{2}, = m\tfrac{2\pi}{3} & m \in \mathbb{Z} & \Longrightarrow \text{Invariant} \\ \neq m\tfrac{\pi}{2}, \neq m\tfrac{2\pi}{3} & m \in \mathbb{Z} & \Longrightarrow \text{Trigonal*} \end{cases}
\end{aligned}
\tag{5.61}
$$

where *Trigonal** has a similar meaning as before.

5.1.5 Tetragonal Crystals

Crystals belonging to the tetragonal class have a stiffness matrix with at most 7 independent constants like trigonal but present a higher degree of symmetry with a fourth order principal axis which conventionally is taken to be the {Z} axis, [50]. The stiffness matrix has the following form:

$$
\begin{pmatrix}
c_{11} & c_{12} & c_{13} & 0 & 0 & c_{16} \\
 & c_{11} & c_{13} & 0 & 0 & -c_{16} \\
 & & c_{33} & 0 & 0 & 0 \\
 & & & c_{44} & 0 & 0 \\
 & & & & c_{44} & 0 \\
 & & & & & c_{66}
\end{pmatrix}
\tag{5.62}
$$

In the default Y configuration the entries of the Christoffel equation are:

$$
\begin{aligned}
\Gamma_{11} &= \rho\omega^2 - (c_{44}k^2 + c_{66}\xi^2) \\
\Gamma_{12} &= c_{16}\xi^2 \\
\Gamma_{13} &= 0 \\
\Gamma_{22} &= \rho\omega^2 - (c_{44}k^2 + c_{11}\xi^2) \\
\Gamma_{23} &= -(c_{13} + c_{44})k\xi \\
\Gamma_{33} &= \rho\omega^2 - (c_{33}k^2 + c_{44}\xi^2)
\end{aligned}
\tag{5.63}
$$

The determinant of this equation will evidently have the required symmetry $\xi \leftrightarrow -\xi$ required for the splitting of the modes into symmetric and antisymmetric families. Due to the zeroes in the Christoffel equation, the expressions for the ratios (5.11) and (5.12) are simplified to:

$$
V^{(n)} = \frac{-\Gamma_{11}}{\Gamma_{12}}
\tag{5.64}
$$

$$
W^{(n)} = \frac{\Gamma_{11}\Gamma_{23}}{\Gamma_{12}\Gamma_{33}}
\tag{5.65}
$$

for which the following relations hold:

$$
\begin{aligned}
V_{n+1} &= V_n & n &= 1, 3, 5 \\
W_{n+1} &= -W_n & n &= 1, 3, 5
\end{aligned}
\tag{5.66}
$$

The boundary conditions obtained by matrix multiplication as before have the coefficients:

$$
\begin{aligned}
D_{xn} &\equiv i\left\{ c_{66}\xi_n - c_{16}\xi_n V^{(n)} \right\} \\
D_{yn} &\equiv i\left\{ -c_{16}\xi_n + c_{11}\xi_n V^{(n)} + c_{13}kW^{(n)} \right\} \\
D_{zn} &\equiv i\left\{ c_{44}kV^{(n)} + c_{44}\xi_n W^{(n)} \right\}
\end{aligned}
\tag{5.67}
$$

and the symmetry relations amongst them are:

$$D_{xn+1} = -D_{xn}$$
$$D_{yn+1} = -D_{yn}$$
$$D_{zn+1} = D_{zn}$$

(5.68)

The 6×6 determinant formed with the boundary conditions can be factorized into two 3×3 subdeterminants leading to the two dispersion relations for the symmetric and antisymmetric modes as in the monoclinic case.

For the Z configuration matters are similar to the above, the Christoffel equation has entries:

$$\Gamma_{11} = \rho\omega^2 - (c_{66}k^2 + c_{44}\xi^2)$$
$$\Gamma_{12} = 0$$
$$\Gamma_{13} = -c_{16}k^2$$
$$\Gamma_{22} = \rho\omega^2 - (c_{44}k^2 + c_{33}\xi^2)$$
$$\Gamma_{23} = -(c_{13} + c_{44})k\xi$$
$$\Gamma_{33} = \rho\omega^2 - (c_{11}k^2 + c_{44}\xi^2)$$

(5.69)

It is easy to see again that the modes will split in two families, symmetric and antisymmetric. Since the computations follow along the same lines as the previous configuration, only the coefficients of the boundary conditions are given for completion:

$$D_{xn} \equiv i\left\{ c_{44}\xi_n \right\}$$
$$D_{yn} \equiv i\left\{ c_{33}\xi_n V^{(n)} + c_{13}kW^{(n)} \right\}$$
$$D_{zn} \equiv i\left\{ c_{44}kV^{(n)} + c_{44}\xi_n W^{(n)} \right\}$$

(5.70)

This configuration does not suppose much novelty with respect to the previous one in terms of coding. The dispersion curves would of course be different but qualitatively the families of modes that exist are the same.

The most interesting situation is found in the X configuration. The Christoffel equation has the entries:

$$\Gamma_{11} = \rho\omega^2 - (c_{44}k^2 + c_{44}\xi^2)$$
$$\Gamma_{12} = 0$$
$$\Gamma_{13} = 0$$
$$\Gamma_{22} = \rho\omega^2 - (c_{66}k^2 + 2c_{16}k\xi + c_{11}\xi^2)$$
$$\Gamma_{23} = c_{16}k^2 - (c_{12} + c_{66})k\xi - c_{16}\xi^2$$
$$\Gamma_{33} = \rho\omega^2 - (c_{11}k^2 - 2c_{16}k\xi + c_{66}\xi^2)$$

(5.71)

Note that the element Γ_{11} only has terms with even powers of ξ whereas the determinant formed with the 2×2 submatrix has terms with even as

144

well as odd powers of ξ. One still needs to analyse the boundary conditions to see if the problem decouples. Indeed, the stress tensor field components lead to the decoupling of the problem so one may split the problem in two. The stress tensor field expressions in this case are:

$$T_{yx}|_{y=\pm h} = \sum_{n=1}^{2} U_x^{(n)} D_{xn} e^{\pm i\xi_n h}$$
$$T_{yy}|_{y=\pm h} = \sum_{n=1}^{4} U_y^{(n)} D_{yn} e^{\pm i\xi_n h} \qquad (5.72)$$
$$T_{yz}|_{y=\pm h} = \sum_{n=1}^{4} U_y^{(n)} D_{zn} e^{\pm i\xi_n h}$$

with

$$D_{xn} \equiv i\{c_{44}\xi_n\}$$
$$D_{yn} \equiv i\Big\{((c_{16}k + c_{11}\xi_n) + (c_{12}k + c_{16}\xi_n)Q^{(n)}\Big\} \qquad (5.73)$$
$$D_{zn} \equiv i\Big\{(c_{66}k + c_{16}\xi_n) + (-c_{16}k + c_{66}\xi_n)Q^{(n)}\Big\}$$

with the ratio $Q^{(n)}$ defined as in equation (5.36). The component T_{yx} corresponds to the x-polarized modes and from the Γ_{11} element it can be seen that this family will in turn split into symmetric and antisymmetric modes. The other two stress tensor field components in equation (5.50) yield a 4×4 determinant which cannot be factorized due to the presence of odd powers of ξ in the corresponding terms of the Christoffel equation. As a consequence there is only one dispersion relation for these, analogous to the Lamb modes polarized in the sagittal plane without definite parity.

The dispersion curves for this case are shown in figure 5.11. The two sets of SH x-polarized modes are plotted in dashed and solid red lines for the symmetric and antisymmetric families respectively. The "Lamb" modes which have no definite parity are plotted in dash-dotted blue lines. The first six displacement vector profiles of the SH and the first five for the "Lamb" at different frequencies have been plotted and signalled with circles in figure 5.11. For the "Lamb" modes, the two-dimensional plot of the mode shape norm (black circles) and phase (solid red lines) is presented in figure 5.12.a, note that the features of the phase are similar to those found in the triclinic case due to the lack of parity of the solution. The three-dimensional plot for the complex displacement vector field is presented in figure 5.12.b. Similarly for "SH" modes whose two- and three-dimensional plots are presented in figures 5.13.a and 5.13.b respectively, they clearly display the expected symmetry. The physical and elastic properties of the material used are given in section 5.4 at the end.

The usual scheme with the rotations of the crystal axes is given below:

$$\phi_{X,Y} \neq m\frac{\pi}{2} \qquad m \in \mathbb{Z} \quad \Longrightarrow \text{Triclinic-like}$$
$$\phi_Z \neq m\frac{\pi}{2} \qquad m \in \mathbb{Z} \Longrightarrow \text{Tetragonal*} \qquad (5.74)$$

where *Tetragonal** has a similar meaning as before.
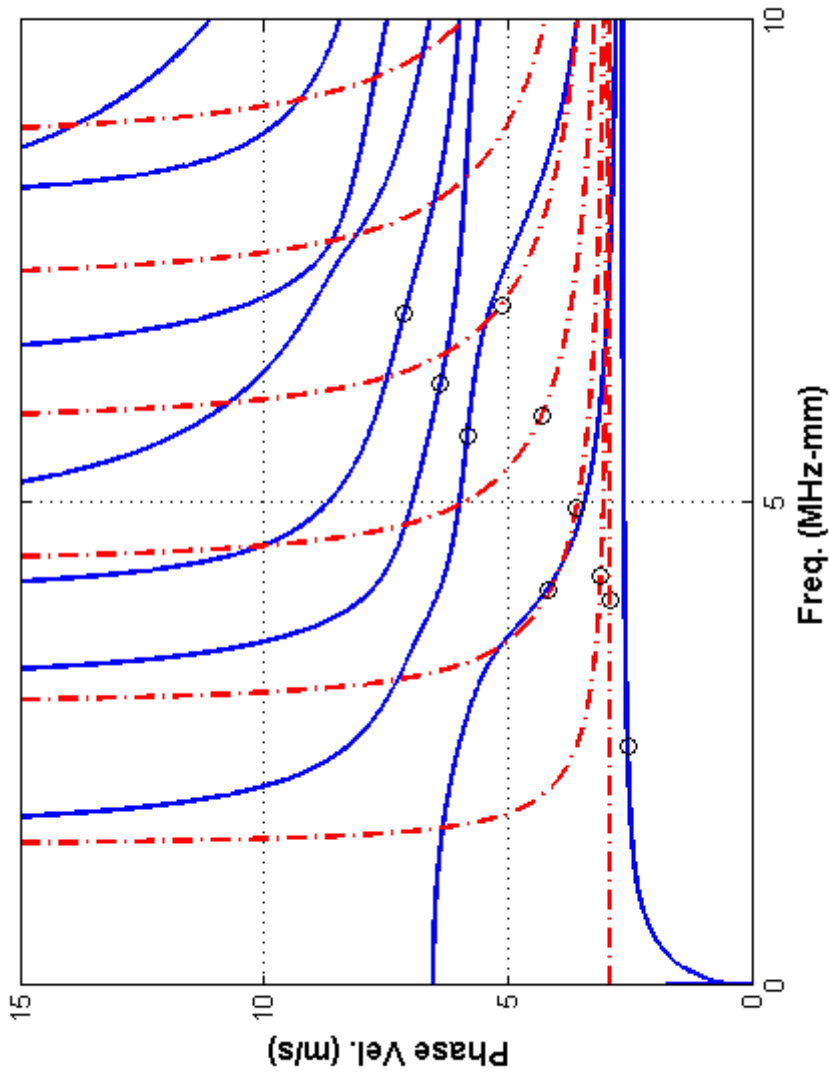
Figure 5.11: Lamb (solid blue line) and SH (red dash-dotted line) modes in a tetragonal 5mm. thick free plate in X configuration with propagation along the {Y} crystal axis. Different PSCM codes were used for each family in order to plot Lamb and SH modes separately. Marked with black circles the first five Lamb and SH modes respectively whose mode shapes are shown in the next two figures 5.12 and 5.13.

146
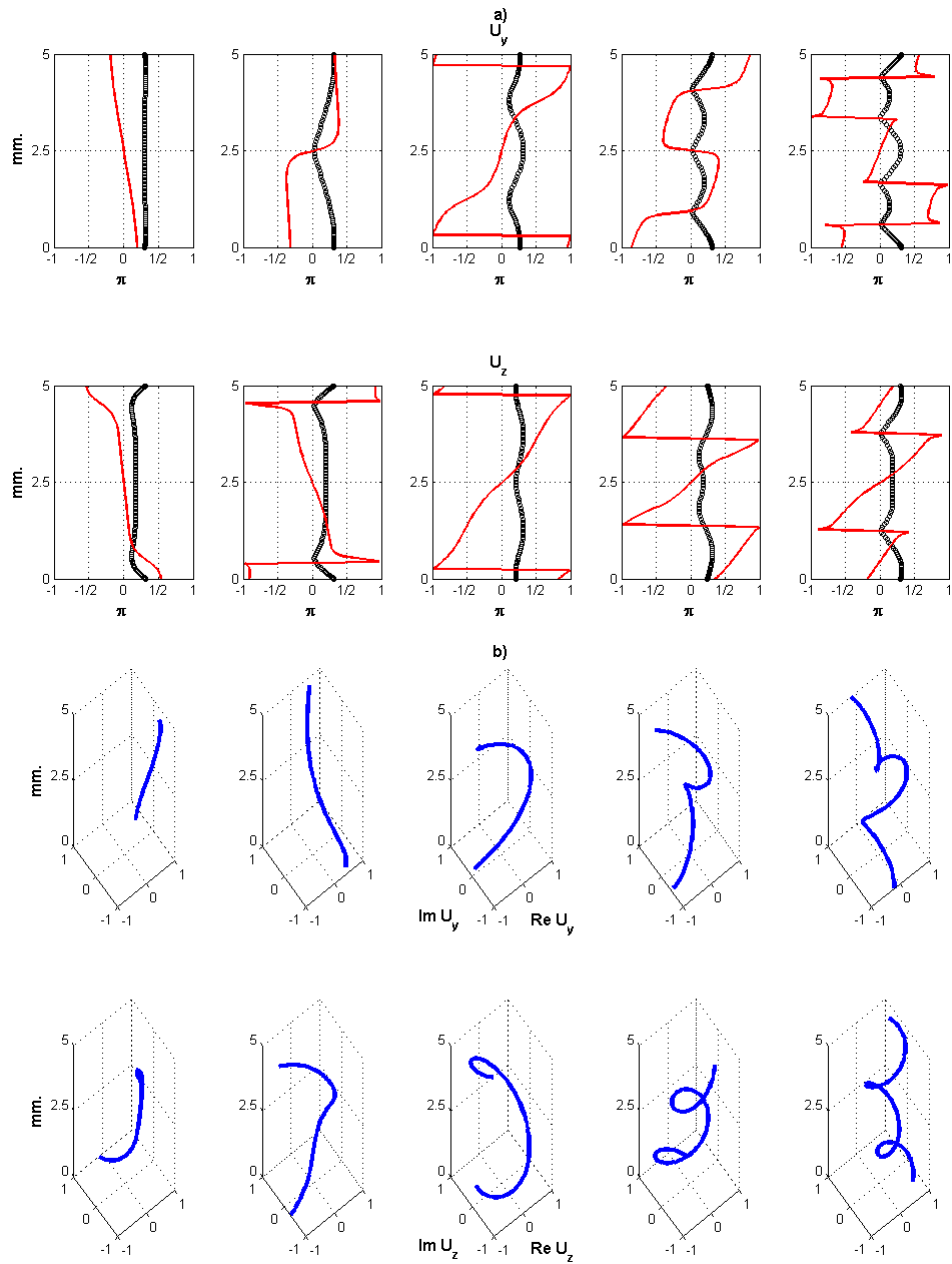
Figure 5.12: Two- and three-dimensional, a) and b) respectively, mode shapes of the first five Lamb modes for the tetragonal 5mm. thick free plate marked with black circles in figure 5.11. In a) the norm of the complex vector field normalized to one is shown in black circles and the phase is shown in solid red lines. In b) the coordinate of the displacement complex vector in complex polar coordinates is shown at each point of the thickness of the plate.

147
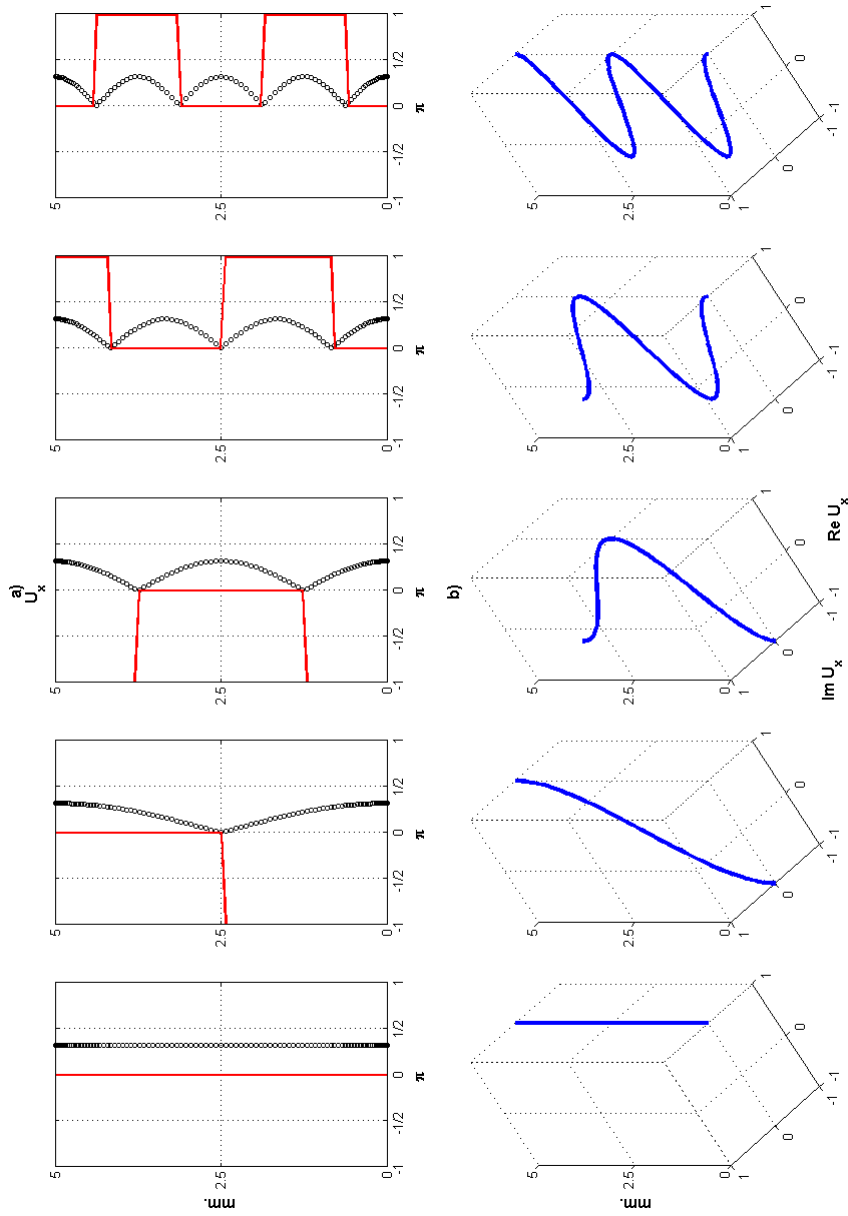
Figure 5.13: Two- and three-dimensional, a) and b) respectively, mode shapes of the first five SH modes for the tetragonal 5mm. thick free plate marked with black circles in figure 5.11. In a) the norm of the complex vector field normalized to one is shown in black circles and the phase is shown in solid red lines. In b) the coordinate of the displacement complex vector in complex polar coordinates is shown at each point of the thickness of the plate. Note that in this particular case, the SH modes are symmetric and antisymmetric even though the Lamb modes are not.

For the tetragonal subclasses $4mm$, 422, $\bar{4}2m$ and $4/mmm$, due to their higher symmetry imposed by dyad axes orthogonal to the principal axis, one has $c_{16} = 0$ when one of these axes is taken along the crystal $\{X\}$ axis, so the stiffness matrix in equation (5.62) is simplified accordingly. In this case, for the default Y configuration the Christoffel equation has the entries:

$$
\begin{aligned}
\Gamma_{11} &= \rho\omega^2 - (c_{44}k^2 + c_{66}\xi^2) \\
\Gamma_{12} &= 0 \\
\Gamma_{13} &= 0 \\
\Gamma_{22} &= \rho\omega^2 - (c_{44}k^2 + c_{11}\xi^2) \\
\Gamma_{23} &= -(c_{13} + c_{44})k\xi \\
\Gamma_{33} &= \rho\omega^2 - (c_{33}k^2 + c_{44}\xi^2)
\end{aligned}
\tag{5.75}
$$

As will be seen shortly, this problem decouples into Lamb and SH modes. Because of the symmetry $\xi \leftrightarrow -\xi$ the modes will be split in symmetric and antisymmetric families. The whole solving procedure follows along the same lines as for the orthorhombic material. The boundary conditions obtained by matrix multiplication have the coefficients:

$$
\begin{aligned}
D_{xn} &\equiv i\left\{c_{66}\xi_n\right\} \\
D_{yn} &\equiv i\left\{c_{11}\xi_n + c_{13}kQ^{(n)}\right\} \\
D_{zn} &\equiv i\left\{c_{44}k + c_{44}\xi_n Q^{(n)}\right\}
\end{aligned}
\tag{5.76}
$$

with $Q^{(n)}$ given by equation (5.36). Following the same steps as for the orthorhombic material one arrives at a 2×2 determinant for SH modes which in turn can be factorized into the product of two factors: one corresponds to the dispersion equation for the symmetric SH modes and the other one to the antisymmetric SH modes. For Lamb modes the 4×4 determinant can be further simplified leading to two 2×2 subdeterminants which yield the dispersion relations for the symmetric and antisymmetric Lamb modes.

The situation for the two remaining Z and X configurations is similar to the above up to a rearrangement of the entries of the stiffness matrix so the details will not be given here.

The usual scheme for rotations is given below:

$$
\begin{aligned}
\phi_{X,Y} &\neq m\tfrac{\pi}{2} & m \in \mathbb{Z} &\implies \text{Monoclinic} \\
\phi_Z &\neq m\tfrac{\pi}{2} & m \in \mathbb{Z} &\implies \text{Tetragonal*}
\end{aligned}
\tag{5.77}
$$

where *Tetragonal** stands for tetragonal crystals which might belong to the same subclass or to the more general classes with non-zero c_{16}.

5.1.6 Hexagonal Crystals

Crystals belonging to the hexagonal class have a stiffness matrix with at most 5 independent constants as a consequence of a sixth order principal axis which conventionally is taken to be the {Z} axis, [50]. The stiffness matrix has the following form:

$$
\begin{pmatrix}
c_{11} & c_{12} & c_{13} & 0 & 0 & 0 \\
 & c_{11} & c_{13} & 0 & 0 & 0 \\
 & & c_{33} & 0 & 0 & 0 \\
 & & & c_{44} & 0 & 0 \\
 & & & & c_{44} & 0 \\
 & & & & & \frac{c_{11}-c_{12}}{2}
\end{pmatrix}
\tag{5.78}
$$

All the equations for each configuration are the same as those for the last subclass of tetragonal crystals but with the value of c_{66} replaced by the one above (equation (5.78)). The computation of the Lamb and SH modes is also the same and will not be pursued here.

The rotation scheme is also similar but presents a characteristic feature of hexagonal materials:

$$
\begin{aligned}
\phi_{X,Y} \neq m\frac{\pi}{2} \quad & m \in \mathbb{Z} \quad \Longrightarrow \text{Monoclinic} \\
\phi_Z = \begin{cases} \neq m\frac{\pi}{2}, \ = m\frac{2\pi}{6} & m \in \mathbb{Z} \Longrightarrow \text{Invariant} \\ \neq m\frac{\pi}{2}, \ \neq m\frac{2\pi}{6} & m \in \mathbb{Z} \Longrightarrow \text{Invariant} \end{cases}
\end{aligned}
\tag{5.79}
$$

This only reflects the well-known and particular feature that hexagonal crystals are transversely isotropic, [50], therefore any rotation about the {Z} axis will leave the crystal invariant.

This class has been extensively studied already and the reader is referred to the literature on the subject, see for instance [5], [7], [32], [13] and [8].

5.1.7 Cubic Crystals

A brief subsection about cubic crystals has been included for completeness. Since this class has been already studied in depth by Solie and Auld in [8] for instance, only a brief comment will be made on the rotation of cubic crystals which also applies to the rest of the classes studied previously.

The rotation scheme for cubic crystals is as follows, some concrete examples can be found in [5]:

$$
\phi_{X,Y,Z} = \begin{cases} \neq m\frac{\pi}{2}, \ = m\frac{\pi}{4} & m \in \mathbb{Z} \Longrightarrow \text{Tetragonal } c_{16} = 0 \\ \neq m\frac{\pi}{2}, \ \neq m\frac{\pi}{4} & m \in \mathbb{Z} \Longrightarrow \text{Tetragonal } c_{16} \neq 0 \end{cases}
\tag{5.80}
$$

It is possible [5] to obtain a stiffness matrix like that of a trigonal $c_{15} = 0$ material from cubic by means of two appropriate rotations, the first takes the stiffness matrix of the cubic crystal to one of tetragonal $c_{16} = 0$ symmetry and then to trigonal $c_{15} = 0$. However, it must be noted that if the latter transformation was performed on a tetragonal $c_{16} = 0$ crystal the result would *not be* trigonal $c_{15} = 0$ but monoclinic as stated in (5.77). This apparent contradiction is explained by noticing that one is merely performing axes transformations but not actually changing the intrinsic properties of the crystals. Even though a cubic crystal's stiffness matrix might *look like* a tetragonal $c_{16} = 0$ in certain coordinates configuration, cubic crystals possess a higher degree of symmetry. The fact that, beginning from two tetragonal $c_{16} = 0$ stiffness matrices, after performing the same transformation different stiffness matrices are obtained (one with a higher degree of symmetry than the other) is a reflection of the fact that the original crystals had different degrees of symmetry: one was indeed genuinely tetragonal $c_{16} = 0$ but the other was a cubic crystal which had undergone a previous rotation.

A similar example is provided by orthorhombic crystals whose stiffness matrix takes the form of a monoclinic crystal upon rotation. However, this transformation can be reversed and the original orthorhombic crystal recovered. If the original crystal was monoclinic, any rotation about the principal axis will produce a different monoclinic crystal, never an orthorhombic, since orthorhombic crystals have 9 independent constants whereas monoclinic have 13 and this intrinsic property of the material does not change when one changes the, otherwise arbitrary, coordinate basis.

From the above discussion and by looking at the rotation schemes for each crystal class that was presented it can be concluded that it is possible to *move* from a given crystal class to another with a lower degree of symmetry but not conversely.

5.2 Anisotropic Crystals in Cylindrical Geometry

In this section the symmetry and coupling properties of solutions for guided waves in single layers with cylindrical geometry will be presented. The study is significantly simpler than in the previous case and the conclusions will be illustrated by simple but general examples. Again, the goal is to gather as much information from the equations of motion and boundary conditions as possible without explicitly solving them.

In order to study axial propagation in cylindrical geometry axes configurations are defined in a similar way to those in cartesian coordinates shown in table 5.1. In cylindrical geometry two sets of axes are again used: spatial axes $\{r, \theta, z\}$ fixed to the cylinder and crystal axes $\{R, \Theta, Z\}$ which are free to rotate with respect to the spatial axes. As before, in the *default* configuration the crystal axes are aligned with the spatial axes. Axes configurations in cylindrical geometry are summarized in table 5.2:

Crystal Configuration Label	Axis Normal to the Cylinder	Propagation Axis
Default R configuration	$\{R\}$	$\{Z\}$
Θ configuration	$\{\Theta\}$	$\{R\}$
Z configuration	$\{Z\}$	$\{\Theta\}$

Table 5.2: Table with the three different crystal axes configuration in cylindrical geometry. In the default R configuration crystal and fixed spatial (plate) axes $\{r, \theta, z\}$ are aligned.

The stress free conditions at the upper and lower boundaries in the spatial axes configuration chosen are expressed by the following set of six equations:

$$T_{rr}|_{r_{inner},r_{outer}} = T_{r\theta}|_{r_{inner},r_{outer}} = T_{rz}|_{r_{inner},r_{outer}} = 0 \qquad (5.81)$$

The investigation will be restricted to waves propagating along the axis of the cylinder, the cases of circumferential propagation can be studied in an entirely analogous way. For axial propagation in cylindrical geometry the only mode symmetry which is possible is of axial type: thus, modes will be axially symmetric, with *harmonic order* n equal to zero, or will have n different from zero and therefore no axial symmetry. In addition and regardless of the value of n, in certain configurations and for some crystals classes decoupling of modes will occur leading to the well-known Torsional and Longitudinal modes, analogues of the SH and Lamb modes in flat geometry. Again, the goal is to know how many independent families of modes exist for a given configuration by studying the structure of the equations of motion and boundary conditions of the case at hand.

For brevity only the steps to study these problems will be given and a summary of the results for the different crystal classes. With the aid of any software which allows for symbolic manipulations it is straightforward to verify the results presented here.

These steps are as follows:

1. Choose crystal class, configuration of crystal axes and *harmonic order n*.

2. Determine from the equations of motion *and* boundary conditions whether the problem presents decoupling or not. For instance, see Auld [5] for expression of these equations in cylindrical coordinates.

3. Identify independent families of modes:

   - If equations decouple in oblique (longitudinal) motion involving only the u_r and u_z components and tangential (in-plane) modes involving only u_θ component, the problem will be split in two simpler subproblems. These two problems can be studied separately and independently. There will be one non-factorable dispersion relation for each family of modes and therefore, since they are independent of each other, crossings can take place amongst modes of these different families.

   - If equations do not yield a decoupled problem, one will only have one dispersion relation which cannot be further factorized into a simpler product and hence, only one family of modes amongst which crossings do not occur.

Modes with different *harmonic order n* can always cross amongst themselves for a fixed crystal and axes configuration since n acts as a parameter thus yielding an independent solution for each value of n.

For cylindrical coordinates the stiffness matrices of the different materials present the same structure as in the cartesian case but it must be noted that now the indices refer to different axes and relate stresses and strains in cylindrical coordinates. More details about the corresponding index conventions in cylindrical geometry can be found in [5].

The expression of the stiffness matrix referred to the spatial axes also changes when rotations of the crystal axes are performed, these changes are the same as those given for the cartesian coordinates in section 5.1 but care must be taken when establishing the correspondence between cartesian and cylindrical configurations. This is straightforward if one uses the reduced and more abstract index notation. An example will clarify this. In reduced index notation the stiffness matrix of an orthorhombic crystal, in cylindrical *and* cartesian coordinates, is given by (5.44). When the coordinate axes are rotated, the elements of the rotation matrix **R** will be used to form the Bond transformation [5]. In the bond transformation, no reference is made to which system, cartesian or cylindrical is being rotated. Therefore given a certain **R**, the transformed stiffness matrix will be the same for that Bond

transformation generated by **R** regardless of the reference system. A rotation about the {R} axis in cylindrical coordinates will generate the same bond transformation, and hence the same transformed stiffness matrix, as a rotation about the {X} in cartesian coordinates. As a consequence of this, the stiffness matrix obtained after the rotation will have the same structure in both systems.

For instance, in cylindrical coordinates, if the original matrix is of an orthorhombic material as in (5.44), after rotating the coordinate axes about the {R} axis, the natural question arises: what will the transformed stiffness matrix look like? This is readily answered by applying the above considerations to this case: the resulting stiffness matrix will have the same structure as the stiffness matrix obtained from (5.44) by an equal rotation about the {X} axis. This resulting stiffness matrix, referred to cylindrical coordinates, has precisely the same structure as that of a monoclinic material in the {X} configuration given in equation (5.34).

In conclusion, when one has a certain crystal in cylindrical geometry and wants to determine, after a rotation, which will be the transformed stiffness matrix all that is needed is to determine which rotation in cartesian coordinates is generated by the same rotation matrix **R** and, with the aid of the rotation schemes presented in section II, find which will be the resulting stiffness matrix in each case. The resulting stiffness matrix in cylindrical coordinates will have the same structure as in cartesian, but their difference in physical meaning must always be observed.

To close this section, the results for cylindrical geometry will be presented in table 5.3. Since crossings can always occur amongst modes of families with different values of n, the only problematic situation is to examine modes with fixed n. Therefore, for each crystal class, and each configuration given in table 5.2 the harmonic order(s) n for which the problem decouples will be given (if any). As explained in step number 3 above, crossings amongst modes can occur in these cases since two independent dispersion relations exist.

Examples of isotropic and some simple anisotropic cylindrical systems can be found in the literature [5], [31]. Cases of particular relevance to this study dealing with general anisotropic media such as triclinic can be found in [46], [63] and [74].

154

Configuration / Crystal Class	R	Θ	Z
Isotropic	$n{=}0$	$n{=}0$	$n{=}0$
Cubic	$n{=}0$	$n{=}0$	$n{=}0$
Hexagonal	$n{=}0$	$n{=}0$	$n{=}0$
Tetragonal $c_{16} = 0$	$n{=}0$	$n{=}0$	$n{=}0$
Tetragonal $c_{16} \neq 0$	X	$n{=}0$	X
Trigonal $c_{15} = 0$	X	X	$n{=}0$
Trigonal $c_{15} \neq 0$	X	X	X
Othorhombic	$n{=}0$	$n{=}0$	$n{=}0$
Monoclinic	X	$n{=}0$	X
Triclinic	X	X	X

Table 5.3: Table with the harmonic order n for which each crystal and configuration decouples. "X" means that the problem is coupled for all values of n. The different configurations are shown in table 5.2. The stiffness matrices in cylindrical coordinates in R, Θ and Z configurations have the same formal structure as the corresponding stiffness matrices in cartesian coordinates in Y, Z and X configurations respectively.

5.3   Discussion of Chapter 5

Properties of independent families and symmetries of guided waves in a flat or cylindrical layer of all classes of anisotropic materials have been studied in this chapter. The approach used has been partly analytical in order to investigate mathematical properties of the solutions and thus gain deeper insight into the physics of each problem and how to classify the modes better in each case. No attempt has been made to find particular solutions for each of the cases studied since a great deal of the most valuable and general information about a given problem can be derived without having the explicit solution. For illustrative purposes and to support the conclusions from the analysis a PSCM scheme has been used to provide numerical examples of selected cases which, to the best of the author's knowledge, have not been addressed in detail or not at all in the literature. The validation of this numerical approach can be found in [21], [46] and [63].

One of the contributions of this chapter is the knowledge that has been gained about the properties of guided wave solutions in several anisotropic crystal classes and configurations which had not been studied until now. Other cases which were studied before have been briefly addressed for completeness and appropriate remarks were made where needed. The intention of this chapter is to provide a comprehensive and complete study of guided waves in anisotropic crystals in planar and cylindrical geometries. Crystal

classes studied with particular detail comprise triclinic, monoclinic, trigonal and tetragonal in various axis configurations. These have displayed interesting combinations of decouplings and symmetries such as the one found in the tetragonal crystals in $\{X\}$ configuration where SH modes present symmetry but Lamb modes do not. Crystals in cylindrical geometry are investigated in section 5.4 but due to the simpler treatment of this geometry the details have been omitted and the results are given in table 5.3. Examples for cylindrical geometry with generally anisotropic media can be found in previous studies such as [46] and [63].

An interesting finding is that for certain crystals and configurations, such as triclinic or monoclinic in $\{\ X\ \}$ configuration anisotropy introduces a $\{y\}$ coordinate dependence in the phase of the complex displacement vector field. This results in the solution not displaying any symmetry and in the mode shape changing its profile as the wave travels through the plate due to the difference in phase of the different points through the thickness of the plate. This study should also clarify under which circumstances crossings amongst modes do actually occur, this topic has been a recurrent point of discussion in the literature, see [26], [27] [28], [18] and more recently using a PSCM scheme in [74].

From a more practical point of view, it is hoped that the conclusions and properties presented in this study will help towards a more efficient and robust implementation of numerical methods for solving elastic guided wave problems. No matter the approach, whether PSCM, root-finding or other, solving algorithms find pairs (k, ω); that is, points in the corresponding (k, ω)-space. The question that naturally arises is how to trace the dispersion curve corresponding to a given mode through this collection of points. For root-finding routines, interpolation algorithms (see [14] for instance) have been extensively used but difficult cases pose a great challenge for them, spectral methods present the same challenge as well. In this chapter, it has been shown that by simply studying the properties of the equations of motion and boundary conditions of each problem, one can derive the mathematical properties of the solutions before any numerical computation is done. By exploiting them, specific codes can use the symmetry conditions (if any) in order to plot *separately* the independent families of modes and avoid the complications inherent to conventional interpolating and tracing routines.

Here it is important to note that for perfectly elastic materials, strictly speaking, having one dispersion relation which cannot be further factorized, thus yielding a family of independent non-crossing modes, does not imply in general that the dispersion curves do not intersect amongst themselves when one takes into account the full three-dimensional spectrum of the problem.

156

This is only true if one considers only the customary two-dimensional plots of $(\text{Re}[k], \omega)$. An example of this is the well-known plot for symmetric Lamb modes first provided by Mindlin [1] and also discussed in the second volume of the book by Auld [5]. The *cut-off* points are those which might seem problematic at first sight, these points are well-defined: a cut-off point is a point in the (k, ω) space (with k complex) where the wavenumber k changes from being purely real to purely imaginary or complex. At these points two different modes will cross, one right-going and the other left-going. These modes can always be distinguished from each other by resorting to physical arguments and considering the direction of energy transportation or decay of the wave as described for instance in Auld [5], also discussed in [29] and more recently in [74]. This gives rise to the *backward propagating modes* with negative group velocity. A detailed discussion of this has been carried out elsewhere and the reader is referred to the literature just mentioned.

It is worth remembering that this situation only takes place in perfectly elastic materials, when attenuation is considered no cut-off points exist since all the dispersion curves' branches are complex. Hence, in these cases, the modes are all well separated in three-dimensional (k, ω)-space, [29] and [74]. Thus, in both elastic and viscoelastic cases, the collection of points obtained from the numerical computations can always be classified and the dispersion curves traced by simply joining these points without the need of any further tracing algorithm or interpolation routine. The case of three-dimensional dispersion curves for elastic materials is slightly more elaborated if one wants to distinguish the modes crossing at the cut-off points as explained above. However, visual inspection and sign of group velocity (slope) consideration suffices to tell one mode from another.

Finally, the considerations made here about the dispersion determinant obtained from the boundary conditions and its non-reducibility carry over to more general cases of multilayer systems. The study of arbitrary multilayer systems will be pursued elsewhere.

5.4   Numerical data for examples of Chapter 5

The physical and geometrical information used for the figures presented in the main text are given here. The number of grid points N varies from one example to another, but it is always at least double the number of modes plotted in the figure in order to keep good accuracy of the results. On a practical level N is chosen to achieve the shortest computation time, that is, if one is interested in the first 10 modes, running a code with $N = 100$ is unnecessary; a value of N between 25 and 30 has consistently been shown to be sufficient.

The parameters for the plate of figures 5.1:

$$\rho = 8938.4 \text{ kg/m}^3 ; \qquad h = 50 \text{ mm} \tag{5.82}$$

h stands for the thickness of the plate. The elastic stiffness matrix is given in GPa:

$$c = \begin{pmatrix} 235.54 & 88.64 & 88.78 & 19.05 & -2.97 & -6.54 \\ & 215.85 & 108.43 & -14.14 & 2.35 & 22.16 \\ & & 215.77 & -4.90 & 0.61 & -15.57 \\ & & & 58.24 & -17.68 & -7.02 \\ & & & & 39.69 & 11.66 \\ & & & & & 44.02 \end{pmatrix} \tag{5.83}$$

The parameters for the monoclinic plate of figures 5.2, 5.3, 5.4, 5.5, 5.6 and 5.7 are as follows:

$$\rho = 8938.4 \text{ kg/m}^3 ; \qquad h = 5 \text{ mm} \tag{5.84}$$

h stands for the thickness of the plate. The elastic stiffness matrix is given in GPa:

$$c = \begin{pmatrix} 201.1 & 89.3 & 122.6 & & & -20.3 \\ & 208.3 & 115.4 & & & 14.1 \\ & & 174.9 & & & 6.2 \\ & & & 63.1 & 16.7 & \\ & & & & 82.4 & \\ & & & & & 37.8 \end{pmatrix} \tag{5.85}$$

Note that the above matrix has been rotated appropriately in order to study the X configuration presented in figures 5.5, 5.6 and 5.7.

The parameters for the trigonal (tellurium) plate of figures 5.8, 5.9 and 5.10 are as follows:

$$\rho = 6250 \text{ kg/m}^3 ; \qquad h = 5 \text{ mm} \tag{5.86}$$

The elastic stiffness matrix is given in GPa:

$$c = \begin{pmatrix} 32.7 & 8.6 & 24.9 & 12.4 & & \\ & 32.7 & 24.9 & -12.4 & & \\ & & 72.2 & & & \\ & & & 31.2 & & \\ & & & & 31.2 & 12.4 \\ & & & & & \frac{c_{(}11)-c_{12}}{2} \end{pmatrix} \tag{5.87}$$

158

The parameters for the tetragonal plate in X configuration of figures 5.11, 5.12 and 5.13 are as follows:

$$\rho = 3420 \text{ kg/m}^3 \; ; \qquad h = 5 \text{ mm} \tag{5.88}$$

h stands for the thickness of the plate. The elastic stiffness matrix is given in GPa:

$$c = \begin{pmatrix} 169.10 & 122.2 & 122.2 & & & \\ & 208.08 & 83.22 & 22.50 & & \\ & & 208.08 & -22.504 & & \\ & & & 36.44 & & \\ & & & & 75.42 & \\ & & & & & 75.42 \end{pmatrix} \tag{5.89}$$

Chapter 6

Symmetry and Coupling of Guided Wave Solutions in Generally Anisotropic Flat and Cylindrical Multi-layer Systems.

In the previous chapter a study of the properties of guided waves in a single layer, which may be flat or cylindrical, composed of anisotropic material of any possible class of symmetry was presented. The study focused on the properties of symmetry and the parity of the families of guided waves, identifying when independent families of modes may exist under different circumstances of crystal symmetry and orientation. The purpose of this chapter is to extend that work to address flat and cylindrical waveguides composed of multiple layers.

Multilayered systems have been studied in the literature and various algorithms exist to compute explicit dispersion curves, see Nayfeh [10] and [11] and Lowe [14] for instance. In these papers the Transfer Matrix Method is used to study SH waves in multi-layered anisotropic media [10] and subsequently more general elastic waves in multi-layered anisotropic systems where special emphasis is laid on the mathematical properties of the transfer matrix and a variety of examples is also presented.

In a later paper, Lowe [14] provides a thorough review and description of the matrix techniques and their development available to that date for solving guided wave problems. Primarily two methods are presented and described to tackle guided wave problems in both single and multilayer systems: the transfer matrix and the global matrix method, both of which are still being

used successfully [16].

Some other articles, studying different aspects of the multiple layer problem in flat geometry are [80], [81] and [82] for flat geometry. More recently Karpfinger *et. al* [83] and Vasudeva *et. al* [35] studied some problems of wave propagation in multiple layer anisotropic cylindrical structures. Some books on the topic of elastic waves also treat the problem of wave propagation in multiple layer systems such as [31].

In this chapter, the Spectral Collocation Method (PSCM for short, [45]) approach is deployed to compute the solutions and provide numerical examples and illustration of the investigations carried out. This method has been validated in the previous chapters and in [21], [46] and [63].

The present study focuses on multiple layer structures composed of arbitrarily anisotropic materials in planar and cylindrical geometry. In flat geometry the results are presented for two- and three-layered systems. It is explained how the conclusions from these examples hold and are generalized to the case of an arbitrary number of layers. Although the proofs and examples presented involve three- and five-layer systems in order to keep the length of the chapter within reasonable limits, their reasoning carries over to systems of an arbitrary number of layers. The proof for an arbitrary number of layers proceeds along the very same lines as that for a smaller number of layers presented in section 6.1.3, thus a detailed presentation of this would not throw much new light into the problem other than cumbersome notation. As in the single layer case, the study of cylindrical structures is much simpler.

The main contribution of the investigation presented in this chapter is the derivation of the coupling and parity properties of the guided wave solutions for generally anisotropic multiple layer systems in flat and cylindrical geometries. These properties depend on the arrangement of the different layers within the system as well as on their individual properties and axis orientation. It is worth emphasizing that the results hold for elastic as well as viscoelastic materials since no other assumption except for homogeneity within each layer is made on the stiffness matrix elements and the partial wave approach is equally valid for deriving the corresponding dispersion relations in both cases.

The results of this investigation can be exploited, as the examples show, in order to obtain more efficient algorithms and determine whether modes cross or not for a given multi-layered system. These results should also help to reduce or eliminate the problem of mode jumping occurring when the tracing algorithm links the points belonging to one mode to those belonging to a different nearby mode. Regardless of the computing algorithm chosen,

researchers will be able to take advantage of the methodology of this chapter to interpret even the most complicated dispersion curves that arise in multi-layered systems.

6.1 Multiple layer systems of anisotropic crystals in flat geometry

In this section, a systematic treatment of guided waves in flat multilayer systems composed of anisotropic layers of arbitrary crystal symmetry and orientation is presented.

Nayfeh [10] studied multi-layered anisotropic media by means of the transfer matrix method and gave an account of the properties of the determinant for an arbitrary system composed of n layers as well as some illustrative examples. The approach taken in the present chapter differs from that of [10] in the sense that the transfer matrix method is not used at all and attention is focused in providing insight about the nature of the solutions rather than in obtaining explicit dispersion relation for particular cases. The goal is to provide a systematic classification of multilayer systems according to the coupling and parity properties of their guided wave solutions. The dispersion curves shown for certain configurations are computed with a PSCM. The examples help illustrate the study and conclusions drawn from the analysis. It must be remembered, that the PSCM is solely used for computation purposes; whereas the partial wave approach is used to discuss the nature of the problems and the properties of the displacement fields.

The first step in the study of multilayer systems is to group and classify the single plate crystal configurations studied in the previous section into different categories according to the symmetry and (de)coupling of their solutions. The aim is to group the various combinations of crystals and their configurations into as few as possible *general types* and then proceed to study the properties of guided wave solutions in the different combinations of these fewer *general types*.

6.1.1 Classification of single plate configurations

By restricting the attention to the similarities between the solutions' symmetry and coupling properties of each material and configuration for single plates studied before, it is possible to group all of them into fewer families. This will facilitate the task of studying the solutions' properties in the different possible combinations that may arise in the case of multiple layer

systems. This is achieved by focusing on what the solutions for materials of different symmetry class can have in common. For instance, Triclinic and Trigonal materials, in any configuration, have in common that their solutions are coupled and have no definite parity; based on this common behaviour in parity and coupling they are grouped together.

Thus the following 5 families given below are proposed. The materials and configurations they comprise are given along with the solutions parity and coupling properties.

- T_C: Triclinic and Trigonal ($c_{15} \neq 0$) in any axes configuration. Solutions are coupled with no definite parity.

- M_D: Trigonal ($c_{15} = 0$) in Y configuration. Monoclinic in X configuration. Solutions are decoupled in Lamb and SH modes with no definite parity.

- $M_C^{S/A}$: Trigonal ($c_{15} = 0$) in X,Z configurations. Monoclinic and Tetragonal ($c_{16} \neq 0$) in Z,Y configurations. Solutions are coupled with definite parity: symmetric and antisymmetric modes.

- Tet_D^*: Tetragonal ($c_{16} \neq 0$) in X configuration. Solutions decouple into Lamb and SH modes. Lamb modes have no definite parity. SH modes are split into symmetric and antisymmetric modes.

- $O_D^{S/A}$: Orthorhombic, Tetragonal ($c_{16} = 0$), Hexagonal, Cubic and Isotropic crystals in any configuration. Solutions decouple into Lamb and SH modes each of which has a definite parity thus splitting into symmetric and antisymmetric modes. Giving a total of four independent sets of solutions.

Note that a material made of a crystal in a certain configuration belonging to one of these categories can, after a rotation or change of configuration fall into a different category. For instance, consider a monoclinic crystal in default Y configuration (with {Y} orthogonal to the plane of the plate and propagation along the {Z} axes, for a description of the three configurations used, see the previous chapter) which belongs to $M_C^{S/A}$. From the scheme presented in section 5.1.2 of the previous chapter for rotations in Monoclinic crystals it can be seen that, if a rotation is performed about any axis orthogonal to the principal {Z} axis, the new stiffness matrix will be like that of a Triclinic material. As a consequence, the modes are coupled and with no symmetry. Therefore, according to the properties of the solution, this new configuration will belong to T_C even if the original configuration was a monoclinic material in a configuration belonging to $M_C^{S/A}$.

6.1.2 Systems with even number of layers

In general, for a system of an even number n of layers, one has the following two possibilities considering the possible symmetry of the array with respect to the middle plane of the system (geometrical plane which is equidistant from both boundaries, but note that in certain cases, this plane does not necessarily coincide with any interface between the different layers)

$$n = 2m \qquad m \in \mathbb{N} \begin{cases} Symmetric \Longrightarrow \text{Always reduces to a } 2m - 1 \text{ system} \\ Non - symmetric \Longrightarrow \text{Cannot be reduced} \end{cases}$$

(6.1)

In symmetric systems the two middle layers are made of the same material and therefore can be regarded as a single layer of double thickness so the above reduction follows immediately. Note that, in order to consider a system as "symmetric", the thicknesses of the different layers must be the same on both sides of the middle plane of it. This means that a system such as $A_t/B_t/B_b/A_b$, where t stands for top and b stands for bottom, where layers A_t and A_b have different thicknesses, would not be symmetric even though its crystal sequence $A/B/A$ is.

The simplest case to begin with is that of a system composed by two layers. It will also be seen that this is actually the only case one needs to consider for now since systems with higher even numbers of layers can be appropriately reduced as explained above.

Symmetric bilayer systems are trivial, they are equivalent to a single layer system of double thickness and the reader is referred to the previous chapter for details on single plate systems. Adding layers to both sides preserving the symmetry of the system leads invariably to systems with odd numbers of layers which will be studied in the next subsection.

Any non-symmetric system, whether with two or more layers is easily dealt with. Assuming that the problem does not decouple, once the boundary and interface continuity conditions for stresses and displacements have been imposed and the corresponding coefficients' determinant set to zero, it is not possible to simplify and factorize the determinant in a product of smaller non-reducible determinants due to the lack of symmetry. This will become more apparent in a simple analytical derivation that will be given later. The result for this case also agrees with the intuitive notion that a system with no symmetry will not have symmetric solutions.

If the problem is decoupled into SH and Lamb modes, the above results hold separately for both solutions which can be studied independently. It must be remembered that, in these cases where decoupling occurs, crossings

will be allowed amongst SH and Lamb modes regardless of whether each separate family has symmetry or not.

Strictly speaking, a four-layer non symmetric system with the two middle layers of the same material is reduced to an equivalent three-layer system, which might or might not be symmetric depending on the combination of thicknesses. This and similar configurations will be regarded as odd-n multilayer systems from the very beginning and will be the subject of investigation in what follows.

It turns out that the above classification for single layer systems can also be used for multilayer systems if attention is restricted to the parity (symmetry) and coupling properties of the global solutions. To illustrate this, consider a bilayer system composed of two different layers. This automatically rules out any category whose solutions might present any symmetry, thus one is only left with the two possibilities: T_C and M_D. Now, the global system will only decouple if *both* layers present decoupling when considered individually. If this is the case, the bilayer system will belong to M_D (one will actually have two simpler problems for SH and Lamb modes each in a bilayer system). If any of the layers fails to present decoupling the global solution will be coupled and hence belong to T_C. This analysis can be repeated inductively for any number of layers and it is very useful when one wants to have an idea of what to expect from a particular multilayer problem and the solution of the individual layer is known. This procedure is also the pillar upon which the generalization to systems of an arbitrary number of layers is built.

Systems with an even number of layers present no further difficulties; the cases of greater interest will arise in multilayer systems with an odd number of layers to be studied next.

6.1.3   Systems with odd number of layers

For a system of an odd number of n layers, one has the following two possibilities considering the possible symmetry of the array of layers with respect to the middle plane of the array:

$$n = 2m + 1 \qquad m \in \mathbb{N} \begin{cases} Nonsymmetric\ (N) \\ Symmetric\ (S) \end{cases} \qquad (6.2)$$

It is easier to proceed first with the N systems. As in the even-n multilayer case, these systems will have solutions with no symmetry with respect to the middle plane of the plate. It should be emphasized that non-symmetric

arrays can be achieved not only by choosing all layers from different materials but also by choosing different thicknesses for layers of the same material. As a consequence, and assuming a coupled system, the boundary and interface continuity conditions will yield a non-reducible determinant for the amplitudes of the displacement vector field which will be the only dispersion relation for the global system. Therefore, no crossings will take place amongst the modes. These systems belong to the T_C category.

Should a non-symmetric system present decoupling, one would obtain a determinant for each family of SH and Lamb modes respectively but the modes would present no symmetry. Again, having two independent dispersion relations derived from the two corresponding non-reducible determinants, SH and Lamb modes will cross. These systems belong to the M_D category.

For symmetric systems, conclusions cannot be drawn so straightforwardly. One of the motivations for this investigation is the question of whether a system which is symmetric will have symmetric solutions or not even if some of its layers have non-symmetric solutions individually. For example, consider a simple system such as $T_C/O_D^{S/A}/T_C$ which could be just a typical orthorhombic, or even isotropic, layer sandwiched between two equal triclinic layers. One can anticipate that the global solution will not be decoupled due to the coupling effect of the triclinic layers. Whether or not the solution will present symmetry as it could be expected from a symmetric arrangement of layers is not so clear. On the one hand, one could argue that due to the presence of the coupling triclinic layers, their lack of symmetry *spreads* throughout the whole system thus rendering the global solution lacking in symmetry too. On the other hand, one could expect the global symmetry of the system (B/A/B) to be somehow reflected in the global solution. In other words, do global symmetries of a system prevail over local ones?

In what follows an answer to this question will be provided and generalized to systems with an arbitrary number of layers. Due to the infinite number of possibilities, where possible, counterexamples will be given to rule out certain combinations and narrow the path towards a final solution. It will be seen that this rules out all possible combinations but one. For this case, a formal proof will be given for SH modes in a five-layer system and, for brevity, it will be explained how this proof is generalized to the case of n layers. As the analysis of single plate systems given in the previous chapter has shown, it is enough to do this derivation for SH modes. More general derivations for Lamb and coupled modes follow exactly along the same lines but the size of the matrix increases enormously and nothing new would be gained by presenting this.

From now on, attention will be focused on systems composed of three layers: B/A/B, where A and B denote the layer type, for instance T_C. All the layers are assumed to have the same thickness since otherwise the system would not be symmetric. The results are summarized in table 6.1 at the end of the study.

The analysis of a given configuration will proceed in two steps. Firstly, one analyses whether the global system decouples or not. This involves checking that the equations of motion as well as the boundary and interface continuity conditions yield two decoupled sets of PDEs. If any of these sets of equations fails to be decoupled, be it the equations or motion or any of the boundary or interface conditions, the global problem will be coupled.

In general, it is fairly easy to know whether the global system decouples or not. Provided the equations of motion of *each* layer of the system and boundary conditions decouple, the only interface continuity conditions which can couple different displacement field's components are those for the stress tensor components. If these are decoupled for *each* individual layer, the interface conditions for the global system will also be decoupled and the global problem can be split into two independent smaller ones. This is analogous to what happened in single plate systems and can be summarized as follows:

The solution of a given multilayer system will be decoupled if and only if the solution in each layer is also decoupled when considered individually.

The axis configuration must remain the same when the layers are considered individually. Note the generality of this well-known conclusion which is *valid for any* multilayer system in flat or cylindrical geometry. So, if one of the layers in the system presents coupling, this will be extended to the whole system.

Once it is known whether decoupling occurs or not one can proceed to study the symmetry of the solutions. If the problem decouples one simply solves two separate and independent problems; if it does not, one has only one problem, albeit bigger, to solve. The coupling or decoupling of the problem would eventually arise as the symmetries are studied but it is worth studying coupling first since certain configurations can have two decoupled families, but not both of them with the same symmetries (recall that this was the case for single tetragonal crystals in X configuration presented in section 5.1.5 of the previous chapter).

This is illustrated in figure 6.1 where the Lamb and SH modes for a system composed of a tetragonal layer in X configuration between two orthorhombic layer are shown. The problem decouples and only the family of SH modes

presents a certain symmetry. Since Lamb modes in the tetragonal layer do not have any parity, the Lamb modes of the system will not have any parity either. In figure 6.1 the dispersion curves of the system are plotted, Lamb modes are shown in solid blue lines and SH modes in dot-dashed red lines. In figure 6.2 the mode shapes of the first five Lamb modes marked with black circles in figure 6.1 are plotted. Figure 6.2.a shows a two-dimensional plot of the norm of the complex vector (black circles) and the phase (solid red lines) and figure 6.2.b displays the same magnitudes but now in three-dimensional space where complex polar coordinates have been used in the horizontal plane and the vertical axis is the thickness of the system. The lack of symmetry of the Lamb modes as well as the symmetry of the SH modes is apparent by looking at the phases across the thickness. It must be remembered that the physically meaningful quantity of the complex displacement vector field is the product $\|U_j(y)\| \; e^{-\beta z} \; \cos(\alpha z - \omega t + \phi_j(y))$. Therefore, the fact that the phase depends on the coordinates results in a displacement vector field with no definite parity as seen in the previous chapter. The mode shapes of the six first SH modes marked with squares in figure 6.1 are shown in figure 6.3.a and figure 6.3.b in two- and three-dimensional plots. It can be seen that these modes do have a definite parity since their phase is, up to a sign, constant throughout the thickness.

As explained above, the aim is to find out whether the global symmetry of a multilayer system is also reflected in its solutions or not. In order to do this, the following starting assumption for 3-layered systems is made:

Assumption 1. *The global solution of a 3-layer symmetric system, with n odd, has a definite parity, odd or even (giving rise to antisymmetric or symmetric modes respectively), with respect to the geometrical middle plane of the system*

Later it will be seen that this can be generalized to arbitrary odd n. In what follows counterexamples to this assumption will be provided thus ruling out certain symmetric configurations. By doing this, the path is narrowed to those symmetric configurations for which that assumption does hold. In these cases a proof is provided.

Counterexample 1. *Assumption 1 does not hold for 3-layer symmetric systems whose middle layer belongs to any of the Triclinic-like categories: T_C or M_D.*

For this counterexample a system like $O_D^{S/A}/T_C/O_D^{S/A}$ will do. $O_D^{S/A}$ is taken to be an orthorhombic crystal and T_C a triclinic crystal, both in default Y configuration: {Y} orthogonal to the plane of the plate and propagation along the {Z} axes. Further details of their physical and elastic
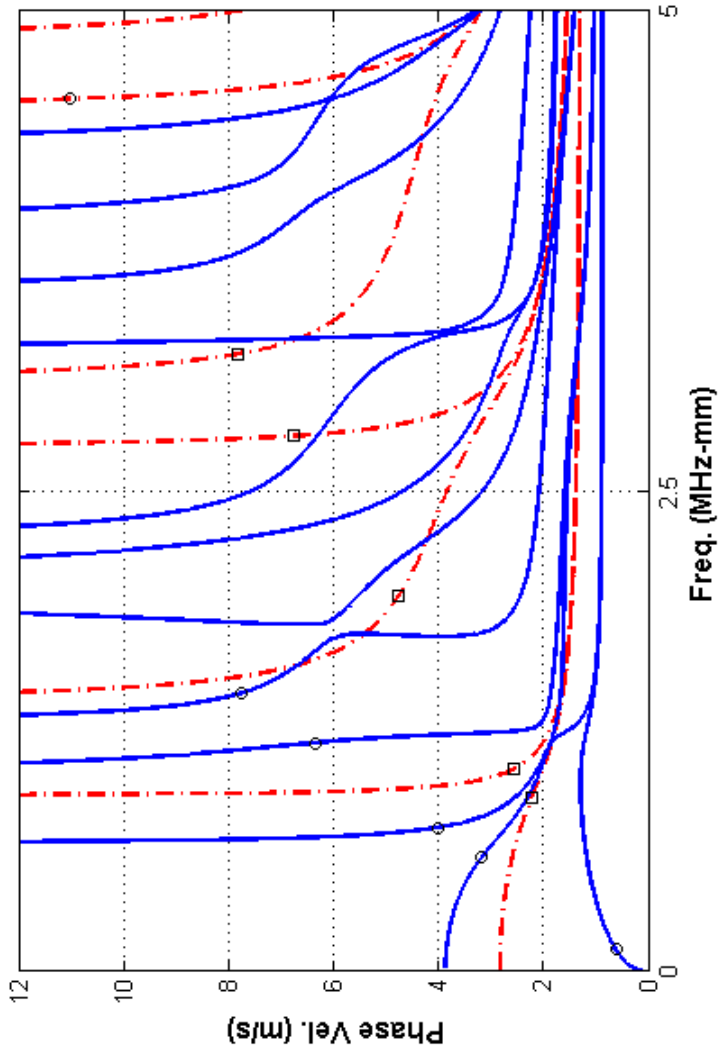
Figure 6.1: Dispersion curves of Lamb (blue solid lines) and SH (dash-dotted red lines) modes for symmetric trilayer system composed of flat Orthorhombic-Tetragonal-Orthorhombic layers. The modes which are marked in circles and squares are plotted in figures 6.2 and 6.3. Orthorhombic plates in Y configuration and tetragonal plate in X configuration with propagation along the {Z} crystal axis.
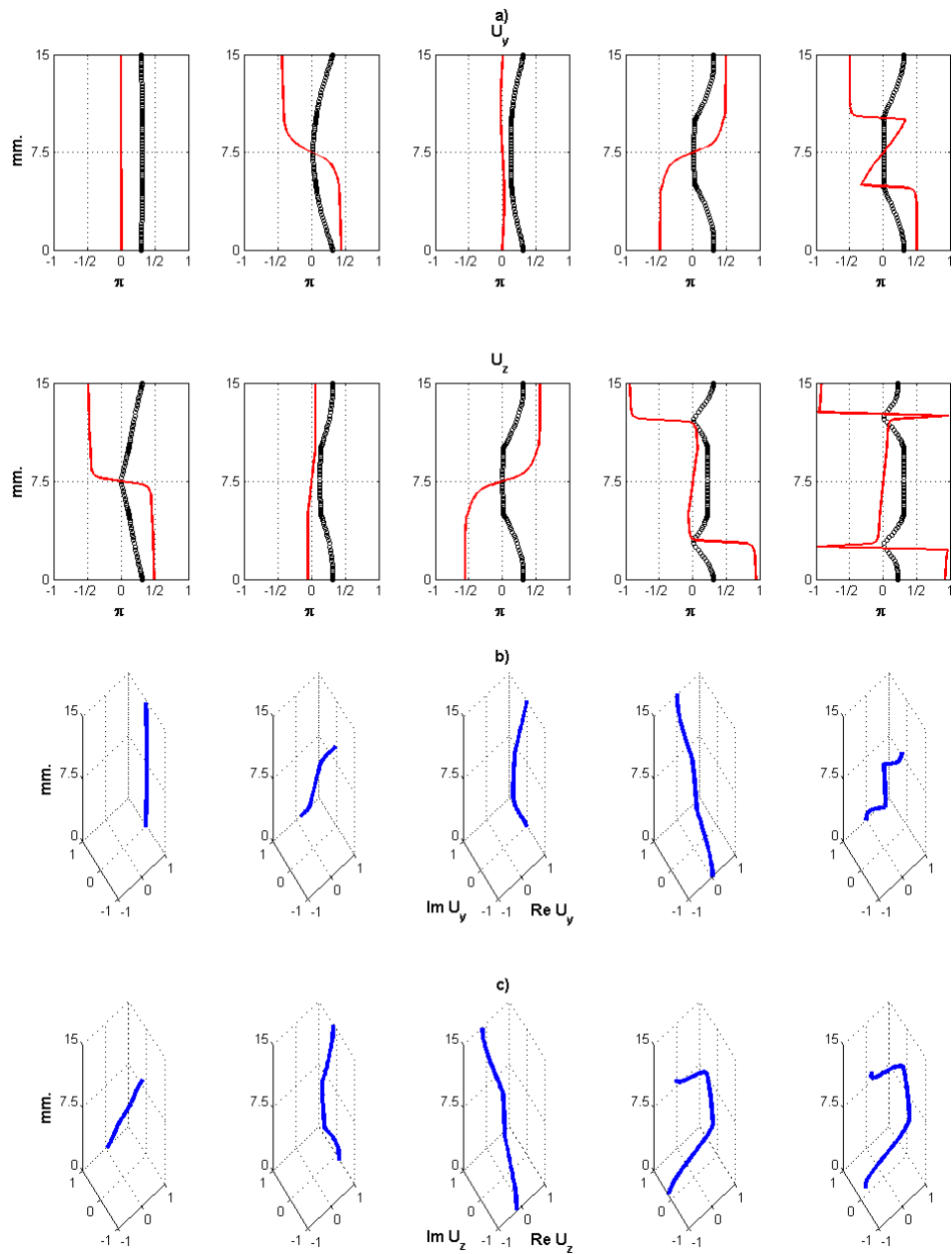
Figure 6.2: Two- and three-dimensional, a) and b) respectively, mode shapes of the first five Lamb modes for the symmetric three-layered system of figure 6.1 composed of Orthorhombic-Tetragonal-Orthorhombic layers. In a) the norm of the complex vector field normalized to one is shown in black circles whereas the phase is shown in solid red lines. In b) the coordinate of the displacement complex vector in complex polar coordinates is shown at each point of the thickness of the plate. Note how the phases are not constant through the thickness and thus the modes have no parity.
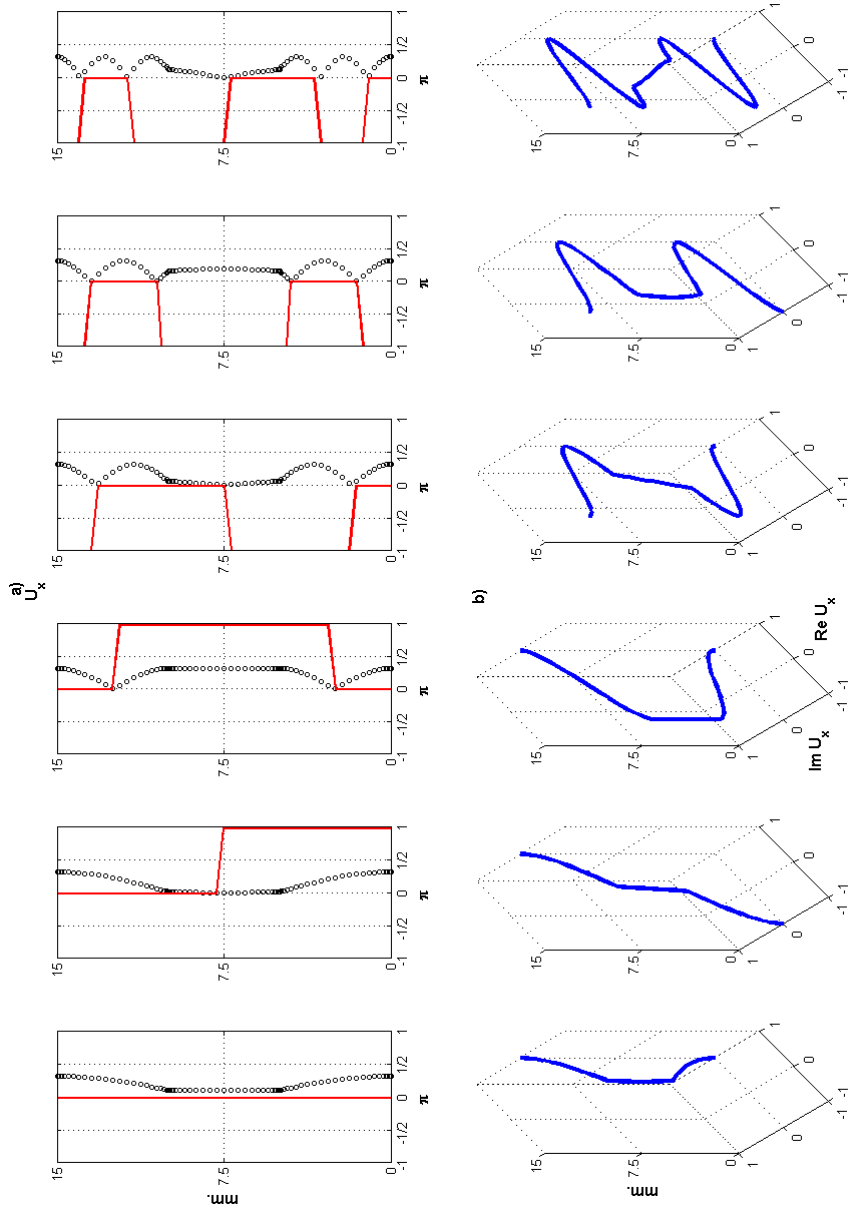
Figure 6.3: Two- and three-dimensional, a) and b) respectively, mode shapes of the first five SH modes for the symmetric three-layered system of figure 6.1 composed of Orthorhombic-Tetragonal-Orthorhombic layers. In a) the norm of the complex vector field normalized to one is shown in black circles and the phase is shown in solid red lines. In b) the coordinate of the displacement complex vector in complex polar coordinates is shown at each point of the thickness of the plate. The phase is constant, up to a sign, through the thickness and thus the modes are symmetric and antisymmetric.

171

properties are given in section 6.4 at the end. The solutions of this system will be coupled due to the presence of the triclinic layer and will have no symmetry. Its dispersion curves are shown in figure 6.4 and the displacement field's profiles for the first five modes (marked with black circles in the dispersion curves) in figures 6.5.a and 6.5.b in two- and three-dimensional spaces respectively. In figure 6.5.a the norm is shown in black circles and the phase in solid red lines. As expected for systems whose solution has no symmetry, the phases of the complex displacement vector field vary across the thickness of the plate.

Had the system been composed in such a way that decoupling occurs, for instance $O_D^{S/A}/M_D/O_D^{S/A}$ with the triclinic layer replaced by a trigonal $c_{15} = 0$, the only difference with respect to the previous case would be that one would have two independent sets of solutions from two different dispersion relations but none of them would display any symmetry.

Conversely, one has as well:

Counterexample 2. *Assumption 1 does not hold for 3-layer symmetric systems whose outer layers belong to any of the Triclinic-like categories: T_C or M_D, and whose middle layer belongs to any of the other three categories: $M_C^{S/A}$, Tet_D^* or $O_D^{S/A}$*

To illustrate this counterexample the dispersion curves and mode shapes of a system $T_C/M_C^{S/A}/T_C$ are presented. The physical properties and further details are given in section 6.4 at the end. Dispersion curves for this system are shown in figure 6.6 and the displacement field's profiles for the first five modes (black circles in figure 6.6) in figures 6.7.a and 6.7.b in two- and three-dimensional spaces respectively. In figure 6.7.a the norm is shown in black circles and the phase in solid red lines. Again, the solution has no symmetry and the phases of the complex displacement vector field vary across the thickness of the plate accordingly.

The above two counterexamples leave only one possibility:

Conclusion 1. *Assumption 1 holds only for systems whose layers belong to categories with symmetry: $M_C^{S/A}$ or $O_D^{S/A}$. In other words, all layers must have solutions with symmetry when considered individually with the same axes configuration as in the multi-layered system.*

Note that layers belonging to Tet_D^*, tetragonal in X configuration, will display symmetry in one of the decoupled families but not in the other. Thus, one should think of two identical systems each for each different family of decoupled modes: SH and Lamb. For SH modes, since all layers present symmetry, the global solution will display symmetry according to
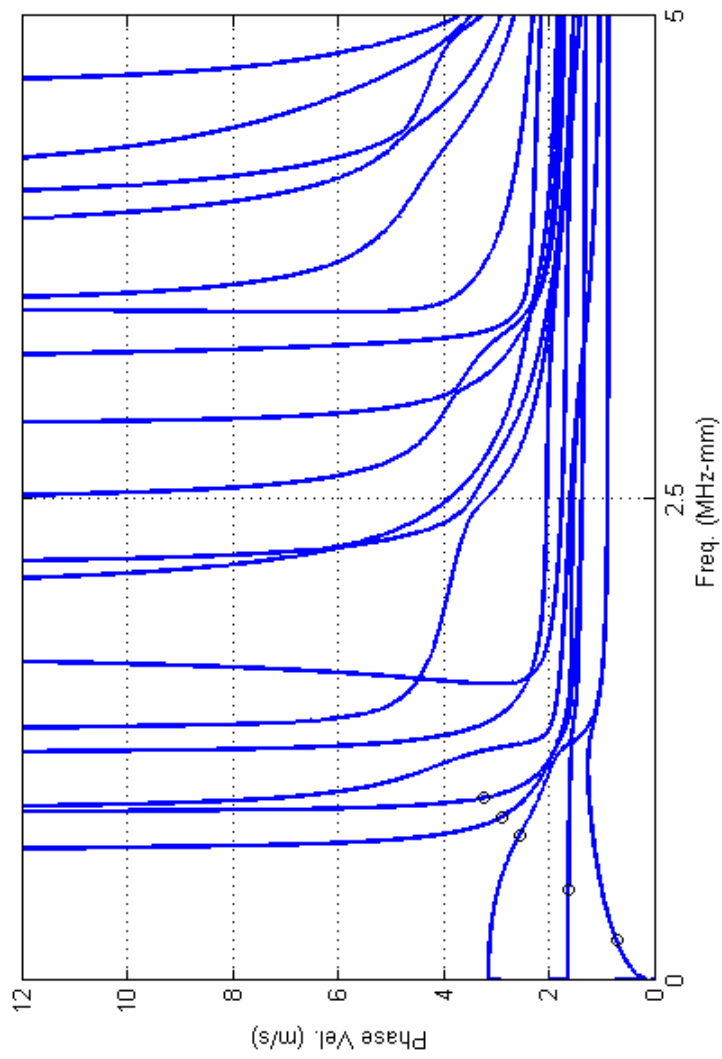
Figure 6.4: Dispersion curves of coupled modes for a symmetric three-layered system composed of flat Orthorhombic-Triclinic-Orthorhombic layers. The modes which are marked in circles are plotted in figure 6.5. No crossings are seen to occur amongst the modes when zooming in. All plates in Y configuration with propagation along the $\{Z\}$ crystal axis.
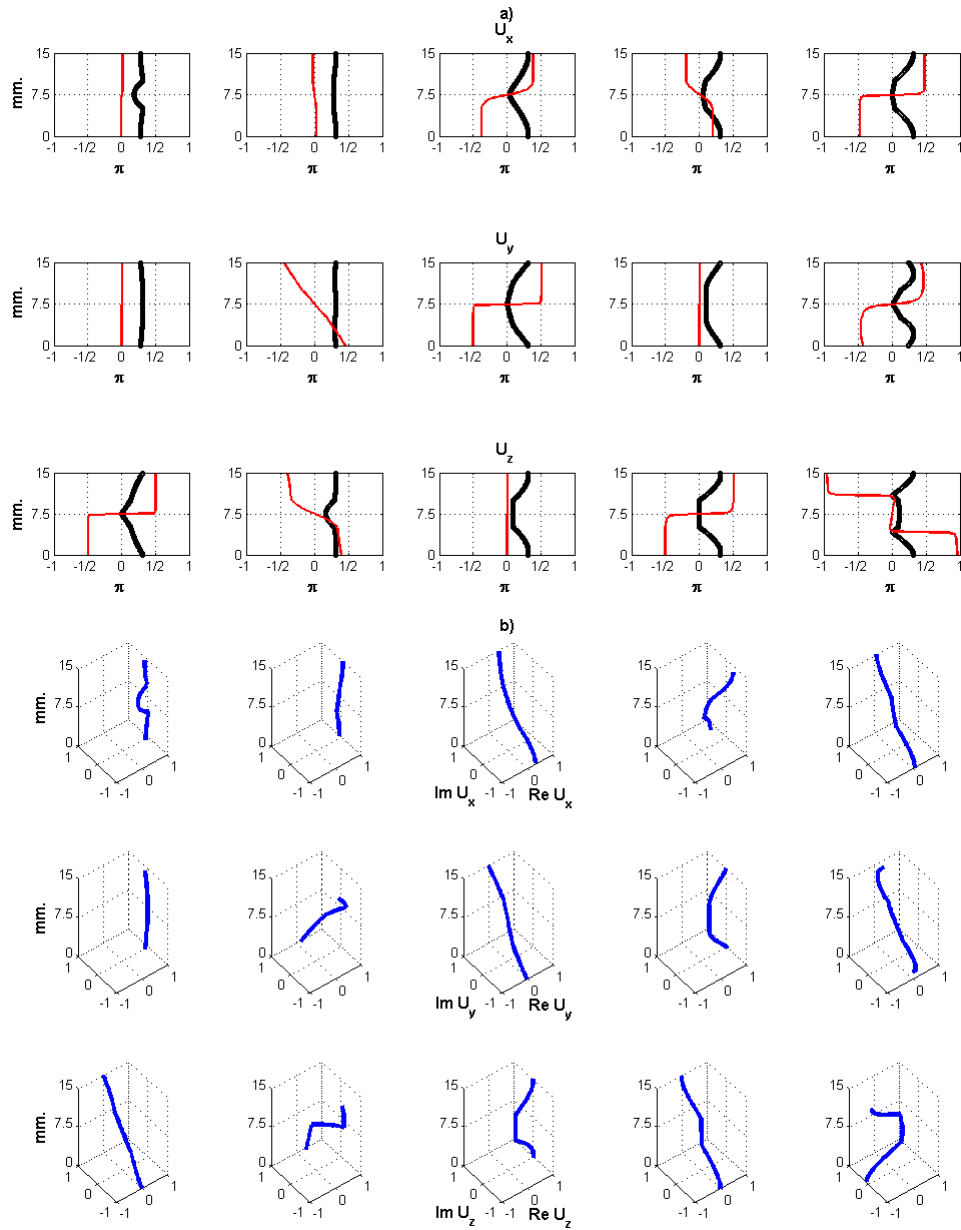
Figure 6.5: Two- and three-dimensional, a) and b) respectively, mode shapes of the first five modes for the symmetric three-layered system of figure 6.4 composed of Orthorhombic-Triclinic-Orthorhombic layers. In a) the norm of the complex vector field normalized to one is shown in black circles whereas the phase is shown in solid red lines. In b) the coordinate of the displacement complex vector in complex polar coordinates is shown at each point of the thickness of the plate.

174
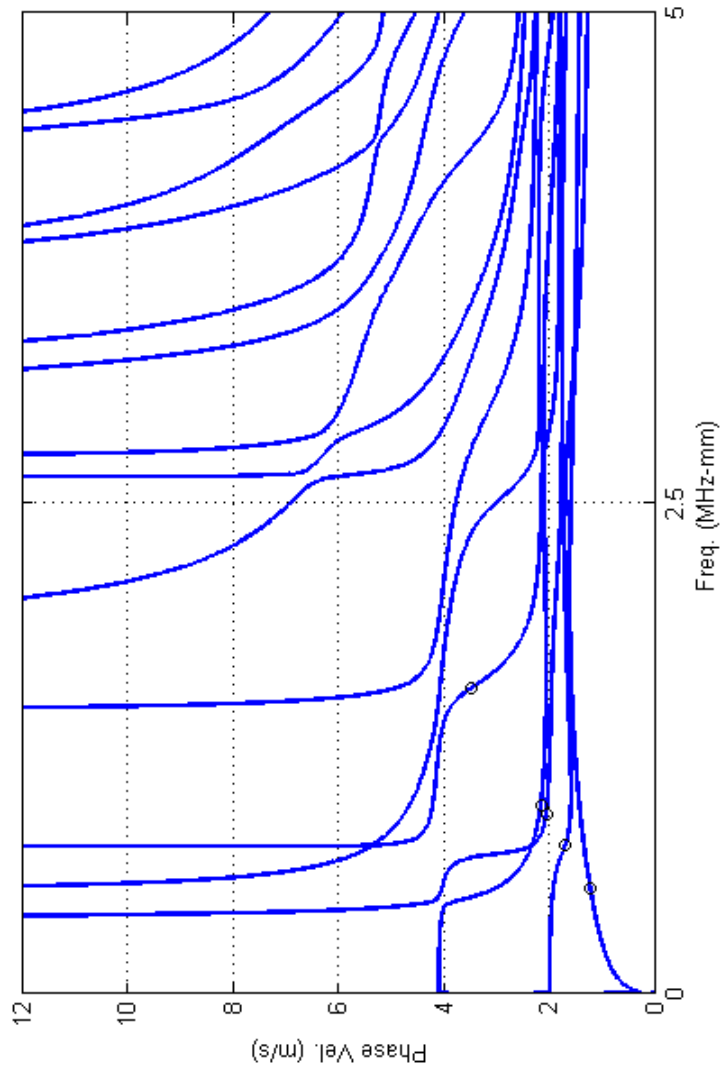
Figure 6.6: Dispersion curves of coupled modes for a symmetric three-layered system composed of flat Triclinic-Monoclinic-Triclinic layers. The modes which are marked in circles are plotted in figure 6.5. No crossings are seen to occur amongst the modes when zooming in. All plates in Y configuration with propagation along the {Z} crystal axis.
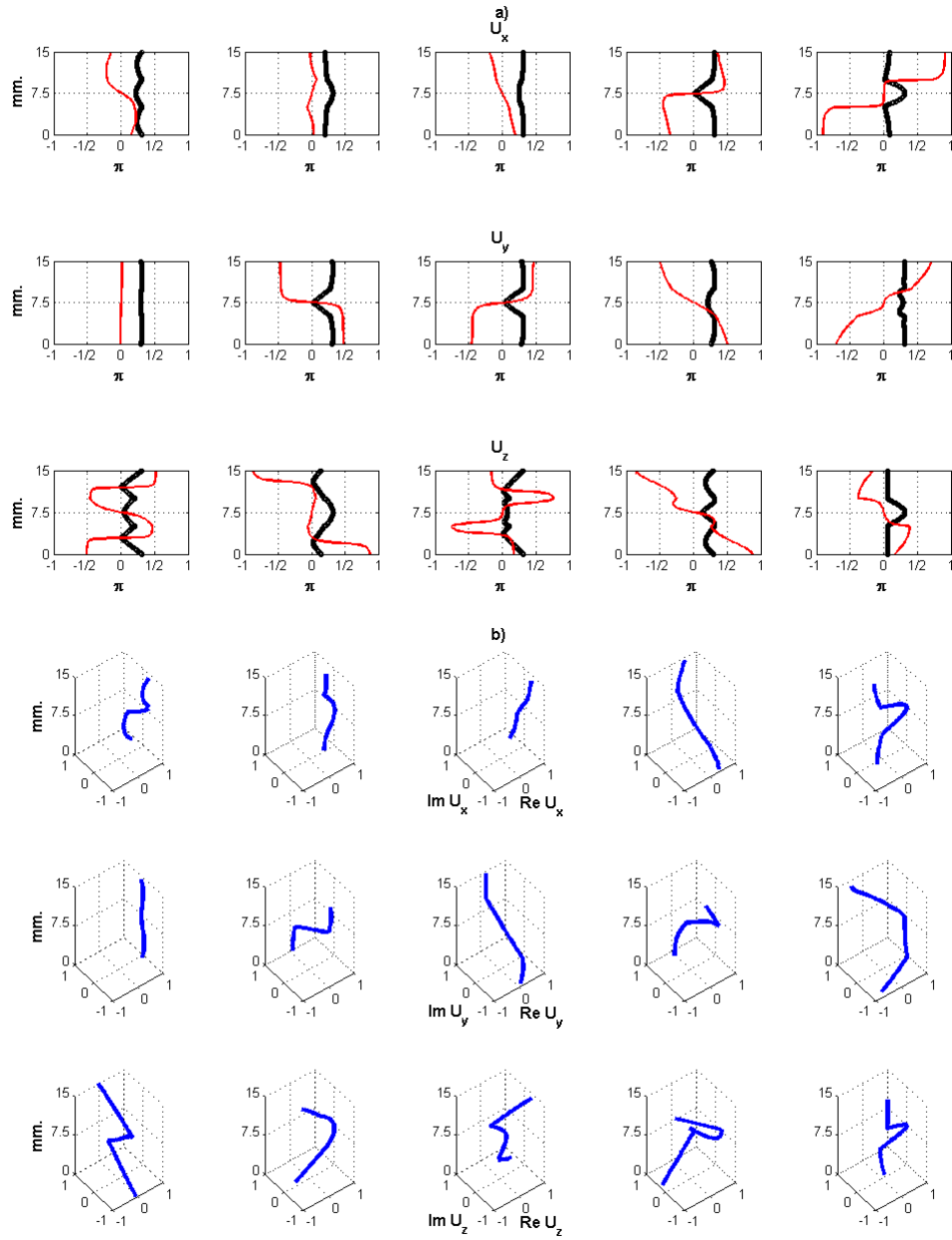
Figure 6.7: Two- and three-dimensional, a) and b) respectively, mode shapes of the first five modes for the symmetric three-layered system of figure 6.6 composed of Triclinic-Monoclinic-Triclinic layers. In a) the norm of the complex vector field normalized to one is shown in black circles whereas the phase is shown in solid red lines. In b) the coordinate of the displacement complex vector in complex polar coordinates is shown throughout the thickness of the plate. The modes do not present any symmetry.

conclusion 1. For Lamb modes however, the tetragonal layer, having no symmetry actually belongs to M_D, and therefore the global solution will have no symmetry according to the counterexamples 1 or 2 depending on which case one is dealing with.

The above discussion and results for the three-layer system B/A/B are summarized in table 6.1 below:

A B	(I) T_C^X	(II) $M_C^{S/A}$	(III) M_D^X, Tet_D^*	(IV) $O_D^{S/A}$
T_C^X	Coupled X	Coupled X	Coupled X	Coupled X
$M_C^{S/A}$	Coupled X	***Coupled*** ***S/A***	Coupled X	***Coupled*** ***S/A***
M_D^X, Tet_D^*	Coupled X	Coupled X	Decoupled X	Decoupled X or *
$O_D^{S/A}$	Coupled X	***Coupled*** ***S/A***	Decoupled X or *	***Decoupled*** ***S/A***

Table 6.1: Table summarizing the properties of the global solution for a three layer system B/A/B depending on the properties of each individual component. The symmetry with respect to the diagonal cells reflects the change in the crystal types of the array B/A/B $\leftrightarrow$ A/B/A. S/A stands for solution with definite parity, X stands for solutions with no definite parity and the asterisk for solutions with properties analogous to Tet_D^*.

Columns labelled with (I) and (III) correspond to systems in counterexample 1. For columns labelled with (II) and (IV) one has: cells which are not highlighted correspond to systems in counterexample 2, and cells which are highlighted correspond to those systems for which the assumption 1 holds. Cells in which the "X or *" appears correspond to the cases described in the paragraph right after conclusion 1 about systems containing Tet_D^* materials.

To close this section, a proof of the assertion made in conclusion 1 above for SH modes in an arbitrary five-layer system will be provided (the three-layer case is much simpler). The determinant of the amplitudes for the displacement vector field in a system of five arbitrary layers C/B/A/B/C complying with the symmetry conditions of conclusion 1 takes the following form in the partial wave framework taking into account the symmetries of the roots ξ and the resulting ones in the stress tensor coefficients. The reader who is not familiar with this formalism for multiple layer systems can find more details in any of the following references [11, 84, 14, 16, 75]:

$$
\begin{bmatrix}
Ce^{ih_3c} & -Ce^{-ih_3c} & 0 & 0 & 0 & 0 & 0 & 0 & 0 & 0 \\
Ce^{ih_2c} & -Ce^{-ih_2c} & -Be^{ih_2b} & Be^{-ih_2b} & 0 & 0 & 0 & 0 & 0 & 0 \\
e^{ih_2c} & e^{-ih_2c} & -e^{ih_2b} & -e^{-ih_2b} & 0 & 0 & 0 & 0 & 0 & 0 \\
0 & 0 & Be^{ih_1b} & -Be^{-ih_1b} & -Ae^{ih_1a} & Ae^{-ih_1a} & 0 & 0 & 0 & 0 \\
0 & 0 & e^{ih_1b} & e^{-ih_1b} & -e^{ih_1a} & -e^{-ih_1a} & 0 & 0 & 0 & 0 \\
0 & 0 & 0 & 0 & Ae^{-ih_1a} & -Ae^{ih_1a} & -Be^{-ih_1b} & Be^{ih_1b} & 0 & 0 \\
0 & 0 & 0 & 0 & e^{-ih_1a} & e^{ih_1a} & -e^{-ih_1b} & -e^{ih_1b} & 0 & 0 \\
0 & 0 & 0 & 0 & 0 & 0 & Be^{-ih_2b} & -Be^{ih_2b} & -Ce^{-ih_2c} & Ce^{ih_2c} \\
0 & 0 & 0 & 0 & 0 & 0 & e^{-ih_2b} & e^{ih_2b} & -e^{-ih_2c} & -e^{ih_2c} \\
0 & 0 & 0 & 0 & 0 & 0 & 0 & 0 & Ce^{-ih_3c} & -Ce^{ih_3c}
\end{bmatrix}
\tag{6.3}
$$

where A, B and C are the coefficients of the stress tensor field for decoupled SH modes with parameters corresponding to each layer type and their symmetries taken into account. The letters a, b and c are the roots for each layer A, B and C respectively. The boundaries of the system are located at $y = \pm h_3$ and its interfaces at $y = \pm h_2$ and $y = \pm h_1$.

The goal is to demonstrate that all the entries in the upper right and bottom left 5×5 blocks can be made zero in order to factorize the determinant into two non-reducible sub-determinants for the two independent families of modes: symmetric and antisymmetric modes.

$$
\begin{bmatrix}
Ce^{ih_3c} & -Ce^{-ih_3c} & 0 & 0 & 0 & 0 & 0 & 0 & 0 & 0 \\
Ce^{ih_2c} & -Ce^{-ih_2c} & -Be^{ih_2b} & Be^{-ih_2b} & 0 & 0 & 0 & 0 & 0 & 0 \\
e^{ih_2c} & e^{-ih_2c} & -e^{ih_2b} & -e^{-ih_2b} & 0 & 0 & 0 & 0 & 0 & 0 \\
0 & 0 & Be^{ih_1b} & -Be^{-ih_1b} & -2A\mathfrak{c}_{1a} & -2iA\mathfrak{s}_{1a} & 0 & 0 & 0 & 0 \\
0 & 0 & e^{ih_1b} & e^{-ih_1b} & -2i\mathfrak{s}_{1a} & -2\mathfrak{c}_{1a} & 0 & 0 & 0 & 0 \\
0 & 0 & 0 & 0 & 2A\mathfrak{c}_{1a} & -2iA\mathfrak{s}_{1a} & -Be^{-ih_1b} & Be^{ih_1b} & 0 & 0 \\
0 & 0 & 0 & 0 & -2i\mathfrak{s}_{1a} & 2\mathfrak{c}_{1a} & -e^{-ih_1b} & -e^{ih_1b} & 0 & 0 \\
0 & 0 & 0 & 0 & 0 & 0 & Be^{-ih_2b} & -Be^{ih_2b} & -Ce^{-ih_2c} & Ce^{ih_2c} \\
0 & 0 & 0 & 0 & 0 & 0 & e^{-ih_2b} & e^{ih_2b} & -e^{-ih_2c} & -e^{ih_2c} \\
0 & 0 & 0 & 0 & 0 & 0 & 0 & 0 & Ce^{-ih_3c} & -Ce^{ih_3c}
\end{bmatrix}
\tag{6.4}
$$

where $\mathfrak{s}_{1a} \equiv \sin(h_1 a)$ and $\mathfrak{c}_{1a} \equiv \cos(h_1 a)$.

Performing the following row operations:

$$
\begin{aligned}
(\tilde{4}^I) &= (\tilde{4}) - (\tilde{6}))\\
(\tilde{5}^I) &= (\tilde{5}) + (\tilde{7})\\
(\tilde{6}^I) &= -((\tilde{6}) + (\tilde{4}))\\
(\tilde{7}^I) &= (\tilde{7}) - (\tilde{5})
\end{aligned}
\tag{6.5}
$$

where the superscript denotes the step in the process. The tilde indicates one is operating with rows. Columns with plain numbers.

One could make trigonometric functions in the rest of the entries by means of the appropriate column and then simplify but this is cumbersome. In order to show that the determinant can be factorized the simplest and fastest way is to continue adding and subtracting rows and columns until all the non-zero entries vanish.

$$
\begin{vmatrix}
Ce^{ih_3c} & -Ce^{-ih_3c} & 0 & 0 & 0 & 0 & 0 & 0\\
Ce^{ih_2c} & -Ce^{-ih_2c} & -Be^{ih_2b} & Be^{-ih_2b} & 0 & 0 & 0 & 0\\
e^{ih_2c} & e^{-ih_2c} & -e^{ih_2b} & -e^{-ih_2b} & 0 & 0 & 0 & 0\\
0 & 0 & Be^{ih_1b} & -Be^{-ih_1b} & -4Ac_{1a} & 4iAs_{1a} & Be^{-ih_1b} & -Be^{ih_1b}\\
0 & 0 & e^{ih_1b} & e^{-ih_1b} & -4is_{1a} & 4c_{1a} & -e^{-ih_1b} & -e^{ih_1b}\\
0 & 0 & -Be^{ih_1b} & Be^{-ih_1b} & 0 & 0 & Be^{-ih_1b} & -Be^{ih_1b}\\
0 & 0 & -e^{ih_1b} & -e^{-ih_1b} & 0 & 0 & -e^{-ih_1b} & -e^{ih_1b}\\
0 & 0 & 0 & 0 & 0 & 0 & Be^{-ih_2b} & -Be^{ih_2b}\\
\end{vmatrix}
\tag{6.6}
$$

180

$$
\begin{bmatrix}
Ce^{ih_3c} & -Ce^{-ih_3c} & 0 & 0 & 0 & 0 & 0 & 0 & 0 & 0 \\
Ce^{ih_2c} & -Ce^{-ih_2c} & -Be^{ih_2b} & Be^{-ih_2b} & 0 & 0 & Be^{-ih_2b} & -Be^{ih_2b} & 0 & 0 \\
e^{ih_2c} & e^{-ih_2c} & -e^{ih_2b} & -e^{-ih_2b} & 0 & 0 & -e^{-ih_2b} & -e^{ih_2b} & 0 & 0 \\
0 & 0 & 2Be^{ih_1b} & -2Be^{-ih_1b} & -4Ac_{1a} & 0 & 0 & 0 & 0 & 0 \\
0 & 0 & 2e^{ih_1b} & 2e^{-ih_1b} & -4i\mathfrak{s}_{1a} & 0 & 0 & 0 & 0 & 0 \\
0 & 0 & 0 & 0 & 0 & 4iA\mathfrak{s}_{1a} & 2Be^{-ih_2b} & -2Be^{ih_2b} & 0 & 0 \\
0 & 0 & Be^{ih_2b} & -Be^{-ih_2b} & 0 & 4c_{1a} & -2e^{-ih_2b} & -2e^{ih_2b} & -Ce^{-ih_2c} & Ce^{ih_2c} \\
0 & 0 & -e^{ih_2b} & -e^{-ih_2b} & 0 & 0 & Be^{-ih_2b} & -Be^{ih_2b} & -e^{-ih_2c} & -e^{ih_2c} \\
0 & 0 & 0 & 0 & 0 & 0 & e^{-ih_2b} & e^{ih_2b} & Ce^{-ih_3c} & -Ce^{ih_3c}
\end{bmatrix}
\tag{6.7}
$$

It can be seen by inspection that the following column operations have been performed to continue *moving* the non-zero entries towards the edges of the determinant.

$$
\begin{aligned}
(3^{II}) &= (3^{I}) - (8^{I}) \\
(4^{II}) &= (4^{I}) - (7^{I}) \\
(7^{II}) &= (7^{I}) + (4^{I}) \\
(8^{II}) &= (8^{I}) + (3^{I})
\end{aligned}
\tag{6.8}
$$

The procedure is now clear, the 2×2 non-zero blocks keep moving at each stage towards the edges of the determinant. For brevity only the transformations needed to complete the factorization will be given and the final result presented. The next set of row operations is:

$$
\begin{aligned}
(\tilde{2}^{III}) &= (\tilde{2}^{II}) - (\tilde{8}^{II}) \\
(\tilde{3}^{III}) &= (\tilde{3}^{II}) + (\tilde{9}^{II}) \\
(\tilde{8}^{III}) &= (\tilde{8}^{II}) + (\tilde{2}^{II}) \\
(\tilde{9}^{III}) &= (\tilde{9}^{II}) - (\tilde{3}^{II})
\end{aligned}
\tag{6.9}
$$

In the fourth stage one performs the following column operations:

$$
\begin{aligned}
(1^{IV}) &= (1^{III}) - (10^{III}) \\
(2^{IV}) &= (2^{III}) - (9^{III}) \\
(9^{IV}) &= (9^{III}) + (2^{III}) \\
(10^{IV}) &= (10^{III}) + (1^{III})
\end{aligned}
\tag{6.10}
$$

The last stage only involves two row operations:

$$
\begin{aligned}
(\tilde{1}^{V}) &= (\tilde{1}^{IV}) + (\tilde{10}^{IV}) \\
(\tilde{10}^{V}) &= (\tilde{10}^{IV}) - (\tilde{1}^{IV})
\end{aligned}
\tag{6.11}
$$

And the result is the factorized determinant of equation (6.12).

Further column operations could be made in order to obtain trigonometric functions in the non-zero entries, but this is not necessary unless one is interested in obtaining the dispersion relations explicitly. The determinant clearly factorizes in to two 5×5 non-reducible sub-determinants each yielding a dispersion relation, one will correspond to symmetric and the other to antisymmetric modes.

This final result is illustrated with an example of a system with the following sequence of materials: $O_D^{S/A}/M_C^{S/A}/O_D^{S/A}$, the physical and geometrical properties are given in section 6.4 at the end. The dispersion curves for this system are shown in figure 6.8. Due to the presence of the monoclinic layer the solution is coupled but will be split into symmetric (solid blue lines) and antisymmetric modes (dot-dashed red lines). The mode shapes for the first five symmetric modes (black circles in figure 6.8) are shown in figures 6.9.a

and 6.9.b. The displacement field's profiles for the first five antisymmetric modes (black squares in figure 6.8) are displayed in figures 6.10.a and 6.10.b. It is clear that the phase is constant throughout the thickness up to a sign thus showing that both families of modes have definite parity: symmetric and antisymmetric.

$$
\begin{bmatrix}
Ce^{ih_3c} & -Ce^{-ih_3c} & 0 & 0 & 0 & 0 & 0 & 0 & 0 & 0 \\
Ce^{ih_2c} & -Ce^{-ih_2c} & -Be^{ih_2b} & Be^{-ih_2b} & 0 & 0 & 0 & 0 & 0 & 0 \\
e^{ih_2c} & e^{-ih_2c} & -e^{ih_2b} & -e^{-ih_2b} & 0 & 0 & 0 & 0 & 0 & 0 \\
0 & 0 & Be^{ih_1b} & -Be^{-ih_1b} & -2Ac_{1a} & 0 & 0 & 0 & 0 & 0 \\
0 & 0 & e^{ih_1b} & e^{-ih_1b} & -2is_{1a} & 0 & Be^{-ih_1b} & -Be^{ih_1b} & 0 & 0 \\
0 & 0 & 0 & 0 & 0 & 2iAs_{1a} & -e^{-ih_1b} & -e^{ih_1b} & -Ce^{-ih_2c} & Ce^{ih_2c} \\
0 & 0 & 0 & 0 & 0 & 2c_{1a} & Be^{-ih_2b} & -Be^{ih_2b} & -e^{-ih_2c} & -e^{ih_2c} \\
0 & 0 & 0 & 0 & 0 & 0 & e^{-ih_2b} & e^{ih_2b} & Ce^{ih_3c} & -Ce^{ih_3c}
\end{bmatrix}
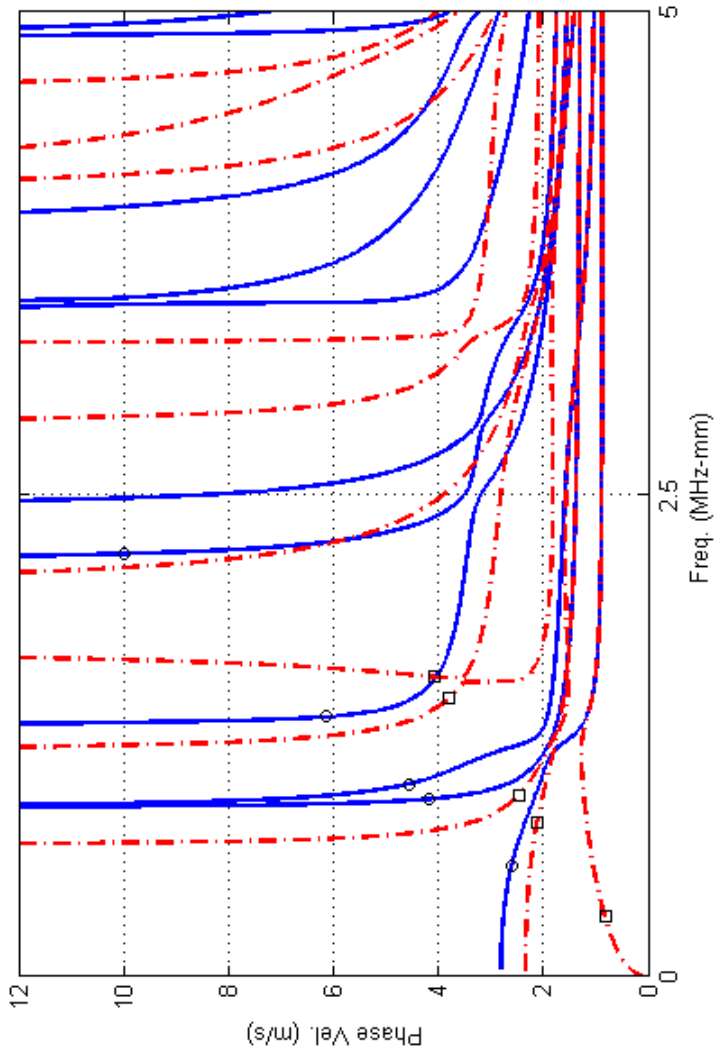$$

(6.12)

183

Figure 6.8: Dispersion curves of Symmetric (blue solid lines) and Antisymmetric (dash-dotted red lines) modes for the symmetric three-layered system composed of flat Orthorhombic-Monoclinic-Orthorhombic layers. The modes which are marked in circles and squares are plotted in figures 6.9 and 6.10. All plates in Y configuration with propagation along the {Z} crystal axis.

Figure 6.9: Two- and three-dimensional mode shapes of the first five Symmetric modes for the symmetric three-layered system of figure 6.8 (black circles) composed of Orthorhombic-Monoclinic-Orthorhombic layers. In a) the norm of the complex vector field normalized to one is shown in black circles whereas the phase is shown in solid red lines. In b) the coordinate of the displacement complex vector in complex polar coordinates is shown throughout the thickness of the plate. The phase of the modes is constant up to a sign throughout the thickness as expected for this family of modes.
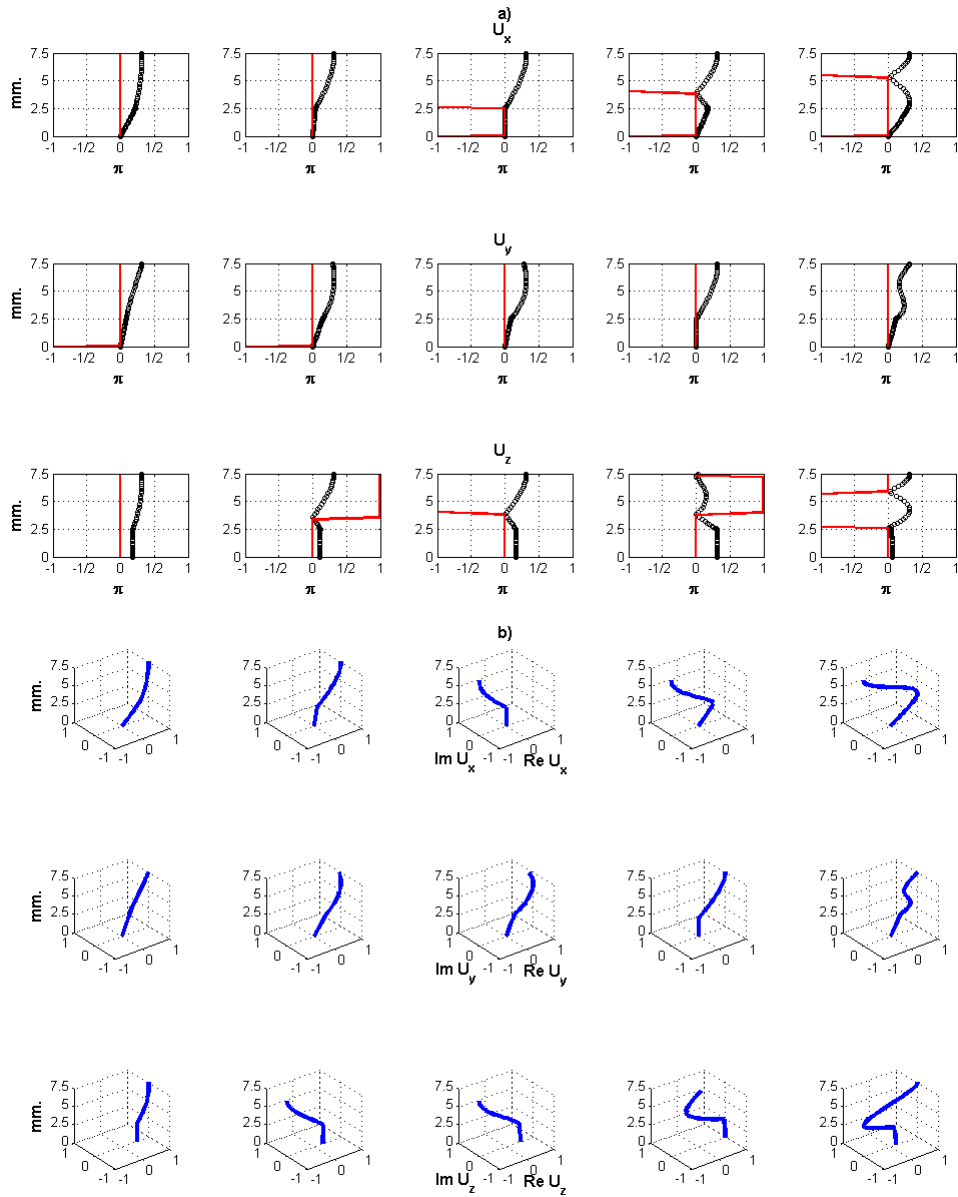
185
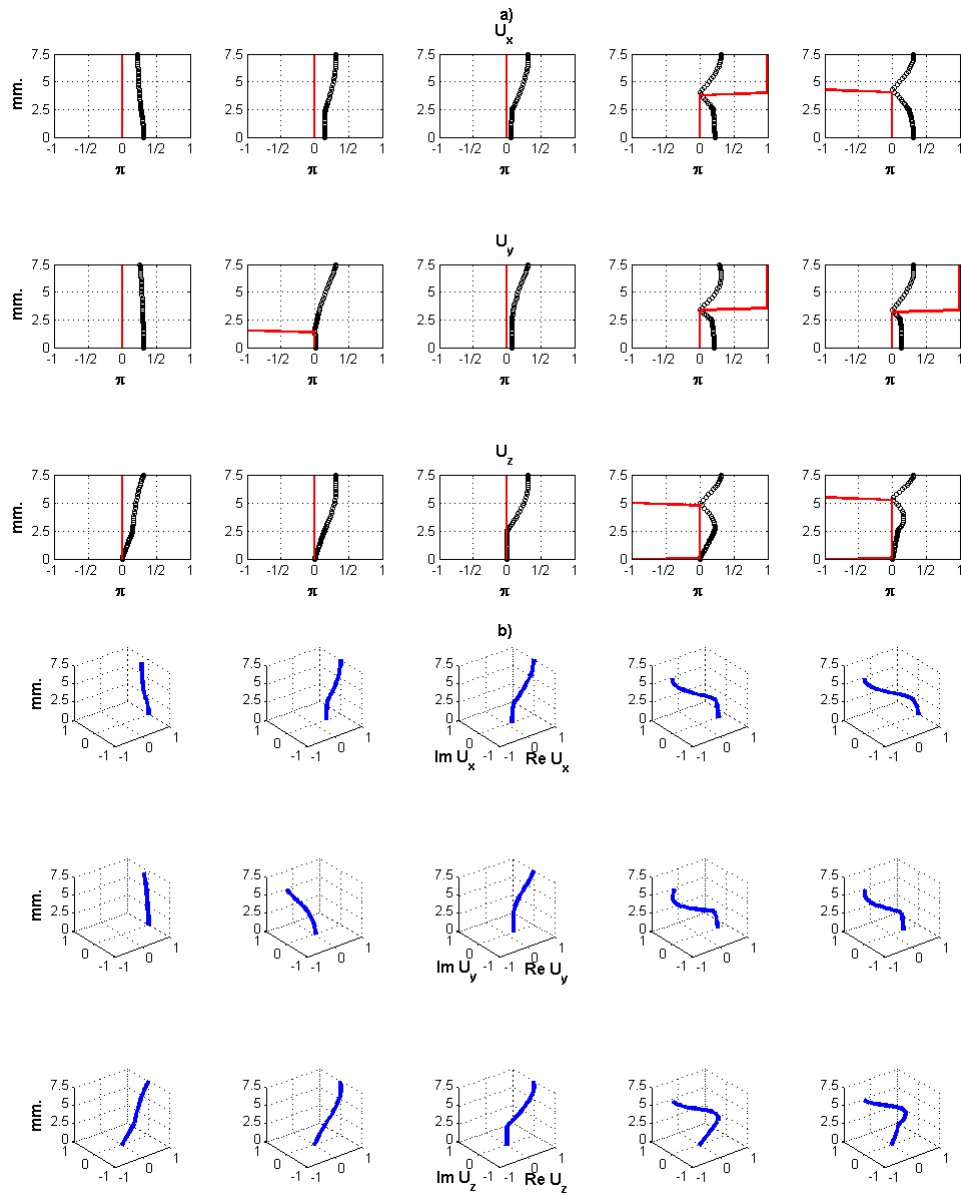
Figure 6.10: Two- and three-dimensional mode shapes of the first five Anti-symmetric modes for the symmetric three-layered system of figure 6.8 (black squares) composed of Orthorhombic-Monoclinic-Orthorhombic layers. In a) the norm of the complex vector field normalized to one is shown in black circles whereas the phase is shown in solid red lines. In b) the coordinate of the displacement complex vector in complex polar coordinates is shown throughout the thickness of the plate.

186

For SH modes, the generalization of the proof to an arbitrary odd number of layers is straightforward but lengthy due to the notational needs required to exploit the symmetry of the matrix when reducing it. The steps are exactly the same as those outlined above. First of all, one combines the columns involving the middle layer in order to obtain trigonometric functions and then, by means of transformations similar to those beginning in equation (6.5), factorizes the central block involving only the middle layer to obtain an expression similar to (6.6). Now, the procedure consists of an alternation of column and row operations and substitutions analogous to those in equations (6.7) and (6.9). After a finite number of iterations the non-zero 2×2 blocks have been *moved out* of the determinant thus leaving a factorized determinant of the form (6.12).

For Lamb modes and coupled modes in an arbitrary odd number of layers the simplification of the determinant goes along the very same lines but for brevity and lack of space is not presented in this chapter. For Lamb modes the size of the non-zero blocks to eliminate is 4×4 and for coupled modes their size is 6×6. Note that in all these derivations it is *essential* that the boundaries and interfaces are disposed in a symmetric fashion with respect to the middle plane of the system $y = 0$, thus reflecting the fact that the thicknesses of the different layers play as important a role in all this procedure as the sequence of materials within the structure. Should this condition fail to be met, the determinant could not be simplified and factorized regardless of the combination of crystal layers and their individual properties.

Thus, for systems complying with the conditions of conclusion 1 the original assumption 1 holds and the global solution will be split into two independent families of modes with definite parity. Further splitting occurs if decoupling exist.

As figure 6.11 shows, these investigations and results hold also when fluid layers are present. In figure 6.11 the dispersion curves of the modes of a system composed of two flat steel layers with a layer of water between them are shown, symmetric modes are plotted in blue solid lines, whereas antisymmetric modes are plotted in red dot-dashed lines. Given that any fluid can be modelled as a solid whose elastic constants are low, the preceding analysis still holds for them and one only needs to take into account the same symmetric or antisymmetric conditions at the centre of the fluid layer as one would do with a solid layer. An analogous result is obtained if a system composed of steel-water-steel-water-steel is studied, the modes are split into symmetric and antisymmetric families.
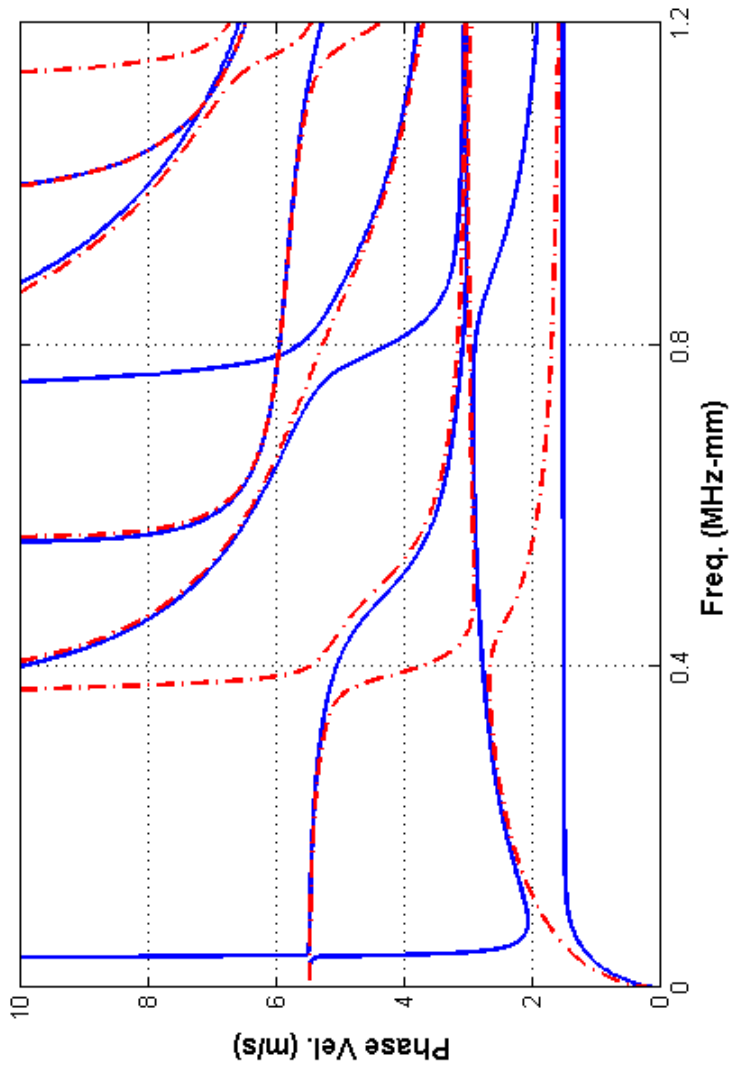
187

Figure 6.11: Dispersion curves of Symmetric (blue solid lines) and Antisymmetric (dash-dotted red lines) modes for symmetric three-layered system composed of flat Steel-Water-Steel layers. Propagation along the {Z} crystal axis. This system was also studied in figures 11 and 12 of [46] where its dispersion curves and modes shapes are respectively shown.

Finally, a comment concerning counterexamples 1 and 2 when systems with more than three layers are considered. Systems in counterexample 1 can be extended by adding layers to the three-layered system and it is clear that if the inner three-layer core does not present symmetry, neither will any of the extended systems no matter what combination of plates is chosen. In order to see this, it is enough to notice that the inner core of three layers behaves like a triclinic-like material since its global solutions have no definite parity. Adding one layer to each side, thus making a five-layered aggregate, takes the system to a configuration equivalent to the three-layered systems considered in counterexample 1 which have a middle layer belonging to either T_C or M_D. Therefore the global solution for the five-layer system will have no symmetry. One can continue this process to increase the number of layers arbitrarily obtaining analogous conclusions as for the three and five layers systems just explained. For systems in counterexample 2 the reasoning follows the same lines and the conclusion is that when layers of triclinic-like material are inserted in a system, in a symmetric fashion but not in the middle position, the global solution will present no symmetry either.

6.2 Multiple layer systems of anisotropic crystals in cylindrical geometry

This final section covers multiple layer systems in cylindrical geometry with axial propagation. The case of circumferential propagation follows along exactly the same lines, it is actually simpler since only one family of modes must be considered, this has not been presented here for brevity. In section 5.2 it was seen that the analysis of cylindrical systems is much simpler than their flat counterparts. This is still true even when multiple layer systems are considered so this section will be very brief. The main results were derived in the single layer study of the previous chapter and will be used and freely referred to.

The goal is again to find how many independent dispersion relations exist for a given configuration. The main result of the single layer study for cylindrical geometry was that the existence of more than one independent dispersion relation was solely determined by the coupling or decoupling of the given problem for a fixed *harmonic order n*. If the problem decouples in torsional and longitudinal modes, two dispersion relations exist and therefore crossings amongst these two families can occur. It was also concluded that families corresponding to different *harmonic orders* $n_1 \neq n_2$ can cross amongst themselves since there are two independent dispersion relations, one for each *harmonic order* n_i. The single layer results for all crystal classes and axis configurations were summarized in table 5.3 in section 5.2.

For multilayer cylindrical systems very little changes. The interface continuity conditions for stresses and displacement vector fields of the layers can lead to the coupling of otherwise decoupled modes. That is, assume the system is composed of two layers and fixed *harmonic order n*. From the results and analysis for a single plate system one knows that, for that family of modes with harmonic order n, the modes are decoupled in torsional and longitudinal for one layer but they are not for the other. As a consequence of the interface continuity conditions, the layer with coupling will also extend this coupling to the other layer. Hence, the global solution of this simple bilayer system is coupled and only one family of non-crossing modes exists.

This reasoning is generalized to any number of layers straightforwardly and one arrives at the conclusion that for a system of n cylindrical layers, it is enough that one single layer presents coupling (when considered individually) for it to be extended through the interfaces to all the other layers of the system. In other words, the only possibility for a cylindrical multilayer system to have decoupled torsional and longitudinal modes is that these modes also exist decoupled in *each* of the composing layers when considered individually.

Torsional and longitudinal modes are axisymmetric modes with $n = 0$ which decouple for most crystal classes and axes configurations except for triclinic crystals when they are always coupled regardless of the axes configuration chosen (see table 5.3 in section 5.2). Therefore, for any crystal classes composing the array of layers, if one is interested in a family with harmonic order $n \geqslant 1$ one can immediately conclude that no decoupling will occur and therefore only one complicated dispersion relation will correspond to the global system. Therefore crossings amongst modes will not take place.

For the particular case of $n = 0$, which is the only one where decoupling can arise, the above discussion yields the conclusion: *for the $n = 0$ family of modes in a cylindrical system with an arbitrary number of layers, decoupling of the global solution in torsional and longitudinal modes will occur if and only if each layer presents such decoupling when considered individually with the same axis configuration.*

This can be checked with the aid of the summary presented in table 5.3 in section 5.2. The two above situations are illustrated by the following two simple examples of bilayer systems which can be generalized to an arbitrary number of layers easily. The geometrical and physical parameters of the materials used in these examples can be found in section 6.4 at the end. Also, it must be remembered that throughout these cases, axial propagation is assumed. In the last example, the first flexural modes of the family with $n = 3$ in a bilayer system composed of two different orthorhombic layers are

studied. For orthorhombic materials it is known that flexural $n = 3$ modes are coupled and therefore, for a system like this, only one dispersion relation exists yielding one family of flexural $n = 3$ modes which will not cross amongst themselves. The dispersion curves for this system are presented in figure 6.12.

The next simpler case could be a system composed of a monoclinic and an orthorhombic plate, both in Θ configuration. Focusing the attention on axisymmetric $n = 0$ modes and according to table 5.3 in section 5.2, both layers would present decoupling for this harmonic order if considered individually yielding torsional and longitudinal modes. Therefore, the interface continuity conditions will not couple those two independent solutions and in the global solution torsional and longitudinal modes will arise from the two independent dispersion relations of the system. An even simpler case, but with essentially the same behaviour, would be to consider the same system with the two isotropic materials studied before for flexural modes but for harmonic order $n = 0$. This would yield again torsional and longitudinal modes in the global solution, examples of such systems can be found in the literature [83].

In the case of two different materials, one of which has decoupled solutions and the other does not ($n = 0$ for a Triclinic-Orthorhombic system for instance according to table 5.3 in section 5.2) the result would be a coupled global solution for the harmonic order in consideration. The continuity interface conditions are responsible for this coupling of modes and therefore only one dispersion relation describes the system and hence the modes will not cross amongst themselves as in the case of torsional and longitudinal modes, even if they have the same harmonic order $n = 0$. An example of such a system Triclinic-Orthorhombic can be found in Figure 4.9 of chapter 4.

With these two examples it is hoped that the procedure to evaluate whether an arbitrary multiple layer cylindrical system will present one or two independent families of modes is clear. Bearing these guidelines in mind it should be possible to develop codes and classify their results in order to plot the independent families separately and avoid the problem of mode crossings even in the most complicated situations. Finally, it must be emphasized that this study has been applied to axial propagation only which presents the richest variety of phenomena. For circumferential propagation, it no longer makes sense to speak of *harmonic order*. The angular wavenumber now simply takes on values in a continuum range. The situation and investigation is thus greatly simplified since one only needs to consider a single family of modes and the only factor which determines the coupling of modes is the anisotropy of the crystals involved and their axis orientations.
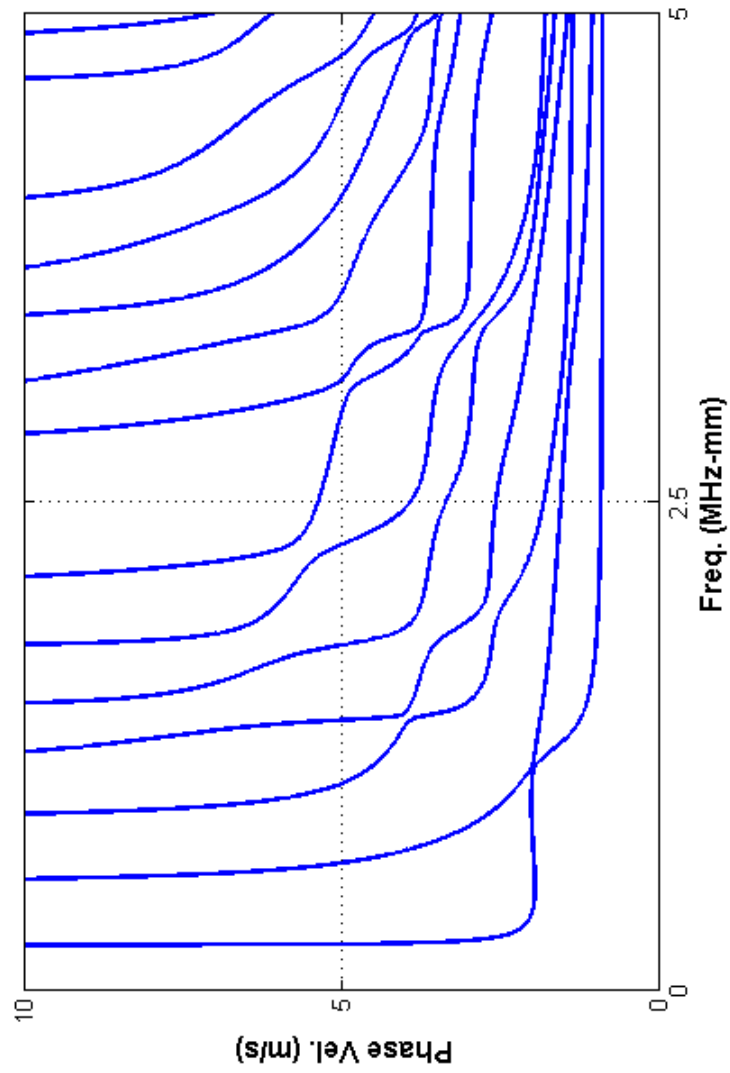
Figure 6.12: Dispersion curves of the Flexural $n = 3$ family of modes in a bilayer cylindrical system composed of two different orthorhombic materials. Only for the lowest harmonic order do these materials present decoupling hence the modes shown in this figure are all coupled and do not cross amongst themselves.

6.3   Discussion of Chapter 6

In this chapter a classification of the crystal classes has been provided according to the parity and coupling properties of their solution. Those with definite parity, symmetric and antisymmetric (S/A) and those with no parity (X). According to the coupling of the solution one has crystals whose solution is coupled (C) and decoupled solutions (D) where Lamb and SH modes arise and can be studied independently. This classification has been used later to study the behaviour of the global solution in multiple layer systems and how these solutions change depending on the combinations of materials chosen. It was also shown that multiple layer systems can also be ascribed to one of the above categories according to the parity and coupling properties of their global solution. This makes it easier to generalize the results presented here for three- or five-layered systems to systems containing an arbitrary number of layers

Multiple layer systems in flat and cylindrical geometry have been investigated and classified according to the properties of their solutions regarding coupling and parity. In the case of flat geometry counterexamples have been appropriately used to rule out certain ambiguous combinations. For Conclusion 1 in section 6.1.3 a proof for SH modes in a five-layer system has been provided and it has been explained how to extend it to the case of an arbitrary number of layers and other types of modes, for the latter it is useful to bear in mind the similar derivation for monoclinic materials carried out in detail in chapter 5.

In the case of cylindrical geometry with axial propagation the situation was simpler. With the aid of table 5.3 in section 5.2, it was explained how it is possible to determine whether the global solution for a given cylindrical structure composed of various layers presents decoupling or not. It was shown that for cylindrical systems the sequence or thicknesses of materials within the array, unlike in flat geometry, does not play any role in the final outcome. Only the crystal classes, the axis configurations and the harmonic order n of the family of modes under study are important.

These investigations and results contribute to a more efficient design of algorithms (be they based on partial wave root-finding routines or PSCM for instance) and to exploit the parity and coupling properties of the solution in advance so that the final result is more robust and the mode jumping phenomenon which sometimes occurs using tracing routines is drastically reduced or totally eliminated.

6.4 Numerical data for examples of Chapter 6

The physical and geometrical information used for the figures presented in the chapter are given here. The number of grid points N varies from one example to another, but it is always at least double the number of modes plotted in the figure in order to keep good accuracy of the results. On a practical level N is chosen to achieve the shortest computation time, that is, if one is interested in the first 10 modes, running a code with $N = 100$ is unnecessary; a value of N between 25 and 30 has consistently been shown to be sufficient.

The parameters for the orthorhombic plates of figures 6.1, 6.2 and 6.3:

$$\rho = 3820 \text{ kg/m}^3 \; ; \qquad h = 5 \text{ mm} \tag{6.13}$$

h stands for the thickness of the plate. The elastic stiffness matrix is given in GPa:

$$c = \begin{pmatrix} 132 & 6.9 & 5.9 & & & \\ & 12.3 & 5.5 & & & \\ & & 12.1 & & & \\ & & & 3.32 & & \\ & & & & 6.21 & \\ & & & & & 6.15 \end{pmatrix} \tag{6.14}$$

The tetragonal plate in X configuration of figures 6.1, 6.2 and 6.3 has the following parameters:

$$\rho = 3420 \text{ kg/m}^3 \; ; \qquad h = 5 \text{ mm} \tag{6.15}$$

h stands for the thickness of the plate. The elastic stiffness matrix is given in GPa:

$$c = \begin{pmatrix} 169.10 & 122.20 & 122.20 & & & \\ & 208.08 & 83.22 & 22.50 & & \\ & & 208.08 & -22.50 & & \\ & & & 36.44 & & \\ & & & & 75.42 & \\ & & & & & 75.42 \end{pmatrix} \tag{6.16}$$

The parameters for the Triclinic plate of figures 6.4, 6.5, 6.6 and 6.7 are as follows:

$$\rho = 8938.4 \text{ kg/m}^3 \; ; \qquad h = 5 \text{ mm} \tag{6.17}$$

h stands for the thickness of the plate. The elastic stiffness matrix is given in GPa:

$$c = \begin{pmatrix} 235.54 & 88.64 & 88.78 & 19.05 & -2.97 & -6.54 \\ & 215.85 & 108.43 & -14.14 & 2.35 & 22.16 \\ & & 215.77 & -4.90 & 0.61 & -15.57 \\ & & & 58.24 & -17.68 & -7.02 \\ & & & & 39.69 & 11.66 \\ & & & & & 44.02 \end{pmatrix} \qquad (6.18)$$

The parameters for the monoclinic plates of figures 6.6 and 6.7 are those given for the orthorhombic plate in 6.14 rotated by $\pi/3.3$ radians about the $\{Y\}$ axes of the crystal.

The parameters for the monoclinic plate in of figures 6.8, 6.9 and 6.10 are as follows:

$$\rho = 8938.4 \text{ kg/m}^3 ; \qquad h = 5 \text{ mm} \qquad (6.19)$$

h stands for the thickness of the plate. The elastic stiffness matrix is given in GPa:

$$c = \begin{pmatrix} 201.1 & 89.3 & 122.6 & & & -20.3 \\ & 208.3 & 115.4 & & & 14.1 \\ & & 174.9 & & & 6.2 \\ & & & 63.1 & 16.7 & \\ & & & & 82.4 & \\ & & & & & 37.8 \end{pmatrix} \qquad (6.20)$$

Parameters for the system of figure 6.11 are as follows. For the steel plate the thickness is $h = 5$ mm and the other physical parameters are those given below:

$$\rho = 7932 \text{ kg/m}^3 ; \qquad h = 2 \text{ mm}; \qquad \mu = 84.29 \text{ GPa}; \qquad \lambda = 113.16 \text{ GPa} \qquad (6.21)$$

For the water layer one has:

$$\rho = 1000 \text{ kg/m}^3 ; \qquad h = 2 \text{ mm}; \qquad \mu = 0 \text{ GPa}; \qquad \lambda = 2.25 \text{ GPa} \qquad (6.22)$$

The parameters of the top orthorhombic layer in the cylindrical system with internal radius $r_i = 30$ mm. of figure 6.12 are:

$$\rho = 5300 \text{ kg/m}^3 ; \qquad h = 10 \text{ mm} \qquad (6.23)$$

h stands for the thickness of the layer. The elastic stiffness matrix is given in GPa:

$$
c = \begin{pmatrix}
239 & 104 & 50 & & & \\
 & 247 & 52 & & & \\
 & & 135 & & & \\
 & & & 65 & & \\
 & & & & 66 & \\
 & & & & & 76
\end{pmatrix}
\tag{6.24}
$$

The inner layer has a thickness of $h = 5$ mm. and the same elastic properties as the orthorhombic material of the first figures whose properties are given in 6.13 and 6.14.

Chapter 7

Dispersion Curves for Waves in Fluid-loaded Orthorhombic Waveguides with a Pseudospectral Collocation Method and Perfectly Matched Layer

Non-destructive Evaluation (NDE) applications often involve inspections of structures which are surrounded by a different medium, fluid or solid, using guided waves. This situation arises for instance when a partially or fully submerged pipe must be checked for defects or corrosion. In these circumstances, the energy of the guided wave may leak from the structure into the surrounding medium through the interface. It is very often the case that the length from the outer surface of the structure to the free surface of the fluid or solid in which it is embedded is large compared to the through-thickness dimension of the inspected structure. Then, it is a good approximation to the problem to regard the surrounding medium as infinite.

With this approximation, guided waves propagating in the structure to be studied leak energy into the surrounding medium and, as a consequence of this loss, become attenuated until they eventually decay. If the structure where the guided waves propagate is a viscoelastic medium, material damping will also contribute and increase the attenuation suffered by the guided waves. The challenge posed by this attenuation, even if only elastic media are considered, is to mathematically account for the infinity of the surrounding medium causing the energy leakage and to develop stable and accurate

numerical algorithms to compute the dispersion curves of such leaky waves robustly. A brief review of some of the results for these problems to date is presented below.

For flat plates immersed in fluid and embedded in solids, exact analytical dispersion relations can be derived by using the partial wave approach, potentials' description or less frequently the Stroh Formalism, see [85] and references therein. Most papers and books on the subject have a section on guided waves travelling in the interface of two media and very often also specialize these results for the case of a fluid half-space, these waves are known as *Stonely* waves, see for instance [31, 5, 84, 6, 50]. A range of different approaches has been used by different authors in order to study leaky modes in flat plates and in more general settings with more complicated waveguides. In [15], Lowe, Pavlakovic *et.al* present a general purpose program, DISPERSE, based on the partial wave description of the fields. Some examples of leaky waves in immersed flat plates are shown in the corresponding section of the user's manual [16]. Ahmad *et.al* [86] resort to the potential description of the fields for modelling leaky waves in hexagonal (transversely isotropic) flat plates immersed in water. Also, by deriving a dispersion relation from the potential description of the fields Nagy and Nayfeh [70] study leaky waves of flat plates immersed in viscous fluids. In a different and more general setting, Castaings and Lowe [17] use a Finite Element (FE) simulation to study leaky guided waves in solid waveguides of arbitrary cross section coupled to an infinite solid medium. Finally, several authors have successfully combined the Semi-analytical Finite Element (SAFE) approach with the Perfect Matched Layer (PML) method first proposed by Berenger [87] to calculate dispersion curves of guided waves in structures embedded in an infinite medium, see for instance [88, 89, 90, 91, 92].

The analogous problem of guided waves with axial propagation in an embedded cylinder has also been studied extensively, for brevity, only a few references are given here. Nagy [93] investigated longitudinal guided wave propagation in transversely isotropic cylinders immersed in fluid by conventional partial wave root-finding (PWRF) routines. Also Nagy and Nayfeh [60] studied the problem of axially symmetric modes in viscoelastic rods immersed in fluid, again with PWRF routines. Later, Pavlakovic and Lowe [16, 94] did extensive work in this area studying extensional and flexural leaky modes in immersed cylinders. Other references where embedded cylinders and their leaky modes are studied by means of PWRF routines are [95, 96]. More general problems studying arbitrary cross sectional waveguides are studied in [97, 98]. Finally, in [92] the PML in cartesian and cylindrical coordinate formulations are compared in the framework of the SAFE method in order to study waveguides of arbitrary cross section. Previous studies of PML in curvilinear coordinates can be found in [99, 100].

The contribution of this chapter is to put forward and validate a new combination of a Pseudospectral Collocation Method (PSCM) and Perfect Matched Layer (PML) for the computation of dispersion curves in open flat and cylindrical waveguides of orthorhombic material. While the PML has been extensively used in combination with FE or FD schemes (see any of the aforementioned references) the possibilities of combining PSCM and PML for dispersion curve computation in open waveguides remains mostly unexplored. The PML approach has been chosen over the Absorbing Layer because the latter typically yields spurious reflections at the interface between the non-absorbing and absorbing regions and lacks the theoretical foundation of the PML, see [101, 91].

A PSCM-PML combination for elastic waveguides was, to the best of my knowledge, first studied by Skelton *et. al.* [102]. In their paper, a free homogeneous isotropic elastic strip with finite width and infinite length is investigated by attaching a PML along the longitudinal dimension in order to achieve the desired wave decay at infinity. Later, Postnova [66] provided an illustrative example using a PSCM-PML combination to compute the complex wavenumbers for two different frequencies in the case of circumferential propagation of guided waves in isotropic cylinders immersed and filled with water.

The cases presented in this chapter go a step further by solving two problems of great practical interest: flat and cylindrical, with axial propagation, immersed orthorhombic waveguides. The numerical approach is validated first in the isotropic and hexagonal cases by comparing the dispersion curves obtained with the PSCM-PML to those given by the software DISPERSE [15] based on the PWRF approach. The validated codes are then used for computation of the dispersion curves of an immersed flat plate and cylinder of orthorhombic symmetry which, to the best of my knowledge, has not been done before.

The PSCM possesses several noteworthy advantages which the more conventional approaches such as PWRF do not possess such as the so called *spectral accuracy* (see [25]), not missing any modes ([24, 21]) thanks to its algebraic approach and its conceptual simplicity. In addition, the great flexibility of the PSCM allows for straightforward and reliable generalizations to more general anisotropic materials which are not as easy to investigate by more conventional approaches. Therefore, it is hoped that this work will complement the existing numerical approaches cited above, further widen the range of available alternatives for dispersion curve computation and pave the way for further research into the possibilities of the PSCM-PML approach for more complicated and general settings.

This chapter is organized as follows. In Section 7.1, the necessary background for the PSCM-PML approach is presented. In Section 7.2 the PSCM-PML results for isotropic and hexagonal immersed plate and cylinder are presented, validated by comparison with results from DISPERSE and discussed. Section 7.3 presents the new results for the orthorhombic immersed plate and cylinder and discusses some of their features. Mode shapes are provided throughout since they offer a good guidance and extra support to assess the correctness of the results. Details about the implementation are also given and physical properties of the problems solved can be found in section 7.5. Finally, Section 7.4 provides a summary and discussion of the results and some suggestions for future work. The last section 7.5 gives the parameters used in the numerical examples used. The investigation presented in this chapter forms the basis for a paper in preparation.

7.1 Perfect Matched Layer and Pseudospectral Collocation Method.

In this section, the PML scheme is explained for the flat case and how to combine it with the PSCM. The cylindrical problem proceeds along the same lines. Further details can be found in any of the references cited throughout the section.

The key ingredient of the PML [87] is to perform a change of variable in the spatial coordinate orthogonal to the propagation direction ({y} for the flat case, {r} for cylindrical geometry) in order to include a complex part which will be responsible for the attenuation of the wave within the PML. This is done in such a way that the spatial coordinate remains real throughout all the physical domain and smoothly becomes complex as it enters the PML range. As a consequence of this, the PML solutions become attenuated in the PML region so it is possible to truncate the computational domain at a finite distance and get a good approximation to the true physical solution of the infinite domain problem. How well this solution converges to the true physical solution depends on the PML parameters. These will be discussed in the forthcoming paragraphs. A more technical account and derivation of many of these features can be found in [103] and references therein. The PML set up is shown in figure 7.1 where the different regions are shown and a possible path for the {y} coordinate into the complex plane is also plotted. See [101] for more technical details and clarifying simple examples.

Figure 7.1 shows the truncated half-space (or a section for the cylindrical case where the plate layer represents the cylinder wall, the inside is vacuum) with the different regions involved. It is also shown how the new PML co-
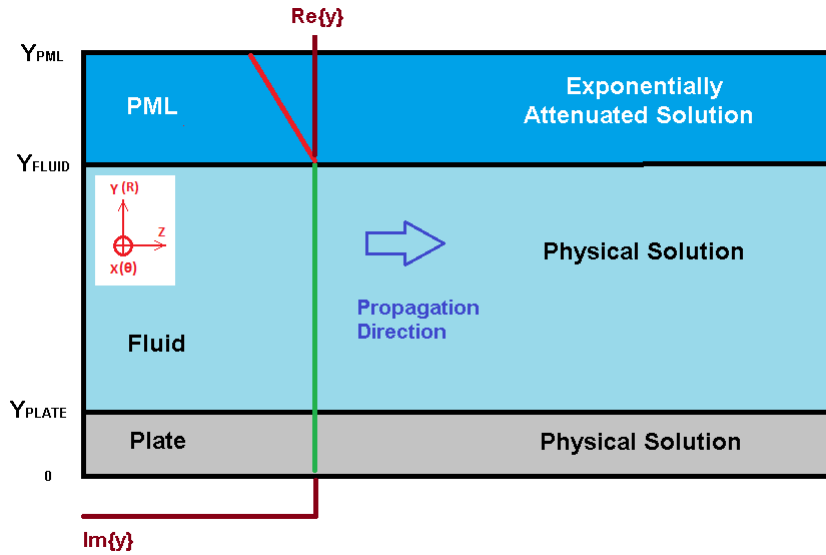
Figure 7.1: Schematic picture of the different layers present in the problem: plate, fluid and PML with their corresponding boundaries. Spatial axes are shown near the top left corner for the plate and cylindrical problems. Wave propagation takes place along the {z} axis in both cases. The path from the real axis (showing in green) into the complex plane (oblique line showing in red) corresponds to the change of variable for the PML explained in section 7.1 and equations (7.2)-(7.4). The nature of the solution is also highlighted according to the region.

ordinate {y} changes along the thickness: it is kept purely real (showing in green) along the finite physical domain, from $y = 0$ until $y = Y_{fluid}$ (plate and fluid), and becomes complex (oblique line showing in red) in the PML region, from $y = Y_{fluid}$ until $y = Y_{PML}$. This change of coordinates is given below in equations (7.2)-(7.4). The central role played by the PML is to artificially attenuate any wave propagating in it while still retaining the true physical solution in the physical domain (solid and fluid). This attenuation allows truncation of the infinite PML domain to a finite domain suitable for numerical computations.

In theory, the PML parameters can be chosen [103] to guarantee that the PML solution in the truncated domain converges to the true physical solution of the infinite physical domain with no spurious eigenvalues. However, numerically this is not always the case as the examples in the present investigations show. Spurious solutions in finite element (FE) simulations are reported also in [103] where they refer to [104] for an explanation of this phenomenon. In the works [90, 91], spurious eigenvalues are also found (cf.

[105, 106]). In [103], it is explained how these spurious eigenvalues can be managed by reducing the interval where the resonances (leaky modes, see Chapter 11 of [107] for a good discussion about leaky modes in the electromagnetic case) grow exponentially in the direction transverse to their propagation direction. In the cases considered here and in [90, 91], this is equivalent to placing the PML as close to the solid waveguide as possible.

The question of how close should the PML be placed is interesting and deserves discussion, in particular, whether it is possible or not to remove the physical fluid layer altogether and place the PML layer next to the solid waveguide. On the one hand, it must be noted that in the conceptual development of the PML, the artificial PML is attached to the physical fluid domain in order to attenuate the solutions thus enabling a truncation that makes computations possible. It is then shown that the PML solution converges to the physical solution in the infinite domain, in particular the PML solution *coincides* with the true physical solution in the unmodified region before the PML: the solid waveguide and the fluid, [103]. Therefore, there are conceptual grounds to retain a non-zero physical fluid layer, *a priori* choosing suitable PML parameters for a given problem is, to the best of my knowledge, an open question, see also [103].

On the other hand, in [103], it is argued how the thickness of the physical fluid layer, where the resonances grow exponentially, may affect the conditions necessary for the good convergence of the PML eigenvalues to the true physical eigenvalues as well as for the absence of non-physical spurious eigenvalues. Their conclusion is that the physical fluid layer should be as narrow as possible. In the particular one-dimensional numerical example (similar to those presented here) studied in [103], the best results for managing the spurious eigenvalues are found for a PML directly attached to the core. It must be emphasized that this alternative, also suggested in [90] though no results are given there, *does not remove* the spurious eigenvalues as can be seen in the examples provided in [103, 90], it simply moves them further away from the true physical resonances. In some instances, if the PML is placed too far away, these spurious eigenvalues will certainly affect the computation of the true resonance as examples in [90] show. As the examples in [103, 90] also show, once the resonances of a problem for a given frequency have been found, moving the PML closer to the core moves the spurious eigenvalues away but does not reveal any more physical resonances which had not been computed before. However, there might be cases, as will be seen in the course of this investigation, where better and more accurate results are actually obtained by placing the PML next to the core.

It can also be argued that, since the attenuation of the leaky modes ([107]) in the propagation direction is caused by the exponential growth in the

transverse direction of the amplitudes of the leaking waves in the fluid region (causing the energy leakage), a fluid layer between the PML and the solid waveguide will help to capture the physics of the problem. This line of reasoning is supported by the fact that trapped modes (with exponential decay into the fluid region) are better computed when the fluid layer is thick, in fact thicker than the fluid layer used for computing the leaky modes as it will be seen in the examples presented here. An analogous situation is reported in [90]. Again, in practice, the inclusion of this fluid layer between the core and the PML is not always desirable as one of the examples will reveal.

The preceding discussion, together with the examples and studies to which it referred, do not seem to lead to a clear answer to whether or not it is better to remove the fluid layer between the PML and waveguide completely. From the numerical investigation carried out for this chapter, it is only possible to conclude that a non-zero fluid layer between the PML and the core works well in the case of cylindrical waveguides. This is not always the case in flat plates where the PML must be placed next to the core in certain problems in order to ensure smooth and good results. Unfortunately, there is no general way to know whether the PML should be directly attached to the core or not but practice shows that it is usually a good idea to start with PML directly attached and increase the distance if the results are not satisfactory. The dependence of the PML position with respect to the problems parameters is yet unclear but from the cases studied in this chapter a *rule of thumb* can be given. It was successfully tested in waveguides of cubic symmetry providing excellent results, though these are not reproduced here for brevity.

In each of the problems presented in this chapter, it will be stated whether or not a fluid layer between PML and core was necessary in order to obtain the results. For the computation of leaky waves, it must be emphasized that this layer (when needed) should not be chosen too thick lest the leaky modes grow too much to be correctly attenuated by the PML, see [103, 90] for a more detailed discussion. This issue and related practical implementation questions are further discussed in section 7.4 of this chapter.

The set up for the immersed flat plate is described in what follows. In order to retain as much generality as possible in the formulation, the displacement description is used for the plate whereas the potential description is used for the surrounding ideal fluid. This *hybrid* approach was used in [46] and gave excellent results. The solid plate is therefore modelled as an orthorhombic material, its equations of motion in terms of the displacement vector fields can be retrieved in [9, 75] and will not be reproduced here again. This is very convenient since one can use the same code for a range of materials whose stiffness matrix has the same block form as orthorhom-

bic; isotropic is the simplest example and is the one chosen here to validate this unexplored approach. Moreover, when the system is symmetric about its middle plane, imposing symmetric and antisymmetric boundary conditions [50], allows one to model only half of the physical domain whereby only one PML for the fluid will be needed, thus greatly simplifying the algorithm.

The fluid surrounding the plate, being ideal and not supporting shear can be modelled by a single scalar longitudinal potential as is the normal practice for the longitudinal waves in isotropic solids:

$$\left(\frac{d}{dy} - k^2 + \rho\omega^2 \right) \Phi_f = 0 \tag{7.1}$$

where Φ_f is the longitudinal potential of the fluid. As usual, the displacement vector field is obtained by taking the gradient of this potential. Further details as well as the analogous expressions for the boundary conditions can be found in any textbook on the subject [5, 6, 31]. The fluid PML begins after the fluid physical domain as shown in figure 7.1. This is attained by performing the aforementioned change of variables described below in more detail. There have been several proposed functions for the PML (see references 23-25 of [90]), one of the most popular will be adopted here since it has given good results in previous studies [66]. The function to be used in the PML interval $[y_f, y_{PML}]$ is as follows:

$$\gamma(y) = 1 + \frac{i}{\omega}\sigma(y) \tag{7.2}$$

where ω is the angular frequency, y is the coordinate through the thickness of the plate (perpendicular to the propagation direction) and with σ given by:

$$\sigma(y) = A\omega \left(\frac{y - y_f}{y_{PML} - y_f} \right)^m \tag{7.3}$$

where A and m are parameters which can be adjusted for each problem, see [88, 91] for a good discussion about the influence of these parameters on the results. y_f is the endpoint of the physical fluid layer and where the PML begins, y_{PML} is the endpoint of the PML. These two values should also be changed from problem to problem and, as it will be seen, even within the same problem, in order to obtain the correct solution. In the physical fluid region $[0, y_f]$ one takes $\gamma(y) = 1$. All these parameters will be further discussed in the next subsection for each of the presented examples.

The above PML function (eq. (7.2)) gives the following change of coordinates for y:

$$y \longrightarrow \tilde{y} = \int_0^y \gamma(s)\mathrm{d}s \tag{7.4}$$

Using Leibniz's rule for the derivatives one has:

$$\frac{d}{dy} \longrightarrow \frac{d}{d\tilde{y}} = \frac{1}{S(y)}\frac{d}{dy} \tag{7.5}$$

where, from equations (7.2) and (7.4), in the PML range $[y_f, y_{PML}]$ one has
:

$$S(y) = \frac{d\tilde{y}}{dy} = 1 + \frac{i}{\omega}\sigma(y) \tag{7.6}$$

and for the second derivatives:

$$\frac{d^2}{dy^2} \longrightarrow \frac{d^2}{d\tilde{y}^2} = \frac{1}{S^2(y)}\frac{d^2}{dy^2} - \frac{1}{S^3(y)}\frac{dS(y)}{dy}\frac{d}{dy} \tag{7.7}$$

Formulae (7.5), (7.6) and (7.7) should be substituted in equation (7.1) in order to obtain the corresponding PML equations of motion:

$$\left(\frac{1}{S^2(y)}\frac{d^2}{dy^2} - \frac{1}{S^3(y)}\frac{dS(y)}{dy}\frac{d}{dy} - k^2 + \rho\omega^2\right)\Phi_f = 0 \tag{7.8}$$

Similar PML equations with extra factors will hold for the boundary and interface conditions, these can be easily derived from the unmodified versions available in any textbook on guided waves [31, 6, 5]. As it was to be expected, those unmodified equations for the fluid physical domain are recovered from equation (7.8) upon taking $\gamma(y) = 1$ in equation (7.4) and proceeding as indicated. All the functions and derivatives defined above can be seen to be continuous at the boundary point y_f between the physical fluid and the fluid PML, hence the term *Perfectly Matched Layer*.

At the end of the PML (see figure 7.1), the following boundary condition for the fluid's potential Φ_f can be taken:

$$\frac{d\Phi_f}{dy}(y_{PML}) = 0 \tag{7.9}$$

but the amplitude of the fields at this end will be seen to vanish or be negligible for physically acceptable solutions.

The modified equation for the fluid longitudinal potential, the equations for the solid layer and the boundary and interface conditions are discretized in the usual way and the PSCM scheme is set up and linearized using the *Companion Matrix Method*, explained in Chapter 3, more details about this procedure can be found in [45, 21, 46, 63, 66]. The equations for the potential description of an isotropic solid and those for an anisotropic medium can be found in [5]. Once the general eigenvalue problem is posed, it can be readily solved with an eigensolver routine and the complex wavenumbers

(the eigenvalues) for a given ω obtained as well as the mode shapes (eigenvectors).

For the cylindrical case the equations of motion, boundary and interface conditions can be found in [5, 6, 31], the PML equations are obtained from the above by following the same procedure to obtain equation (7.8) after making the following formal change in equations (7.2) to (7.6), see also [66, 92, 99, 100]:

$$y \longrightarrow r \tag{7.10}$$

7.2 Validation of the PSCM-PML: isotropic and hexagonal fluid-loaded elastic waveguides in flat and cylindrical geometries.

In this section, several problems of practical interest are used to illustrate and validate the PSCM-PML approach.

The flat isotropic elastic plate immersed in fluid is presented first since isotropic materials, being the simplest, only have 2 independent elastic constants in their stiffness matrix. The dispersion curves and attenuation for the symmetric modes are shown in figures 7.2.a and 7.2.b. The red circles are the solutions given by the PSCM-PML and the solid black lines are those obtained with the software DISPERSE based on a PWRF routine. It can be seen that the agreement is excellent. The mode shapes for three modes at roughly ~ 0.45 MHz, marked in the figures with blue asterisks, are presented in figure 7.3. In the (solid) region of the waveguide, where no exponential increase or decrease of the amplitude exists, they also showed excellent agreement with those given by DISPERSE. As it was to be expected, in the fluid region outside of the waveguide, DISPERSE showed an exponential increase of the wave's amplitude with distance from the plate, whereas the PSCM-PML solution shows a decline of the far field because of the presence of the PML. The mode shapes are interpreted as follows: in black is plotted the displacement field in the solid structure, in blue the displacement field in the fluid and in red the displacement field in the PML. It can be seen how the amplitude of the wave in the fluid (showing in blue) decreases exponentially in the PML region (showing in red), this is precisely the aforementioned effect of the PML on every wave travelling within it. Had the PML not been present, the leaky wave's amplitude would have kept on increasing exponentially instead of decreasing thus rendering the computation inaccurate due to the unwanted reflections taking place at the end of the truncated domain. The numerical data for the steel plate and cylinder to be presented as well as for the values used for the water can be found in section 7.5 at the end.

For this case, the PML parameters were $A = 2\pi$ and $m = 2$. The grid in the fluid layer had $N = 120$ grid points of which 78 formed the PML. The thickness of the fluid layer was $H_f \sim 3\ h_{sol}$ where $h_{sol} = 5$ mm is the plate half-thickness. It is clear that, for a given thickness of the fluid layer, the higher the number of grid points in the PML, whereby its thickness increases, the closer the PML lies from the interface with the plate. For leaky modes in general, it is convenient to place the PML as close to this interface as possible so that the leaky modes enter the PML before they have had time for growing too much. By doing this, the PML manages to attenuate the mode enough in order to attain complete or almost vanishing amplitude at the end of the PML and minimize the effect of unwanted reflections. The effects of the PML parameters on the spectrum have been studied elsewhere, see [103, 88, 102, 90, 91, 92] for instance, but it is noteworthy and fortunate that the general remarks, analytical and numerical, presented in those studies were found to remain valid for the PSCM-PML combination thus providing guidance when choosing the above values for the PML parameters, the reader is referred to the aforementioned papers and references therein for further details.

In order to obtain clean dispersion curves and eliminate the spurious modes, careful post-processing is needed. In the codes used for these examples, the filtering process proceeded in two stages. Firstly, in order to ensure convergence, every computation was run for two different values of N and compared; while the lower resolution solution was used for filtering, to be explained next. The lower resolution iteration in this case had $N = 100$ of which 80 points formed the PML.

The real part of the wavenumber was found to have slightly better convergence than the imaginary part so it was the perfect candidate for a filtering criterion. Also, as is common in discretized approaches, spurious solutions depend strongly on the number of grid points. This phenomenon was also observed in our simulations where the spurious resonances contaminating the solution underwent drastic changes when small changes in N were made.

In practice and for most of the frequency range shown, only modes whose absolute value of the difference between the real parts of the wavenumber in both iterations was less than 1 m^{-1} were retained. For the last modes in the range, roughly from ~ 2.5 MHz upwards, this difference had to be increased to 10 m^{-1} because of the higher value of the real part of the wavenumber. Note that, in both cases, the relative error is no more than $0.1 - 1\%$ in the whole range, which is an excellent result in terms of convergence. After this first convergence check stage most of the radiative modes were eliminated, sometimes even all of them. Note that the terminology found in the liter-
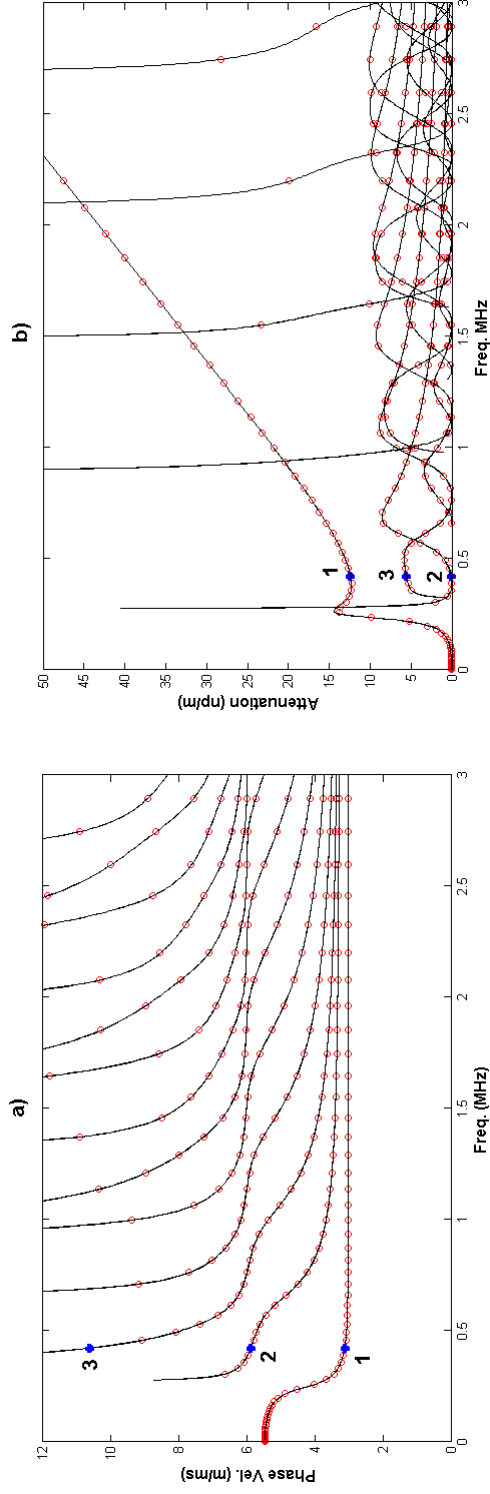
Figure 7.2: Dispersion (a) and attenuation (b) curves for symmetric leaky modes in an immersed 10 mm thick elastic steel plate. The solutions obtained by the PSCM-PML are given in red circles and those given by DISPERSE plotted in solid black lines. Propagation takes place along the {z} axis and the {y} axis is perpendicular to the plane of the plate. SH modes are not computed because the code was designed only for Lamb modes. This is because SH modes, being shear and the fluid being ideal, will not couple to the fluid and hence do not radiate. The SH modes of a plate immersed in an ideal fluid are just the SH modes of the same plate in vacuum since the boundary conditions in both cases are the same.

Figure 7.3: Mode shapes from the PSCM-PML for the three symmetric modes marked with blue asterisks in figure 7.2 at ~ 0.45 MHz. Only the half-thickness is plotted. The solid region showing in black, fluid region in blue and fluid PML in red.

ature, namely radiative modes, for the spurious resonances and discretized continuous spectrum can be potentially misleading. These are not to be confused with the sought true resonances or leaky waves which in fact radiate energy into the surrounding medium.
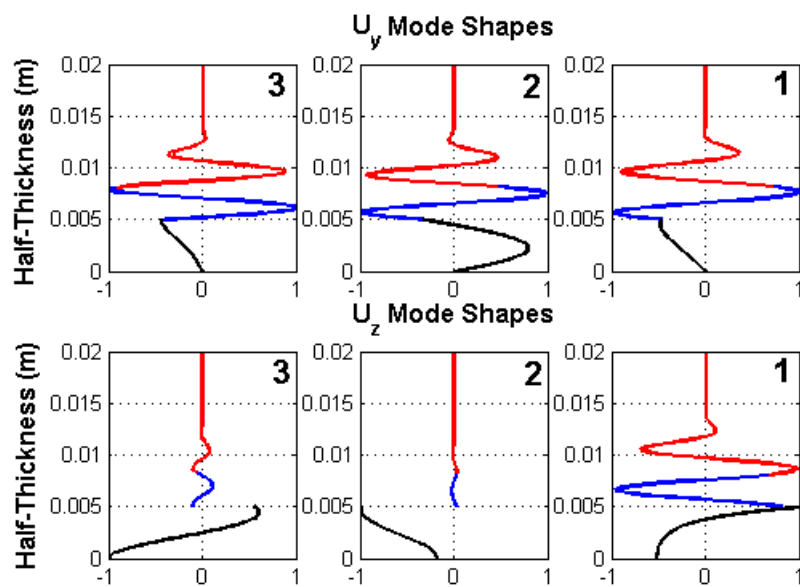
In order to double check the results obtained from the previous filter and eliminate the remaining spurious modes completely, a second filter based on more physical arguments was introduced. This second filtering stage is based on the energy carried by the wave and it is a natural generalization of the kinetic energy of an arbitrary continuous body. The expression is given also in [90, 91] but it is reproduced here for convenience.

$$E_i = \frac{1}{2} \int_{-h_i}^{h_i} \rho_i \mathbf{v}_i^{\dagger} \mathbf{v}_i \, \mathrm{d}y_i \qquad (7.11)$$

where the subindex i refers to the layer being considered (waveguide or core, fluid layer and PML), h_i is the thickness of the i-th layer, ρ_i its density, $\mathbf{v}_i = \frac{\partial \mathbf{u}_i}{\partial t}$ is its displacement velocity column vector, the dagger indicates transposition and complex conjugation and the integration is performed through the thickness of the system so that E_i has units of energy per unit length [J/m].

In the course of this investigation, it has been observed that, as it was to be expected, the energy of the leaky modes is primarily concentrated within the waveguide whereas that of radiative modes is primarily concentrated outside of the waveguide. The difference between the energies in the plate for leaky and radiative modes was of one order of magnitude or bigger. Thus, the second filtering stage checked the differences between adjacent modes and detected the mode for which the aforesaid leap took place. That radiative mode and the subsequent lower radiative modes were eliminated and only the leaky physical solution retained. Another alternative [90, 91] to be introduced and used later in this investigation consists of considering the fraction of the total energy which goes into the PML in order to sort the results accordingly.

It must be noted that radiative modes were mostly found in the lower part of the dispersion curves' diagram. After having selected only those eigenvalues with a low imaginary to real part of wavenumber ratio (propagating modes, see [63]), then they were ordered according to their absolute values and a clear boundary separating leaky and radiative modes was found. This has facilitated greatly the filtering labour since, once the first and highest radiative mode was found, it was straightforward to discard all the other lower radiative modes. This is in agreement with the spectrum structure presented in [103, 90] which is discussed in Section IV. In figures 7.4.a and

7.4.b, the dispersion curves and attenuation for antisymmetric modes computed by the PSCM-PML (red for those above the 1.5 m/ms, sound velocity in water, and blue for those below) are presented before any filtering. For guidance, the solutions given by DISPERSE are also given in solid black lines.

The radiative modes can be seen to lie mostly at the bottom of the figure making it almost impossible to distinguish the hidden Quasi-Scholte [108, 109] mode and the lowest antisymmetric mode. The difference with the next figures 7.5.a and 7.5.b where the filters were used is striking, especially in regard to the attenuation.

The dispersion curves and attenuation for the antisymmetric modes in the same immersed plate are shown in figures 7.5.a and 7.5.b. As before, red circles (leaky modes) and blue diamonds (Quasi-Scholte mode) are the solutions given by the PSCM-PML and the solid black lines are those obtained with the software DISPERSE which is based on a PWRF routine. For this family of modes, it was not possible to obtain satisfactory results with good convergence in the region close to zero frequency due to the dominant presence of radiative modes which, in the complex plane, lie very close to the Quasi-Scholte mode and lowest antisymmetric mode. This is suspected to be the cause of the discrepancy between both sets of solutions in the attenuation plot of the lowest antisymmetric mode (fig.7.5.b at ~ 0.2 MHz) which was also found in examples of cubic and hexagonal plates. It must also be noted that, for the PWRF routine, this region is also very problematic and the results given close to zero frequency might not be fully reliable. A possible solution to this problem is mentioned in the last section discussing future work. Except for this, the agreement between both sets of solutions is again very good.

The mode shapes for three modes at ~ 0.75 MHz, marked in the figures with blue asterisks, are presented in figure 7.6. Note how, as in the symmetric mode shapes, the amplitude of the fields begins to grow in the fluid and as soon as it enters the PML the attenuation damps the mode until it vanishes at the end of the PML.

The Quasi-Scholte [108, 109] mode deserves a separate discussion because of its peculiar properties and because its computation requires a completely different set of parameters to those introduced above for the leaky modes. The Scholte mode is a particular case arising in solid-fluid interfaces for infinite half-spaces of the more general waves known as Stoneley waves propagating in solid-solid interfaces [5, 6, 31]. These waves are concentrated in the interface of the two half-spaces and the extent occupied by the field in the adjoining media decreases as the frequency increases which results in

211
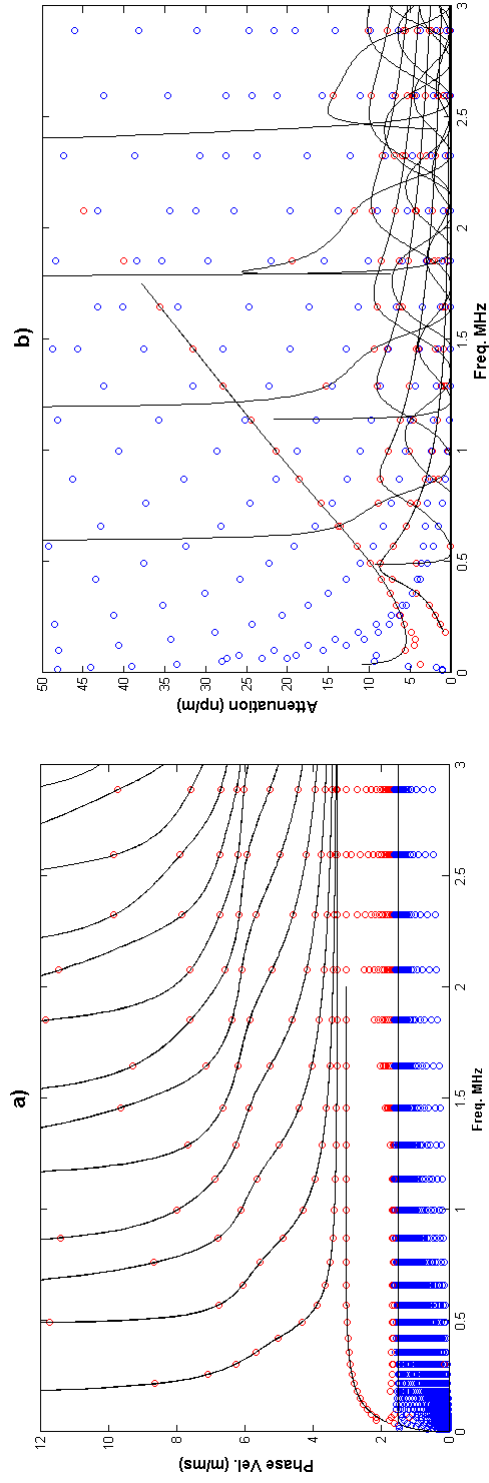
Figure 7.4: Unfiltered dispersion (a) and attenuation (b) curves for antisymmetric modes in an immersed 10 mm thick elastic steel plate. The solutions obtained by the PSCM-PML are given in circles: blue for those above the 1.5 m/ms (sound velocity in water) and red for those below. The solid black lines are the solutions given by DISPERSE. Propagation takes place along the {z} axis and the {y} axis is perpendicular to the plane of the plate. These figures illustrate how the radiative spurious modes (red circles mostly) make it difficult to differentiate the right curves clearly.
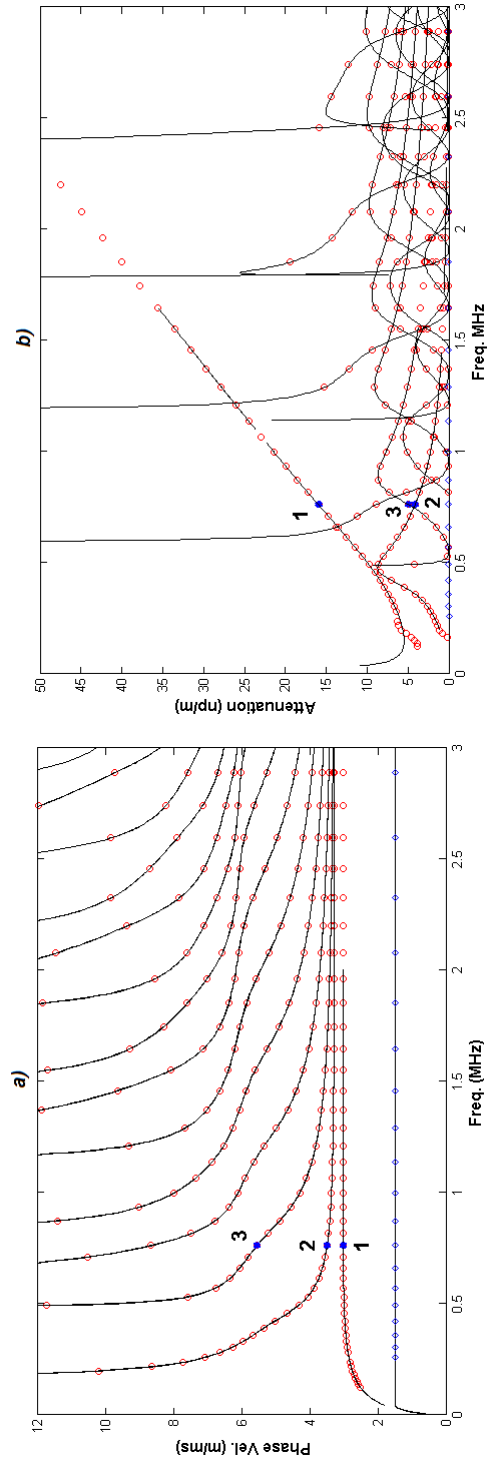
Figure 7.5: Filtered dispersion (a) and attenuation (b) curves for antisymmetric modes in the immersed 10 mm thick elastic steel plate showing in figure 7.4 after filtering. The solutions obtained by the PSCM-PML are given in red circles for leaky modes and in blue diamonds for the Quasi-Scholte mode. Solutions given by DISPERSE plotted in solid black lines. Propagation takes place along the {z} axis and the {y} axis is perpendicular to the plane of the plate.
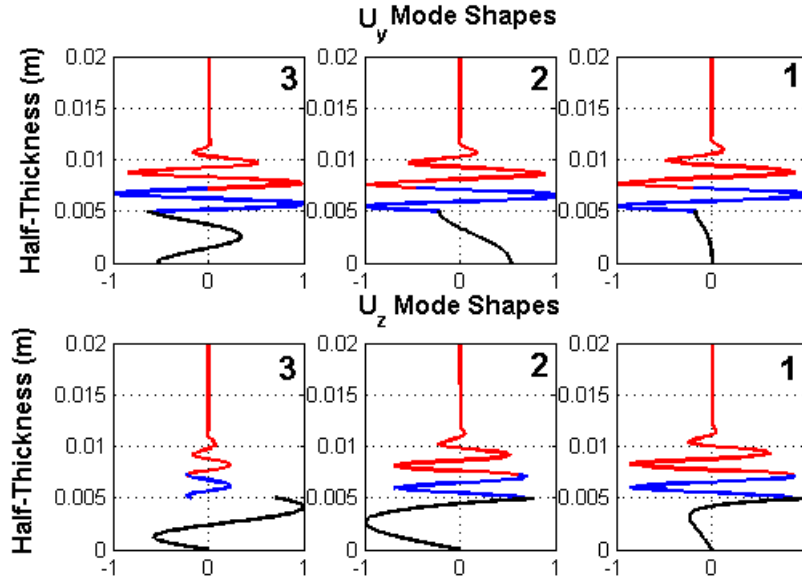
Figure 7.6: Mode shapes from the PSCM-PML for the three antisymmetric modes marked with blue asterisks in figure 7.5 at ∼ 0.75 MHz. Only the half-thickness is plotted. The solid region showing in black, fluid region in blue and fluid PML in red.

a smaller penetration length of the mode into fluid and solid. The Scholte mode at the single interface between two half-spaces can exist at any frequency and is perfectly non-dispersive, with a speed a little lower than that of bulk waves in the fluid. However, there is also a related mode, known as the Quasi-Scholte mode, which travels in an immersed layer. Now the waveguide has two boundaries, and the waves, whilst exhibiting broadly similar behaviour to the Scholte case, have frequency-dependent characteristics. At low frequency they have a low speed and are dispersive, but as frequency increases the speed converges on that of the Scholte wave. At the high frequency limit they tend to a pair of independent Scholte waves, one at each of the two fluid-solid interfaces. Both the Scholte and Quasi-Scholte modes trap the energy in the vicinity of the interface, and are perfectly non-attenuative; for more details see [108, 109].

The challenge posed by these modes to the PSCM-PML is to capture this behaviour in precisely the region most contaminated with spurious modes. In order to allow the characteristic exponential decay of the Quasi-Scholte mode in the fluid layer, the PML must be placed far from the solid-fluid interface and its thickness reduced, contrary to what happened with leaky

214

waves. By doing this, when the Quasi-Scholte mode reaches the PML its amplitude will almost be zero due to its exponential decay and the PML will reduce the wave's amplitude even further so that the limit of vanishing fields at infinity is correctly mimicked.

This exponential decay behaviour of the Quasi-Scholte mode (marked with a red asterisk in the dispersion curve in fig.7.5.a at ~ 1.65 MHz) can be seen perfectly in figure 7.7.a. A detail of the displacement field within the structure is given in figure 7.7.b. It can be clearly seen how the displacement vector field vanishes in the centre of the plate but it is non-zero towards the interface solid-liquid, as a consequence of this, the energy is concentrated towards the region around the solid-fluid interface.

Below, a table (table 7.1) is presented summarizing the different sets of parameters used to plot some of the 19 points of the quasi-Scholte mode shown in figures 7.5.a and 7.5.b. Only values for odd points are shown for brevity, though they capture the general trends of the parameters in the whole range. Note how the thickness of the fluid layer has been substantially increased with respect to the value used for leaky modes whereas the PML thickness has been significantly reduced in order to allow for the Quasi-Scholte mode to decay by itself before entering the PML. Note also that the value of the attenuation is practically zero: always of an order of magnitude less than 10^{-7} np/m which is a very good result. The numbers in the third row account for the fraction of grid points in the fluid layer which compose the PML (determining its thickness). These are taken with respect to the total $N = 120$ of the fluid layer, when the result is not an integer, the immediate next integer is assumed. The choice of these parameters and those for the other examples will be discussed shortly in more detail.

Point #	1	3	5	7	9	11	13	15	17	19
H_f/h_{sol}	60	57	55	35	30	18	18	18	18	15
N_{PML} Fraction	0.20	0.20	0.25	0.35	0.30	0.25	0.18	0.20	0.18	0.18
Attenuation (np/m) $\sim$	10^{-8}	10^{-7}	10^{-7}	10^{-7}	10^{-7}	10^{-7}	10^{-7}	10^{-7}	10^{-7}	10^{-7}

Table 7.1: PML parameters for the odd points of the Quais-Scholte mode plotted in figures 7.5.a, 7.5.b and 7.7. Point number 1 corresponds to the lowest frequency point of the Quasi-Scholte mode displayed.

It can be seen that the parameters are very different from the ones used for the leaky modes and vary across the frequency range. This trend is preserved for the more general anisotropic cases to be presented in both flat and cylindrical geometry. As the Quasi-Scholte mode approaches a surface wave and the energy becomes even more concentrated in the interface, with
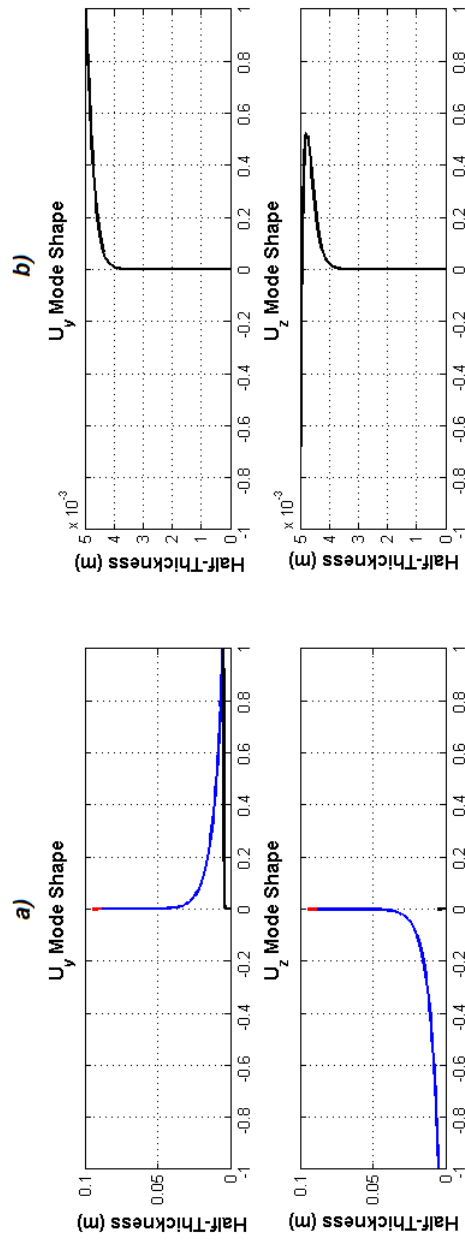
Figure 7.7: a): Mode shapes for the Quasi-Scholte mode marked with a red asterisk at ~ 1.65 MHz in figure 7.5. Only the half-thickness is plotted. The solid region showing in black, fluid region in blue and fluid PML in red. b): Solid region detail of the Quasi-Scholte mode presented in a).

216

the consequent stronger exponential decay, it can be seen that the distance from the interface solid-fluid to the beginning of the PML can be reduced. The fraction of the grid points used for the PML varies much less though, due to the reduction of the fluid layer's thickness, the PML thickness is reduced accordingly. The order of magnitude for the attenuation of the Quasi-Scholte mode is seen to be extremely small, thus providing confirmation of the known non-decaying (zero attenuation) nature of the mode.

To finish with the study of isotropic immersed waveguides the results for a hollow elastic isotropic 5mm thick cylinder with inner radius $r_i = 20$mm immersed in water are presented along with the necessary settings. The discussion is briefer since the same principles regarding the PML values can be applied here.

The parameters' values used for this problem differ slightly from those used in the flat plate but show the same trends in regard to leaky modes and to the Quasi-Scholte mode. The number of grid points in the fluid was $N = 100$ of which 70 constituted the PML. The parameters of the fluid layer and PML are similar to those used before with $H_f \sim 3 - 3.5 \quad h_{sol}$ where $h_{sol} = 5$ mm is the thickness of the cylindrical shell whose internal radius is $r_i = 20$mm. The PML parameters are again $A = 2\pi$ and $m = 2$.

Once more, two filtering stages are introduced. In the first, convergence is checked in an analogous way as that described for the plate with a tolerance of $\Delta \mathrm{Re}\{k\} = 0.5 - 1 \text{ m}^{-1}$ for the real part of the wavenumber (again giving a relative error between iterations similar to the one obtained in the flat case). The lower resolution iteration was carried out with $N = 80$ of which 64 constituted the PML, as before the highest resolution solution is shown here. The second filter checks the energy distribution of the modes and for this case, it has been found more convenient and useful to use the distribution of energy of the modes to identify the physically acceptable solutions.

For physically acceptable solutions most of the energy is concentrated in the solid and fluid domains whereas the energy in the PML is much smaller. The opposite situation is found for radiative spurious modes. This observation motivates the aforementioned alternative filter based on the fraction of the total energy which goes into the PML. The percentage of energy compared to the total which is found in the physically meaningful domains (solid and fluid) is found to be greater than $50 - 60\%$ for leaky and Quasi-Scholte modes and much smaller for radiative modes. This alternative filter was also proposed and successfully used in [90, 91, 92]. It must be emphasized that a similar splitting of energy into the different domains takes place generally for any waveguide. In particular, this was also the case in the previously studied flat isotropic immersed plate but there, the first filtering option was

found to perform better than the one just introduced. Finding the appropriate combination of parameters for leaky waves is fairly easy and can be done well within one hour starting with a PML directly attached to the core. If results are not satisfactory in terms of convergence or energy distribution, more iterations for a PML placed further away should be made until the best set is found, this is tipically achieved within two or three more iterations. Note that increasing the PML distance to the core unecessarily will yield poor results because the function will grow too much to be attenuated by the PML. These iterations are made for a few equispaced values of the frequency in the desired range, it is by no means necessary to cover the whole range at this stage. For the Quasi-Scholte mode, finding the appropriate combination of parameters takes a longer period of time, tipically about 2 to 3 hours. It usually happens that one set of parameters is a very good starting point, sometimes even the appropriate choice, for a different problem. This is the reason why they have been given in the text and in section 7.5.

The dispersion curves and attenuation for the axially symmetric modes propagating along the cylinder axis are shown in figures 7.8.a and 7.8.b. As before, red circles (leaky modes) and blue diamonds (Quasi-Scholte mode) are the solutions given by the PSCM-PML and the solid black lines are those obtained with the software DISPERSE, which uses a PWRF routine. It is worth noting that for this geometry, most of the modes can be traced back towards zero frequency much further than in the flat case.

Note that the mode right above the Quasi-Scholte is axially symmetric and, as can be seen from figures 7.8.a and 7.8.b, it is highly attenuative. A mode of similar features was also reported in [96].

Finally, for the Quasi-Scholte mode in the cylinder, the PML parameters had to be readjusted a little but not as much as for the flat case, the most notable difference was in the fluid layer thickness which, for most of the frequency range, was $H_f \sim 6 \quad h_{sol}$. It must be noted that, even for the larger frequency ranges, the Quasi-Scholte mode was still found using the same PML parameters as for the leaky waves. However, the above value provided with a better behaviour of the mode at infinity and thus was kept as a better result. In the region close to zero frequency however, where the mode is actually dispersive and a larger fraction of energy goes deeper into both media, good results were achieved with similar values as those used for leaky modes.

The attenuation of the quasi-Scholte mode was $\sim 10^{-3}$ Np/m for most of the range shown although in some regions, specially ~ 0.2 MHz, it was not possible to attain better and stable values than 0.1 Np/m. This and the fact that the attenuation could not be reduced down to $\sim 10^{-7}$ Np/m

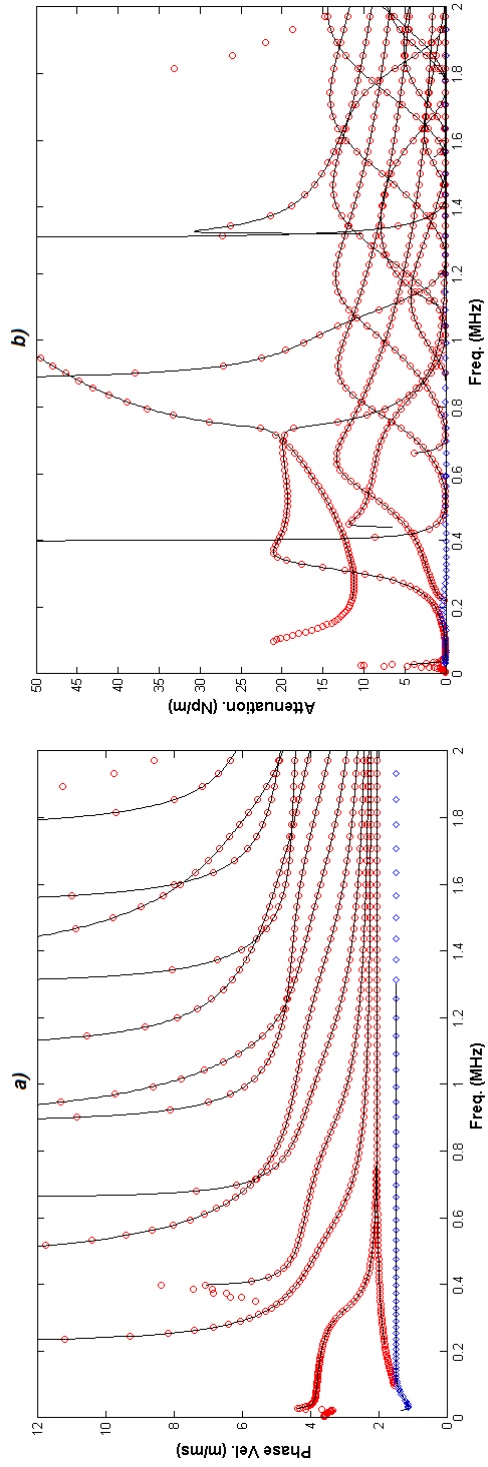Figure 7.8: Dispersion (a) and attenuation (b) curves for axisymmetric modes propagating axially in an immersed hollow elastic brass cylinder of internal radius $r_i = 20$ mm and 5 mm of wall thickness with vacuum inside. The solutions obtained by the PSCM-PML are given in red circles for leaky modes and in blue diamonds for the Quasi-Scholte mode. Solutions given by DISPERSE plotted in solid black lines.

as in the flat plate is most likely caused by the failure to achieve as good an exponential decay in the fluid region as the one observed in the flat case. The Quasi-Scholte mode shape showed a sharp, almost exponential, decay in the fluid domain and the first part of the PML but oscillations towards the end of the PML cause the amplitude of the tangential field to be non-zero at the end of the PML. Several attempts were made to compute the Quasi-Scholte mode with a set of PML parameters more similar to the one used in the flat case, that is, with a much thicker fluid region and thinner PML, but the results were found to be even worse. In spite of this, its convergence for different N and that of the other modes is excellent, the real and imaginary parts agree very well with the results given by DISPERSE and the mode shapes of the Quasi-Scholte mode within the cylinder region matched excellently those given by DISPERSE. For a more detailed discussion about the Quasi-Scholte mode and its applications to NDE the reader can see [108, 109].

To complete the validation of the PSCM-PML the results for hexagonal (transversely isotropic) fluid-loaded waveguides are presented and compared to those computed using DISPERSE as it was done in the isotropic case. The first example is the immersed elastic transversely isotropic plate. The symmetric modes' dispersion curves and attenuation are shown in figures 7.9.a and 7.9.b respectively. For the antisymmetric modes, the dispersion curves and attenuation are show in figures 7.10.a and 7.10.b respectively. In both figures, the red circles correspond to the solutions obtained by the PSCM-PML and the solid black lines to those obtained with DISPERSE. The line of blue asterisks at 1.479 m/ms in figure 7.10.a and with zero attenuation (see figure 7.10.b) correspond to the Quasi-Scholte mode. This mode was partly found by DISPERSE though is not reproduced in the figure for clarity. For this problem the number of grid points was $N = 100, 120$ for the two iterations, as before the results presented here are those for the highest N (highest resolution). The best match, contrary to the isotropic case, was found for a PML directly attached to the waveguide, so no physical fluid layer between PML and waveguide was present in this case and hence the PML had the same N as the waveguide. The plate half-thickness was $h_{sol} = 5$ mm and the PML thickness was taken to be $H_{PML} = 5\ h_{sol}$. The other PML parameters were as before $A = 2\pi$ and $m = 2$. In order to obtain the propagating regions of the dispersion branches as in the previous cases, only the modes with a wavenumber ratio $Im\{k\}/Re\{k\}$ smaller than 0.8 were kept. The first filter checks for accuracy of the results between both iterations, only modes whose absolute value of the difference between the real parts of the wavenumber in both iterations was less than 10^{-3} m^{-1} ($\Delta Re\{k\} = 10^{-3}$m^{-1}) were retained which gave relative errors of $\sim 10^{-3}$ % or less in the leaky modes. The second filtering stage checks the fraction of the total energy (waveguide and PML) in the physical domain

(only the waveguide in this case). For leaky modes the filtering threshold was set to $E_{SOLID} > 0.1\, E_{TOTAL}$. This is not as high as the 50-60% of the isotropic plate and might rise the question of whether or not these eigenvalues are true leaky modes at all. Fortunately, all doubts are dissipated when one looks at the fraction of the total energy for the discarded modes (spurious resonances and essential spectrum) which was found to be $E_{SOLID} \sim (10^{-5} - 10^{-11})\, E_{TOTAL}$, therefore it is clear that the retained modes have a much larger fraction of energy in the waveguide and thus are the sought physical leaky modes. It is also remarkable that the above choice of PML parameters works for the whole range of frequencies so there is no need of any further readjustment. The PML parameters for obtaining the Quasi-Scholte mode follow a similar trend to that shown in table 7.1 and are also tabulated (see table 7.2) in section 7.5 at the end, the physical parameters for the plate and water are also given there.

Interestingly, in this case the best fit to DISPERSE's solution is obtained with no fluid layer between the PML and the waveguide, in constrast with the situation in the isotropic plate where a fluid region existed between the PML and the waveguide. When checking the best choice of PML parameters the option of a fluid layer between PML and waveguide was also contemplated and analysed. In particular, the filter used for the isotropic plate which compared the orders of magnitude of the energy in the solid region was used. It was found that, for the lowest symmetric mode, in the frequency range $\sim 0.2 - 0.3$ MHz where it makes the turn (see figure 7.9), the threshold for the difference in E_{SOLID} between two adjacent modes (see paragraph immediately below equation (7.11) had to be increased by almost one order of magnitude compared to the rest of the frequency range. This was an indicator that the PML parameters had not been chosen appropriately and a different choice, given in the previous paragraph, was found to be the correct one. This was also reflected in the fact that no change of parameters whatsoever was needed in order to obtain the antisymmetric family of modes. The difference between the results obtained with and without a fluid layer between PML and waveguide were not drastic (mostly affecting only the lowest symmetric and antisymmetric modes in the attenuation peak region) but big enough to investigate different choices of parameters. This behaviour was also observed in a similar example with a plate of cubic material and it was also with the PML next to the waveguide when the best fit to DISPERSE's results was found. Unfortunately, from these results it is not possible to derive any empirical formula relating the distance of the PML to the waveguide to the problem's parameters. However, a good practical prescription or *rule of thumb* would be to keep the PML parameter choice which needs the least readjustment through the frequency range under study and if any further tuning of any parameter must be done, this has to be as smooth as possible. For instance, in the example just discussed, a change by
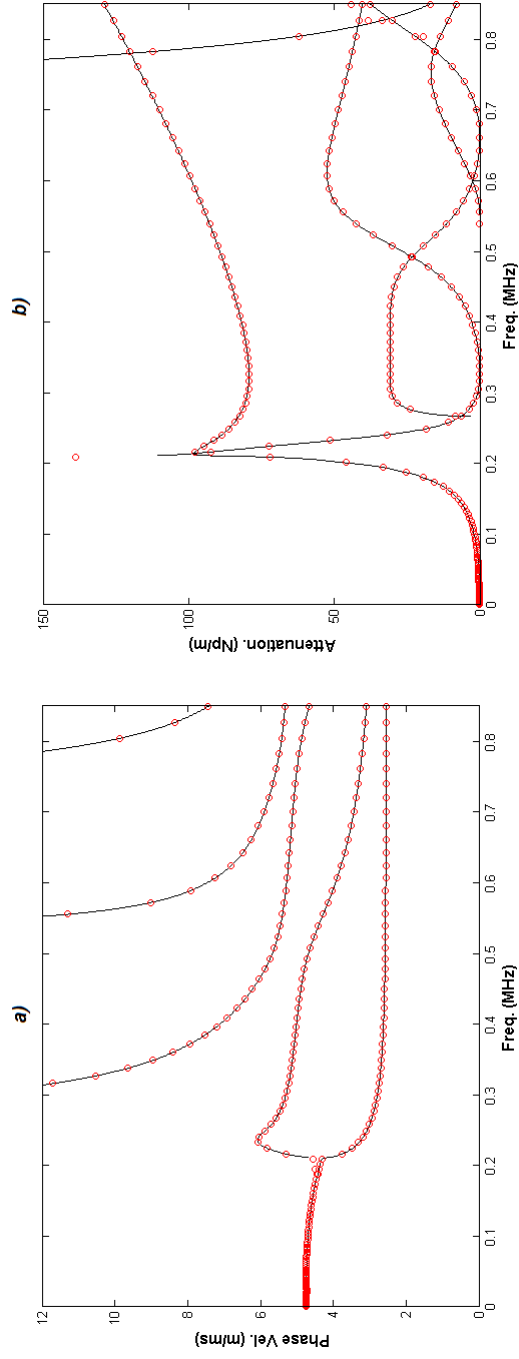
Figure 7.9: Dispersion (a) and attenuation (b) curves for symmetric leaky modes in an immersed 10 mm thick elastic hexagonal (transversely isotropic) plate. The solutions obtained by the PSCM-PML are given in red circles and those given by DISPERSE plotted in solid black lines. Propagation takes place along the {z} axis and the {y} axis is perpendicular to the plane of the plate. Crystal axes aligned with spatial ones just mentioned.

Figure 7.10: Dispersion (a) and attenuation (b) curves for antisymmetric modes in an immersed 10 mm thick elastic hexagonal (transversely isotropic) plate. The solutions obtained by the PSCM-PML are given in red circles for leaky modes and in blue asterisks for the Quasi-Scholte mode. Solutions given by DISPERSE plotted in solid black lines. Propagation takes place along the {z} axis and the {y} axis is perpendicular to the plane of the plate. Crystal axes are parallel to the axes of the plate.

one order of magnitude of a parameters in a limited region of the frequency range studied is anything but smooth and therefore, other PML parameters choices should be sought.

To close this section the results for the axially symmetric modes in a transversely isotropic rod are presented and compared to the solution given by DISPERSE. The dispersion curves and attenuation can be seen in figures 7.11.a and 7.11.b respectively. The blue circles correspond to the leaky modes found with the PSCM-PML approach and the red diamonds at the bottom correspond to the Quasi-Scholte mode also found by the PSCM-PML. DISPERSE's solution is showing in black solid lines. The agreement between both sets of solutions is excellent. In figure 7.12, the mode shapes for the four lowest modes at 2.5 MHz are shown, the one on the right hand side corresponds to the Quasi-Scholte mode and shows clearly the desired exponential decay. These mode shapes were also compared to DISPERSE in order to double check the results and excellent match was found again. The PML parameters for the leaky modes in this case are as follows: $N = 80, 100$ for each region (waveguide and fluid), the radius of the rod was $r_{rod} = 5$ mm, the fluid layer had a thickness of $H_F = 2.8\ r_{rod}$, in each iteration with different values of N, the PML had 64 and 70 grid points respectively, $A = 2\pi$, $m = 2$, $E_{SOLID} > 0.5\ E_{TOTAL}$ and $\Delta \mathrm{Re}\{k\} = 1\mathrm{m}^{-1}$ (giving a relative error of 0.1 % or less). The PML parameters needed for the Quasi-Scholte mode are given in table 7.3 in section 7.5 at the end. The physical properties of the waveguide and fluid are the same as for the flat hexagonal plate studied previously.

7.3   Orthorhombic fluid-loaded elastic waveguides in flat and cylindrical geometries.

In this section, the validated PSCM-PML codes are used to compute the dispersion curves of an orthorhombic waveguide loaded with fluid in cylindrical and flat geometries. Orthorhombic materials are more challenging than transversely isotropic since they have 9 independent stiffness constants whereas the hexagonal materials have only 5. To the best of my knowledge there are no results to compare with for these types of waveguides in flat or cylindrical geometries so the main guidance to obtain the solution will be the filters introduced above, checking accuracy for different N iterations and total energy fraction in physical regions; the mode shapes, in particular that of the elusive Quasi-Scholte mode and finally the eigenvalue spectrum structure.

As before the first problem to be addressed is an immersed orthorhombic flat plate. The dispersion curves and attenuation can be seen in figures
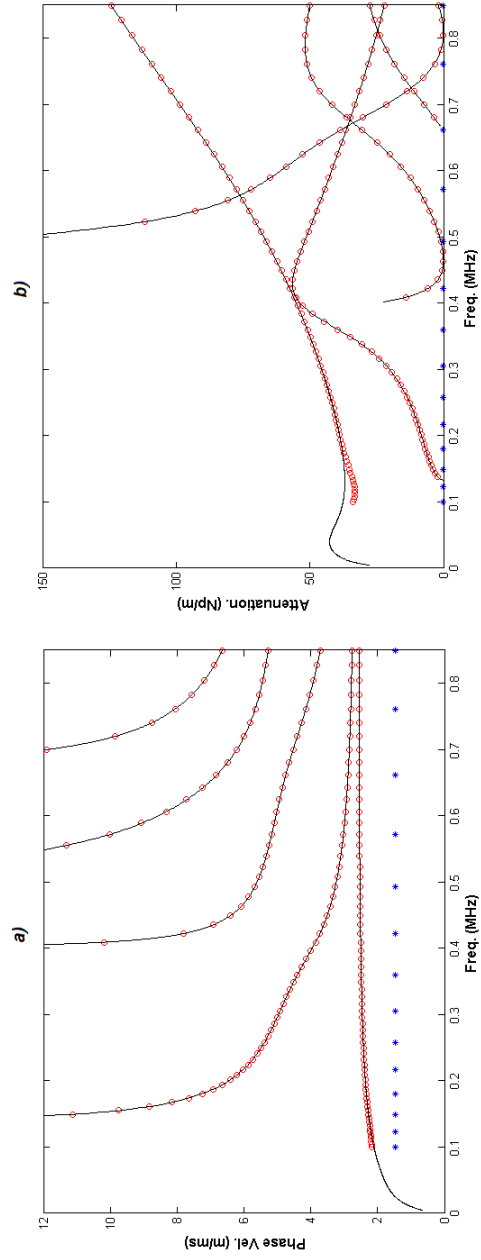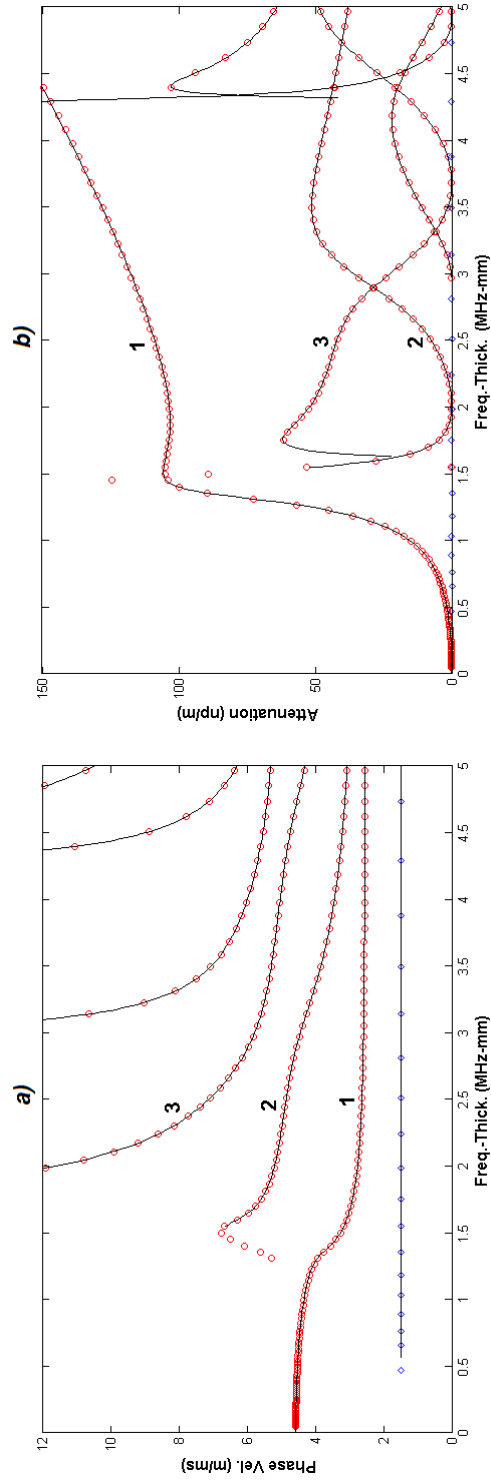
Figure 7.11: Dispersion (a) and attenuation (b) curves for axisymmetric modes propagating axially in an immersed elastic hexagonal (transversely isotropic) rod with radius $r_{rod} = 5$ mm. The solutions obtained by the PSCM-PML are given in red circles for leaky modes and in blue diamonds for the Quasi-Scholte mode. Solutions given by DISPERSE plotted in solid black lines. Crystal axes are parallel to the axes of the cylinder.

Figure 7.12: Mode shapes from the PSCM-PML for the three lowest axially symmetric modes and Quasi-Scholte (right hand side) mode at 2.5 MHz in the hexagonal rod of figure 7.11. The solid region (waveguide) showing in black, fluid region in blue and fluid PML in red. The vertical axis for the Quasi-Scholte mode reaches a higher value because of the necessary increase of thickness of the fluid-PML layers in order to compute it.

7.13.a and 7.13.b respectively. The symmetric modes are plotted in blue circles, antisymmetric modes in black asterisks and the Quasi-Scholte mode in red diamonds. The first attempt was obviously made by using the same choice of PML parameters as the one used for the hexagonal case. This combination was found inefficient and many spurious resonances and essential spectrum were plotted along with the true leaky modes. Fortunately, only the filter which checks the fraction of total energy which goes into the waveguide needed adjustment, the right threshold for leaky modes was $E_{SOLID} > 0.01 \, E_{TOTAL}$, this is again an order of magnitude less that the one used for the hexagonal case but the spurious resonances and essential spectrum were found in the range $E_{SOLID} \sim 10^{-5} \, E_{TOTAL}$ or less, the rest of the parameters are the same as those used for the hexagonal plate described above including plate half-thickness, $\Delta \mathrm{Re}\{k\}$ and relative error below 10^{-3} %. Note that the energy threshold is set higher (0.01) than the approximate range of values found ($\sim 10^{-5}$) in order to ensure leaky modes are retained. At certain frequencies some spurious resonances or essential spectrum can have a slightly higher fraction of energy if they lie close to the leaky modes and hence setting the energy threshold to (10^{-5}) would yield wrong results.
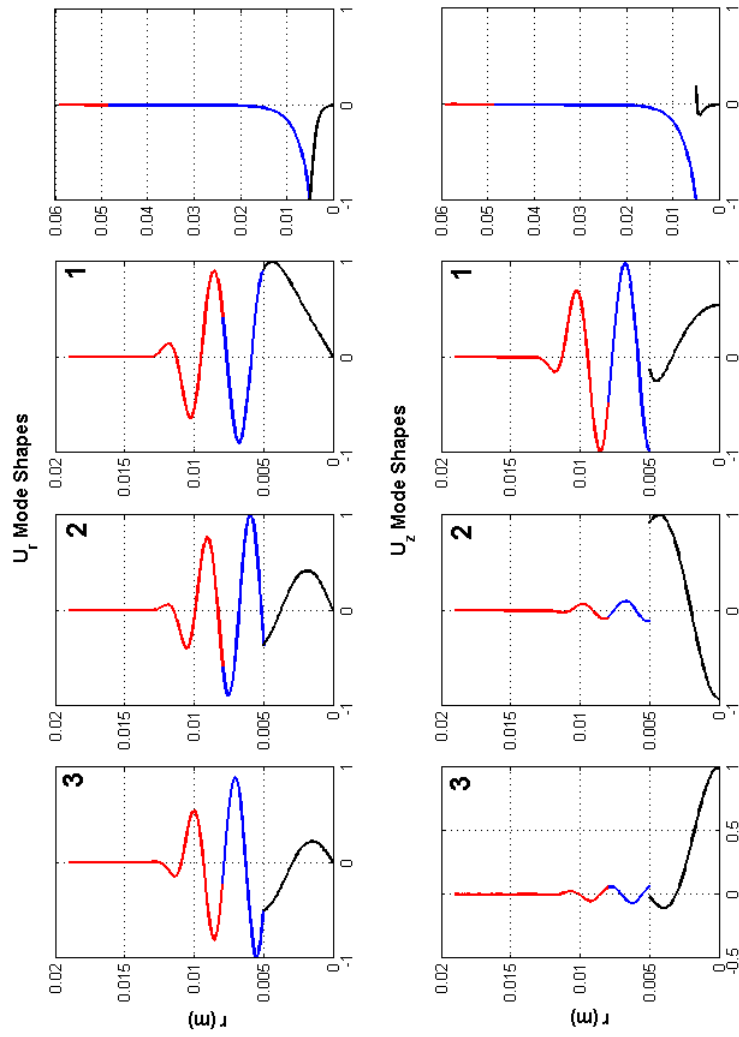
The mode shapes for the lowest antisymmetric mode and for the Quasi-Scholte mode at 0.21 MHz are presented in figure 7.14, the black line represents the field in the solid waveguide, the blue line in the fluid layer (if any) and the red line the fields in the PML. Note that no blue region is showing for the leaky mode since the PML has been taken to lie next to the waveguide. The Quasi-Scholte mode shows the desired exponential decay and its phase velocity lies below that of longitudinal waves in water, the PML parameters to obtain it are tabulated in section 7.5, see table 7.4.

The results for axially symmetric modes in a hollow cylindrical waveguide of the same material are presented next. Dispersion curves and attenuation for this problem are shown in figures 7.15.a and 7.15.b respectively, the blue circles are the longitudinal modes and the black diamonds correspond to the Quasi-Scholte mode. The cylinder has an inner radius of $r_i = 5$ mm and wall thickness of $h_{sol} = 20$ mm, the rest of the material and fluid properties are the same as in the previous flat waveguide. Again a first search was performed with the same PML parameters as those used in the hexagonal case. It was found that the threshold for the total fraction of energy in the physical region (waveguide and fluid) had to be adjusted slightly as the frequency increased, $E_{SOLID} > 0.50 \, E_{TOTAL}$ in the first third of the frequency range, $E_{SOLID} > 0.55 \, E_{TOTAL}$ in the middle third and $E_{SOLID} > 0.65 \, E_{TOTAL}$ in the last third. This is a good example of the prescription given above: one of the parameters needs to be adjusted but its progression is smooth and without any abrupt changes throughout the frequency range. The accuracy
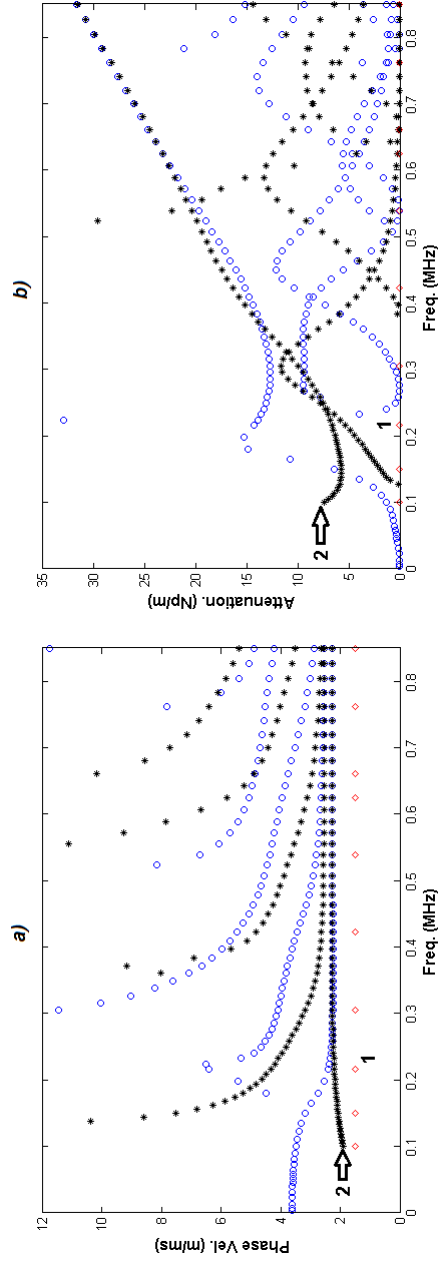
Figure 7.13: Dispersion (a) and attenuation (b) curves obtained with the PSCM-PML for symmetric (blue circles), antisymmetric (black asterisks) leaky modes and Quasi-Scholte mode (red diamonds) in an immersed 10 mm thick elastic orthorhombic plate. Propagation takes place along the {z} axis and the {y} axis is perpendicular to the plane of the plate. Crystal axes are parallel to the axes of the plate.
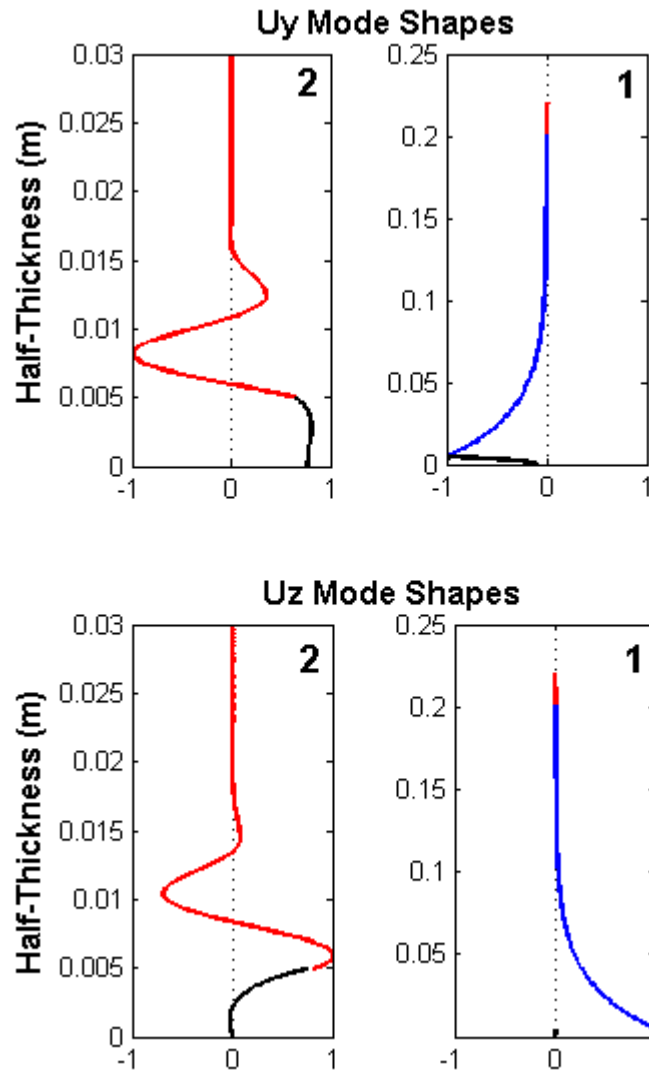
Figure 7.14: Mode shapes from the PSCM-PML for the lowest antisymmetric mode (left) and Quasi-Scholte (right) mode at 0.21 MHz in the orthorhombic plate of figure 7.13 (see corresponding numbers). The solid region (waveguide) showing in black, fluid region in blue and fluid PML in red. The vertical axis for the Quasi-Scholte mode reaches a higher value because of the necessary increase of thickness of the fluid-PML layers in order to compute it.

for the different N iteration is still $\Delta\mathrm{Re}\{k\} = 1\mathrm{m}^{-1}$ (giving a relative error of 0.01 % or less). The mode shapes for the lowest longitudinal mode and the Quasi-Scholte mode at 0.76 MHz are given in figure 7.16, again the desired exponential decay for the Quasi-Scholte mode is correctly captured. The PML parameters for the Quasi-Scholte mode are tabulated in section 7.5 at the end, see table 7.5.

As indicated at the beginning of this section, similar eigenvalue spectrum analysis to that carried out in [103, 90, 91, 92] revealed, *regardless of material symmetry or geometry*, the same structure of the computed spectrum which is composed of the following eigenvalues: true resonances (point spectrum corresponding to the physical leaky modes), essential spectrum (corresponding to a continuum of modes propagating mainly in the fluid) and spurious resonances which do not correspond to any physical entity, they arise from the implementation. What here and in [90] are termed *radiative* modes comprise the latter two types of the list. The essential spectrum, appearing discretized as a consequence of the numerical implementation, though not of interest here, is not an incorrect solution. As it was to be expected (cf. [103, 90]), the part of the discretized essential spectrum computed appears as a straight line emanating from the real axis. The truly wrong results correspond to the spurious resonances which, in the complex plane, normally appear near the discretized essential spectrum and physical resonances (leaky modes) and do not follow any definite pattern, [103, 90]. Fortunately, by an appropriate choice of PML parameters they can be pushed far from the physical resonances (leaky modes) thus making their filtering easier.

Figure 7.17a.-c. shows the spectrum structure for the symmetric modes at different frequencies of the three immersed elastic flat plates studied in this chapter: isotropic at 2.6 MHz (a), hexagonal at 0.42 MHz (b) and orthorhombic at 0.57MHz (c). This similarity is of great help for assessing the correctness of the results when studying problems for which no prior results exists such as the orthorhombic waveguides investigated in this last section. It is expected that similar spectrum structures appear for more general anisotropic materials such as monoclinic or triclinic.

7.4 Discussion of Chapter 7

In this chapter a new combination of PSCM and a PML has been presented and validated to compute dispersion curves in immersed elastic orthorhombic waveguides in flat and cylindrical geometry.

The solutions given by the PSCM-PML algorithm for the isotropic and hexagonal immersed plates were compared to those given by the software
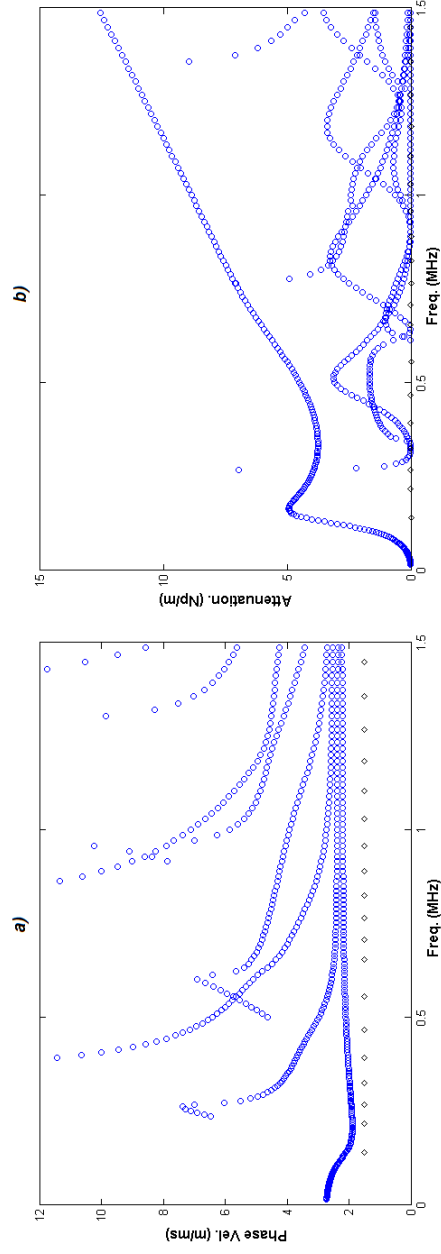
Figure 7.15: Dispersion (a) and attenuation (b) curves for axisymmetric modes (blue circles) and Quasi-Scholte mode (black diamonds) propagating axially in an immersed hollow elastic orthorhombic cylinder of internal radius $r_i = 5$ mm and $h_{sol} = 20$ mm of wall thickness with vacuum inside. Crystal axes are parallel to the axes of the cylinder.
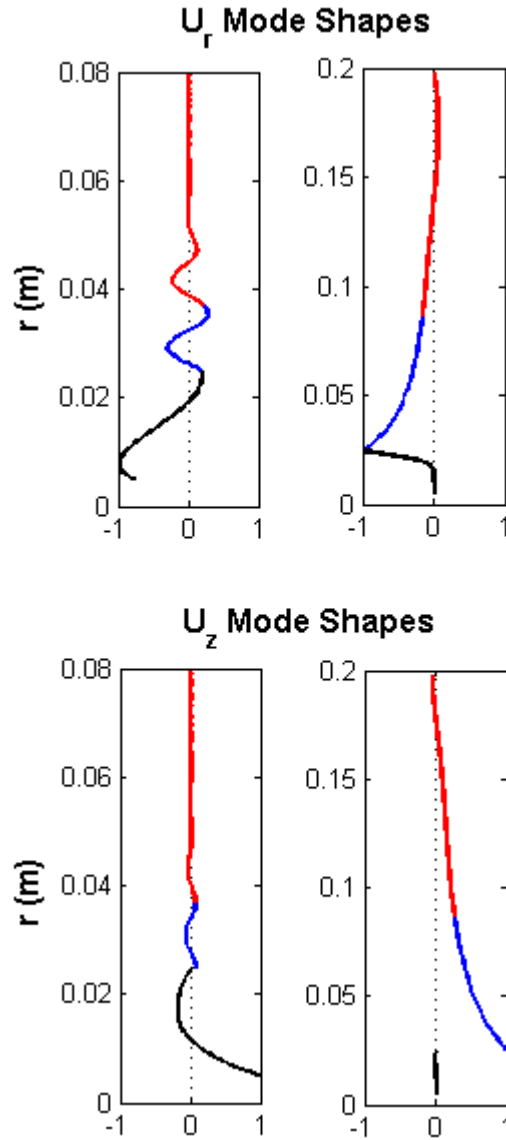
Figure 7.16: Mode shapes from the PSCM-PML for the lowest axially symmetric (left) mode and Quasi-Scholte (right) mode at 0.76 MHz in the orthorhombic cylinder of figure 7.15. The solid region (waveguide) showing in black, fluid region in blue and fluid PML in red. The vertical axis for the Quasi-Scholte mode reaches a higher value because of the necessary increase of thickness of the fluid-PML layers in order to compute it.
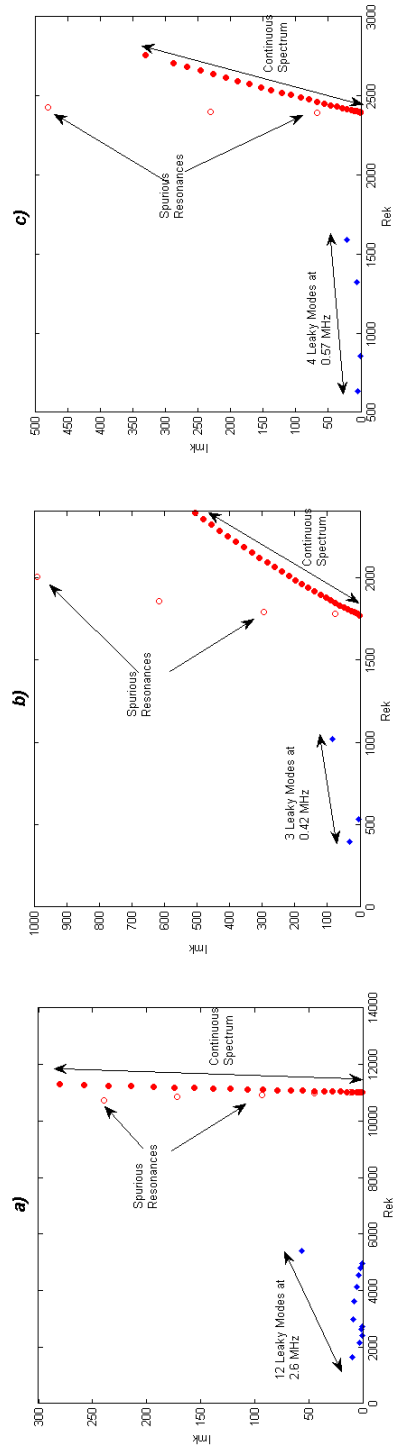
Figure 7.17: Spectrum structure of the three immersed plates studied in this chapter: symmetric leaky modes (solid blue diamonds), essential or continuous spectrum (red solid circles) and spurious resonances (empty red circles). For the isotropic plate showing in figure 7.2, the 12 symmetric leaky modes at 2.6 MHz are shown in (a), for the hexagonal plate showing in figure 7.9, the 3 symmetric leaky modes at 0.42 MHz are shown are shown in (b) and for the orthorhombic plate showing in figure 7.13, the 4 symmetric leaky modes at 0.57 MHz are shown are shown in (c). In these figures, the vertical axis is the wavenumber's imaginary part and the horizontal axis its real part.

DISPERSE based on PWRF routines. The agreement between the two sets of solutions was excellent for the frequency range studied. The PML managed to attenuate the leaky modes sufficiently so that vanishing amplitude was achieved at the PML's end. The exponential decay behaviour of the Quasi-Scholte mode in the plate was also achieved by increasing the thickness of the fluid domain and decreasing that of the PML obtaining again excellent results. However, it was not possible to extend the antisymmetric solutions as far back towards zero frequency as its symmetric counterparts.

The solutions given by the other PML-PSCM scheme for computing the dispersion curves of axially-symmetric guided waves (cf.[66] for the circumferential propagation problem with another PSCM-PML scheme) in an elastic isotropic and hexagonal immersed cylinders were also presented and compared to those given by DISPERSE again finding excellent agreement. Moreover, it was possible to find solutions even in the region close to zero frequency though the exponential decay of the Quasi-Scholte mode was not as good as the one attained in its flat counterpart. A notable improvement of these two PSCM-PML schemes with respect to the one presented in [66] is that the solutions were extended to a range of frequencies rather than to a few values. This task, as it was explained, is not trivial and requires a careful tuning of the parameters in order to obtain the correct results in each region.

In the two above problems, the solutions given by the PSCM-PML were filtered in two stages: in the first, convergence of results for different number of grid points N was sought, this showed to be a very efficient way of getting rid of most of the unwanted radiative spurious modes. In the second, a filter based on energy arguments was used to rule out the remaining spurious values, if any. It was shown by means of a figure how dramatic the difference is before and after this filtering process.

Section 7.3 presented the solutions (dispersion curves, attenuation and mode shapes) for fluid-loaded orthorhombic waveguides in flat and cylindrical geometry using the validated PSCM-PML combination. For leaky modes, the PML parameters used for their hexagonal counterparts proved to be an excellent starting point. Eventually, the same parameters used for the hexagonal waveguide gave good results for the orthorhombic case except for the energy based filter which needed some readjustment. Moreover, in order to ensure that the right solution was being selected at each frequency, the mode shapes and spectrum structure was also checked following the general guidelines given in the literature and which proved fruitful throughout the validation. In the future, it would be interesting to compute the solutions to these problems with a different approach such as the SAFE method used in [90, 91, 92] and compare them to the ones given in the present chapter. This would help gaining further understanding of how the PML works when

234

anisotropic waveguides are considered and would be a first step towards studying the most general cases of anisotropic materials.

The thickness of the fluid layer between the PML and the waveguide which was discussed in section 7.1, is an important point with far reaching consequences if one is interested in developing tools which need as little intervention on the part of the practitioner as possible. Currently and as the previous investigation and others cited here show, this thickness is almost solely dictated by the numerical features of each particular problem and it is not possible to know *a priori* what its optimum value should be. This question becomes even more important when one studies combinations for which little or no knowledge of the solution is available, a typical example are the dispersion curves of leaky modes in generally anisotropic immersed plates (see [110, 111, 85]). Fortunately, the qualitative behaviour of the PML studied in [103] can be very useful for a wider range of problems as the two new cases for orthorhombic waveguides presented here reflect. The spectrum structure is expected to undergo changes due to the change in the parameters of the problem (plate material, fluid and geometry) but its qualitative behaviour will retain the most characteristic features showing a similar distribution of physical resonances, essential spectrum and spurious resonances as was confirmed by the problems presented in this investigation, see figure 7.17.

Taking the above into account, a good future approach to fully autonomous codes and simulations for leaky modes would be to take the initial thickness of the fluid layer as zero and gradually increase it checking for self-convergence of the results obtained, the radiative modes should present very big changes, especially the spurious resonances. This should be supplemented by checks on the energy distribution amongst the different layers and most importantly, checking the difference in magnitude of the energy within the waveguide for leaky modes and the remaining radiative modes which is expected to be large. Finally, the geometrical structure of the spectrum [103] could be useful in cases where the essential spectrum begins significantly further from the true resonances. In such cases, and after the spurious resonances have been pushed far enough from the true resonances by adjusting the proximity of the PML to the waveguide, it should be possible to find a radius in the complex plane within which mostly, or even only, true resonances are found. This would work in any of the examples presented in figure 7.17. This extra check could be added to the above filters but it must be emphasized that the final results must *invariably* comply with the requirement of good convergence for different grid sizes.

Future work will also focus in further exploiting and developing PSCM-PML schemes for more general anisotropic materials such as monoclinic

or triclinic whose stiffness matrices do not have block form as those for isotropic, hexagonal or orthorhombic materials for instance.

7.5   Numerical data for examples of Chapter 7

In this brief section the parameters used for the computations presented in the chapter are given. The physical properties of the steel plate immersed in water presented in figures 7.2, 7.4, 7.5 and 7.4 are:

$$\rho = 7932 \text{ kg/m}^3; \qquad c_L = 5960 \text{ m/s}; \qquad c_S = 3260 \text{ m/s} \qquad (7.12)$$

The water for the above examples had the following specifications:

$$\rho = 1000 \text{ kg/m}^3; \qquad c_f = 1480 \text{ m/s} \qquad (7.13)$$

For the brass cylinder of figure 7.8 the physical parameters are:

$$\rho = 8400 \text{ kg/m}^3; \qquad c_L = 4400 \text{ m/s}; \qquad c_S = 2200 \text{ m/s} \qquad (7.14)$$

the water surrounding the cylinder has slightly different properties as that used for the plate:

$$\rho = 1000 \text{ kg/m}^3; \qquad c_f = 1500 \text{ m/s} \qquad (7.15)$$

This innocent looking difference has noticeable effects, especially on the attenuation and on the Quasi-Scholte mode.

The parameters for the hexagonal plate of figures 7.9 and 7.10 are as follows:

$$\rho = 1650 \text{ kg/m}^3 \qquad (7.16)$$

and the stiffness matrix is given in GPa by:

$$c = \begin{pmatrix} 42.1 & 18.4 & 17.1 & & & \\ & 42.1 & 17.1 & & & \\ & & 44.2 & & & \\ & & & 11.7 & & \\ & & & & 11.7 & \\ & & & & & \frac{c_{11}-c_{12}}{2} \end{pmatrix} \qquad (7.17)$$

The physical properties of the surrounding water are the same as those given in equation (7.15) above.

The PML parameters needed for computing some of the points (odd points) in the Quasi-Scholte mode of the hexagonal plate of figure 7.10 are given in table 7.2 to provide guidance. Again point number one corresponds to the

lowest frequency point of the Quasi-Scholte mode displayed in 7.10. The computation was carried out for two iterations with different $N = 100, 120$. When only a single value of N_{PML} Fraction appears in the table it means that the same value was used for both iterations; values separated by a vertical bar correspond to the N_{PML} Fraction values for the first and second iteration respectively.

Point #	1	3	5	7	9	11	13
H_{PML}/h_{sol}	50	30	20	23	18	13	12.1
N_{PML} Fraction	0.30|0.35	0.30|0.35	0.20|0.25	0.18|0.23	0.20	0.19	0.18
Attenuation (np/m) $\sim$	10^{-7}	10^{-6}	10^{-6}	10^{-6}	10^{-8}	10^{-6}	10^{-7}

Table 7.2: PML parameters for the odd points of the Quais-Scholte mode in the hexagonal plate plotted in figure 7.10. Point number 1 corresponds to the lowest frequency point of the Quasi-Scholte mode displayed. $\Delta\mathrm{Re}\{k\} = 10^{-2}\mathrm{m}^{-1}$ (giving a relative error of 10^{-4} % or less).

A similar table for the Quasi-Scholte mode in the hexagonal rod of figure 7.11 is given in table 7.3 below. The first point in the table corresponds to the lowest frequency point plotted in figure 7.11. For some combination

Point #	1	3	5	7	9	11	13	15	17
H_f/h_{sol}	55	49	29	24	20.9	18.2	12.5	10.45	10.03
N_{PML} Fraction	0.4|0.3	=	=	=	=	=	=	=	=
Attenuation (np/m) $\sim$	10^{-3}	10^{-2}	10^{-4}	10^{-7}	10^{-9}	10^{-6}	10^{-6}	10^{-6}	10^{-6}

Table 7.3: PML parameters for the odd points of the Quasi-Scholte mode in the hexagonal rod plotted in figure 7.11. Point number 1 corresponds to the lowest frequency point of the Quasi-Scholte mode displayed. $\Delta\mathrm{Re}\{k\} = 1\mathrm{m}^{-1}$ (giving a relative error of 10^{-2} % or less).

of PML parameters, negative (though very close to zero) values of the attenuation are obtained. This happens frequently since the algorithm fails to converge exactly to the theoretical value which is exactly zero. A slight change in the PML parameters solves this situation and gives a positive value of attenuation though the mode shapes is sometime slightly deteriorated. In these cases, it is the mode shape which should determine which is the appropriate combination of PML parameters rather than the value of the attenuation itself (which is very close to zero in both cases), the value of the phase velocity is left unchanged. The mode shape for the Quasi-Scholte mode plotted in figure 7.12 was obtained with the following combination of parameters: $H_f/h_{sol} = 10.8$; $N_{PML} = 0.4|0.3$ and the attenuation in (np/m) $\sim 10^{-6}$.

The physical parameters for the orthorhombic plate of figure 7.13 and for

the orthorhombic cylinder of figure 7.15 are as follows:

$$\rho = 8938.4 \text{ kg/m}^3 \qquad (7.18)$$

and the stiffness matrix is given in GPa by:

$$c = \begin{pmatrix} 210.3 & 70 & 132 & & & \\ & 231.3 & 111 & & & \\ & & 170 & & & \\ & & & 58.2 & & \\ & & & & 109.4 & \\ & & & & & 24.2 \end{pmatrix} \qquad (7.19)$$

The physical properties of the surrounding water are the same as those given in equation (7.15) above.

The PML parameters for the Quasi-Scholte mode (*all points*) in the orthorhombic plate shown in figure 7.13 are given in table 7.4 below.
  For the Quasi-Scholte mode in the orthorhombic rod shown in figure 7.15

Point #	1	2	3	4	5	6	7	8	9	10
H_f/h_{sol}	80	55	43	31	23	17.18	14.1	12.9	12.3	10.6
N_{PML} Fraction	0.35	0.20	0.19	=	0.20	=	0.30	=	=	=
Attenuation (np/m) $\sim$	10^{-7}	10^{-7}	10^{-6}	10^{-6}	10^{-6}	10^{-7}	10^{-7}	10^{-7}	10^{-6}	10^{-6}

Table 7.4: PML parameters for the odd points of the Quasi-Scholte mode in the orthorhombic plate plotted in figure 7.13. Point number 1 corresponds to the lowest frequency point of the Quasi-Scholte mode displayed. Point 3 corresponds to the mode shape of the Quasi-Scholte mode in the orthorhombic plate showing in figure 7.14. $\Delta \text{Re}\{k\} = 1\text{m}^{-1}$ (giving a relative error of 10^{-2} % or less).

the PML parameters are given in table 7.5 below.

Point #	1	3	5	7	9	11	13	15	17	19
H_f/h_{sol}	90	70	19	14	8.65	8.65	8.58	8.439	8	6.9
N_{PML} Fraction	0.7|0.6	=	=	=	=	=	0.8|0.7	=	=	=
Attenuation (np/m) $\sim$	10^{-4}	10^{-5}	10^{-3}	10^{-3}	10^{-2}	10^{-2}	10^{-4}	10^{-4}	10^{-5}	10^{-5}

Table 7.5: PML parameters for the odd points of the Quasi-Scholte mode in the orthorhombic rod plotted in figure 7.15. Point number 1 corresponds to the lowest frequency point of the Quasi-Scholte mode displayed. Point 9 corresponds to the mode shape of the Quasi-Scholte mode in the orthorhombic plate showing in figure 7.16. $\Delta \text{Re}\{k\} = (10^{-3} - 1)\text{m}^{-1}$ (giving a relative error of 10^{-3} % or less).

Chapter 8

Two-Dimensional Pseudospectral Collocation Method for Vibrating Rectangular Membranes

In non-destructive Evaluation (NDE) applications inspections and analysis of natural vibration modes in structures which have much more complex geometries than flat plates and cylindrical or spherical shells are often encountered. In most of these cases, analytical expressions are not available due to the great complexity of the equations involved and one can only resort to finite element (FE) simulations or similar methods to solve these problems. It would be interesting to explore other alternatives if only to have a wider range of approaches available to cross-check the results when some uncertainty arises.

In this chapter, one such alternative is put forward. Pseudospectral Collocation Methods (PSCM) are extremely flexible and can be generalized to study higher dimensional problems, some simple examples can be found in [25, 102]. Some problems of elastic waves such as vibrating finite membranes, plates or finite cross sectional waveguides require displacement fields which depend on two variables. It is in these situations where 2D-PSCM can be applied and in this chapter steps are taken in this direction.

The main contribution of this chapter is to extend the PSCM approach and present a two-dimensional PSCM scheme to obtain the frequencies of a rectangular vibrating plate. These results are compared to the exact solution which can be computed analytically ([6]). This is a first and necessary step towards studying the propagation of elastic waves along a waveguide with rectangular cross section which is of great practical interest. The vi-

brating rectangular membrane possesses particular interest for the latter problem because the rectangular cross section of the waveguide would have to be modelled in a similar fashion to that described for the rectangular membrane. Therefore, it is hoped that this simpler problem will help to clarify that essential part. It must also be noted that the problem of a rectangular waveguide is significantly harder since it involves a displacement three-dimensional vector field, whereas the vibrating membrane only involves a one dimensional vector field accounting for the perpendicular displacement of the membrane.

The chapter is organized as follows. In section 8.1, the two-dimensional PSCM for the rectangular vibrating membrane is presented. It is explained how to construct the two-dimensional grid as well as the corresponding differentiation matrices by using the Kronecker product of one-dimensional differentiation matrices for each independent coordinate. The results of the computation are presented in section 8.2 and they are compared to the exact solution which can be found in [6]. Section 8.3 provides a summary and discussion of the results and some suggestions for future work. The last section, 8.4, gives the numerical data used in the computation.

8.1 Two-dimensional Pseudospectral Collocation Method: Outline of the Method

In this section a simple two-dimensional PSCM scheme is presented to study a vibrating membrane. The main motivation for this is to show how to develop two-dimensional schemes in rectangular coordinates which allows the study of the problem of elastic wave propagation along a waveguide with rectangular cross section.

The problem chosen to illustrate the method is a rectangular vibrating membrane with clamped edges. This leads to a simple Laplace equation on the plane [6]. The reader not too familiar with the PSCM will find relevant background in [25] (which contains a two-dimensional example of the analogous circular problem in polar coordinates) and of particular relevance to elastic waves in [21].

The equation to be solved for the rectangular vibrating membrane is:

$$\Delta u(x, y; t) = \Big(\frac{\partial^2}{\partial x^2} + \frac{\partial^2}{\partial y^2} \Big) u(x, y; t) = \frac{1}{c^2} \frac{\partial^2}{\partial t^2} u(x, y; t) \qquad (8.1)$$

where the field $u(x, y; t)$ accounts for the out-of-plane displacement and c is the sound propagation velocity for the plate's material. The Dirichlet
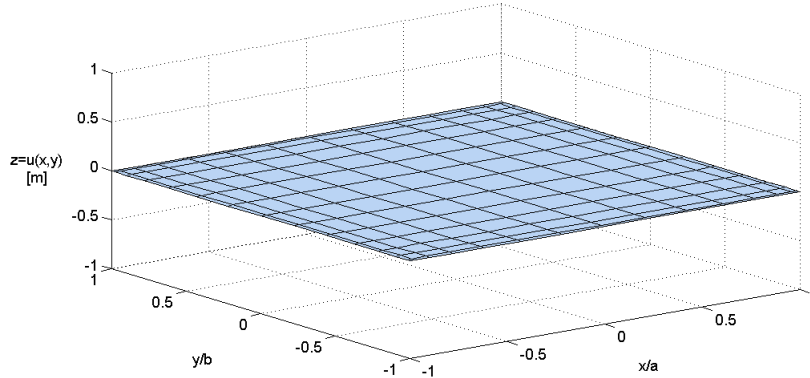
Figure 8.1: Scheme of the unperturbed flat plate of the problem with the Chebyshev grid along both adimensional coordinate axes, it can be seen how the grid becomes denser towards the boundaries. The transverse displacement is $z = u(x, y)$.

boundary conditions for a membrane with edges clamped are:

$$u(-a, y; t) = u(x, -b; t) = u(a, y; t) = u(x, b; t) = 0 \qquad (8.2)$$

For rectangular domains such as this, where the function depends on both coordinates, one needs to set up a two dimensional grid. This is in contrast to what happens in the simpler case of waveguides where invariance of the solution in the horizontal coordinate is assumed and therefore, only the through-thickness coordinate needs to be taken into account yielding a simpler one-dimensional formulation.

The PSCM is based on the discretization of the physical domain and on the subsequent substitution of the derivatives and physical quantities by their discretized analogues: differentiation matrices (DMs) and discretized vector fields. This discretization depends on the choice of the polynomial basis. For the problem at hand, where the physical domain is a two-dimensional bounded region of the plane the best choice are the Chebyshev polynomials. The $N \times N$ DMs are generated from the non-uniform Chebyshev grid of N points for each coordinate existing in the problem, two in this case, see figure (8.1) for a schematic plot of the problem's set up. The two dimensional Chebyshev has been plotted and it can be seen that the distribution of points is not even in the interval but they are clustered towards the boundaries which yields a denser grid towards the corners.

This process and relevant formulae are given in [25, 24, 45]. For details

about the one dimensional analogue applied to anisotropic elastic guided waves see [21, 46]. Accordingly, the 1-st derivatives with respect to x and y are approximated by the corresponding 1-st order Chebyshev DMs obtained from the two grids for the x and y coordinates:

$$\frac{\partial}{\partial y} \Longrightarrow \mathbf{D}_y \qquad \frac{\partial}{\partial x} \Longrightarrow \mathbf{D}_x \tag{8.3}$$

Higher order DMs are obtained by simple multiplication, that is, for the m-th derivative with respect to y the corresponding DM is given by $\mathbf{D}_y^{(m)} = (\mathbf{D}_y)^m$. Note that, different values of N can be chosen for each coordinate according to taste or discretization needs, for the purpose of illustrating the method the same N is taken here without loss of generality. In order to construct the Laplace operator for the equation (8.1), one needs to take the Kronecker product of the differentiation matrices above with the identity matrix in the other coordinate's space:

$$\Delta \longrightarrow D_x^2 \otimes I_y + I_x \otimes D_y^2 \tag{8.4}$$

By following the standard separation of variables procedure, the time-harmonic solutions sought have the form:

$$u(x, y; t) = X(x)Y(y)e^{i\omega t} \tag{8.5}$$

therefore, the spatial part of the solution to be found can be expressed as follows:

$$U(x, y) = X(x)Y(y) \longrightarrow \tilde{U} = X_x \otimes Y_y \tag{8.6}$$

Where $\tilde{U}$ is the *vector of vectors*: $\tilde{U} = \left[\tilde{U}_x(X_x \otimes Y_y), \tilde{U}_y(X_x \otimes Y_y), \tilde{U}_z(X_x \otimes Y_y) \right]^T$. Finally, taking into account the time-harmonic form of the solution and equations (8.4) and (8.6) above, the discretized equation to be solved is:

$$\left(D_x^2 \otimes I_y + I_x \otimes D_y^2 \right) \tilde{U} = -\left(\frac{\omega}{c} \right)^2 \tilde{U} \tag{8.7}$$

Or more concisely:

$$\mathfrak{L} \, \tilde{U} = \omega^2 \, \mathfrak{M} \, \tilde{U} \tag{8.8}$$

This is a conventional general matrix eigenvalue problem. One still needs to take into account the boundary conditions in equation (8.2). After the discretization described above, these are immediately transformed into the following by means of the above introduced *vector of vectors* $\tilde{U}$ (eq. (8.6)):

$$\tilde{U}(-a, y) = \tilde{U}(x, -b) = \tilde{U}(a, y) = \tilde{U}(x, b) = 0 \tag{8.9}$$

However, due to the Kronecker product, one must be a little bit more careful than in the one-dimensional case when inserting them into the discretized

Laplace operator. As in the one dimensional case [21, 46], the top and bottom rows of the matrices in each coordinate space correspond to the top and bottom boundaries of the domain, that is, $x = -a$ (bottom) corresponds to the N-th bottom row of I_x, D_x^2 or any other matrix in x-space and $x = a$ (top) corresponds to the 1-st top row. Analogous considerations hold for $y = -b, b$ and matrices in the y-space.

In order to illustrate how the boundary conditions must be inserted, it is easier to consider one of the terms in equation (8.7). The Kronecker product $D_x^2 \otimes I_y$ yields an $N^2 \times N^2$ matrix like the following:

$$\begin{pmatrix} (D_x^2)_{1j} & \mathfrak{o} & \ldots & \mathfrak{o} \\ \mathfrak{o} & (D_x^2)_{2j} & \ldots & \mathfrak{o} \\ \vdots & \vdots & \ddots & \vdots \\ \mathfrak{o} & \mathfrak{o} & \ldots & (D_x^2)_{nj} \end{pmatrix}_{N^2 \times N^2} \tag{8.10}$$

The top matrix-row $1j$, now composed of $N \times N$ matrices, corresponds to the condition $y = b$ with x taking values in its whole range according to the row considered within the matrix D_x^2; similarly for the bottom matrix-row nj which corresponds to the condition $y = -b$ with x ranging through its domain. As explained, within each of these matrix-rows, x varies through its whole range $[-a, a]$ according to the row of D_x^2 considered. Any conditions to be imposed in the ranges $(x, -b)$ and (x, b) will be inserted into these matrix-rows. These ranges (x, b) and $(x, -b)$ correspond to the following rows in the Kronecker product matrix $D_x^2 \otimes I_y$: for (x, b) rows 1 to N and for $(x, -b)$ rows $((N - 1)N + 1)$ to N^2.

The conditions on the edges $(-a, y)$ and (a, y) are imposed in a similar way. However, note now that one needs to consider only the top and bottom rows of every matrix D_x^2 and let the y coordinate range over its domain. This means one needs to insert the boundary conditions imposed on $(-a, y)$ and (a, y) in the top and bottom rows of each block $(D_x^2)_{ij}$ with $i = 2, 3..., (N-1)$ which accounts for fixing $x = -a, a$ and letting y vary from $y = -b$ to $y = b$ in each case. These ranges $(-a, y)$ and (a, y) correspond to the following rows in the Kronecker product matrix: rows $iN + 1$ with $i = 1, 2..., (N - 2)$ for the edge (a, y) and rows iN with $i = 2, 3..., (N - 1)$ for the edge $(-a, y)$. The four corners correspond to rows $1, N, ((N - 1)N + 1)$ and N^2. Similar considerations apply to the other matrix $I_x \otimes D_y^2$ in equation (8.7).

The boundary conditions in equation (8.9) are expressed by the corresponding product of identity matrices; this is the analogue of the one-dimensional case for similar clamped conditions:

$$\tilde{U} = X_x \otimes Y_y = I_x \otimes I_y \tag{8.11}$$

By taking the rows of the above Kronecker product as indicated in the two paragraphs above, inserting them into the corresponding rows on the left hand side of equation (8.7) and setting to zero the same rows on the right hand side, the boundary conditions in equation (8.9) are accounted for.

8.2 Vibrating Rectangular Membrane with a 2D-PSCM.

The above scheme has been implemented and the first modes found with excellent accuracy. The results are presented in table 8.1 along with the exact solution derived from the equation ([6]):

$$\omega_{mn}^2 = \pi^2 c^2 \left(\frac{n^2}{(2a)^2} + \frac{m^2}{(2b)^2} \right) \tag{8.12}$$

The results for the first 12 angular frequencies with $N = 30$ grid points are presented below in table 8.1. The numerical data used for this example can be found in section 8.4 at the end.

The accuracy for this simple case is strikingly good as in the case of simple one-dimensional schemes for SH modes in a plate, this is known as *spectral accuracy*, more details about the PSCM rate convergence can be found in Chapters 1 and 4 of ([25]). A discussion about the relative advantages of PSCM with respect to FE schemes can also be found in [24, 45]. For more complicated and general problems the accuracy is generally not as high but it is still very good, see [21, 46] for some one-dimensional cases and discussion. Therefore, it is expected that, thanks to the *spectral accuracy*, equally good results are obtained for more complicated two-dimensional problems.
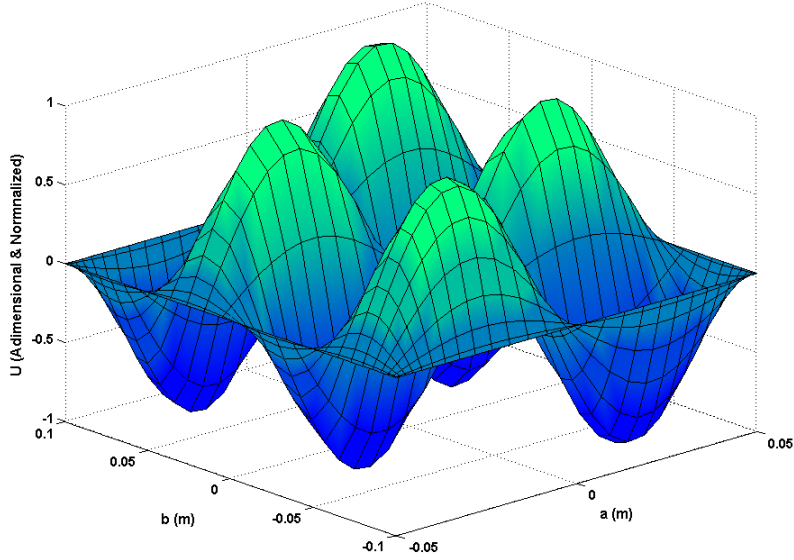
Figure 8.2: Vibration pattern for the $(n = 2, m = 4)$ mode in a rectangular clamped membrane obtained as an eigenfunction with a two-dimensional PSCM scheme.

One of the advantages of PSCM schemes is that, in addition to the eigenvalues, one also obtains the corresponding eigenfunctions with no extra coding effort. In figure 8.2, the mode's $(n = 2, m = 4)$ vibration pattern is shown.

Mode #	Exact Solution (rad Hz)	2D-PSCM (rad Hz)	Relative Error (10^{-12} %)
1	39970496340.613	39970496340.587	66.29
2	63952794144.984	63952794144.939	70.39
3	103923290485.546	103923290485.526	19.15
4	135899687557.971	135899687557.996	18.13
5	159881985362.333	159881985362.348	9.45
6	159881985362.343	159881985362.348	2.98
7	199852481702.944	199852481702.935	4.58
8	231828878775.404	231828878775.404	0.17
9	255811176579.777	255811176579.756	8.09
10	295781672920.359	295781672920.343	5.34
11	319763970724.697	319763970724.696	0.34
12	319763970724.704	319763970724.696	2.58

Table 8.1: Comparison of the results given by the 2D-PSCM and the exact solution for a rectangular vibrating membrane with clamped edges.

8.3 Discussion of Chapter 8

In this chapter, a PSCM two-dimensional new extension for a clamped vibrating rectangular membrane was put forward as a first step for modelling rectangular cross sections in waveguides with more general 2D-PSCM schemes. The results were compared with the exact solution obtained analytically [6] and both sets of solutions presented excellent agreement. The two-dimensional PSCM presented here is hoped to serve as a first step towards studying wave propagation in waveguides with rectangular cross sections where two-dimensional grids are essential.

8.4 Numerical data for examples of Chapter 8

The parameters used for the vibrating membrane of figure 8.1 are:

$$a = 50 \text{ mm}; \qquad b = 100 \text{ mm}; \qquad c = 5692 \text{ m/s} \qquad (8.13)$$

Chapter 9

Closing Remarks.

9.1 Review of Results and Conclusions.

Throughout this thesis, a Pseudospectral Collocation Method (PSCM) has been successfully developed in order to solve a range of elastic guided wave problems of particular interest to NDE. After the introduction, in the second chapter, the foundation and initial set up was laid by developing PSCM schemes for guided waves in elastic anisotropic media. The crystal classes studied ranged from the most simple isotropic media to the most general *triclinic* crystals with 21 different elastic constants. This was done for flat and cylindrical geometries, both with axial and circumferential propagation, free plates as well as for single and multiple layer systems. This is an important step forward since the triclinic material is the most general case comprising all the other cases as particular subcases and had not been solved until now due to its computational complexity. In particular, any other crystal with lower symmetry whose axes are arbitrarily oriented with respect to those of the plate can be modelled with the code developed for triclinic materials, thus, fibre composites with arbitrary orientation can now be solved. This was extremely difficult or not possible with other more conventional approaches. Attention was also given to imperfect boundary conditions which are sometimes convenient to simulate in some practical applications. Finally, fluid layers between solid layers were also considered. In these cases, it was essential to use a *hybrid description* of the fields involved: retaining the displacement field description for the solid whereas the potential description was used in the fluid layers. The results have been validated with the existing literature as well as with the results given by the software DISPERSE developed in the NDT group at Imperial College London which is based in the partial wave approach.

In the third chapter, guided waves in viscoelastic materials were studied. To account for material damping two different models were considered: *Hys-*

teretic (frequency independent) and *Kelvin-Voigt* (frequency dependent). It was also shown that the PSCM schemes needed to be modified and linearized by means of the *Companion Matrix Technique* in order to recast the problem into a general eigenvalue form which allowed for finding the complex wavenumber for a given value of the angular frequency. Thanks to its algebraic approach for solving the problem, complex eigenvalues pose no particular challenge for the PSCM. In this chapter, flat and cylindrical plates and multiple layer systems, including viscoelastic materials, were solved up to the most general anisotropy class, namely *triclinic*. Only lowly attenuated modes, *propagating modes*, with small imaginary part were considered since they are the most important for the majority of NDE applications. The generalization to viscous fluids was also addressed obtaining very good results, though cases with very low viscosity must be handled with care. A *hybrid description* was needed again for the fluid layers. The results for the cases involving fluid as well as for some others involving only isotropic materials were validated with DISPERSE and experimental data available in the literature cited in section 3.5 of Chapter 3. All the results involving viscoelastic anisotropic media were validated with Semi-Analytical Finite Element (SAFE) simulations which were designed and run by my colleague Dr. Fan Zheng. Excellent results were achieved in every case as can be seen from the examples presented in this chapter.

In the fourth chapter, the capabilities of the PSCM schemes developed in the previous chapter were further exploited to find the full three-dimensional spectrum of guided waves. This was achieved by considering also modes whose imaginary part is very high or which are purely imaginary (only arising in the case of elastic materials). Although it entailed no significant complication for the PSCM approach, this is an important achievement since three-dimensional dispersion curves are usually very hard to find by more conventional methods such as partial wave based root finding (PWRF) routines. From a practical point of view, it is often clarifying and helpful to display the dispersion curves in three dimensional space so that a better understanding of the nature of the mode is achieved since two-dimensional plots might sometimes look incomplete and confusion might arise in the areas where the modes run very close to each other.

All the examples and problems studied in the three chapters just reviewed have highlighted the advantages and robustness of the PSCM approach which are summarized here. First of all, a most remarkable feature is the conceptual simplicity of the method: the physical domain is discretized with a grid and *differentiation matrices* are computed from the chosen *global interpolant polynomials*. These matrices are used to recast the Partial Differential Equations (PDE) into matrix form thus turning the differential problem in to a purely algebraic eigenvalue problem. This simplicity allows

for extraordinary flexibility and portability of the PSCM as has been shown when solving the most general case of triclinic materials, intractable by more conventional methods, or when combining both the displacement fields and potential fields in cases where fluid layers are involved. From these two ingredients, *global interpolant polynomials* and algebraic approach, two of the most important properties and advantages of the PSCM are derived: firstly, a strikingly high accuracy in the results, known in the literature as *spectral accuracy*, which is achieved thanks to the use of *global interpolant polynomials* as opposed to the well-known *local interpolant polynomials* used in Finite Element (FE) approaches. Secondly, equally good performance when computing real and complex eigenvalues thanks to the algebraic approach which differs fundamentally from root finding routines where the roots must be sought in the complex plane rendering the calculation unstable and unreliable in many a case.

In addition, PSCM do not suffer from model-caused stiffness such as is the case in most FE approaches where the structures in the model have higher stiffness than the real ones; while this can be overcome with FE by refining the grid, the PSCM offers the advantage that this issue simply does not have to be considered. Another advantage of the PSCM is that, up to a certain number of modes (well within the practically useful margin), it is much faster than PWRF routines. This speed is illustrated in [21] with an example of an isotropic waveguide and circumferential propagation showing that the PSCM was faster than PWRF computing more than the first 300 modes. The PSCM remains much faster than the PWRF for more complicated cases too. Last but not least, and thanks again to the algebraic approach, when a problem is solved not only does one obtain the eigenvalues, which are the roots of the dispersion relation, but also the eigenvectors, which are the mode shapes for the fields involved, with no extra coding effort whatsoever.

One of the main challenges posed to all methods available for computing dispersion curves is how to link the points (roots or eigenvalues) obtained from the computation in order to trace the dispersion curves of the problem. This is non-trivial when crossings amongst modes occur and a good deal of effort and discussion has been devoted to this topic in the past years (see references given in Chapters 5 and 6). In Chapter 5, an investigation of the parity and coupling properties of the solutions in flat and cylindrical generally anisotropic plates is carried out motivated by this problem of mode crossings. The main idea for solving the problem of correctly identifying modes when they cross is to find some invariant quantity or property which is preserved throughout the dispersion curve of the mode and allows to tell one mode (or group of modes) from another.

In Chapter 5, it is shown that parity (type of symmetry or lack thereof with respect to the origin of coordinates) is the best candidate for this purpose. The analysis and investigation is based on the partial wave formalism and the PSCM is used to provide and solve numerical examples illustrating the investigation. Parity properties of solutions for some materials and commonly encountered axes configurations have been known for years and hence the focus is put on the remaining unexplained cases, including for instance triclinic, and on clarifying how they relate to the previously studied ones to make a coherent whole. It is seen how the parity properties of the solutions can be known *a priori* before any computation is done by studying the terms in the Christoffel equation for each problem and by checking the reducibility of the dispersion determinant obtained from imposing the boundary conditions. The outcome of this process shows how many independent families of modes (one for every non-reducible dispersion determinant) with or without a definite parity exist. When decoupling of the displacement vector field components occurs, the problem is simplified even further (consider Lamb and SH modes for instance) but the same considerations of parity and determinant reducibility apply to each family. After having dealt with flat plates, cylindrical plates and rods are considered though the analysis is much simpler as can be seen in section 5.2.

Chapter 6 presents a generalization of the above developed approach to study parity and coupling properties in multiple layer systems. The analysis is again carried out for the flat and cylindrical cases and based on the partial wave formalism. In these cases, coupling between modes due to the presence of interfaces between the different layers plays a much more important role in the final properties of the solution than in single-layered systems and gives rise to interesting combinations and non-trivial situations. By grouping the different crystal classes into fewer categories according to the previously derived parity and coupling properties of the guided wave solutions, it is possible to investigate the different combinations that might arise when multiple layers are considered. The partial wave approach is still the key to this analysis and the PSCM is used to support the conclusions with examples. The most important result of this chapter is that guided wave solutions for multiple layer flat systems will only present a definite parity when each of the layers composing the aggregate, considered individually, support modes with the same parity properties. This gives rise to symmetric and antisymmetric families of modes in the guided wave solution of the multilayer system which are independent of each other. The same is valid if one considers mode decoupling: for the global solution to be decoupled each of the individual layers must present decoupling. In section 6.2, cylindrical systems with multiple layers are considered by generalizing the investigation carried out in section 5.2 for their single layer counterparts. The analysis is again much simpler than in the flat case.

The results presented in Chapter 6, as those derived in the previous chapter, allow for an improvement in the computation of dispersion curves for multiple layer systems. Once the multiple layer system is set up, one can know before any computation is done how the modes' families are going to be classified and thus design a code accordingly in order to plot one independent family of modes at a time and avoid the problem of mode crossing. It is remarkable and worth emphasizing that these results are general in the sense that they can be applied to *any* numerical method used to compute dispersion curves and it is by no means restricted to the PSCM employed and developed in this thesis and the examples within.

In the seventh chapter, a new combination of a PSCM and *Perfectly Matched Layer* (PML) is put forward in order to solve the problem of an isotropic and transversely isotropic plates immersed in ideal fluid. Its cylindrical analogue is also developed for axially propagating modes in an isotropic and transversely isotropic cylinders immersed in ideal fluid. The results are presented for a range of frequencies which requires a fine tuning of the parameters of the algorithm in each of the regions. Particular attention is given to the trapped modes which normally lie amongst spurious radiative modes and require a careful filtering, normally requiring several filtering stages. This is explained in detail and a table shows the values used in the computation. The results and their potential are excellent taking into account the complexity of the problem and the fact that very little was done in terms of combining PSCM and PML. The results are validated with solutions given by DISPERSE. Some minor discrepancies as well as their possible causes are also discussed.

And last but not least, in Chapter 8 a two-dimensional PSCM method for a rectangular vibrating membrane was presented. The main features of the extension to two-dimensional grids were outlined and illustrated with the simple example of the rectangular membrane whose solution can be computed analytically thus providing a perfect test-bench for the 2D PSCM. These two-dimensional grids are the cornerstone for modelling waveguides whose cross section has a rectangular cross section. The code presented for a rectangular membrane cannot be directly applied to the rectangular waveguide case but the methodology for constructing the grid and boundary conditions can be extended to more general cases such as waveguides with rectangular cross section. It is hoped that this chapter encourages further developments in this direction.

9.2 Future Work.

The first and most immediate work to be done is to put into practice in a stand-alone programme the results derived in Chapters 5 and 6. This would entail designing a programme which, by itself, could classify the problem at hand according to the findings presented in these chapters and thus select the appropriate set of codes to compute the independent families of modes separately. Some work has been done in this direction already for the simplest case of single elastic flat plates and the results are good so it is hoped that the extension for multiple layer systems will be just as successful.

Problems of guided waves in viscoelastic materials will also benefit from this by plotting the different families of modes separately as explained. In these cases, since the dispersion curves now lie in three dimensional space, and not in a plane as in the elastic case, the problem of crossings does not occur and any interpolation routine should work for tracing the dispersion curves through the computed collection of points. However, it must be noted that complex numbers are not a *totally ordered set* like the real numbers. Hence, a classification of modes can only be carried out according to the modulus of the eigenvalues and care must be taken to track each mode correctly without assuming that the lowest mode in one frequency iteration will correspond to the lowest mode in the next. In general this will be true as long as the two frequencies lie close enough to each other. If the above does not give the desired results, the energy flux and direction should be considered as a further mode property to aid in the tracing of a dispersion curve. Biorthogonality relations [5] might help as well.

In the problem of embedded structures only the foundations have been laid with the codes and cases presented in Chapter 7. However, the full potential of these two codes has not been exploited in full due to lack of time. It is immediately possible to perform computations for the very same cases of plate and cylinder but including material damping in the structure by simply adding the corresponding imaginary part to the elastic constants of the material. In such cases, attenuation of the waves is caused because of two different physical mechanisms: energy leakage into the infinite surrounding medium and material damping. However, one must be careful when studying the attenuated modes since for large values of material damping the dispersion loci can be quite different from their elastic counterparts. All the mode post processing and general principles of exponential decay within the PML described in Chapter 7 for leaky modes remain valid in these cases too and, in fact, one should expect the material damping to facilitate the exponential decay at infinity.

It would also be interesting to plot the full three-dimensional spectrum of

embedded structures; this would not entail any further modification of the codes but extending the post processing to eigenvalues with higher imaginary parts. This might sound easy but it can be a lot harder than in the case of free structures since the true modes might now lie hidden amongst the spurious radiative modes. Energy and convergence arguments such as those presented in Chapter 7 should help in this task.

Performing the same computations for elastic or viscoelastic anisotropic materials whose stiffness matrix has block form (isotropic, cubic, hexagonal, tetragonal and orthorhombic) could also be done with the existing codes. In fact, the codes used for the isotropic cases given in Chapter 7 are written for an orthorhombic material, so one only needs to change the input of the code to obtain the results for leaky modes in an orthorhombic plate straightaway and begin with its analysis. Except for isotropic and transversely isotropic (hexagonal) materials, to the best of my knowledge, no further results about leaky waves in anisotropic structures have been published and it would be very interesting to see what changes occur in the dispersion loci when leakage is present. Given its novelty, a very exhaustive and careful study of each mode would be necessary in order to ensure that one is picking up the right solution. Confronting the results with a SAFE simulation would definitely desirable.

A few tests were also run for inhomogeneous anisotropic materials where the stiffness matrix entries varied according to simple functions of the thickness of the structure. These codes reproduced the appropriate limit of the corresponding homogeneous materials and showed excellent convergence. Unfortunately, there is not much material available for validation and comparison but this would also be worth investigating taking into account the increasing interest in functionally graded materials.

Continuing the task begun in Chapter 8 with two-dimensional grids would open a new path towards modelling waveguides with rectangular finite cross section and propagation in the longitudinal direction. The example presented in this thesis is mostly of academic and illustrative interest and it is hoped that it will serve to encourage further investigation in this direction. A challenge that will have to be addressed is to account for the different and concurring boundary conditions at the corners of the domain. A possible alternative is to modify the polynomials accordingly so that the boundary conditions are automatically taken into account. However, this would need to be tested first in simpler cases and then generalized to more complicated and realistic settings. Should this approach work for a single waveguide, it could be possible to generalize it to the "multiple-layer" analogue in two dimensions which might allow for constructing models for guided waves with more complex cross sections such as T or I. Although it is possible to model

such structures with FE simulations, achieving this with the PSCM would bring all the advantages and flexibility of the PSCM into a new area within the field of elastic guided waves.

Finally, the numerical methods employed in this thesis could be extended to more complicated settings including piezoelectric materials where the magnetic field is coupled to the tension field. Some areas from material science dealing with phononic and photonic interactions in crystals could also make use of similar numerical schemes to address their problems.

Bibliography

[1] Mindlin, R. D., 1960. "Waves and vibrations in isotropic, elastic plates". *Structural Mechanics. (Eds. J.N. Goodier and N. Hoff)*, pp. 199–323.

[2] Pao, Y.-H., 1962. "The dispersion of flexural waves in an elastic circular cylinder, part ii". *Journal of Applied Mechanics*, **29**, pp. 61–64.

[3] Mindlin, R. D., and Pao, Y.-H., 1960. "Dispersion of flexural waves in elastic circular cylinder". *Journal of Applied Mechanics*, **27**, pp. 513–520.

[4] Gazis, D. C., 1958. "Exact analysis of the plane-strain vibrations of thick walled hollow cylinders". *J. Acoust. Soc. Am.*, **30**, pp. 786–794.

[5] Auld, B. A., 1990. *Acoustic Fields and Waves in Solids, 2nd Ed.* Krieger Publishing Company, Florida, pp. pp. 1–878.

[6] Graff, K. F., 1991. *Wave Motion in Elastic Solids.* Dover, New York, pp. pp. 1–649.

[7] Achenbach, J. D., 1973. *Wave propagation in elastic solids.* North-Holland, Amsterdam, pp. pp. 1–440.

[8] Solie, L. P., and Auld, B. A., 1973. "Elastic waves in free anisotropic plates". *Journal of the Acoustical Society of America*, **54 (1)**, pp. 50–65.

[9] Nayfeh, A. H., and Chimenti, D. E., 1989. "Free wave propagation in plates of general anisotropic media". In Review of Progress in Quantitative Non-destructive Evaluation, D. Thompson and D. Chimenti, eds., Plenum Press, New York, p. 181.

[10] Nayfeh, A. H., 1989. "The propagation of horizontally polarized shear waves in multilayered anisotropic media". *Journal of the Acoustical Society of America*, **86 (5)**, pp. 2007–2012.

[11] Nayfeh, A. H., 1990. "The general problem of elastic wave propagation in multilayered anisotropic media". *Journal of the Acoustical Society of America,* **89 (4)**, pp. 1521–1531.

[12] Rokhlin, S., and Wang, Y., 2002. "Stable recursive algorithm for elastic wave propagation in layered anisotropic media: stiffness matrix method". *Journal of the Acoustical Society of America,* **112 (3)**, pp. 822–834.

[13] Li, Y., and Thompson, R. B., 1990. "Influence of anisotropy on the dispersion characteristics of guided ultrasonic plate modes". *Journal of the Acoustical Society of America,* **87 (5)**, pp. 1911–1931.

[14] Lowe, M., 1995. "Matrix techniques for modeling ultrasonic waves in multilayered media". *IEEE Trans. Ultrason. Ferroelectr. Freq. Control,* **42**, pp. 525–542.

[15] Pavlakovic, B., Lowe, M., Alleyne, D., and Cawley, P., 1987. "Disperse: A general purpose program for creating dispersion curves". *Review of Progress in Quantitative Non-destructive Evaluation,* **16**, p. 185.

[16] Pavlakovic, B., and Lowe, M., 2013. *DISPERSE User's Manual, Version 2.0.20B.* pp. pp. 1–209.

[17] Castaings, M., and Lowe, M., 2008. "Finite element model for waves guided along solid systems of arbitrary section coupled to infinite solid media". *Journal of the Acoustical Society of America,* **123 (2)**, pp. 696–708.

[18] Bartoli, I., Marzani, A., Lanza di Scalea, F., and Viola, E., 2006. "Modeling wave propagation in damped waveguides of arbitrary cross-section". *Journal of Sound and Vibration,* **295**, pp. 685–707.

[19] Fan, Z., Castaings, M., Lowe, M. J. S., Biateau, C., and Fromme, P., 2013. "Feature-guided waves for monitoring adhesive shear modulus in bonded stiffeners". *NDT & E Int.,* **54**, pp. 96–102.

[20] Towfighi, S., Kundu, T., and Ehsani, M., 2002. "Elastic wave propagation in circumferential direction in anisotropic cylindrical curved plates". *Journal of Applied Mechanics,* **69**, pp. 283–291.

[21] Adamou, A., and Craster, R., 2004. "Spectral methods for modelling guided waves in elastic media". *Journal of the Acoustical Society of America,* **116 (3)**, pp. 1524–1535.

[22] Karpfinger, F., Gurevich, B., and Bakulin, A., 2008. "Modeling of axisymmetric wave modes in a poroelastic cylinder using the spectral

method". *Journal of the Acoustical Society of America,* **124 (4)**, pp. EL230–EL235.

[23] Fornberg, B., 1996. *A Practical Guide to Pseudoespectral Methods.* pp. pp. 1–231.

[24] Boyd, J. P., 2001. *Chebyshev and Fourier Spectral Methods.* Dover, New York, pp. pp. 1–688.

[25] Trefethen, L., 2000. *Spectral Methods in MATLAB.* SIAM, Philadelphia, pp. pp. 1–181.

[26] Fiorito, R., Madigosky, W., and Überall, H., 1979. "Resonance theory of acoustic waves interacting with an elastic plate.". *Journal of the Acoustical Society of America,* **66 (6)**, pp. 1857–1866.

[27] Überall, H., Hosten, B., Deschamps, M., and Gerard, A., 1994. "Repulsion of phase-velocity dispersion curves and the nature of plate vibrations.". *Journal of the Acoustical Society of America,* **96 (2)**, pp. 908–917.

[28] Werby, M. F., and Überall, H., 2002. "The analysis and interpretation of some special properties of higher order symmetric lamb waves: The case for plates..". *Journal of the Acoustical Society of America,* **111 (6)**, pp. 2686–2691.

[29] Simonetti, F., and Lowe, M., 2005. "On the meaning of lamb mode nonpropagating branches". *Journal of the Acoustical Society of America,* **118(1)**, pp. 186–192.

[30] Rokhlin, S., Chimenti, D., and Nayfeh, A., 1989. "On the topology of the complex wave spectrum in a fluid-coupled elastic layer". *Journal of the Acoustical Society of America,* **85 (3)**, pp. 1074–1080.

[31] Rose, J. L., 1999. *Ultrasonic Waves in Solid Media.* Cambridge University Press, Cambridge, pp. pp. 1–476.

[32] Nayfeh, A. H., and Chimenti, D. E., 1989. "Free wave propagation in plates of general anisotropic media". *Journal of Applied Mechanics,* **56**, pp. 881–886.

[33] Onoe, M., McNiven, H. D., and Mindlin, R. D., 1962. "Dispersion of axially symmetric waves in elastic rods". *Journal of Applied Mechanics,* **29**, pp. 61–64.

[34] Zemanek, J., 1972. "An experimental and theoretical investigation of elastic wave propagation in a cylinder". *Journal of the Acoustical Society of America,* **51**, pp. 265–283.

[35] Vasudeva, R., Sudheer, G., and Vema, A., 2008. "Dispersion of circumferential waves in cylindrically anisotropic layered pipes in plane strain". *Journal of the Acoustical Society of America,* **123 (6)**, pp. 4147–4151.

[36] Karpfinger, F., Gurevich, B., and Bakulin, A., 2008. "Modeling of wave dispersion along cylindrical structures using the spectral method". *Journal of the Acoustical Society of America,* **124 (2)**, pp. 859–865.

[37] Yu, B., Yang, S., Gan, C., and Lei, H., 2013. "A new procedure for exploring the dispersion characteristics of longitudinal guided waves in a multilayered tube with weak interface". *Journal of Nondestructive Evaluation,* **32 (3)**, pp. 263–276.

[38] Levesque, D., and Piche, L., 1992. "A robust transfer matrix formulation for the ultrasonic response of multi-layered absorbing media". *J. Acoust. Soc. am.,* **92**, pp. 452–467.

[39] Hosten, B., and Castaings, M., 2003. "Surface impedance matrices to model the propagation in multilayered media". *Ultrasonics,* **41**, pp. 501–507.

[40] Gavric, L., 1995. "Computation of propagative waves in free rail using a finite element technique". *Journal of Sound Vibration,* **185**, p. 531543.

[41] Castaings, M., Bacon, C., Lowe, M., and Fan, Z., 2008. "Torsional waves propagation along a waveguide of arbitrary cross section immersed in a perfect fluid". *Journal of the Acoustical Society of America,* **124 (4)**, pp. 2002–2010.

[42] Lowe, M., and Fan, Z., 2009. "Elastic waves guided by a welded joint in a plate". *Proceedings of the Royal Society A 2009 465,* **124 (4)**, pp. 2053–2068.

[43] Marzani, A., Viola, E., Bartoli, I., Lanza di Scalea, F., and Rizzo, P., 2008. "A semi-analytical finite element formulation for modeling stress wave propagation in axisymmetric damped waveguides". *Journal of Sound and Vibration,* **318**, pp. 488–505.

[44] Gottlieb, D., and Orszag, S., 1977. *Numerical Analysis of Spectral Methods: Theory and Applications.* SIAM, Pennsylvania, pp. pp. 1–179.

[45] Weideman, J., and Reddy, S., 2000. "A matlab differentiation matrix suite". *ACM Transactions on Mathematical Software,* **26 (4)**, pp. 465–519.

[46] Hernando Quintanilla, F., Lowe, M., and Craster, R., 2015. "Modelling guided elastic waves in generally anisotropic media using a spectral collocation method". *Journal of the Acoustical Society of America,* **137 (3)**, pp. 1180–1194.

[47] Karpfinger, F., Valero, H., Gurevich, B., Bakulin, A., and Sinha, B., 2010. "Spectral-method algorithm for modeling dispersion of acoustic modes in elastic cylindrical structures". *Geophysics,* **75 (3)**, pp. H19–H27.

[48] Zharnikov, T., Syresin, D., and Hsu, C.-J., 2013. "Application of the spectral method for computation of spectrum of anisotropic waveguides". In Proceedings on Meetings on Acoustics, Acoustical Society of America.

[49] Rokhlin, S., and Wang, Y., 1991. "Analysis of boundary conditions for elastic wave interaction with an interface between two solids". *Journal of the Acoustical Society of America,* **89 (2)**, pp. 503–515.

[50] Dieulesaint, E., and Royer, D., 1996. *Elastic Waves in Solids.* Springer Verlag, Berlin Heidelberg, pp. pp. 1–392.

[51] Kaplunov, J., Kossovich, L. Y., and Nolde, E., 1997. *Dynamics of thin walled elastic bodies.* Elsevier, New York, pp. pp. 1–240.

[52] Wang, C., Reddy, J., and Lee, K., 2000. *Shear deformable beams and plates. Relationships with classical solutions.* Elsevier, New York, pp. pp. 1–312.

[53] Viktorov, I. A., 1967. *Rayleigh and Lamb Waves.* Plenum, New York, pp. pp. 1–168.

[54] Kreiss, H., and Oliger, J., 1972. "Comparison of accurate methods for the integration of hyperbolic equations". *Tellus,* **24**, p. 199.

[55] Orszag, S., 1972. "Comparison of pseudospectral and spectral approximation". *Stud. Appl. Math.,* **51**, p. 253.

[56] Fornberg, B., 1975. "On a fourier method for the integration of hyperbolic equations". *SIAM (Soc. Ind. Appl. Math.,* **12**, p. 509.

[57] Karpfinger, F., Valero, H., Gurevich, B., Bakulin, A., and Sinha, B., 2010. "Spectral-method algorithm for modeling dispersion of acoustic modes in elastic cylindrical structures". *Geophysics,* **75 (3)**, pp. H19–H27.

[58] Kocabas, S., Veronis, G., Miller, D., and Fan, S., 2009. "Modal analysis and coupling in metal-insulator-metal waveguides". *Physical Review B,* **79**, p. 035120.

[59] Gridin, D., Adamou, A., and Craster, R., 2004. "Electronic eigenstates in quantum rings: Asymptotics and numerics". *Physical Review B,* **69**, p. 155317.

[60] Nagy, P. B., and Nayfeh, A. H., 1996. "Viscosity induced attenuation of longitudinal guided waves in fluid-loaded rods". *Journal of the Acoustical Society of America,* **100 (3)**, pp. 1501–1508.

[61] Cawley, P., Lowe, M., and Neau, G., 2001. Understanding attenuative lamb wave propagation in composites. Tech. rep., DERA.

[62] Bernard, A., Lowe, M., and Deschamps, M., 2001. "Guided waves energy velocity in absorbing and non-absorbing plates". *Journal of the Acoustical Society of America,* **110 (1)**, pp. 186–196.

[63] Hernando Quintanilla, F., Fan, Z., Lowe, M., and Craster, R., 2015. "Guided waves' dispersion curves in anisotropic viscoelastic single- and multi-layered media". *Proceedings of the Royal Society A,* **471**, pp. 1–23.

[64] Bridges, T., and Morris, P., 1984. "Differential eigenvalue problems in which the parameter appears nonlinearly". *Journal of Computational Physics,* **55**, pp. 437–460.

[65] Pagneux, V., and Maurel, A., 2001. "Determination of lamb mode eigenvalues". *Journal of the Acoustical Society of America,* **110(3)**, pp. 1307–1314.

[66] Postnova, J. A., 2008. "Trapped modes in non-uniform elastic waveguides: asymptotic and numerical methods". PhD thesis, Imperial College London.

[67] Hayashi, T., Song, W. J., and Rose, J. L., 2003. "Guided wave dispersion curves for a bar with an arbitrary cross-section, a rod and rail example". *Ultrasonics,* **41**, pp. 175–183.

[68] Wilcox, P., Evans, M., Lowe, M. J. S., and Cawley, P., 2002. "Dispersion and excitability of guided acoustic waves in isotropic beams with arbitrary cross-section". In Review of Progress in Quantitative Nondestructive Evaluation, D. Thompson and D. Chimenti, eds., Vol. 21, Plenum Press, New York, pp. 203–210.

[69] Predoi, M. V., Castaings, M., Hosten, B., and Bacon, C., 2007. "Wave propagation along transversely periodic structures.". *Journal of the Acoustical Society of America,* **121**, pp. 1935–1944.

[70] Nagy, P. B., and Nayfeh, A. H., 1997. "Excess attenuation of leaky lamb waves due to viscous fluid loading". *Journal of the Acoustical Society of America,* **101 (5)**, pp. 2649–2658.

[71] Ma, J., Lowe, M., and Simonetti, F., 2007. "Measurement of the properties of fluids inside pipes using guided longitudinal waves". *IEEE Transactions on Ultrasonics, Ferroelectrics, and Frequency Control,* **54 (2)**, pp. 647–658.

[72] Kumar, R., 1972. "Dispersion of axially symmetric waves in empty and fluid-filled cylindrical shells". *Geophysics,* **27**, pp. 317–329.

[73] Castaings, M., Le Clezio, E., and Hosten, B., 2002. "Modal decomposition method for modeling the interaction of lamb waves with cracks". *Journal of the Acoustical Society of America,* **112 (6)**, pp. 2567–2582.

[74] Hernando Quintanilla, F., Lowe, M., and Craster, R., 2015. "Full 3d dispersion curve solutions for guided waves in generally anisotropic media". *Journal of Sound and Vibration,* **363**, p. 545559.

[75] Rokhlin, S., Chimenti, D., and Nagy, P., 2011. *Physical Ultrasonics of Composites.* Oxford University Press,Oxford, pp. 1–378.

[76] Brown, J. M., Abramson, E. H., and Angel, R. J., 2006. "Triclinic elastic constants for low albite". *Physics and Chemistry of Minerals,* **33 (4)**, pp. 256–265.

[77] Shuvalov, A. L., 1999. "On the theory of wave propagation in anisotropic plates.". *The Royal Society,* **456**, pp. 2197–2222.

[78] Ting, T. C. T., 1996. *Anisotropic Elasticity: Theory and Applications.* Oxford University Press,Oxford, pp. 1–592.

[79] Morse, R. W., 1954. "Compressional waves along an anisotropic circular cylinder having hexagonal symmetry". *Journal of the Acoustical Society of America,* **26**, pp. 1018–1021.

[80] Thomson, W., 1950. "Transmission of elastic waves through a stratified solid medium". *Journal of Applied Physics,* **21 (89)**, pp. 89–93.

[81] Haskell, N. A., 1951. "The dispersion of surface waves in multilayered media". *Bulletin of the Seismological Society of America*, pp. 17–34.

[82] Thrower, E. N., 1964. "The computation of the dispersion of elastic waves in layered media". *Journal of Sound and Vibration,* **2 (3)**, pp. 210–226.

[83] Karpfinger, F., Valero, H., Gurevich, B., Bakulin, A., and Sinha, B., 2010. "Tube wave signatures in cylindrically layered poroelastic media computed with spectral method". *Geophysical Journal International,* **183**, pp. 1005–1013.

261

[84] Nayfeh, A. H., 1995. *Wave Propagation in Layered Anisotropic Media: with Application to Composites.* North Holland series in Applied Mathematics and Mechanics (Elsevier)., pp. 1–329.

[85] Shuvalov, A. L., Poncelet, O., and Deschamps, M., 2006. "Analysis of the dispersion spectrum of fluid-loaded anisotropic plates: leaky-wave branches.". *Journal of Sound and Vibration,* **296**, pp. 494–517.

[86] Ahmad, F., Kiyani, N., Yousaf, F., and Shams, M., 2002. "Guided waves in a fluid-loaded transversely isotropic plate". *Mathematical Problems in Engineering,* **8 (2)**, pp. 151–159.

[87] Berenger, J., 1994. "A perfectly matched layer for the absorption of electromagnetic waves.". *Journal of Computational Physics,* **114**, pp. 185–200.

[88] Basu, U., and Chopra, A. K., 2003. "Perfectly matched layers for time-harmonic elastodynamics of unbounded domains: theory and finite-element implementation.". *Computer Methods in applied mechanics and engineering,* **192**, pp. 1337–1375.

[89] Qi, Q., and Geers, T., 1998. "Evaluation of the perfectly matched layer for computational acoustics.". *Journal of Computational Physics,* **139**, pp. 166–183.

[90] Treyssede, F., Nguyen, K.-L., A.-S., B.-B., and C., H., 2012. "On the use of a safe-pml technique for modelling two-dimensional open elastic wavegudies.". In Proceedings of the Acoustics 2012 Nantes Conference, Societe Francaise d'Acoustique, pp. 674–678.

[91] Treyssede, F., Nguyen, K.-L., A.-S., B.-B., and C., H., 2014. "Finite element computation of trapped and leaky elastic waves in open stratified waveguides.". *Wave Motion,* **51**, pp. 1093–1107.

[92] Nguyen, K.-L., Treyssede, F., and C., H., 2015. "Numerical modeling of three-dimensional open elastic waveguides combining semi-analytical finite element and perfectly matched layer methods". *Journal of Sound and Vibration,* **344**, pp. 158–178.

[93] Nagy, P. B., 1995. "Longitudinal guided wave propagation in a transversely isotropic rod immersed in fluid.". *Journal of the Acoustical Society of America,* **98 (1)**, pp. 454–457.

[94] Pavlakovic, B., and Lowe, M., 1999. "A general purpose approach to calculating the longitudinal and flexural modes of multi-layered, embedded, transversely isotropic cylinders". *Review of Progress in Quantitative Non-destructive Evaluation,* **18**, pp. 239–246.

[95] Sinha, B. K., Plona, T. J., Kostek, S., and Chang, S.-K., 1992. "Axisymmetric wave propagation in fluid-loaded cylindrical shells.". *Journal of the Acoustical Society of America,* **92 (2)**, pp. 1132–1155.

[96] Aristegui, C., Lowe, M., and Cawley, P., 2001. "Guided waves in fluid-filled pipes surrounded by different fluids.". *Ultrasonics,* **39**, pp. 367–375.

[97] Fan, Z., Lowe, M., Castaings, M., and Bacon, C., 2008. "Torsional waves propagation along a waveguide of arbitrary cross section immersed in a perfect fluid.". *Journal of the Acoustical Society of America,* **124 (4)**, pp. 2002–2010.

[98] Mazzotti, M., Marzani, A., and Bartoli, I., 2014. "Dispersion analysis of leaky guided waves in fluid-loaded waveguides of generic shape.". *Ultrasonics,* **54 (1)**, pp. 408–418.

[99] Collino, F., and Monk, P., 1996. "The perfectly matched layer in curvilinear coordinates". *Institut National de Recherche en Informatique et en Automatique,* **Rapport de Recherche 3049**, pp. 1–52.

[100] Teixeira, F., and Chew, F. C., 1997. "Pml-fdtd in cylindrical and spherical grids". *IEEE Microwave and guidedwave letters,* **7 (9)**, pp. 285–287.

[101] Johnson, S. G., 2010. "Notes on perfectly matched layers (pmls)". *Notes for the courses 18.369 and 18.336 at MIT: http://math.mit.edu/ stevenj/18.369/pml.pdf,* pp. 1–18.

[102] Skelton, E. A., Adams, S. D. M., and Craster, R. V., 2007. "Guided elastic waves and perfectly matched layers.". *Wave Motion,* **44**, pp. 573–592.

[103] Kim, S., and Pasciak, J. E., 2009. "The computation of resonances in open systems using a perfectly matched layer.". *Mathematics of Computation,* **78 (267)**, pp. 1375–1398.

[104] Zworski, M., 2002. "Numerical linear algebra and solvability of partial differential equations.". *Comun. Math. Phys.,* **229**, pp. 293–307.

[105] Kim, S., and Pasciak, J. E., 2010. "Analysis of the spectrum of a cartesian perfectly matched layer (pml) approximation to acoustic scattering problems.". *Journal of Mathematical Analysis and Applications,* **361**, pp. 420–430.

[106] Kim, S., 2014. "Cartesian pml approximation to resonances in open systems in $\mathbb{R}^2$.". *Applied Numerical Mathematics,* **81**, pp. 50–75.

[107] Collin, R. E., 1960. *Field Theory of Guided Waves.* McGraw-Hill, New York, pp. 1–606.

[108] Cegla, F. B., Cawley, P., and Lowe, M. J. S., 2005. "Material property measurement using the quasi-scholte modea waveguide sensor.". *J. Acoust. Soc. Am.,* **117 (3)**, pp. 1098–1107.

[109] Cegla, F. B., Cawley, P., and Lowe, M. J. S., 2006. "Fluid bulk velocity and attenuation measurements in non-newtonian liquids using a dipstick sensor.". *Measurement Science and Technology-IOP,* **17**, pp. 264–274.

[110] Shuvalov, A. L., 2002. "Theory of plane subsonic elastic waves in fluid-loaded anisotropic plates.". *Proceedings of the Royal Society,* **458**, pp. 1323–1352.

[111] Shuvalov, A. L., Poncelet, O., and Deschamps, M., 2006. "Analysis of the dispersion spectrum of fluid-loaded anisotropic plates: flexural-type branches and real-valued loops.". *Journal of Sound and Vibration,* **290**, pp. 1175–1201.